Alena Ayzenberg

Transmission-Propagation Operator Theory and Tip-Wave Superposition Method for sub-salt shadow wavefield description

Thesis for the degree of Philosophiae Doctor

Trondheim, October 2015

Norwegian University of Science and Technology
Faculty of Engineering Science and Technology
Department of Petroleum Engineering
and Applied Geophysics

NTNU
Norwegian University of
Science and Technology

NTNU
Norwegian University of Science and Technology

Thesis for the degree of Philosophiae Doctor

Faculty of Engineering Science and Technology Department
of Petroleum Engineering and Applied Geophysics

ISBN 978-82-326-1188-1 (printed ver.)
ISBN 978-82-326-1189-8 (electronic ver.)
ISSN 1503-8181

Doctoral theses at NTNU, 2015:266

Printed by NTNU Grafisk senter

“Everything is hard before it is easy” – von Goethe.

Summary

TPOT&TWSM. Synthetic wave modeling in media with interfaces of complex geometrical shape is one of the main problems in the mathematical wave theory and its applications. Oil companies are concerned with increasing the resolution capability of seismic data for complex oil-and-gas deposits associated with salt domes, basalt traps, reefs, lenses, etc. Specialists and engineers traditionally apply numerical or approximate analytical methods to search for a compromise between the modeling speed and its correctness. In inhomogeneous block media with complex shaped intefraces, there is a problem of describing separate wave fragments (for example, primary waves), not only describing the total wavefield. This separate description of any wavefield fragments has triggered this study. We therefore propose applying the rigorous analytical Transmission-Propagation Operator Theory (TPOT) in terms of operators of propagation in blocks and transmission (reflection/refraction) at curved interfaces between the blocks. This theoretical approach allows the solution of different seismic problems in inhomogeneous media with 'shadow' zones of different complexity. The term shadow means zones where the rays penetrate according to the generalized Fermat's principle, not the conventional Fermat's principle. In addition to TPOT, we have modified the Tip-Wave Superposition Method (TWSM) on a Graphics Processing Unit (GPU) cluster in the mid-frequency range accounting for shadow zones. Publications demonstrate that there is good comparison between the TWSM results and the laboratory observations, numerical solvers and other analytical solutions. The investigation of TPOT&TWSM is so far on the canonical models level. We further plan to consider real models as well, but this is not discussed in the present thesis.

TPOT is based on two main theoretical principles: 1) rigorous explicit description of the propagation operators in domains/layers; the propagation in shadow zones is handled by the generalization of the conventional Fermat's and Huygens' principles for an arbitrary boundary case; and 2) rigorous explicit representation of the transmission (reflection/refraction) operators at curved interfaces; the transmission at the curved interface is handled by the generalization of the conventional Snell's law and the conventional plane wave transmission (reflection/refraction) coefficients. TPOT is a universal solution for wave problems in complex media because it solves the problem rigorously; this solution describes the total wavefield and its separate wave fragments.

Feasible fundamental solution (FFS) in shadow. In all problems with curved interfaces, shadow zones will be obtained because the concave parts of the interfaces create shadows behind. In TPOT&TWSM, shadow is handled as follows. All the interface points are connected to each other by a straight segment. If the segment intersects the interface, we consider that these two points do not 'see' each other, otherwise they do 'see' each other. After this procedure, propagation is 'allowed' only between those points which 'see' each other. A shadow function is responsible for the removal of the propagation between those points which do not 'see' each other. This shadow function is added in the kernel of the conventional propagation Kirchhoff-type operator and, therefore, corrects for the Green's function in the kernel according to the shadow zones present. Consequently this new kernel is feasible and handles shadow zones. We call it the 'feasible fundamental solution' (or the feasible Green's function). Having this feasible kernel, the propagation operator also becomes feasible and is used as a propagation computational tool in shadow.

Generalized plane waves are an analog of the conventional transmission (reflection/refraction) plane waves for the curved interface case. This generalization is obtained by introducing a local coordinate system which is fixed at the reference interface point, and leads to a space-spectral form of the boundary conditions. The new kernel of the transmission operator is the transmission coefficient based on the generalized plane wave.

TWSM computes the TPOT analytical solution in the mid-frequency range on a GPU cluster and visualizes it on a seismogram. Earlier, TWSM was run on conventional parallel systems, but we now have improved the execution time by implementing this program on the GPU system. It approximates the operators of propagation in blocks and transmission at curved interfaces in the mid-frequency (seismic frequency) range. TPOT principle 1 leads to the application of TWSM to forward and inverse seismic problems by separate wavefield description; it is done by TWSM description of the wavefield in the form of tip-wave beams, connecting the elements of the seismic model. The TWSM description of the wavefield in domains/layers with geometrical shadow zones is done by accounting for shadow by correcting the propagation operator kernel. This is a generalization of such cases as edge and tip waves from sharp edges and vertices; and cascade diffraction, for example creeping waves and 'whispering galleries' bending along the concave parts of interfaces. TPOT principle 2 leads to TWSM evaluation of the transmitted tip-wave beams accounting for head waves at curved interfaces. The transmission operators at curved interfaces are approximated by the effective (integrated) transmission (reflection/refraction) coefficients accounting for both curvatures of the interface. If it is necessary to account for surface waves, TWSM can reproduce them on a seismogram. This is not an area that is studied in this thesis.

Comparisons. Publications prove that TWSM decrease the relative AVO inversion error from 20 to 4 percent. The comparison with laboratory data demonstrates an error from 1 to 4 percent. The comparison with the finite difference method gave an 3 percent error approximately. The comparison with the theoretical approaches gave an error of 2 to 3 percent approximately.

Advantages of TPOT&TWSM. TPOT&TWSM conceptually differ from the numerical methods being exploited to solve forward and inverse seismic problems. The numerical methods represent the total solution of the equation systems, while TPOT provides not only the total wavefield but also its wave structure expressed by separate waves. Each separate wave can be represented on a seismogram without representation of the rest of the wavefield. Moreover, the solution is derived in analytical form before using TWSM programming software. TWSM just visualizes each wave fragment or group of them given by TPOT in the mid-frequency range. The method is strictly speaking valid for $\frac{h_{\max}}{\lambda_d} = [1, 99]$, where λ_d is the dominant wave length and $h_{\max}$ is the maximum depth of the model. The relative error is independent of the amplitude of all the wave fragments. Therefore, all the waves on the seismogram are represented equally accurately. Moreover, TWSM gives the wave-transfer matrix description in each block/layer independently of the other blocks/layers and sources/receivers definitions.

Applications of TPOT&TWSM. TPOT&TWSM have been applied to primary extraction (multiple removal); subsalt shadow wavefield description; wavefield description for 3D inhomogeneous media with curved interfaces/reflectors. TWSM programming software can be used for different forward problems, such as the planning of acquisition systems, wave description of physical/laboratory modeling, the description of individual waves. It also can be used for inverse problems, such as imaging in the case of laterally inhomogeneous overburden and AVO inversion.

Thesis results. The thesis contains the two main results: a theoretical description of the feasible fundamental solution choice (Chapter 2) and the comparison of TWSM with the edge wave theory for V-, U- and W-models (Chapters 3, 4, and 5).

Preface

I would like to thank a lot of people who have supported and helped me during my PhD work.

First of all, I highly acknowledge my supervisor, Professor Alexey Stovas, for giving me an opportunity to study in Norway and travel to many interesting conferences and seminars. He has always been ready to find time for a discussion with me and accepted my sometimes strange research opinions.

In addition, I acknowledge my head of department, Professor Egil Tjåland, he gave me much sound advices during my PhD study and helped me practice my Norwegian.

My deepest gratitude is to my colleagues and at the same time relatives, my father Dr. Arkady Aizenberg and my sister PhD Milana Ayzenberg, for giving me a lot of attention and sharing the most interesting ideas with me. They have always encouraged me to be active and curious in research.

I wish to express my deep sorrow for my diffraction friend and a highly respected person in diffraction research Professor Kamill Klem-Musatov who recently passed away and did not see my completed PhD thesis. Even after I had moved to Norway, we stayed in touch and discussed our diffraction projects via e-mail.

I am deeply thankful to my new colleagues and friends from my department at the Norwegian University of Science and Technology: Professor Harald Asheim, Professor Ketil Hokstad, Professor Martin Landrø, Professor Børge Arntsen, Professor Bjørn Ursin, Postdoc. Wiktor Weibull, Postdoc. Kamal'deen Omosanya, Yi Liu, Amir Ghaderi, Mehran Namani, Torbjørn Pedersen, Yuriy Ivanov, Katie Aurand, Terje Solbakk, Vegard Hagen and Chen-Long Wang.

I also acknowledge my colleagues and friends at the Institute of Petroleum Geology and Geophysics SB RAS in Novosibirsk Russia: Nikolay Zyatkov, Ekaterina Rakshaeva, Anton Duchkov and Tatiana Nefedkina for useful discussions and fruitful time spend together; Professor Kees Wapenaar at Delft University of Technology is thanked for a review

of my first paper; Jan Pajchel and Ola-Petter Munkvold from Statoil ASA in Bergen and Trondheim Norway for giving me good advices during my PhD work; Fredrik Andersson from Lund University for inviting me to visit his university.

I also acknowledge Professor Dirk Gajewski for giving me a chance to make a short and useful exchange visit to University of Hamburg; in addition I am deeply thankful to Dr. Ekkehart Tessmer and Vladimir Kazei for the research cooperation which we still continue. Additional thanks are extended to Ivan Abakumov for discussing Finite Difference modeling methods and their classifications and differences between them.

I deeply thank my colleagues Zuzana Jechumtálová, Tijmen Jan Moser, Leo Eisner, Andrej Bóna, Dirk Kraajpoel, Ivan Pšenčík and Tariq Alkhalifah for very good and effective diffraction discussions of my poster at the APSLIM-2015 workshop.

I am grateful to Stewart Clark, Marco D'oleire, Toan Dao and Anna Mackie for correcting the English style in my thesis. I was happy to learn more about this tricky language.

Special acknowledgements go to the organizing committee of EAGE/SPE Middle East Subsalt workshop 2016 for giving me an opportunity to join the committee and getting practice in organization and speaking in English.

Last, but not least, I would like to thank my family for giving me love and care independently on my good and hard times: my mother Lydia for that she has always believed in me and loved me. I am also very thankful to my relatives Kåre and Solveig, my brother-in-law Oddvar and my nephew Kristoffer for having good holidays in Bergen.

Contents

Chapter 1

Thesis introduction

1.1 Modeling methods

It is conventionally accepted to classify modeling methods into three main groups: physical (laboratory), numerical and analytical modeling approaches. It is also common to test these methods against each other. This Chapter briefly discusses the ideas in the approaches and the differences between them.

1.1.1 Physical modeling methods

Physical modeling is one of basic tools in geophysical research. This Subsection follows the ideas in the Introduction to Tantsereva *et al.* (2015). Wavefield propagation in complex media with edges and shadow zones leads to different diffraction effects. Correct physical modeling of these diffractions is used for testing different numerical and analytical modeling methods. In the SEAM project (Fehler & Keliher (2011)), several numerical modeling codes were compared to the reference method. Such an approach has limitations, especially if the propagation occurs in a complex medium with strong-contrast surfaces and surface irregularities, because all of the methods, including the reference method, are based on different assumptions. This approach of using a laboratory method as a reference method in diffraction studies was frequently used in the past. In contrast with in situ experiments, high-quality data are collected under controlled conditions for a known configuration. Moreover, unlike synthetic reference methods, in laboratory experiments, the real waves propagate through models with no numerical approximations. Howes *et al.* (1953) used reduced scale models to study and demonstrate the geometry of the propagation, reflection, refraction, and diffraction of sound pulses radiated from a point source. Grannemann (1956) compared theoretical results with experimental results for the relative amplitude of the diffracted pulses from a wedge in a solid. Angona (1960) demonstrated the mechanism for double diffraction and the difference in amplitude decay and moveout between reflection and diffraction for a fault model. Hilterman (1970) recorded sections from models of typical geological structures such as synclines, anticlines and faults in order to observe diffraction which could not be predicted by the ray theory. Pant *et al.* (1992) used 2-D scale models and synthetic seismograms to study diffraction artifacts and interpretation pitfalls on seismic profiles over a vertical fault model and a rectangular mound model. Jocker *et al.* (2006) presented and validated a first-order scattering theory for wave propagation in the presence of objects with dimensions comparable to the wavelength against ultrasonic measurements of the acoustic wavefields scattered by single spheres placed in a homogeneous background medium. An additional control for both laboratory and synthetic data is necessary as misfits between laboratory and synthetic data may be observed due to uncertainties in the laboratory data and the various assumptions of the modeling methods.

1.1.2 Numerical modeling methods

Groups of numerical methods. Seismic numerical modeling is a common approach for wave simulation. The objective is to predict the wavefield that a set of sensors would record, given a model and a source in this model. This technique has been used for seismic interpretation and inversion. Another important application of seismic modeling is the evaluation and design of seismic surveys. There are many approaches to seismic numerical modeling. Carcione *et al.* (2002) and Virieux *et al.* (2011) classify them into five main groups: 1) direct (finite-difference/FD) methods; 2) integral-equation methods; 3) spectral method; 4) the pseudo-spectral and finite volume methods and 5) the continuous or discontinuous Galerkin finite-element methods. The choice between these different approaches depends on the applications.

Direct/finite difference(FD) methods. To solve the wave equation by FD methods, the model is discretized in a finite number of points. These techniques are also called grid methods and full-wave equation methods, since the solution represents the total wavefield. These methods do not have restrictions on the material variability and are very accurate with the condition that a sufficiently fine grid is used. These techniques can handle different geologies and are well suited in snapshots which are important for interpretation. However, a disadvantage of FD methods is that they require more computational expense than approximate analytical methods.

Integral-equation methods are based on the wavefield integral representations in terms of the point sources waves. These methods are based on Huygens' principle, formulated by Huygens in 1690 in a heuristic way. Huygens' work explains that the wavefield can, in some cases, be considered as the superposition of the volume point sources wavefields and, in other cases, such as the superposition of the boundary point sources wavefields. Both forms of Huygens' principle are still in use, and we have volume integral equations as well as boundary integral equations. These methods are more restrictive in their application than FD methods. However, for specific geometries, such as bounded objects in a homogeneous embedding, boreholes, or geometries containing many small-scale cracks or inclusions, the integral-equation methods are very efficient and give accurate solutions. Due to their more analytic character, they also have been useful in the derivation of imaging methods based on the Born approximation, as described in Cohen *et al.* (1986) and Bleistein *et al.* (2001). The volume integral method in form of Born approximation also can be used for wavefield modeling, see Moser (2012).

The spectral method is very efficient and accurate but is restricted to simple structures, for example layered structures. The spectral formulation reads as follows: the partial differential equations are first formulated in dual spaces, such as the space Fourier domain, where the partial derivatives are transformed into algebraic forms. The difficulty here is to express the boundary conditions when necessary, as well as the excitation conditions, in this new space. However, it can ease the expression of the source excitation, for example, the plane-wave decomposition-based approaches. Such approaches are widely used for the modeling of reflected wavefields in media where the velocity only varies vertically. Horizontally layered structures with no lateral velocity variations are examples where such modeling is largely applicable, see Ursin (1983) and Tsvankin (1995). This methodology is fundamental to processing techniques, such as the prediction and removal of seabed and internal multiples, deterministic wavelet estimation, and decomposition of the full wavefield into upgoing and downgoing waves, which is done in Ikelle & Amundsen (2005). The plane-wave decomposition is a powerful and computationally efficient tool. It is the basis for approaches such as phase-shift extrapolation, the screen-propagator method, the reflectivity method, the generalized ray method (Kennett (1983)) and the Radon ($\tau-p$) transform (Gazdag (1978), Stolt (1978), Wu (1994) and de Hoop & Bleistein (1997)).

The pseudo-spectral and finite volume methods are based on the strong formulation of the partial differential equations, which are easy to implement and give a good compromise between accuracy, efficiency and flexibility. The strong formulation states: the partial differential equations are verified specifically on discrete points on which the continuum is interpolated, or their integral forms should be satisfied. An example of a pseudo-spectral method is described in Tessmer & Kosloff (1994). We could select a global spatial discretization (which often is presented as a modal approach), such as the pseudo-spectral methods where the partial derivatives are estimated by going back and forth in the dual domain (for example, Fourier, Legendre or Chebychev domains), which leads to specific regular/non-regular sampling, for details see Kosloff & Baysal (1982), Druskin & Knizhnerman (1988), Seriani & Priolo (1994) and Priolo, Carcione & Seriani (1994). We could also consider spatial discretization with local support, and more specifically, the FD method that is widely used in many fields (Levander (1988), Mackie *et al*. (1993), Robertsson, Blanch & Symes (1994), Newman & Alumbaugh (1999), Pitarka (1999), Taflove & Hagness (2000) and Moczo, Robertsson & Eisner (2007)). The idea in the finite volume methods (Virieux (2011)) consists of writing the partial differential equations in a first-order (pseudo) conservative form and taking the integral over the computational domain. In certain cases, this integral form of the partial differential equations can be obtained directly from the physical conservation laws. The local lower-order interpolation of the fields allows an intuitive construction, which leads to correctness of this formulation. We proceed with the geometrical interpretation, not with the variational approach. This technique appears to have the flexibility to describe the medium using complex meshing, while retaining the simple approach of the FD method.

The continuous or discontinuous Galerkin finite-element methods (Zienkiewicz & Morgan (1983)) are based on the weak formulation, which leads to more accurate representations of the geology and, therefore, to more accurate solutions, although with higher computational costs. The test functions are identical to the basis functions on which the expected solution is expanded. The weak formulation is stated as follows: the partial differential equations are verified globally over the elements that use a discrete norm for the solution. This method is general and includes the strong formulation, using a specific norm expressed through Dirac comb and using operators as distributions. The weak formulation (Virieux (2011)) is obtained by multiplying the partial differential equations by the test functions (unlike the finite volume methods), by integrating over the given domain and by carrying out the integration by the parts that reduce the derivation order of the fields (that weakens the derivability conditions by transferring them to the test functions). In the classical continuous Galerkin finite-element approach (Virieux (2011)), the fields from the differential equations are assumed to be continuous in the entire computation domain. They are decomposed in the local piece-wise functional basis, which is also used for the test functions. Some of the limitations of the continuous Galerkin finite element approach can be addressed (Virieux (2011)) by the discontinuous Galerkin finite-element method, even if some of the field components need to be discontinuous across the interfaces, namely the test functions, together with the fields, are a priori not continuous at the boundaries of the element.

1.1.3 Analytical modeling methods

Rigorous analytical solutions are known only for simple models. Singly scattered wavefields were studied by Friedlander (1958) for wedge-like canonical models. Jones (1973) extended the approach for double scattering. A short review of the theoretical developments since 1973 is given in Chu *et al.* (2007). In spite of extensive theoretical studies on the analytical solutions for canonical diffraction problems, the transition to the general problems was not a straightforward task, see Anokhov (1999). Klem-Musatov (1994) suggested a new theoretical approach to the problem. He wrote that the solution for sector models can be obtained using a Neumann iterative technique as a sequential substitution in the wave equation and boundary conditions. This technique is not restricted to canonical models and can be generalized to more realistic models, if needed. Brannan *et al.* (2004) studied multiply-scattered wavefields for a simplified model. The implementation of analytical solutions in the boundary integral equation method for more complicated diffracting models (general piecewise smooth interfaces) was studied by Chandler-Wilde *et al.* (2012).

Asymptotic high-frequency methods refer to the asymptotic ray theory (Cerveny (2005)), the geometrical theory of diffraction by Keller (1962), the physical theory of diffraction (Ufimtsev (1981)), and the uniform theory of diffraction (Capolino & Albani (2005)). Klem-Musatov *et al.* (2008) generalized the results obtained by Klem-Musatov (1994) to non-canonical piecewise smooth interfaces for singly scattered wavefields and formulated the edge and tip diffraction theory. This theory, based on the ordinary and generalized Fresnel integrals, works well in the presence of caustics. An improved implementation of the edge-wave and tip-wave technique was suggested in the Tip-Wave Superposition Method (TWSM) for modeling of singly scattered wavefields for general piecewise smooth interfaces (Klem-Musatov *et al.* (2008)). The extension of the Neumann iterative technique modified by Klem-Musatov (1994) was extended for multiply scattered wavefields in layered and blocked media by A.M. Aizenberg (1993). Asymptotic high-frequency methods are frequently used in seismic modeling and imaging. These methods are approximate, since they do not take the complete wavefield into account. However, they are very efficient. Especially for large three-dimensional models, the speedup in computer time is significant. These methods consider the wavefield as an ensemble of certain events, each arriving at a certain traveltime and having a certain amplitude. Asymptotic methods, due to their efficiency, have played a very important role in seismic imaging based on the Born approximation for heterogeneous reference velocity models. Another application of these methods is modeling and identification of specific events on seismic records.

1.2 TPOT&TWSM method

A recently development was a rigorous Transmission-Propagaton Operator Theory (TPOT) and its mid-frequency visualization by the Tip-Wave Superposition Method (TWSM). TPOT&TWSM divides the modeling into two major steps (A.M. Aizenberg *et al.* (2011), A.M. Aizenberg & A.A. Ayzenberg (2015)/Chapter 2 of this thesis and A.A. Ayzenberg *et al.* (2015)/Chapter 5 of this thesis):

1) TPOT analytical solution of the seismic forward problem: separation of the solution into wave fragments;

2) TWSM solution visualization in the form of a seismogram: separation of the seismogram into each wave fragment seismogram.

1.2.1 Transmission-Propagation Operator Theory (TPOT)

The Transmission-Propagation Operator Theory (TPOT) is an analytical mathematical tool for wavefield description in 3D inhomogeneous macro-layered and macro-block media. This TPOT (A.M. Aizenberg *et al.* (2011))

1) is a generalized hybrid method combining the potential theory of the single and double layer and the theory of space-time spectrum decomposition;

2) introduces a new statement of the seismic initial-boundary problem in terms of wave motion, using two unknown before operators: the convolutional transmission operator at curved interface and the feasible propagation operator in an inhomogeneous block;

3) obtains a rigorous analytical solution of seismic problems in finite time window (seismogram) in the form of a sum of a multiple reflected-refracted wave series.

New problem statement. First of all, the conventional problem statement in terms of the particle motion is transformed into an unknown earlier equivalent statement in terms of the propagating waves. The new statement consists of two integral equation systems: the surface propagation equations are expressed through the feasible propagation operators combined with the generalized plane-wave decomposition operators; and the surface transmission equations are expressed through the convolutional transmission operators.

The transmission operators in the boundary conditions are written as a generalized space-spectral Weyl decomposition for wave modes at the vicinity of curved interface/reflector (Klem-Musatov *et al.* (2004) and Klem-Musatov *et al.* (2005)). The kernels of these operators have explicit form and contain the generalized reflection/refraction plane (with respect to the curved interface) wave coefficients and depend on local material parameters of the two contacting media at the contact reference point, see M.A. Ayzenberg *et al.* (2007) and M.A. Ayzenberg *et al.* (2009).

The propagation operators are expressed through a given matrix explicit kernel. This kernel is the 'feasible fundamental solution' (FFS) which describes cascade diffraction as a wavefield propagating into shadow zones behind concave interface parts; this feasible fundamental solution corrects for the free space Green's function in shadow zones (A.M. Aizenberg & A.A. Ayzenberg (2015)/Chapter 2 of this thesis).

Feasible fundamental solution (FFS) in shadow.

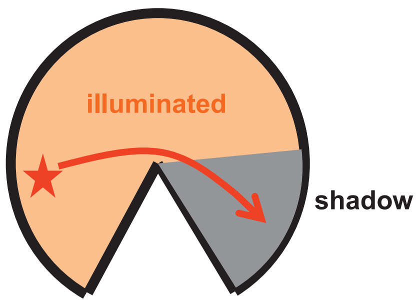

Figure. For the given source: the illuminated zone (orange) and the shadow zone (grey).

Shadow originally is an optic term that is caused by an obstacle. The light rays are diffracted by the obstacle and penetrate into the shadow zone (Figure). If the obstacle has a complex shape, diffraction forms cascade diffraction. In acoustic, elastic, porous, fractured, fluid-saturated, microstructured and other media, the presence of shadow (sub-salt, sub-basalt zones etc.) can make the subsurface image and the subsurface wavefield modeling very complicated. TPOT proposes using the so-called 'feasible fundamental solution' (FFS) which is a mathematical description of the wavefield in one 3D medium with shadow zones. This FFS uses a shadow function which controls the presence/absence of shadow zones. All the interface points are connected to each other by a straight segment, if the segment intersects the interface, we say that these two points do not 'see' each other, otherwise they do 'see' each other. After this procedure, the propagation is 'allowed' by the shadow function only between those points which 'see' each other. The shadow function is added in the kernel of the conventional propagation Kirchhoff-type operator and, therefore, corrects for the Green's function in the kernel according to the shadow zones that exist. This new kernel is thus feasible and handles shadow zones. We call it the 'feasible fundamental solution' (or the feasible Green's function).

Solution. Using the new problem statement, we obtain a rigorous analytical solution as a sum of the reflected/refracted wave series visualized on a seismogram. Each wave of the given reflection/refraction order is described as the transmission-propagation composite operator multiplied by the previous order term. The action of the composite propagation-transmission(reflection/refraction) operator is dependent on the wave code. The wave code is chosen by the wavefield trajectory, see for example in A.M. Aizenberg *et al.* (2011).

Features of TPOT. When working technically with integral operators, the two TPOT operators obey the following two key principles: 1) rigorous explicit representation of the propagation operators in domains/layers in an inhomogeneous medium; the kernel of these operators is feasible and generalizes the conventional Fermat's and Hyugens' principles for the arbitrary boundary case with shadow; and 2) rigorous explicit representation of the transmission (reflection/refraction) operators at curved interfaces; the transmission operators handle curved interfaces by the introduction of a Gaussian local coordinate system and have the plane-wave transmission (reflection/refraction) coefficients in the kernel.

Advantages of TPOT. The wave statement of the problem has an advantage over the particle motion statement as it provides a description of both the total wavefield and its separate wave fragments. Therefore, the new TPOT theory has been applied to solve forward seismic problems in complex media with shadow and has been used as a primary extraction/multiple removal tool.

1.2.2 Tip-Wave Superposition Method (TWSM)

TWSM is a visualization of TPOT solutions in the mid-frequency range in form of seismograms, as described in A.M. Aizenberg & Klem-Musatov (2010), M.A. Ayzenberg *et al.* (2007) and M.A. Ayzenberg *et al.* (2009). TWSM uses approximation for the transmission and propagation operators in the mid-frequency range, also provides the imitation of separate wave events. Tests from M.A. Ayzenberg *et al.* (2007), Favretto-Cristini *et al.* (2014) and Tantsereva *et al.* (2014) demonstrate that this visualization method is able to handle irregularities such as caustics, diffraction events, head waves and creeping waves which cannot be properly handled by the geometrical ray theory (Cerveny (2005)) or the geometrical diffraction theory (Keller (1962), Capolino & Albani (2005) and Ufimtsev (1981)). The ability to work with the transmission and propagation operators in the mid-frequency range in each block independently, gives the possibility of using TWSM as a computational kernel in interface-oriented inversion and imaging, see for example M.A. Ayzenberg *et al.* (2007).

Features of TWSM. TWSM approximates the transmission and propagation operators based on the two key principles: 1) visualization of wavefield as interference of tip-wave beams, connecting small triangular elements of the seismic model interfaces; visualization of individual tip-wave beams in geometrical shadow zones accounting for cascade diffraction: diffraction by sharp edges, creeping waves along the concave parts of the interfaces, waves of the ‘whispering galleries’ along the convex parts of the interfaces etc. (the ‘feasible fundamental solution’ in the kernel is approximated by n terms, in this thesis we consider n=2); and 2) visualization of the transmission (reflection/refraction) of tip-wave beams accounting for head waves at curved interfaces; the transmission operators at curved interfaces are approximated by the effective (integrated) transmission (reflection/refraction) coefficients accounting for both curvatures of the interface.

1.2.3 Advantages of TPOT&TWSM

TPOT&TWSM differ conceptually from numerical methods being exploited for the direct and inverse seismic problems. Existing numerical methods numerically solve the actual system of equations and represent the total wavefield. TPOT provides the rigorous explicit solution of the actual equation system in terms of the mathematical wave theory and provides not only the total wavefield but also its wave structure expressed by separate waves. Moreover, the solution is given in analytical form before using the TWSM programming software. TWSM just visualizes each propagating wave fragment or group of them given by TPOT in the mid-frequency range. The relative error of the computation of any wave fragment does not depend on its amplitude. Since the relative error is universal for each wave fragment, the relative error does not change when the amplitude changes.

1.3 Thesis content

This thesis consists of the Introduction, four Chapters and Closing remarks.

The Introduction outlines the research problem and represents its place in the area of research.

Chapter 2 is a paper "Feasible fundamental solution of the multiphysics wave equation in inhomogeneous domains of complex shape" published in Wave Motion on 27 November 2014. This paper discusses the shadow challenge in the seismic research and gives the analytical feasible fundamental solution which is the generalization of the free-space source wavefield on arbitrary boundary and medium case. The choice of the feasible fundamental solution is done by a shadow function which takes into account the boundary shape and the corresponding shadow zones. We describe how to construct this shadow function in acoustic and general homogeneous and inhomogeneous cases. The feasible fundamental solution is used as a kernel of the propagation operator in order to account for shadow when solving transmission-propagation problems.

Chapter 3 is a paper "Feasible source wavefield for acoustic V-model with shadow in the form of double diffraction approximation" submitted to Geophysical Journal International on 26 January 2015, resubmitted on 11 August 2015. This paper performs an implementation of the feasible fundamental solution idea described in Chapter 2. The paper considers a V-model and presents a synthetic source wavefield description in the V-model shadow, considering only the double diffraction. The result is compared to the edge wave theory solution.

Chapter 4 is also a paper "Feasible source wavefield for acoustic U- and W-model with shadow in the form of double diffraction approximation" submitted to Geophysical Journal International on 27 January 2015, resubmitted on 11 August 2015. This paper performs an implementation of the feasible fundamental solution idea described in Chapter 2. The paper considers a U- and W-model and gives a synthetic source wavefield description in the U- and W-model shadow, considering only the double diffraction. The result is compared to the edge wave theory solution.

Chapter 5 is a further paper "Primary source wavefield below overhang of 3D 2-block acoustic medium" submitted to Geophysical Journal International on 30 June 2015. This paper represents a transmission-propagation problem solution in V- and U-model shadow. This solution is the superposition of V- and U-shadow solutions described in Chapters 3 and 4 and a double-transmitted wavefield.

1.4 References

Aizenberg, A.M., 1993. A system of irregular fundamental solutions to wave equation in a three-dimensional inhomogeneous medium, Russian Geology and Geophysics, 34(4), 105-113.

Aizenberg, A.M. & Ayzenberg, A.A., 2015. Feasible fundamental solution of the multiphysics wave equation in inhomogeneous domain of complex shape, Wave Motion, 53, 66-79.

Aizenberg, A.M., Ayzenberg, M.A. & Klem-Musatov, K.D., 2011. Seismic diffraction modeling with the Tip-Wave Superposition Method, 73th EAGE Conference and Exhibition, EAGE, Extended Abstracts, B018.

Aizenberg, A.M. & Klem-Musatov, K.D., 2010. Progress in seismic diffraction theory – From edge and tip waves to multiple reflections-transmissions with diffractions, Extended Abstracts, 72-th EAGE Conference, Barcelona, Spain, G034.

Angona, F. A., 1960. Two-dimensional modeling and its application to seismic problems, Geophysics, 25, 468–482, doi: 10.1190/1.1438719.

Anokhov, S., 1999. On problem of the rigorous diffraction quantitative description. Semiconductor Physics, Quantum Electronics and Optoelectronics, 2(4), 66-69.

Ayzenberg, A.A., Zyatkov, N., Aizenberg, A.M. & Stovas, A., 2015. Primary source wavefield below overhang of 3D 2-block acoustic medium, Geophysical Journal International, submitted.

Ayzenberg, M.A., Aizenberg, A.M., Helle, H.B., Klem-Musatov, K.D., Pajchel, J. & Ursin, B., 2007. 3D diffraction modeling of singly scattered acoustic wavefields based on the combination of surface integral propagators and transmission operators, Geophysics, 72, 5, SM19-SM34.

Ayzenberg, M., Tsvankin, I., Aizenberg, A.M. & Ursin, B., 2009. Effective refection coefficients for curved interfaces in TI media, Geophysics, 74, WB33-WB53.

Bleistein, N., Cohen, J. K. & Stockwell (junior), J. W., 2001. Mathematics of multidimensional seismic imaging, migration and inversion, Springer.

Brannan, J.R., Ervin, V.J., Duan, J. & Razoumov, L., 2004. A Wiener-Hopf approximation technique for a multiple plate diffraction problem, Mathematical Methods in the Applied Science, 27, 19-34.

Capolino, F. & Albani, M., 2005. Time domain double diffraction at a pair of coplanar skew edges, IEEE Transactions on Antennas and Propagation, 53(4), 1455-1469.

Carcione, J. M., Herman, G. C. & ten Kroode, A. P. E., 2002. Seismic modeling, Geophysics, 67, 1304–1325.

Chandler-Wilde, S.N., Graham, I.G., Langdon, S. & Spence, E.A., 2012. Numerical-asymptotic boundary integral methods in high-frequency acoustic scattering, Acta Numerica, 21, 89-305.

Chu, D., Stanton, T.K. & Pierce, A.D., 2007. Higher-order acoustic diffraction by edges of finite thickness, Journal of the Acoustical Society of America, 122(6), 3177-3194.

Cerveny, V., 2005. Seismic Ray Theory, Cambridge University Press.

Cohen, J. K., Hagin, F. G. & Bleistein, N., 1986. Three-dimensional Born inversion with an arbitrary reference, Geophysics, 51, 1552–1558.

de Hoop, M. V. & Bleistein, N., 1997. Generalized Radon transform inversions for reflectivity in anisotropic elastic media, Inverse Problems, 13, 669–690.

Druskin, V. & Knizhnerman, L., 1988. A spectral semi-discrete method for the numerical solution of 3-D non-stationary problems, electrical prospecting. Izv. Acad. Sci. USSR, Physics of Solid Earth (Russian, translated into English) 8, 63–74.

Favretto-Cristini, N., Tantsereva, A., Cristini, P., Ursin, B., Komatitsch, D., Aizenberg, A.M., 2014. Numerical modeling of zero-offset laboratory data in a strong topographic environment: results for a spectral-element method and a discretized Kirchhoff integral method, Earthq Sci (2014) 27(4):391–399.

Fehler, M. & Keliher, P. J., 2011. SEAM Phase I: Challenge of subsalt imaging in Tertiary basins, with emphasis on deepwater Gulf of Mexico, SEG.

Friedlander, F.G., 1958. Sound Pulses, Cambridge University Press, Cambridge.

Gazdag, J., 1978. Wave equation migration with the phase-shift method, Geophysics, 43, 1342-1351.

Grannemann, W.W., 1956. Diffraction of a longitudinal pulse from a wedge in a solid, Journal of the Acoustical Society of America, 28, 494-497, doi: 10.1121/1.1908368.

Hilterman, F., 1970. Three-dimensional seismic modeling, Geophysics, 35, 1020–1037, doi: 10.1190/1.1440140.

Howes, E., Tejada-Flores, L. & Randolph, L., 1953. Seismic model study, Journal of the Acoustical Society of America, 25, 915–921, doi: 10.1121/1.1907218.

Ikelle, L. & Amundsen, L., 2005. Introduction to Petroleum Seismology, Investigations in Geophysics, No. 12, SEG.

Jocker, J., Spetzler, J., Smeulders, D. & Trampert, J., 2006. Validation of fast-order diffraction theory for the traveltimes and amplitudes of propagating waves, Geophysics, 71(6), T167-T177.

Jones, D.S., 1973. Double knife-edge diffraction and ray theory, The Quarterly Journal of Mechanics and Applied Mathematics, 26(1), 1-18.

Keller, J.B., 1962. Geometrical theory of diffraction, Journal of the Optical Society of America, 52, 116-130.

Kennett, B.L.N., 1983. Seismic Wave Propagation in Stratified Media. Cambridge University Press.

Klem-Musatov, K.D., 1994. Theory of seismic diffractions, SEG.

Klem-Musatov, K.D., Aizenberg, A.M., Helle, H.B. & Pajchel, J., 2004. Reflection and transmission at curvilinear interface in terms of surface integrals, Wave Motion, 39, 77–92.

Klem-Musatov, K., Aizenberg, A.M., Helle, H.B. & Pajchel, J., 2005. Reection and transmission in multilayered media in terms of surface integrals, Wave Motion, 41, 293-305.

Klem-Musatov, K.D., Aizenberg, A.M., Pajchel, J. & Helle, H.B., 2008. Edge and Tip Diffractions: Theory and Applications in Seismic Prospecting, Geophysical Monograph Series, No. 14, SEG, Tulsa, USA.

Kosloff, D. & Baysal, E., 1982. Forward modeling by a Fourier method. Geophysics, 47, 1402-1412.

Levander, A.R., 1988. Fourth-order finite-difference P-SV seismograms. Geophysics, 53, 1425-1436.

Mackie, R.L., Madden, T.R. & Wannamaker, P.E., 1993. Threedimensional magnetotelluric modeling using difference equations – theory and comparison to integral equation solutions. Geophysics, 58, 215–226.

Moczo, P., Robertsson, J.O.A. & Eisner, L., 2007. The finite-difference time-domain method for modeling of seismic wave propagation, Advances in Wave Propagation in Heterogeneous Earth (eds R.-S. Wu, V. Maupin and R. Dmowska), pp. 421–516, Academic Press.

Moser, T.J., 2012. Review of Ray-Born Forward Modeling for Migration and Diffraction Analysis, Stud. Geophys. Geod., 56, 411-432.

Newman, G.A. & Alumbaugh, D.L., 1999. Electromagnetic modeling and inversion on massively parallel computers, Threedimensional Electromagnetics (eds M. Oristaglio and B. Spies), pp. 299–321. SEG.

Pant, D. R., Greenhalgh, S. A. & Zhou, B., 1992. Physical and numerical model study of diffraction effects on seismic profiles over simple structures, Geophysical Journal International, 108, 906–916, doi: 10.1111/j.1365-246X.1992.tb03479.x.

Pitarka, A., 1999. 3D elastic finite-difference modeling of seismic motion using staggered grids with nonuniform spacing. Bulletin of the Seismological Society of America, 89, 54–68.

Priolo, E., Carcione, J.M. & Seriani, G., 1994. Numerical simulation of interfacewaves by high-order spectralmodeling techniques. Journal of the Acoustical Society of America, 95, 681-693.

Robertsson, J., Blanch, J. & Symes, W.W., 1994. Viscoelastic finitedifference modeling. Geophysics, 59, 1444-1456.

Seriani, G. & Priolo, E., 1994. Spectral element method for acoustic wave simulation in heterogeneous media, Finite Elements in Analysis and Design, 16, 337-348.

Stolt, R.H., 1978. Migration by Fourier transform, Geophysics, 43, 23-48.

Taflove, A. & Hagness, C., 2000. Computational Electrodynamics: The Finite-difference Time-domain Method. Artech House.

Tantsereva, A., Ursin, B., Favretto-Cristini, N., Cristini, P. & Aizenberg, A.M., 2014. Numerical modeling of 3D zero-offset laboratory data by a discretized Kirchhoff integral method. Geophysics, 79(2), T77-T90.

Tantsereva, A., Ursin, B., Favretto-Cristini, N., Cristini, P. & Aizenberg, A.M., 2015. Numerical and physical modeling of scattered waves from a viscoelastic layer with complex shape, GASA, submitted.

Tessmer, E. & Kosloff, D., 1994. 3-D elastic modeling with surface topography by a chebychev spectral method. Geophysics, 59, 464–473.

Tsvankin, I., 1995. Seismic Wavefields in Layered Isotropic Media, Samizdat Press.

Ufimtsev, P.Y., 1981. Fundamentals of the physical theory of diffraction. McGraw-Hill Book Co., New York.

Ursin, B., 1983. Review of elastic and electromagnetic wave propagation in horizontally layered media, Geophysics, 48, 1063–1081.

Virieux, J., Calandra, H. & Plessix, R.-E., 2011. A review of the spectral, pseudo-spectral, finite-difference and finite-element modelling techniques for geophysical imaging, Geophysical Prospecting, 59, 794–813, doi: 10.1111/j.1365-2478.2011.00967.x.

Wu, R.-S., 1994. Wide-angle elastic wave one-way propagation in heterogeneous media and an elastic wave complex-screen method, Journal of Geophysical Research, 99, 751–766.

Zienkiewicz, O.C. & Morgan, K., 1983. Finite Elements and Approximation. Wiley and Sons.

Chapter 2

Feasible fundamental solution of the multiphysics wave equation in inhomogeneous domains of complex shape

Arkady M. Aizenberg[a], Alena A. Ayzenberg[b *]

[a] Senior Scientific Researcher, Institute of Petroleum Geology and Geophysics, Russian Academy of Sciences, Ac. Koptyug Pr. 3, 630090 Novosibirsk, Russia,
tel.: +7 383 335 6457, fax: +7 383 333 2513, e-mail: AizenbergAM@ipgg.sbras.ru
[b] PhD student, Norwegian University of Science and Technology (NTNU), S.P. Andersens veg 15a, 7491 Trondheim, Norway,
tel.: +47 90 840 729, fax: +47 73 944 472, e-mail: alena.ayzenberg@ntnu.no

Presented at the 74th EAGE Conference & Exhibition, Copenhagen, Denmark, 2012. Published in Wave Motion, 27 November 2014.

2.1 Abstract

Fundamental solutions of the linear equations governing mechanical and electromagnetic oscillations are kinematically represented by delay time along ray trajectories. The fundamental solutions can contain components which are not physically justified, if their ray trajectories are partly located outside the actual medium in accordance with Fermat's principle. To exclude all non-physical components and consider only the physically feasible fundamental solution, ray trajectories and delay time must satisfy the generalized Fermat's principle, as introduced by Hadamard in 1910. We introduce a rigorous dynamic description of this feasible fundamental solution satisfying the generalized Fermat's principle and being physically justifiable. The description is based on an integral condition of absolute absorption at the boundary of an effective medium. This condition selects a subset of the physically feasible fundamental solutions. We prove that, in homogeneous domains, the feasible fundamental solution is the sum of the Green's function for the unbounded medium and an operator Neumann series describing cascade diffraction at the boundary. In inhomogeneous domains we represent the feasible fundamental solution by an equation with a volume integral operator. The integral kernel contains the feasible fundamental solution for a homogeneous domain. We introduce feasible surface and volume integral operators that eliminate the unfeasible wavefields in the geometrical shadow zones.

2.2 Introduction

Fundamental solutions of the linear equations governing mechanical and electromagnetic occillations are key elements of the mathematical theory of wave propagation. It is theoretically known that fundamental solutions are defined ambiguously and contain an arbitrary term which cannot be justified by experiment. The initial boundary value problems of the linear wave propagation theory require a unique solution. Such a solution is independent of choice of the concrete fundamental solution, used in a solving method. The simplest fundamental solution is usually considered the most convenient for practical reasons. The classical Green's function of an unbounded medium satisfying the classical Fermat's principle is often a preferred choice.

The problem becomes more complex when analyzing the full wavefield. Its interference structure needs to be represented as the sum of the source wavefield and the wavefields scattered at the boundaries and medium heterogeneities. The source wavefield is represented by a superposition of fundamental solutions. It is as ambiguous as the fundamental solutions are. A fundamental solution can propagate only inside the actual medium and does not exist out of it. In media of complex geometrical shapes, the fundamental solution may contain artefacts (physically unfeasible wavefields) that propagate along the ray trajectories, partly beyond the boundary of the considered domain. Fundamental solutions that describe observable point source wavefields are considered feasible in this paper. To exclude artefacts from the source wavefield it is necessary to analytically describe the feasible fundamental solution in the domains with arbitrary boundary shapes [1], [2], [3].

The problem of describing feasible fundamental solutions was first addressed by Hadamard using the theory of characteristics in 1910. Hadamard described the kinematic properties of these solutions using the generalized Fermat's principle for arbitrary domains [3]. According to this definition, the front of the fundamental solution propagates only along nonclassical rays that belong entirely to the domain of consideration. Kinematic properties of the wave front in domains with arbitrary boundaries can be correctly described using the Huygens' principle (see details in § 5 and § 6 of Chapter 2 in [3]). While the front is inside a considered domain it has a classical shape. Part of the front that interects a boundary and propagates outside a domain is physically non-feasible and is not further taken into account.

The physically feasible part of the front starts to creep into the concave parts of a boundary and propagates into the shadow zones for classical rays. In addition, nonclassical rays propagate inside this domain in the shadow zones for classical rays. Part of these nonclassical rays belongs to a curved boundary of a domain (see §5 Chapter 2 in [3]). We thus conclude that physically feasible fundamental solutions depend on the actual shape of the domain.

After Hadamard's work there were numerous attempts to use rigorous or approximate formulations of the initial boundary value problems of mathematical wave theory in order to find physically feasible fundamental solutions. Friedlander gives the detailed rigorous Hadamard's description of the propagation of front of the fundamental solution for concave boundaries [3]. Although the generalized Fermat's principle, as introduced by Hadamard, states that it is necessary to exclude the nonphysical components of the fundamental solution, it does not provide a solution for how to obtain the feasible fundamental solution.

The problem of obtaining the feasible fundamental solution first appears in the work of Kirchhoff in 1881, where a heuristic principle of absolute absorption was proposed [4], [5]. Let us consider this principle with the example of a homogeneous acoustic domain. In a convex domain this principle is not applicable as radiation propagates from any point source to any boundary point along the ray. Therefore, in such a domain, a point source wavefield can be computed at any point of a boundary. In a concave-convex domain this principle should be applied because radiation propagates from a point source along rays only to points of the 'illuminated' parts of the boundary. Radiation does not propagate to points of the 'shadowed' parts of the boundary because the ray is intercepted by a 'shadowing' convex part of the boundary. In such a situation Kirchhoff suggested to take into account 'absolute absorption' at 'shadowed' concave parts of the boundary by the vanishing a wavefield at points of the 'shadowed' parts of the boundary.

Kirchhoff attempted to justify this principle [4], [5]. He obtained an approximate description of the fundamental solution for a half-plane slit in a homogeneous medium. Several papers show that direct application of Kirchhoff's principle leads to the fundamental solutions containing unadmissible singularities in the vicinity of the edge bounding the illuminated part of the boundary [4], [5].

For practical reasons, the contemporary research focused on the problems of the scattering of plane, cilindrical and spherical waves in homogeneous media with simple boundaries. Some of the approaches used are: the method of variables' separation; the method of spectral decomposition; the theory of multiple diffraction based on the locality principle [6], allowing addition of diffraction in source wavefield in shadow zones; the theory of edge and tip waves [7], [8]; and the hybrid (numerical-asymptotic) boundary integral method [9]. Rigorous methods are applicable to describe diffraction at wedge-shaped boundaries [3], [6], [7], [9]. A combination of the spectral decomposition method and locality property is applied to diffraction at polygons and polyhedrons [6], [9]. Various approximate methods of calculation of the fundamental solution are applicable to diffraction at concave boundaries (circular, parabolic or hyperbolic cylinders) of open domains [3], [5]. All the proposed approaches satisfy the generalized Fermat's principle inside geometrical shadow zones.

The exact analytical solution of all rigorous diffraction problems takes into account the geometrical shadow zones for the direct wavefield. As an example, we consider a problem of an impulse diffraction at a wedge with perfect boundary conditions. The detailed description of the solution of the problem, Green's function, is represented by formula (5.2.10) in [3] (see Fig. 5.2). Green's function is represented by the sum of the direct wavefield (5.4.6) and the reflected wavefield which is out of the scope of this paper. The direct wavefield is composed of the direct wave with its shadow zone and the diffracted wave, smoothing a discontinuity in amplitude at the shadow boundary. Time arrival of the direct wavefield satisfies the generalized Fermat's principle as front of the diffracted wave in the shadow zone retards with respect to the standard Fermat's principle. The direct wavefield can be considered as the feasible fundamental solution in any shadowed domain.

Revival of interest in the theory of feasible fundamental solutions in media with complex boundaries is stimulated by the introduction of an analytical solution of the initial boundary value problem for layered medium with curved interfaces [1], [2], [8], [10], [11], [12], [13]. This solution uses surface and volume integral operators with kernels that are built on the feasible fundamental solutions. A mathematical formulation of the absorption condition at regular curved boundaries of acoustic domains was introduced in [14], [15]. These results were later generalized to elastic porous fluid-saturated layers in [16], [17]. The absorption condition contains a matrix absorption operator and takes into account shadow zones. The physically feasible fundamental solution is thus represented as the sum of the

Green's function for an unbounded medium and an operator Neuman series describing cascade diffraction at the boundary. Numerical modeling of the first-term approximation of the cascade diffraction is presented in [18], [19], [20].

This paper generalizes these results to arbitrary effective domains, having complex microscopic structure and boundaries. Our experience has shown that we had to derive the feasible fundamental solution for each case separately. We therefore decided to obtain the uniform solution for the general case in order to use it later on for all different cases.

The paper consists of Introduction, eight Sections and Conclusions. Sections 2.3-2.7 detail the derivation of the feasible fundamental solution for homogeneous domains. Section 2.8 shows the derivation of the feasible fundamental solution for inhomogeneous domains. In Section 2.9 we introduce the feasible surface and volume integral operators for homogeneous domains. In Section 2.10 we introduce the feasible surface and volume integral operators for inhomogeneous domains. Conclusions summarize the main results of the paper. Appendix provides the short introduction into governing equations for the medium.

2.3 The statement of the problem for a homogeneous domain

The problem for an inhomogeneous domain is solved into two steps. We first derive the solution for a homogeneous domain. After that, we use this solution for deriving the solution of the inhomogeneous domain. In this Section we consider the statement of the problem in the homogeneous domain. The boundary has complex geometrical shape.

We consider the 'physical' domain $\mathbb{D} \subset \mathbb{R}^3$ and its 'mathematical' complement $\mathbb{R}^3 \setminus \mathbb{D}$. The boundary of $\mathbb{D}$ is a piecewise regular surface $\mathbb{S}$. The curved part $\mathbb{S} \cap \mathbb{B}$ of the boundary has a finite area. Part $\mathbb{S} \setminus \mathbb{B}$ of the boundary is one or more planes. We denote the boundary of an unbounded part at infinity as $\mathbb{S}^{+\infty}$. The radius-vector x designates an arbitrary point in $\mathbb{D} \subset \mathbb{R}^3$. Radius-vector s denotes either a boundary point on $\mathbb{S}$ or a point in $\mathbb{D}$ which is infinitesimally close to $\mathbb{S}$. In each point of the boundary the normal $\mathrm{n}(\mathrm{s})$ is directed inwards a domain. Here, and subsequently, all continuously differentiable functions and twice continuously differentiable functions are referred to as the smooth functions and the regular functions correspondingly.

Introducing into consideration the fundamental vectors $\mathrm{f}_l(\mathrm{x}, \mathrm{y}, \omega)$ ($l = \overline{1, m}$, $m \in N$), similar in structure to the vector $\mathrm{u}(\mathrm{x}, \omega)$ defined in Appendix, we build the stationary fundamental matrix solution

$$\mathrm{F}(\mathrm{x}, \mathrm{y}, \omega) = \{\mathrm{f}_1(\mathrm{x}, \mathrm{y}, \omega) \quad \mathrm{f}_2(\mathrm{x}, \mathrm{y}, \omega) \quad \dots \quad \mathrm{f}_m(\mathrm{x}, \mathrm{y}, \omega)\}^T \tag{1}$$

The stationary fundamental matrix (1) satisfies the problem for the feasible fundamental solution in homogeneous domain $\mathbb{D}$ in a complete form

$$
\begin{cases}
\left[\mathrm{D_x} + \bar{\mathrm{M}}(\omega)\right] \mathrm{F}(\mathrm{x}, \mathrm{y}, \omega) = -\delta(\mathrm{x} - \mathrm{y})\, \mathrm{I}\,, \\
\langle RC \rangle: \quad \iint\limits_{\mathbb{S}^{\infty+}} \mathrm{G}(\mathrm{x}, \mathrm{s}, \omega)\, \mathrm{N_s}\, \mathrm{F}(\mathrm{s}, \mathrm{y}, \omega)\, dS(\mathrm{s}) = 0\,, \\
\langle EC \rangle: \quad \iint\limits_{\{\mathbb{S}^{\mathrm{E}}\}} \mathrm{G}(\mathrm{x}, \mathrm{s}, \omega)\, \mathrm{N_s}\, \mathrm{F}(\mathrm{s}, \mathrm{y}, \omega)\, dS(\mathrm{s}) = 0\,, \\
\langle VC \rangle: \quad \iint\limits_{\{\mathbb{S}^{\mathrm{V}}\}} \mathrm{G}(\mathrm{x}, \mathrm{s}, \omega)\, \mathrm{N_s}\, \mathrm{F}(\mathrm{s}, \mathrm{y}, \omega)\, dS(\mathrm{s}) = 0, \\
\langle AC \rangle: \quad \Theta(\mathrm{s}, \mathrm{s}', \omega)\, \mathrm{F}(\mathrm{s}', \mathrm{y}, \omega) = 0\,,
\end{cases}
\tag{2}
$$

where δ is the delta-function and I is the identity matrix.

We note that a solution F of *t*-hyperbolic system in (2) is not unique because it contains an arbitrary function satisfying this system with the zero column on the right hand side. Because a set of such solutions does not satisfy any special boundary condition, we call any matrix solution as the fundamental matrix solution (see detailed definitions in [21]).

We note that the integral in radiation condition $\langle RC \rangle$ in (2) is over the surface $\mathbb{S}^{+\infty}$. Set of fundamental matrices contains divergent and convergent solutions. We chose divergent fundamental matrix F, namely which satisfies radiation condition $\langle RC \rangle$ at the infinite part of $\mathbb{D}$ [22], [23].

In the vicinity of edges and vertices of boundaries, some fundamental solutions contain singular terms which are physically inadmissible (for details, see [4], [5], [24], [25], [26], [27], [28], [29], [30]). To eliminate these terms we may choose one of two options. One option is to propose an implicit description which bounds a set of admissible solutions by defying appropriate functional space. We choose another option in statement (2). This option is to define explicitly the edge $\langle EC \rangle$ and vertex $\langle VC \rangle$ conditions at irregular points of the boundary in terms of the surface integral operators. The radii of the cylinders $\{\mathbb{S}^{\mathrm{E}}\}$ and the spheres $\{\mathbb{S}^{\mathrm{V}}\}$ are infinitesimally small.

The kernel of the integral operator in (2) contains an arbitrary term, which describes ‘nonphysical’ radiation in the ‘shadowed’ zones of domain $\mathbb{D}$. Therefore, the fundamental solution (4) can contain an arbitrary term of nonfeasible nature. To exclude the nonfeasible term we introduce an additional mathematical condition at boundary $\mathbb{S}$ in (2). This condition realizes the principle of "absolute absorption". We denote the required absorption condition at the boundary by symbol $\langle AC \rangle$ and introduce some unknown integral operator $\Theta(\mathrm{s}, \mathrm{s}', \omega)$ acting over surface $\mathbb{S}$. Determination of the explicit form of an integral operator $\Theta(\mathrm{s}, \mathrm{s}', \omega)$ is a main target for this paper.

We write the solution (1) of the system in (2) in domain $\mathbb{D}$ as the integral representation similar to equation (68) from [31] in form

$$\mathrm{F}(\mathrm{x}, \mathrm{y}, \omega) = \mathrm{G}(\mathrm{x}, \mathrm{y}, \omega) + \iint\limits_{\mathbb{S} \cup \mathbb{S}^{+\infty} \cup \{\mathbb{S}^{\mathrm{E}}\} \cup \{\mathbb{S}^{\mathrm{V}}\}} \mathrm{G}(\mathrm{x}, \mathrm{s}, \omega)\, \mathrm{N}_{\mathrm{s}}\, \mathrm{F}(\mathrm{s}, \mathrm{y}, \omega)\, dS(\mathrm{s}) \ , \tag{3}$$

where matrix N_{s} is described in [31], [32], [33]. The closed surface of integration is represented by $\mathbb{S} \cup \mathbb{S}^{\infty} \cup \{\mathbb{S}^{\mathrm{E}}\} \cup \{\mathbb{S}^{\mathrm{V}}\}$, where the cylindrical surfaces $\{\mathbb{S}^{\mathrm{E}}\}$ have their axes along edges, and the spherical surfaces $\{\mathbb{S}^{\mathrm{V}}\}$ have their centers at vertices [24], [28], [29], [34].

Substituting the conditions $\langle RC \rangle$, $\langle EC \rangle$, and $\langle VC \rangle$ from (2) into (3), we obtain the fundamental solution

$$\mathrm{F}(\mathrm{x}, \mathrm{y}, \omega) = \mathrm{G}(\mathrm{x}, \mathrm{y}, \omega) + \iint\limits_{\mathbb{S}} \mathrm{G}(\mathrm{x}, \mathrm{s}, \omega)\, \mathrm{N}_{\mathrm{s}}\, \mathrm{F}(\mathrm{s}, \mathrm{y}, \omega)\, dS(\mathrm{s}) \tag{4}$$

Introducing into consideration the fundamental vectors $\mathrm{g}_l(\mathrm{x}, \mathrm{y}, \omega)$ ($l = \overline{1, m}$, $m \in N$), we build the stationary fundamental matrix solution

$$\mathrm{G}(\mathrm{x}, \mathrm{y}, \omega) = \left[\mathrm{g}_1(\mathrm{x}, \mathrm{y}, \omega) \quad \mathrm{g}_2(\mathrm{x}, \mathrm{y}, \omega) \quad \dots \quad \mathrm{g}_m(\mathrm{x}, \mathrm{y}, \omega) \right] . \tag{5}$$

Therefore we need to continue the material parameters from the domain to its complement to choose matrix G. Accounting for this parameter continuation, it is possible to consider system from (2) in the whole space $\mathbb{R}^3$ with the following material parameters

$$\bar{\mathrm{M}}^{\mathrm{C}}(\omega) = \bar{\mathrm{M}}(\omega), \quad \mathrm{x} \in \mathbb{R}^3 \ . \tag{6}$$

It is then possible to assume that G is defined not only in points $\mathrm{x} \in \mathbb{D}$, but also in points $\mathrm{x} \in \mathbb{R}^3 \setminus \mathbb{D}$ of the ‘mathematical half-space. It should be noticed that in many publications the divergent fundamental solution (5) is conventionally called the free space Green function. Therefore G is a solution of the problem in $\mathbb{R}^3$:

$$\begin{cases} \left[\mathrm{D}_{\mathrm{x}} + \bar{\mathrm{M}}^{\mathrm{C}}(\omega)\right] \mathrm{G}(\mathrm{x}, \mathrm{y}, \omega) = -\,\delta(\mathrm{x} - \mathrm{y})\,\mathrm{I}\,, \\ \langle RC \rangle : \ \iint\limits_{\mathbb{S}^\infty} \mathrm{G}(\mathrm{x}, \mathrm{s}, \omega)\, \mathrm{N}_{\mathrm{s}}\, \mathrm{G}(\mathrm{s}, \mathrm{y}, \omega)\, dS(\mathrm{s}) = 0\,. \end{cases} \tag{7}$$

Matrix G must satisfy radiation conditions to eliminate physically inadmissible waves incoming from the infinite part of domain $\mathbb{D}$. A comprehensive analysis represented in [22] and [23] allows us to choose an actual formulation of the radiation conditions in domains of complex shape, in accordance with the used mathematical apparatus. As soon as representation (3) uses the apparatus of surface integral operators we write the radiation condition. In (7), G satisfies the radiation condition at infinite sphere $\mathbb{S}^\infty = \mathbb{S}^{+\infty} \cup \mathbb{S}^{-\infty}$ in space $\mathbb{R}^3$.

2.4 The boundary value problem for the fundamental solution

In this Section we reduce the integral representation (4) to the boundary integral equation for the feasible fundamental matrix F in homogeneous domain.

To simplify notations we denote the surface integral operator of Kirchhoff's type in (4) as follows

$$\mathrm{K_G}(\mathrm{x}, \mathrm{s}, \omega)\langle\ldots\rangle = \iint_{\mathbb{S}} \mathrm{G}(\mathrm{x}, \mathrm{s}, \omega)\, \mathrm{N_s}\, \langle\ldots\rangle\, dS(\mathrm{s}) \ . \tag{8}$$

With help of the operator (8) we rewrite the integral representation (4) in operator form

$$\mathrm{F}(\mathrm{x}, \mathrm{y}, \omega) = \mathrm{G}(\mathrm{x}, \mathrm{y}, \omega) + \mathrm{K_G}(\mathrm{x}, \mathrm{s}', \omega)\, \mathrm{F}(\mathrm{s}', \mathrm{y}, \omega) \ , \tag{9}$$

where s' is a point of integration.

In representation (9) the boundary values of the feasible fundamental matrix are unknown. We let a point x tend to a point s at the boundary and obtain a limit equation for the boundary values of the feasible fundamental solution

$$\mathrm{F}(\mathrm{s}, \mathrm{y}, \omega) = \mathrm{G}(\mathrm{s}, \mathrm{y}, \omega) + \mathrm{K_G}(\mathrm{s}, \mathrm{s}', \omega)\, \mathrm{F}(\mathrm{s}', \mathrm{y}, \omega) \ . \tag{10}$$

In (10) we denote the surface integral operator of Kirchhoff's type at points of boundary as follows

$$\mathrm{K_G}(\mathrm{s}, \mathrm{s}', \omega)\langle\ldots\rangle = \iint_{\mathbb{S}} \mathrm{G}(\mathrm{s}, \mathrm{s}', \omega)\, \mathrm{N_{s'}}\, \langle\ldots\rangle\, dS(\mathrm{s}') \ . \tag{11}$$

For further simplification of formulae we omit argument ω in some formulae.

From the theory of surface integral operators (see, for example, in [24], [34], [35], [36]) it is known that the operator (8) is an operator of orthogonal projection with properties

$$K_G \, K_G = K_G \tag{12}$$

and

$$\left\| K_G \right\| = 1 \ . \tag{13}$$

It is known (see in [24], [34], [35], [36]) that the matrix (5) belongs to the kernel of operator (8). Then the identity

$$K_G(s, s') \, G(s', y) \equiv 0 \tag{14}$$

is valid.

Taking into account (14) the representation (10) can be rewritten in the form

$$V(s, y) = K_G(s, s') \, V(s', y) \ , \tag{15}$$

where $V(s', y) = F(s', y) - G(s', y)$ is a scattered component of the fundamental solution (10)
.

Since the operator (8) has eigenvalue 1 [24], [34], [35], [36], the equation (15) has infinite amount of solutions. Therefore equation (10) has an infinite number of solutions, some of which can be physically nonfeasible fundamental matrices in a domain $\mathbb{D}$. Repeatable substitution of equation (10) in itself does not change this equation because of properties (12) and (14). Therefore the method of simple iteration, which is necessary for obtaining an analytical solution, is not applicable to equation (10).

2.5 The integral absorption condition at the boundary

In this Section we derive the integral absorption condition at the boundary of the homogeneous domain in analogy to integral absorption condition for acoustic and porous fluid-saturated domain [14], [15], [16], [17].

We rewrite the equation (10) with help of an auxiliary unknown matrix operator, H, with norm less than 1 [37]. Using operator H we split the matrix operator (8) in form

$$\mathrm{K_G}(\mathrm{s,s'}) = \mathrm{H}(\mathrm{s,s'}) + \left[\mathrm{K_G}(\mathrm{s,s'}) - \mathrm{H}(\mathrm{s,s'})\right] . \tag{16}$$

Substituting representation (16) in equation (10), we obtain the equivalent equation

$$\mathrm{F(s, y)} = \mathrm{G(s, y)} + \mathrm{H(s, s')\, F(s', y)} + \left[\mathrm{K_G(s, s')} - \mathrm{H(s, s')}\right] \mathrm{F(s', y)} . \tag{17}$$

Moving the second term from the right hand side to the left hand side of equation (17) and using the existence of operator $\left[\mathrm{I}-\mathrm{H}\right]^{-1}$, we obtain

$$\begin{aligned} \mathrm{F(s, y)} = {} & \left[\mathrm{I(s, s')} - \mathrm{H(s, s')}\right]^{-1} \left[\mathrm{K_G(s', s'')} - \mathrm{H(s', s'')}\right] \mathrm{F(s'', y)} + \\ & + \left[\mathrm{I(s, s')} - \mathrm{H(s, s')}\right]^{-1} \mathrm{G(s', y)}. \end{aligned} \tag{18}$$

The equation (18) is similar to equation (7.2) from paper [37], in which the operator and the vector are given by formulas (7.24) and (7.25).

The set of solutions of equation (18) is also the set of solutions of equation (10) and consists of two subsets of boundary matrices: $\mathrm{F} \in Ker\left[\mathrm{K_G}-\mathrm{H}\right]$ which corresponds to the identity $\left[\mathrm{K_G}-\mathrm{H}\right]\mathrm{F} \equiv \mathrm{O}$ and $\mathrm{F} \notin Ker\left[\mathrm{K_G}-\mathrm{H}\right]$ which does not correspond to this identity. We suppose that one of those subsets consists of the feasible fundamental matrices. In order to choose the subset consisting of the feasible fundamental matrices we use the following heuristic arguments. We begin with the first subset $\mathrm{F} \in Ker\left[\mathrm{K_G}-\mathrm{H}\right]$. Substituting the identity $\left[\mathrm{K}_{\mathrm{G}}-\mathrm{H}\right]\mathrm{F}=\mathrm{O}$ in (18), we obtain $\mathrm{F}=\left[\mathrm{I}-\mathrm{H}\right]^{-1}\mathrm{G}$. Let us suppose that $\mathrm{H}=$, where O is the null operator. Then, from (18), we obtain $\mathrm{F}=\mathrm{G}$, where G is the feasible fundamental solution for an unbounded space. Therefore the condition $\mathrm{F}\in Ker\left[\mathrm{K}_{\mathrm{G}}-\mathrm{H}\right]$ extracts the feasible fundamental matrices for an unbounded space. We then suppose that the condition $\mathrm{F}\in Ker\left[\mathrm{K}_{\mathrm{G}}-\mathrm{H}\right]$ extracts the feasible fundamental matrices in case of an arbitrary domain as well. In further Sections we justify this choice. Therefore we do not consider further the second subset $\mathrm{F}\notin Ker\left[\mathrm{K}_{\mathrm{G}}-\mathrm{H}\right]$, which describes nonfeasible radiation.

Using the above mentioned resoning, we extract the feasible fundamental matrix $\mathrm{F}(\mathrm{s}',\mathrm{y})$ with help of the integral 'absorption' condition at the boundary introduced in (2)

$$\langle AC\rangle:\quad \Theta(\mathrm{s},\mathrm{s}',\omega)\,\mathrm{F}(\mathrm{s}',\mathrm{y},\omega)=0\ , \tag{19}$$

using a required operator

$$\Theta(\mathrm{s},\mathrm{s}')\equiv \mathrm{K}_{\mathrm{G}}(\mathrm{s},\mathrm{s}')-\mathrm{H}(\mathrm{s},\mathrm{s}')\ . \tag{20}$$

Taking into account (20) equation (17) leads to the boundary integral equation of the second kind

$$\mathrm{F}(\mathrm{s},\mathrm{y})=\mathrm{H}(\mathrm{s},\mathrm{s}')\,\mathrm{F}(\mathrm{s}',\mathrm{y})+\mathrm{G}(\mathrm{s},\mathrm{y})\ . \tag{21}$$

Since the norm of H is less then 1, homogeneous equation $\mathrm{F}=\mathrm{H}\,\mathrm{F}$ has only the primitive solution, and solutions of equations (21) can be written in explicit form

$$\mathrm{F}(\mathrm{s},\mathrm{y})=\left[\mathrm{I}(\mathrm{s},\mathrm{s}')-\mathrm{H}(\mathrm{s},\mathrm{s}')\right]^{-1}\mathrm{G}(\mathrm{s}',\mathrm{y})=\sum_{n=0}^{\infty}\mathrm{H}^{n}(\mathrm{s},\mathrm{s}')\,\mathrm{G}(\mathrm{s}',\mathrm{y})\ . \tag{22}$$

Solution (22) can be also derived directly from equation (18), taking into account this condition (20).

We then find a required form of operator H in condition (20). Substituting the right hand side of (21) into (19) with operator (20), we obtain the next chain of equalities

$$\begin{aligned} \mathrm{O} &\equiv \left[\mathrm{K_G} - \mathrm{H}\right]\mathrm{F} = \mathrm{K_G}\,\mathrm{F} - \mathrm{H}\,\mathrm{F} = \mathrm{K_G}\left[\mathrm{G} + \mathrm{H}\,\mathrm{F}\right] - \mathrm{H}\,\mathrm{F} = \\ &= \mathrm{K_G}\,\mathrm{G} + \mathrm{K_G}\,\mathrm{H}\,\mathrm{F} - \mathrm{H}\,\mathrm{F} = \left[\mathrm{K_G}\,\mathrm{H} - \mathrm{H}\right]\mathrm{F}, \end{aligned} \tag{23}$$

where the term $\mathrm{K_G}\,\mathrm{G}$ is equal to the zero matrix according to (14). From (23) we conclude that

$$\mathrm{K_G}\,\mathrm{H} \equiv \mathrm{H}\ . \tag{24}$$

We then search for the operator H, such that (24) is correct. Equallity (24) is trivially valid if $\mathrm{H} = \mathrm{K_G}$. But such a choice is not appropriate, because the norm of H must be less than 1. Therefore it is sufficient to choose this operator in a composite form [37]

$$\mathrm{H}(\mathrm{s},\mathrm{s}') = \mathrm{K_G}(\mathrm{s},\mathrm{s}'')\,\mathrm{A}(\mathrm{s}'',\mathrm{s}')\ , \tag{25}$$

where A is unknown operator with norm less than 1.

Using the composite operator (25), we rewrite the required absorption operator (20) in explicit form

$$\Theta(\mathrm{s},\mathrm{s}') = \mathrm{K_G}(\mathrm{s},\mathrm{s}') - \mathrm{K_G}(\mathrm{s},\mathrm{s}'')\,\mathrm{A}(\mathrm{s}'',\mathrm{s}')\ . \tag{26}$$

Any solution of problem (2) with the operator (26) in the absorption condition $\langle AC\rangle$ is a physically feasible fundamental solution.

We have used all the information to derive operator A except the property $\|\mathrm{A}\| < \|\mathrm{K_G}\|$ which we now use. Substitution of operator (25) in operator equality (16) results in the equality

$$K_G(s,s') = K_G(s,s'')\,A(s'',s') + \left[K_G(s,s') - K_G(s,s'')\,A(s'',s') \right] . \qquad (27)$$

Taking property (12) of operator K into account, operator equality (27) can be represented as:

$$K_G(s,s') = A(s,s') + \left[K_G(s,s') - A(s,s') \right]. \qquad (28)$$

An explicit form of operator A is given in the next Section.

2.6 Absorption operator at the boundary

First, we consider a case of homogeneous medium with one constant wave velocity v. Representation (28) can be realized by different methods. We choose the method of splitting the operator K_G, that brings a physical meaning to the mathematical formulation of the required absorption condition at boundary (20). It is logical to use the well-known splitting of the surface integral in representation (9), that was earlier applied for finding the mathematical formulation of the 'absolute absorption' principle at boundary of homogeneous acoustic medium (see for example in [5]). Using physical reasoning, it was suggested to divide the surface of integration $\mathbb{S}$ in representation (9) into its virtual part $\mathbb{S}_0(\mathrm{y})$, 'not illuminated' from point y, and its virtual part $\mathbb{S}_1(\mathrm{y})$, 'illuminated' from point y. But a reasonable method of finding the boundary values at the 'not illuminated' parts of surface $\mathbb{S}_0(\mathrm{y})$ is still not suggested. Kirchhoff suggested neglecting them but it was mathematically noncorrect (see detailed discussion in [5]).

For constructing operator A further we use the principle of dividing the surface of integration into two virtual parts. But instead of nonreasonable 'vanishing' the boundary values at the virtual part of boundary $\mathbb{S}_0(\mathrm{y})$ we use rigorous mathematical condition (20). To rigorously formulate this principle for splitting (28) in the case of homogeneous medium, we kinematically sort the physically feasible and nonfeasible rays (ray trajectories). This sorting is based on combining Hadamard's generalization of the Fermat's principle (see details in [3]) and geometric optics generalized for t-hyperbolic symmetric systems of the first order partial differential equations (for example, see in [39]). We consider a set of rays $\mathbb{L}(\mathrm{s},\mathrm{s}')$ which have a form of segments $\mathbb{L}(\mathrm{s},\mathrm{s}')=[\mathrm{s},\mathrm{s}']$ in homogeneous medium, filling free space $\mathbb{R}^3$. These segments connect virtual limit points s and s' of boundary $\mathbb{S}$. The segments are defined in homogeneous unbounded medium, where the "mathematical" supplement $\mathbb{R}^3\setminus\mathbb{D}$ has the same material parameters as domain $\mathbb{D}$. When considering an arbitrary shape of boundary the set of segments is splitted into two subsets.

The first subset contains those segments which have all points inside domain $\mathbb{D}$, namely $\mathbb{L}(\mathrm{s},\mathrm{s}')=[\mathrm{s},\mathrm{s}']\cap\mathbb{S}=\varnothing$. It is necessary to note that after infinitesimal shift of limit points s and s', the segment remains inside domain. Each internal segment will be characterised by the integer-valued function $h(\mathrm{s},\mathrm{s}')=0$, which fixes the absence of intersection of the segment and domain boundaries. Such segments are physically feasible, because they define the "physical" ray $\mathbb{L}(\mathrm{s},\mathrm{s}')$.

The second subset containes those segments which have some points outside domain $\mathbb{D}$, namely $\mathbb{L}(\mathrm{s},\mathrm{s}')=[\mathrm{s},\mathrm{s}']\cap \mathrm{S}\neq\varnothing$. We will characterise such segments by the integer-valued function $h(\mathrm{s},\mathrm{s}')=1$, which fixes the existence of intersection of the segment and domain boundary. Such segments are physically nonfeasible, because they define the "mathematical" ray $\mathbb{L}(\mathrm{s},\mathrm{s}')$.

Therefore, we have the integer-valued function

$$h(\mathrm{s},\mathrm{s}')=\begin{cases}0, & \mathbb{L}(\mathrm{s},\mathrm{s}')=[\mathrm{s},\mathrm{s}']\cap\mathbb{S}=\varnothing\,,\\ 1, & \mathbb{L}(\mathrm{s},\mathrm{s}')=[\mathrm{s},\mathrm{s}']\cap\mathbb{S}\neq\varnothing\,,\end{cases} \tag{29}$$

which extracts the virtual shadow zones at the boundary of the domain. Substituting the shadow function (29) into the integrand of the surface integral operator (11), we define the required absorption operator by the formula

$$\mathrm{A}(\mathrm{s},\mathrm{s}')\langle\ldots\rangle=\iint_{\mathbb{S}} h(\mathrm{s},\mathrm{s}')\,\mathrm{G}(\mathrm{s},\mathrm{s}')\,\mathrm{N}_{\mathrm{s}'}\langle\ldots\rangle\,dS(\mathrm{s}')\ . \tag{30}$$

Secondly, we consider a case of homogeneous medium with p constant wave velocities v_i where $i=1,\ldots,p$ (see details in [18], [38], [39], [40]). In this case the absorption operator A is also given by formula (30) because the shadow function (29) is based on the straight rays $\mathbb{L}(\mathrm{s},\mathrm{s}')=[\mathrm{s},\mathrm{s}']$ which are the same for any wave velocity v_i in homogeneous medium (see for example in [5], [39]).

It is necessary to notice that the absorption operator (30) propagates only physically nonfeasible wavefields from an arbitrary point to all points of corresponding virtual shadow zone at boundary. This denies the heuristic Kirchhoff integral (see for example in [5]). Since the integration surface in operator (30) does not contain the singular point of the kernel, it is not difficult to show that the norm of the operator (30) and, hence, composite operator $K_G A$ is less than 1 (see detailed proof in [36]).

2.7 Feasible fundamental solution for a homogeneous domain

For convenience we rewrite the formula (9) in the form of the spatial representation of the feasible fundamental matrix

$$\mathrm{F}(\mathrm{x},\mathrm{y}) = \mathrm{G}(\mathrm{x},\mathrm{y}) + \mathrm{K}_{\mathrm{G}}(\mathrm{x},\mathrm{s})\,\mathrm{F}(\mathrm{s},\mathrm{y}) \ , \tag{31}$$

where the boundary values (22) accounting for the operator equality (25) are in the final form of

$$\mathrm{F}(\mathrm{s},\mathrm{y}) = \left[\mathrm{I}(\mathrm{s},\mathrm{s}') - \mathrm{K}_{\mathrm{G}}(\mathrm{s},\mathrm{s}'')\,\mathrm{A}(\mathrm{s}'',\mathrm{s}')\right]^{-1} \mathrm{G}(\mathrm{s}',\mathrm{y}) \ . \tag{32}$$

As the norm of the operator $\mathrm{K}_{\mathrm{G}}\,\mathrm{A}$ is less than 1, it is possible to avoid calculation of the inverse operator in (32) by decomposing it into the Neuman series

$$\begin{aligned}\mathrm{F}(\mathrm{s},\mathrm{y}) &= \sum_{n=0}^{\infty}\left[\mathrm{K}_{\mathrm{G}}(\mathrm{s},\mathrm{s}'')\,\mathrm{A}(\mathrm{s}'',\mathrm{s}')\right]^{n} \mathrm{G}(\mathrm{s}',\mathrm{y}) = \\ &= \mathrm{G}(\mathrm{s},\mathrm{y}) + \sum_{n=1}^{\infty}\left[\mathrm{K}_{\mathrm{G}}(\mathrm{s},\mathrm{s}'')\,\mathrm{A}(\mathrm{s}'',\mathrm{s}')\right]^{n} \mathrm{G}(\mathrm{s}',\mathrm{y}).\end{aligned} \tag{33}$$

Series (33) contains both the matrix operator that is composed from conventional surface integral operator K_{G} defined by formula (11) and absorption operator A introduced by formula (30).

Because series (33) is convergent, it is possible to interprete each term of this series as follows: the zero term of this series is represented by the fundamental matrix G for the unbounded homogeneous medium which can contain a nonfeasible component. If a nonfeasible component is absent then the series vanishes identically as $\mathrm{A} \equiv \mathrm{O}$. If a nonfeasible component is present, then the first ($n=1$) term of the series contains both the contribution of single and double diffractions and a nonfeasible component of the fundamental matrix G with a minus sign. Each n-th ($n>1$) term of the series contains the diffraction contribution of the $(2n-1)$-th and $(2n)$-th orders and nonfeasible component of the diffraction contribution of the ($n-1$)-th term with the minus sign. The above analysis shows that series (33) can be considered as the rigorous explicit description of the so-called cascade diffraction including creeping wavefields and wavefields of the whispering galleries.

Substituting formula (33) into representation (31), we obtain

$$\mathrm{F}(\mathrm{x},\mathrm{y}) = \mathrm{G}(\mathrm{x},\mathrm{y}) + \mathrm{K_G}(\mathrm{x},\mathrm{s}) \sum_{n=1}^{\infty} \left[\mathrm{K_G}(\mathrm{s},\mathrm{s''})\,\mathrm{A}(\mathrm{s''},\mathrm{s'})\right]^n \mathrm{G}(\mathrm{s'},\mathrm{y}) \ . \tag{34}$$

Formula (34) defines the unique feasible fundamental solution F for each chosen initial term G. As we can choose G by different ways, the feasible fundamental matrix F is also defined nonuniquelly. It is necessary to notice that the introduction of the absorption condition $\langle A\,C \rangle$ in the statement of the problem (26) extracts the specific fundamental solution in form (34) from the set of the fundamental solutions, but without a proof of its physical feasibility. Analytical justification of its physical feasibility in a case of a canonical model represented by a half-slit in a free space is given in [14]. Numerical justification of the physical feasibility of solution (34) is given in [18], [19], [20], [30].

2.8 The feasible fundamental solution for an inhomogeneous domain

In this Section we consider the statement of the problem in the inhomogeneous domain. After that, we use the solution of the homogeneous domain for solving the problem in the inhomogeneous domain.

We consider now a smoothly inhomogeneous domain $\mathbb{D}$ with a boundary $\mathbb{S}$. The matrix of material parameters M of domain $\mathbb{D}$ is represented by formula (A.16). We define the feasible fundamental solution for inhomogeneous domain as a solution of the problem

$$\begin{cases} \left[\mathrm{D_x} + \mathrm{M}(\mathrm{x},\omega)\right] \mathrm{F}(\mathrm{x},\mathrm{y},\omega) = -\,\delta(\mathrm{x}-\mathrm{y})\,\mathrm{I}\,, \\ \langle RC \rangle : \quad \iint\limits_{\mathbb{S}^\infty} \overline{\mathrm{F}}(\mathrm{x},\mathrm{s},\omega)\,\mathrm{N_s}\,\mathrm{F}(\mathrm{s},\mathrm{y},\omega)\,dS(\mathrm{s}) = 0\,, \\ \langle EC \rangle : \quad \iint\limits_{\{\mathbb{S}^E\}} \overline{\mathrm{F}}(\mathrm{x},\mathrm{s},\omega)\,\mathrm{N_s}\,\mathrm{F}(\mathrm{s},\mathrm{y},\omega)\,dS(\mathrm{s}) = 0\,, \\ \langle VC \rangle : \quad \iint\limits_{\{\mathbb{S}^V\}} \overline{\mathrm{F}}(\mathrm{x},\mathrm{s},\omega)\,\mathrm{N_s}\,\mathrm{F}(\mathrm{s},\mathrm{y},\omega)\,dS(\mathrm{s}) = 0, \\ \langle AC \rangle : \quad \iint\limits_{\mathbb{S}} \overline{\mathrm{F}}(\mathrm{x},\mathrm{s},\omega)\,\mathrm{N_s}\,\mathrm{F}(\mathrm{s},\mathrm{y},\omega)\,dS(\mathrm{s}) = 0\;. \end{cases} \tag{35}$$

Any solution of the problem (35) is the feasible fundamental solution for inhomogeneous domain.

The radiation condition $\langle RC \rangle$ and the edge $\langle EC \rangle$ and vertex $\langle VC \rangle$ conditions for the feasible fundamental solution F in the inhomogeneous domain are written by analogy to (2).

The absorption condition $\langle AC \rangle$ for the inhomogeneous domain in (35) is different from the absorption condition in the problem (26) for the homogeneous domain. The condition in (35) expresses an auxiliary requirement of the absorption of the wavefields of nonphysical sources, located outside the domain. If the integral over $\mathbb{S}$ is not identically equal to zero then the boundary values F contain wavefields of nonphysical sources, located outside a domain. If this summand is identically equal to zero then the boundary values of F can be nonzero, but can not contain wavefields of nonphysical sources, located outside a domain.

Taking into account (A.16), we rewrite system (A.15) as *t*-hyperbolic system in (2) for the homogeneous domain with modified right-hand side

$$\left[\mathrm{D}_{x} + \bar{\mathrm{M}}\right] \mathrm{F}(x, y) = -\delta(x - y)\,\mathrm{I} - \Delta\mathrm{M}(x)\,\mathrm{F}(x, y), \quad supp\,\Delta\mathrm{M} \in \mathbb{D} \cap \mathbb{B}\ . \tag{36}$$

To obtain the integral representation for the fundamental solution of equation (36), we rewrite the divergence theorem in matrix-vector form from [31] in our designaton as

$$\begin{aligned}&\iiint\limits_{\mathbb{D}} \left[\bar{\mathrm{F}}^{\mathrm{T}}(z, x)\,\mathrm{K}\,\mathrm{D}_{z}\,\mathrm{F}(z, y) - \left(\mathrm{D}_{z}\,\bar{\mathrm{F}}(z, x)\right)^{\mathrm{T}} \mathrm{K}\,\mathrm{F}(z, y) \right] dV(z) = \\ &= \iint\limits_{\mathbb{S} \cup \mathbb{S}^{+\infty} \cup \{\mathbb{S}^{E}\} \cup \{\mathbb{S}^{V}\}} \bar{\mathrm{F}}^{\mathrm{T}}(s, x)\,\mathrm{K}\,\mathrm{N}_{s}\,\mathrm{F}(s, y)\, dS(s)\,,\end{aligned} \tag{37}$$

where kernels $\bar{\mathrm{F}}$ of integral operators in (37) are based on the feasible fundamental solution $\bar{\mathrm{F}}(x, y, \omega)$ for the homogeneous domain, defined by formula (34). Calculating the volume integral of the left hand side of equality (37), we obtain

$$\begin{aligned}&\iiint\limits_{\mathbb{D}} \left[\bar{\mathrm{F}}^{\mathrm{T}}(z, x)\,\mathrm{K}\,\mathrm{D}_{z}\,\mathrm{F}(z, y) - \left(\mathrm{D}_{z}\,\bar{\mathrm{F}}(z, x)\right)^{\mathrm{T}} \mathrm{K}\,\mathrm{F}(z, y) \right] dV(z) = \\ &= \iiint\limits_{\mathbb{D}} \left[\bar{\mathrm{F}}^{\mathrm{T}}(z, x)\,\mathrm{K}\left[-\delta(z - y)\,\mathrm{I} - \mathrm{M}(z)\,\mathrm{F}(z, y)\right] - \left[-\delta(z - x)\,\mathrm{I} - \bar{\mathrm{M}}\,\bar{\mathrm{F}}(z, x)\right]^{\mathrm{T}} \mathrm{K}\,\mathrm{F}(z, y) \right] dV(z)\,.\end{aligned} \tag{38}$$

From properties of the generalized function δ and the fundamental matrix we conclude that the right hand side of (38) can be transformed to

$$\begin{aligned}&\iiint\limits_{\mathbb{D}} \left[\bar{\mathrm{F}}^{\mathrm{T}}(z, x)\,\mathrm{K}\left[-\delta(z - y)\,\mathrm{I} - \mathrm{M}(z)\,\mathrm{F}(z, y)\right] - \left[-\delta(z - x)\,\mathrm{I} - \bar{\mathrm{M}}\,\bar{\mathrm{F}}(z, x)\right]^{\mathrm{T}} \mathrm{K}\,\mathrm{F}(z, y) \right] dV(z) = \\ &= -\bar{\mathrm{F}}^{\mathrm{T}}(y, x)\,\mathrm{K} - \iiint\limits_{\mathbb{D}} \left[\bar{\mathrm{F}}^{\mathrm{T}}(z, x)\,\mathrm{K}\,\mathrm{M}(z)\,\mathrm{F}(z, y) \right] dV(z) + \\ &\qquad + \mathrm{K}\,\mathrm{F}(x, y) + \iiint\limits_{\mathbb{D}} \left[\left(\bar{\mathrm{M}}\,\bar{\mathrm{F}}(z, x)\right)^{\mathrm{T}} \mathrm{K}\,\mathrm{F}(z, y) \right] dV(z) = \\ &= -\bar{\mathrm{F}}^{\mathrm{T}}(y, x)\,\mathrm{K} + \mathrm{K}\,\mathrm{F}(x, y) - \iiint\limits_{\mathbb{D}} \left[\bar{\mathrm{F}}^{\mathrm{T}}(z, x)\,\mathrm{K}\,\Delta\mathrm{M}(z)\,\mathrm{F}(z, y) \right] dV(z)\,.\end{aligned} \tag{39}$$

Substituting (39) into left hand side of (37) we obtain the equality

$$
\begin{aligned}
\mathrm{K}\,\mathrm{F}(\mathrm{x},\mathrm{y}) = \overline{\mathrm{F}}^{\mathrm{T}}(\mathrm{y},\mathrm{x})\,\mathrm{K} + \iiint_{\mathbb{D}} \left[\overline{\mathrm{F}}^{\mathrm{T}}(\mathrm{z},\mathrm{x})\,\mathrm{K}\,\Delta\mathrm{M}(\mathrm{z})\,\mathrm{F}(\mathrm{z},\mathrm{y})\right] dV(\mathrm{z}) \\
+ \iint_{\mathbb{S}\cup\mathbb{S}^{+\infty}\cup\{\mathbb{S}^{\mathrm{E}}\}\cup\{\mathbb{S}^{\mathrm{V}}\}} \overline{\mathrm{F}}^{\mathrm{T}}(\mathrm{s},\mathrm{x})\,\mathrm{K}\,\mathrm{N}_{\mathrm{s}}\,\mathrm{F}(\mathrm{s},\mathrm{y})\,dS(\mathrm{s})\,.
\end{aligned}
\tag{40}
$$

Using the reciprocity property of an arbitrary fundamental matrix solution and multiplying the equality (40) from the left side by matrix K^{-1}, we obtain the equality

$$
\begin{aligned}
\mathrm{F}(\mathrm{x},\mathrm{y}) = \overline{\mathrm{F}}(\mathrm{x},\mathrm{y}) + \iiint_{\mathbb{D}} \left[\overline{\mathrm{F}}(\mathrm{x},\mathrm{z})\,\Delta\mathrm{M}(\mathrm{z})\,\mathrm{F}(\mathrm{z},\mathrm{y})\right] dV(\mathrm{z}) \\
+ \iint_{\mathbb{S}\cup\mathbb{S}^{+\infty}\cup\{\mathbb{S}^{\mathrm{E}}\}\cup\{\mathbb{S}^{\mathrm{V}}\}} \overline{\mathrm{F}}(\mathrm{x},\mathrm{s})\,\mathrm{N}_{\mathrm{s}}\,\mathrm{F}(\mathrm{s},\mathrm{y})\,dS(\mathrm{s})\,.
\end{aligned}
\tag{41}
$$

The surface integral in (41) is identically equal to zero because of conditions in problem (35). We then transform (41) to form

$$
\mathrm{F}(\mathrm{x},\mathrm{y}) = \overline{\mathrm{F}}(\mathrm{x},\mathrm{y}) + \iiint_{\mathbb{D}\cap\mathbb{B}} \overline{\mathrm{F}}(\mathrm{x},\mathrm{z})\,\Delta\mathrm{M}(\mathrm{z})\,\mathrm{F}(\mathrm{z},\mathrm{y})\,dV(\mathrm{z})\ , \tag{42}
$$

where the integral is taken in the domain $\mathbb{D}\cap\mathbb{B}$ rather than in $\mathbb{D}$ because $\Delta\mathrm{M}=0$ in $\mathbb{D}\setminus\mathbb{B}$. The kernel of the integral operator and the first term in (42) are represented by the feasible fundamental matrix $\overline{\mathrm{F}}(\mathrm{x},\mathrm{y})$ for the homogeneous domain. We notice that the solution (42) is formal as it is a volume integral equation. Solving this equation with respect to F is a difficult analytical problem, which is considered in [40], [41]. We do not consider solving equation (42) as it is outside of the scope of this paper.

2.9. Feasible surface and volume integral operators for a homogeneous domain

By analogy to the surface integral operator (8) for homogeneous domain, we introduce into consideration the feasible surface integral operator for homogeneous domain

$$\mathrm{K_F}(\mathrm{x},\mathrm{s})\langle\ldots\rangle = \iint\limits_{\mathbb{S}} \mathrm{F}(\mathrm{x},\mathrm{s})\,\mathrm{N_s}\langle\ldots\rangle\, dS(\mathrm{s}) \;, \tag{43}$$

where F is the feasible fundamental matrix for homogeneous domain. Operator (43) has a property $\mathrm{K_F}\,\mathrm{K_F} = \mathrm{K_F}$. Substituting its integral representation (31) for $\mathrm{y}\to\mathrm{s}'$ with boundary values in form (32) into the kernel of operator (43), we obtain the feasible surface integral operator in homogeneous domain

$$\mathrm{K_F}(\mathrm{x},\mathrm{s}')\langle\ldots\rangle = \mathrm{K_G}(\mathrm{x},\mathrm{s})\,\mathrm{K_F}(\mathrm{s},\mathrm{s}') + \mathrm{K_G}(\mathrm{x},\mathrm{s}') \;, \tag{44}$$

where the feasible surface integral operator at the boundary has form

$$\mathrm{K_F}(\mathrm{s},\mathrm{s}') = \left[\mathrm{I}(\mathrm{s},\mathrm{s}'') - \mathrm{K_G}(\mathrm{s},\mathrm{s}''')\,\mathrm{A}(\mathrm{s}''',\mathrm{s}'')\right]^{-1}\mathrm{K_G}(\mathrm{s}'',\mathrm{s}') . \tag{45}$$

Substituting the representation (31) for $\mathrm{y}\to\mathrm{s}'$ with boundary values in form (33) into the kernel of the operator (43), we can decompose the feasible surface integral operator (44) into the Neumann-type operator series

$$\mathrm{K_F}(\mathrm{s},\mathrm{s}') = \mathrm{K_G} + \sum_{n=1}^{\infty}\left[\mathrm{K_G}\;\mathrm{A}\right]^n \mathrm{K_G} = \mathrm{K_G}(\mathrm{s},\mathrm{s}') + \mathrm{K_G}(\mathrm{s},\mathrm{s}''')\,\mathrm{A}(\mathrm{s}''',\mathrm{s}'')\,\mathrm{K_G}(\mathrm{s}'',\mathrm{s}') + \ldots \;. \tag{46}$$

In addition to the surface integral operator (43) we introduce into consideration the feasible volume integral operator for homogeneous domain

$$\mathrm{R_F}(\mathrm{x},\mathrm{y})\langle\ldots\rangle = \iiint\limits_{\mathbb{D}} \mathrm{F}(\mathrm{x},\mathrm{y})\langle\ldots\rangle\, dV(\mathrm{y}) , \tag{47}$$

where F is the feasible fundamental solution. By substituting the feasible fundamental solution of homogeneous domain (34) in the kernel of the operator (47), we obtain the feasible volume operator for homogeneous domain in terms of Neumann series

$$\mathrm{R}_{\mathrm{F}}(\mathrm{x},\mathrm{y}) = \iiint\limits_{\mathbb{D}} \sum_{n=0}^{\infty} \left[\mathrm{K}_{\mathrm{G}}(\mathrm{x},\mathrm{s})\,\mathrm{A}(\mathrm{s},\mathrm{s}')\right]^{n} \mathrm{G}(\mathrm{s}',\mathrm{y}) \langle\ldots\rangle \, dV(\mathrm{y}) = \sum_{n=0}^{\infty} \left[\mathrm{K}_{\mathrm{G}}(\mathrm{x},\mathrm{s})\,\mathrm{A}(\mathrm{s},\mathrm{s}')\right]^{n} \mathrm{R}_{\mathrm{G}}(\mathrm{s}',\mathrm{y}) \,, \tag{48}$$

where

$$\mathrm{R}_{\mathrm{G}}(\mathrm{x},\mathrm{y})\langle\ldots\rangle = \iiint\limits_{\mathbb{D}} \mathrm{G}(\mathrm{x},\mathrm{y})\langle\ldots\rangle \, dV(\mathrm{y}) \,. \tag{49}$$

2.10 Feasible surface and volume integral operators for an inhomogeneous domain

By analogy to the feasible surface integral operator for homogeneous domain (43) we introduce into consideration the feasible surface integral operator for inhomogeneous domain

$$\mathrm{K_F}(\mathrm{x}, \mathrm{s})\langle\ldots\rangle = \iint_{\mathbb{S}} \mathrm{F}(\mathrm{x}, \mathrm{s})\, \mathrm{N_s}\langle\ldots\rangle\, dS(\mathrm{s}) \ , \tag{50}$$

where F is the feasible fundamental solution for inhomogeneous domain. If point x tends to surface $\mathbb{S}$, then operator (50) has a property $\mathrm{K_F}\,\mathrm{K_F} = \mathrm{K_F}$. Substituting (42) in (50) we obtain

$$\mathrm{K_F}(\mathrm{x}, \mathrm{s}) = \mathrm{K}_{\overline{\mathrm{F}}}(\mathrm{x}, \mathrm{s}) + \mathrm{R}_{\overline{\mathrm{F}}}(\mathrm{x}, \mathrm{z})\,\Delta\mathrm{M}(\mathrm{z})\,\mathrm{K_F}(\mathrm{z}, \mathrm{s}) \ . \tag{51}$$

In addition to the surface integral operator (50) we introduce into consideration the feasible volume integral operator for inhomogeneous domain

$$\mathrm{R_F}(\mathrm{x}, \mathrm{y})\langle\ldots\rangle = \iiint_{\mathbb{D}} \mathrm{F}(\mathrm{x}, \mathrm{y})\langle\ldots\rangle\, dV(\mathrm{y}), \tag{52}$$

where F is the feasible fundamental solution for inhomogeneous domain. By substituting the feasible fundamental solution for inhomogeneous domain (42) in the kernel of the operator (52), we obtain the feasible volume integral operator for inhomogeneous domain

$$\mathrm{R_F}(\mathrm{x}, \mathrm{y}) = \mathrm{R}_{\overline{\mathrm{F}}}(\mathrm{x}, \mathrm{y}) + \mathrm{R}_{\overline{\mathrm{F}}}(\mathrm{x}, \mathrm{z})\,\Delta\mathrm{M}(\mathrm{z})\,\mathrm{R_F}(\mathrm{z}, \mathrm{y}), \tag{53}$$

where $\mathrm{R}_{\overline{\mathrm{F}}}$ is given by formula (47). The representation (53) represents the operator $\mathrm{R_F}$ for inhomogeneous domain with help of operator $\mathrm{R}_{\overline{\mathrm{F}}}$ for homogeneous domain with a simpler kernel.

2.11 Conclusions

In this paper we proposed an analytical description of the fundamental solution of the multiphysics wave equation which is dependent on the geometrical shape of the domain of effective medium. We introduced the integral condition of absolute absorption at the boundary which selects the feasible fundamental solution. The feasible fundamental solution in homogeneous domains is represented by the Neumann series with explicit operator and zero-order term. The operator contains the surface integral operator and an absorption operator. The zero-order term is chosen as a Green's function for unbounded medium. The absorption operator is zero for convex domains. We introduce the feasible fundamental solution for inhomogeneous domains as an equation with a volume integral operator. The kernel of this operator is based on the feasible fundamental solution for homogeneous domains. Using the feasible fundamental solutions we obtained the feasible surface and volume integral operators with the appropriate kernels in homogeneous and inhomogeneous domains. In contrast to the conventional fundamental solution (Green's function for the unbounded medium) designed for modeling of the total wavefield, the feasible fundamental solution allows us to evaluate separate wave fragments. The feasible fundamental solution opens a perspective of the theoretical description of wavefields in the form of the superposition of the separate waves, multiply reflected and transmitted at curved boundaries in real medium. The feasible fundamental solutions can be used for the development of the wavefield modeling methods in complex media with shadow zones. The feasible fundamental solution can improve modeling methods for complex media with different phases (elastic skeleton, fluid and/or gas in pores, anisotropy, etc).

2.12 Acknowledgements

The authors wish to thank the Research Centres of Statoil ASA in Trondheim and Bergen (Norway) for their support of this study. We are grateful to our colleagues Kamill D. Klem-Musatov and Anton Duchkov from IPGG SB RAS (Novosibirsk, Russia), Nikolay Zyatkov, Gennady Demidenko and Gleb Dyatlov from Novosibirsk State University (Novosibirsk, Russia), Jan Pajchel, Milana Ayzenberg and Ola-Petter Munkvold from Statoil ASA (Bergen and Trondheim, Norway), Hans B. Helle from Odin Petroleum (Bergen, Norway) and Fredrik Andersson from Lund University (Lund, Sweden) for constructive discussions. The authors wish to thank Kees Wapenaar for the usefull discussions on the topic of the matrix formalism for *t*-hyperbolic systems and for spending his time for reviewing the complex text of the paper. The authors would like to thank Anna Mackie for her valuable comments and advices on improvement the linguistic style of the paper.

2.13 Appendix. The multiphysics wave equation

There are many theoretical methods of building a macroscopic effective model of microscopic, heterogeneous (multiphase) medium (see reviews in papers [21], [42], [43], [44], [45]). In spite of differences between various methods, it is shown that elastic oscillations of sceleton and acoustic oscillations of fluids, connected to electromagnetic fields of piezoelectric and electrocinetic nature, in effective model can be described by t-hyperbolic system of equations of first order (see for example in [21], [31], [32], [33], [38], [39], [45], [46]) or equivalent hyperbolic system of equations of second order (see for example in [21], [43], [44], [47]). The difference between effective models, obtained by different methods, is seen only in variations of the scalar components of the matrix of macroscopic material medium parameters. These variations are caused by differences in a set of microscopic physical phenomena, taken into account in different methods. Therefore we consider, without loss of generality, a t-hyperbolic system of arbitrary size [31], [32] (version of this paper improved in 2010 was also available for us), [33], [38], [39], [46].

We consider mechanical and electromagnetic oscillations in an arbitrary domain of effective medium with material parameters independent of time. Such oscillations can be described by the linear t-hyperbolic system of first order partial differential equations [38], [39], [48]

$$\mathrm{C}_0(\mathrm{x})\partial_t \mathrm{u}(\mathrm{x},t)+\sum_{n=1}^{3}\mathrm{C}_n(\mathrm{x})\partial_n \mathrm{u}(\mathrm{x},t)+\mathrm{C}(\mathrm{x})\mathrm{u}(\mathrm{x},t)=-\mathrm{f}(\mathrm{x},t), \quad \mathrm{x}\in\mathbb{D}\subset\mathbb{R}^3, \tag{A.1}$$

where $\mathrm{u}(\mathrm{x},t)$ is a column composed of n required scalar functions, $\mathrm{f}(\mathrm{x},t)$ is the volumetric density of outer forces, and ∂_t and ∂_n are the time and coordinate x_n derivatives respectively. Matrices $\mathrm{C}_0(\mathrm{x})$, $\mathrm{C}_n(\mathrm{x})$ and $\mathrm{C}(\mathrm{x})$ of the material parameters have dimension $n\times n$. Matrices $\mathrm{C}_0(\mathrm{x})$ and $\mathrm{C}_n(\mathrm{x})$ satisfy the properties

$$\begin{aligned}\mathrm{C}_0(\mathrm{x})&=\mathrm{C}_0^T(\mathrm{x})>0,\\ \mathrm{C}_n(\mathrm{x})&=\mathrm{C}_n^T(\mathrm{x}),\end{aligned} \tag{A.2}$$

and matrix $\mathrm{C}(\mathrm{x})$ is generally nonsymmetric. Superscript T denotes transposition. Since system (A.1) generalizes the acoustic, elastic and electromagnetic wave equations, we call this system the multiphysics wave equation.

Column $\mathrm{u}(\mathrm{x},t)$ contains kinematic and dynamic field strengths [48]. Kinematic field strengths, such as components of particle velocity vectors and electric field vectors, can be collected in the kinematic subcolumn $\mathrm{u}_k(\mathrm{x},t)$. Dynamic field strengthes, such as components of stress tensors and magnetic field vectors, can be collected in the dynamic subcolumn $\mathrm{u}_d(\mathrm{x},t)=\begin{pmatrix}\mathrm{u}_{d1} & \mathrm{u}_{d2} & \mathrm{u}_{d3}\end{pmatrix}^T$. We notice that a one-index notation for the two-index tensors is wide spread (for example, see in [38], [42], [46], [48]). Because the symmetric 3×3 tensors have only 6 independent components in solids and viscous fluids and one component (pressure) in nonviscous fluids, in the general case, dynamic subcolumn contains independent strengthes in columns u_{d1} and u_{d2} and dependent dynamic field strengthes in column u_{d3}. Therefore we have an augmented system of equations. To reduce this system to the ordinary system with respect to a nondegenerate dynamic subcolumn $\mathrm{u}_d(\mathrm{x},t)=\begin{pmatrix}\mathrm{u}_{d1} & \mathrm{u}_{d2}\end{pmatrix}^T$, we exclude column u_{d3} [48], [49], [50]. Finally, we write column $\mathrm{u}(\mathrm{x},t)=\begin{pmatrix}\mathrm{u}_k & \mathrm{u}_{d1} & \mathrm{u}_{d2}\end{pmatrix}^T$ in form that is invariant to any type of effective medium, because splitting in three subcolumns $\mathrm{u}_k(\mathrm{x},t)$, $\mathrm{u}_{d1}(\mathrm{x},t)$ and $\mathrm{u}_{d2}(\mathrm{x},t)$ does not depend on a type of effective medium.

It is known (for example, see comments in [33], [38]) that in the general case the differential operator in (A.1) is not selfadjoint. This property leads to the consideration of the fundamental solution for the differential operator, adjoint to operator in (A.1), and overcomplication in Green's formula which is necessary in our study. For simplicity and convenience, we rewrite the differential operator in (A.1) in terms of the matrix differential operator formalism, as introduced in papers [31], [32], [33], [48]. We then can use the fundamental matrix solution and the corresponding Green's formula, as introduced in these papers.

We then represent the original system governing mechanical and electromagnetic oscillations written in terms of the nabla formalism as system of two matrix equations [46]

$$\begin{aligned} &A_{11}\,\partial_t u_k + \begin{bmatrix} D_{x1} & D_{x2} \end{bmatrix} \begin{pmatrix} u_{d1} \\ u_{d2} \end{pmatrix} + B_{11}\,u_k + \begin{bmatrix} B_{12} & B_{13} \end{bmatrix} \begin{pmatrix} u_{d1} \\ u_{d2} \end{pmatrix} = -f_k\,, \\ &\begin{bmatrix} A_{22} & A_{23} \\ A_{23}^T & A_{33} \end{bmatrix} \partial_t \begin{pmatrix} u_{d1} \\ u_{d2} \end{pmatrix} + \begin{bmatrix} D_{x1}^T \\ D_{x2}^T \end{bmatrix} u_k + \begin{bmatrix} B_{21} \\ B_{31} \end{bmatrix} u_k + \begin{bmatrix} B_{22} & B_{23} \\ B_{32} & B_{33} \end{bmatrix} \begin{pmatrix} u_{d1} \\ u_{d2} \end{pmatrix} = -\begin{pmatrix} f_{d1} \\ f_{d2} \end{pmatrix}, \end{aligned} \tag{A.3}$$

where A_{11} is the generalized density-permittivity matrix, A_{ij} are the generalized compliance-permeability matrices, B_{ij} are some matrices, f_k and f_{di} are the volume densities of external forces, and D_{xi} are the matrix differential operators. The pair of matrix equations (A.3) can be combined into system similar to system (A.1)

$$A(x)\partial_t u(x,t) + D_x\,u(x,t) + B(x)u(x,t) = -f\,(x,t) \tag{A.4}$$

where $f\,(x,t) = \begin{pmatrix} f_k & f_{d1} & f_{d2} \end{pmatrix}^T$, the matrices written as

$$A(x) = \begin{bmatrix} A_{11} & O & O \\ O & A_{22} & A_{23} \\ O & A_{23}^T & A_{33} \end{bmatrix}, \quad B(x) = \begin{bmatrix} B_{11} & B_{12} & B_{13} \\ B_{21} & B_{22} & B_{23} \\ B_{31} & B_{32} & B_{33} \end{bmatrix} \tag{A.5}$$

can be obtained by simple rewriting of corresponding matrices in [31], [32], [33]. Comparing matrices in (A.4) and (A.1), we obtain equalities $A = C_0$ and $B = C$, and a decomposition of the matrix operator in form

$$D_x = \begin{bmatrix} O & D_{x1} & D_{x2} \\ D_{x1}^T & O & O \\ D_{x2}^T & O & O \end{bmatrix} = \sum_{n=1}^{3} C_n\,\partial_n\,, \quad C_n = \begin{bmatrix} O & C_{n1} & C_{n2} \\ C_{n1}^T & O & O \\ C_{n2}^T & O & O \end{bmatrix}. \tag{A.6}$$

Notice that the internal block structure of the differential operator D_x and matrices C_n in (A.6) is invariant to a type of effective medium. The operator D_x and matrices C_n, $A(x)$ and $B(x)$ have the necessary properties of symmetry

$$\begin{aligned} &\mathrm{D}_{\mathrm{x}}^{T} = -\,\mathrm{K}\,\mathrm{D}_{\mathrm{x}}\,\mathrm{K}\,, \quad \mathrm{D}_{\mathrm{x}}^{T} = \mathrm{D}_{\mathrm{x}}\,, \quad \mathrm{C}_{n}^{T} = -\,\mathrm{K}\,\mathrm{C}_{n}\,\mathrm{K}\,, \quad \mathrm{C}_{n}^{T} = \mathrm{C}_{n}\,, \\ &\mathrm{A}^{T}\left(\mathrm{x}\right) = \mathrm{K}\,\mathrm{A}\left(\mathrm{x}\right)\mathrm{K}\,, \quad \mathrm{A}^{T}\left(\mathrm{x}\right) = \mathrm{A}\left(\mathrm{x}\right) > 0\,, \\ &\mathrm{B}^{T}\left(\mathrm{x}\right) = \mathrm{K}\,\mathrm{B}\left(\mathrm{x}\right)\mathrm{K}\,. \end{aligned} \tag{A.7}$$

Notice that matrix $\mathrm{B}(\mathrm{x})$ is generally nonsymmetric. Diagonal matrix K obeys the property $\mathrm{K}^{T} = \mathrm{K}^{-1} = \mathrm{K}$ and contains +1 and -1 in special order (see more details in [31], [32], [33]).

As the explicit form of the matrices $\mathrm{A}(\mathrm{x})$ and $\mathrm{B}(\mathrm{x})$, the operators $\mathrm{D}_{\mathrm{x}1}$ and $\mathrm{D}_{\mathrm{x}2}$ and matrices C_{n1} and C_{n2} is not relevant to this paper, we do not provide their detailed description. Some examples of the matrices $\mathrm{A}(\mathrm{x})$ and $\mathrm{B}(\mathrm{x})$, the operator D_{x} and the column $\mathrm{u}(\mathrm{x},t)$ are given in the version of paper [32] improved in 2010 and in paper [33]. The differential operators for the acoustic, electromagnetic and elastodynamic wave propagation are similar to the operator D_{x} in (A.6).

We notice that the differential operators for the coupled elastodynamic and electromagnetic wave propagation in piezoelectric media [33] and in fluid-saturated porous media with electrolyte [32] are the block-diagonal matrices. These matrices are not similar to the differential operator D_{x} in (A.6) that is not the block-diagonal matrix. Below we show that in case of fluid-saturated porous media with electrolyte, this contradiction can be avoided after the necessary rearranging of matrix (D10) from [32]. This rearranging corresponds to the rearranging of the internal structure of column $\mathrm{u} = \left(\mathrm{u}_1 \quad \mathrm{u}_2 \quad \mathrm{u}_3\right)^{T}$ to column $\mathrm{u} = \left(\mathrm{u}_k \quad \mathrm{u}_{d1} \quad \mathrm{u}_{d2}\right)^{T}$.

We write three subcolumns $\mathrm{u}_1 = \left(\mathrm{E} \quad \mathrm{H}\right)^{T}$, $\mathrm{u}_2 = \left(\mathrm{v}^{s} \quad -\tau_1^{b} \quad -\tau_2^{b}\right)^{T}$ and $\mathrm{u}_3 = \left(\mathrm{w} \quad p\right)^{T}$ from formulae (F13) in [32] as three rearranged subcolumns

$$\mathrm{u}_k = \begin{pmatrix} \mathrm{E} \\ \mathrm{v}^{s} \\ \mathrm{w} \end{pmatrix}, \quad \mathrm{u}_{d1} = \begin{pmatrix} \mathrm{H} \\ -\tau_1^{b} \\ p \end{pmatrix}, \quad \mathrm{u}_{d2} = \left(-\tau_2^{b}\right)\,. \tag{A.8}$$

The components of subcolumns (A.8) and matrices (A.5) are explicitly given in the improved version of paper [32]. Diagonal matrix K corresponding to subcolumns (A.8) reads

$$\mathrm{K} = diag\left[\mathrm{K}_k, \mathrm{K}_{d1}, \mathrm{K}_{d2}\right] \tag{A.9}$$

with diagonal matrices $\mathrm{K}_k = diag[\mathrm{I}, \mathrm{I}, \mathrm{I}]$, $\mathrm{K}_{d1} = diag[-\mathrm{I}, -\mathrm{I}, -1]$, $\mathrm{K}_{d2} = diag[-\mathrm{I}]$, and the identity 3×3 matrix $\mathrm{I} = diag[1,1,1]$. Matrix (A.9) is a result of the necessary rearranging of matrix (D19) from [32].

Omitting derivation, we show the off-diagonal matrix elements of the differential operators

$$\mathrm{D}_{\mathrm{x}1} = \begin{bmatrix} \mathrm{D}_0^T & \mathrm{O} & 0 \\ \mathrm{O} & \mathrm{D}_1 & 0 \\ \mathrm{O} & \mathrm{O} & \nabla \end{bmatrix} = \sum_{n=1}^{3} \mathrm{C}_{n1}\, \partial_n , \quad \mathrm{D}_{\mathrm{x}2} = \begin{bmatrix} \mathrm{O} \\ \mathrm{D}_2 \\ \mathrm{O} \end{bmatrix} = \sum_{n=1}^{3} \mathrm{C}_{n2}\, \partial_n \ . \tag{A.10}$$

We rewrite four matrix differential operators in (A.10) using their decomposition with matrix coefficients in form

$$\begin{gathered} \mathrm{D}_0 = \begin{bmatrix} 0 & -\partial_3 & \partial_2 \\ \partial_3 & 0 & -\partial_1 \\ -\partial_2 & \partial_1 & 0 \end{bmatrix} = \sum_{n=1}^{3} \mathrm{I}_{0n}\, \partial_n , \quad \mathrm{D}_1 = \begin{bmatrix} \partial_1 & 0 & 0 \\ 0 & \partial_2 & 0 \\ 0 & 0 & \partial_3 \end{bmatrix} = \sum_{n=1}^{3} \mathrm{I}_{1n}\, \partial_n , \\ \mathrm{D}_2 = \begin{bmatrix} 0 & \partial_3 & \partial_2 \\ \partial_3 & 0 & \partial_1 \\ \partial_2 & \partial_1 & 0 \end{bmatrix} = \sum_{n=1}^{3} \mathrm{I}_{2n}\, \partial_n , \quad \nabla = \begin{bmatrix} \partial_1 \\ \partial_2 \\ \partial_3 \end{bmatrix} = \sum_{n=1}^{3} \mathrm{I}_n\, \partial_n , \end{gathered} \ . \tag{A.11}$$

where 3×3 matrices $\mathrm{I}_{0n} = \left[\delta_{i(n-1)}\, \delta_{(n+1)j} - \delta_{i(n+1)}\, \delta_{(n-1)j}\right]$, $\mathrm{I}_{1n} = \left[\delta_{in}\, \delta_{nj}\right]$, and $\mathrm{I}_{2n} = \left[\delta_{i(n-1)}\, \delta_{(n+1)j} + \delta_{i(n+1)}\, \delta_{(n-1)j}\right]$, and 3×1 matrix $\mathrm{I}_n = \left[\delta_{in}\right]$ are composed from the Kronecker deltas, $i, j = 1, 2, 3$. When value of index $n-1$ is less than 1, then we assume its value 3. When value of index $n+1$ is more than 3, then we assume its value 1. Using formulae (A.10) and (A.11), we write matrices C_{n1} and C_{n2} by formulae

$$\mathrm{C}_{n1} = \begin{bmatrix} \mathrm{I}_{0n}^T & \mathrm{O} & 0 \\ \mathrm{O} & \mathrm{I}_{1n} & 0 \\ \mathrm{O} & \mathrm{O} & \mathrm{I}_n \end{bmatrix}, \quad \mathrm{C}_{n2} = \begin{bmatrix} \mathrm{O} \\ \mathrm{I}_{2n} \\ \mathrm{O} \end{bmatrix} . \tag{A.12}$$

Accounting for explicit form of the symmetric matrices C_n and relationship (A.6), we justify the equality of systems (A.4) and (A.1) in case of the coupled elastodynamic and electromagnetic wave propagation.

Notice that the internal block structure of the differential operators $\mathrm{D}_{\mathrm{x}1}$ and $\mathrm{D}_{\mathrm{x}2}$ in (A.10) and matrices C_{n1} and C_{n2} in (A.12) is not invariant, because it depends strongly on a chosen type of effective medium. It is seen from comparing the differential operators and matrices with those for piezoelectric medium [33]. In piezoelectric medium subcolumns (A.8) contract to $\mathrm{u}_k = \begin{pmatrix} \mathrm{E} & \mathrm{v}^s \end{pmatrix}^T$, $\mathrm{u}_{d1} = \begin{pmatrix} \mathrm{H} & -\tau_1^b \end{pmatrix}^T$, and $\mathrm{u}_{d2} = \begin{pmatrix} -\tau_2^b \end{pmatrix}$. Then the differential operators $\mathrm{D}_{\mathrm{x}1}$ and $\mathrm{D}_{\mathrm{x}2}$ in (A.10) contract to $\mathrm{D}_{\mathrm{x}1} = \begin{bmatrix} \mathrm{D}_0^T & \mathrm{O} \\ \mathrm{O} & \mathrm{D}_1 \end{bmatrix}$ and $\mathrm{D}_{\mathrm{x}2} = \begin{bmatrix} \mathrm{O} \\ \mathrm{D}_2 \end{bmatrix}$, and matrices C_{n1} and C_{n2} in (A.12) contract to $\mathrm{C}_{n1} = \begin{bmatrix} \mathrm{I}_{0n}^T & \mathrm{O} \\ \mathrm{O} & \mathrm{I}_{1n} \end{bmatrix}$ and $\mathrm{C}_{n2} = \begin{bmatrix} \mathrm{O} \\ \mathrm{I}_{2n} \end{bmatrix}$.

Folowing concepts in [51], we represent the matrices of the material parameters in domain $\mathbb{D}$ in form

$$\begin{aligned} \mathrm{A}(\mathrm{x}) &= \bar{\mathrm{A}} + \Delta\mathrm{A}(\mathrm{x}), \quad supp\,\Delta\mathrm{A} \in \mathbb{D} \cap \mathbb{B}, \\ \mathrm{B}(\mathrm{x}) &= \bar{\mathrm{B}} + \Delta\mathrm{B}(\mathrm{x}), \quad supp\,\Delta\mathrm{B} \in \mathbb{D} \cap \mathbb{B}. \end{aligned} \tag{A.13}$$

The elements of the matrices $\Delta\mathrm{A}(\mathrm{x})$ and $\Delta\mathrm{B}(\mathrm{x})$ are smooth functions. The matrices $\bar{\mathrm{A}}$ and $\bar{\mathrm{B}}$ are constant.

We use the direct and inverse Fourier transforms

$$
\begin{aligned}
\mathrm{u}(\mathrm{x}, \omega) &= \frac{1}{\sqrt{2\pi}} \int_{0}^{+\infty} \mathrm{u}(\mathrm{x}, t) \exp(+i\,\omega\, t)\, dt\,, \\
\mathrm{u}(\mathrm{x}, t) &= \frac{1}{\sqrt{2\pi}} \int_{-\infty}^{+\infty} \mathrm{u}(\mathrm{x}, \omega) \exp(-i\,\omega\, t)\, d\omega\,.
\end{aligned}
\tag{A.14}
$$

The Fourier transforms (A.14) further allow direct consideration of the stationary solution $\mathrm{u}(\mathrm{x}, \omega)$.

Applying the direct Fourier transform to equation (A.4) we obtain the multiphysics wave equation

$$
\left[\mathrm{D}_{\mathrm{x}} + \mathrm{M}(\mathrm{x}, \omega)\right] \mathrm{u}(\mathrm{x}, \omega) = -\,\mathrm{f}(\mathrm{x}, \omega)\ , \tag{A.15}
$$

where

$$
\begin{aligned}
&\mathrm{M}(\mathrm{x},\omega) = \bar{\mathrm{M}}(\omega) + \Delta\mathrm{M}(\mathrm{x},\omega), \\
&\bar{\mathrm{M}}(\omega) = -\,i\,\omega\,\bar{\mathrm{A}} + \bar{\mathrm{B}}, \quad \mathrm{x} \in \mathbb{D}, \\
&\Delta\mathrm{M}(\mathrm{x},\omega) = \begin{cases} -\,i\,\omega\,\Delta\mathrm{A}(\mathrm{x}) + \Delta\mathrm{B}(\mathrm{x}), & \mathrm{x} \in \mathbb{D} \cap \mathbb{B}, \\ 0\,, & \mathrm{x} \in \mathbb{D} \setminus \mathbb{B}\ . \end{cases}
\end{aligned}
\tag{A.16}
$$

Accounting for (A.7) we see that matrix $\mathrm{M}(\mathrm{x},\omega)$ obeys the property

$$
\mathrm{M}^{T}(\mathrm{x},\omega) = \mathrm{K}\,\mathrm{M}(\mathrm{x},\omega)\,\mathrm{K}\ . \tag{A.17}
$$

We notice that the properties (A.7) and (A.17) define the reciprocity of any solution of the multiphysics wave equation (A.15). Wapenaar and Douma discuss more properties of matrix $\mathrm{M}(\mathrm{x},\omega)$ in Section II from [33].

2.14 References

[1] M. Ayzenberg, A.M. Aizenberg, B. Ursin, Tip-wave superposition method with effective reflection and transmission coefficients: A new 3D Kirchhoff-based approach to synthetic seismic modeling, Leading Edge, 2009, 28, 582-588.

[2] K. Klem-Musatov, A. Aizenberg, H.B. Helle, J. Pajchel, Reflection and transmission at curvilinear interface in terms of surface integrals, Wave Motion, 2004, 39, 1, 77-92.

[3] F.G. Friedlander, Sound Pulses, Cambridge, Cambridge University Press, 1958.

[4] H. Hönl, A.W. Maue, K. Westpfahl, Theorie der Beugung, Handbuch der Physik, Band XXV/1, Springer-Verlag, Berlin, 1961.

[5] F. Kottler, Diffraction at a black screen, Part I: Kirchhoff's theory, In: Progress in Optics, Volume IV (E. Wolf, ed.) NorthHolland Publishing Co., Amsterdam 1965, 281-314.

[6] V.A. Borovikov, Diffraction at polygons and polyhedrons, “Nauka” Press, Moscow, 1966 (in Russian).

[7] K. Klem-Musatov, Theory of Seismic Diffractions, Investigations in Geophysics, No. 9, SEG, Tulsa, 1994.

[8] K.D. Klem-Musatov, A.M. Aizenberg, J. Pajchel, H.B. Helle, Edge and Tip Diffractions: Theory and Applications in Seismic Prospecting, Geophysical Monograph Series, No. 14, SEG, Tulsa, USA, 2008.

[9] S.N. Chandler-Wilde, I.G. Graham, S. Langdon, E.A. Spence, Numerical-asymptotic boundary integral methods in high-frequency acoustic scattering. Acta Numerica, Cambridge University Press, 2012, pp. 89–305.

[10] A.M. Aizenberg, K.D. Klem-Musatov, Progress in seismic diffraction theory – From edge and tip waves to multiple reflections-transmissions with diffractions, Extended Abstracts of the 72-th EAGE Conference & Exhibition (2010) G034.

[11] A.M. Aizenberg, M.A. Ayzenberg, K.D. Klem-Musatov, Seismic diffraction modeling with the tip-wave superposition method, Extended Abstracts of the 73-th EAGE Conference & Exhibition (2011) B018.

[12] M.A. Ayzenberg, A.M. Aizenberg, H.B. Helle, K.D. Klem-Musatov, J. Pajchel, B. Ursin, 3D diffraction modeling of singly scattered acoustic wavefields based on the combination of surface integral propagators and transmission operators, Geophysics, 2007, 72, 5, SM19-SM34.

[13] M. Ayzenberg, I. Tsvankin, A.M. Aizenberg, B. Ursin, Effective refection coefficients for curved interfaces in TI media, Geophysics, 2009, 74, WB33-WB53.

[14] A.M. Aizenberg, A.A. Ayzenberg, Feasible fundamental solution to the acoustic wave equation in a heterogeneous halfspace with a regular boundary, Proceedings of the International Conference on Mathematical Methods in Geophysics "MMG-2008" dedicated to the 80th anniversary of A.S. Alekseev, 13-15 October 2008, 1–6.

[15] A.M. Aizenberg, A.A. Ayzenberg, Fundamental solution of the acoustic wave equation which satisfies the integral absorption condition at a regular boundary of a half-space, Proceedings of the International Conference "Differential Equations. Function Spaces. Approximation Theory" dedicated to the 100th anniversary of Sergey Sobolev, Russian Academy of Sciences, 2008, 89 (in Russian).

[16] A.M. Aizenberg, A.A. Ayzenberg, J. Pajchel, Feasible fundamental matrix of the seismic-electromagnetic wave equation in a curved fractured and porous fluid-saturated layer, Dynamics of solid media, Proceedings of Lavrentiev's Institute of Hydrodynamics, Russian Academy of Sciences, 2010, 126, 20-25 (in Russian).

[17] A.A. Ayzenberg, A.M. Aizenberg, Feasible fundamental matrix of the seismic-electromagnetic wave equation in a curved elastic porous fluid-saturated layer, Proceedings of the International Conference "Contemporary Problems of Computational Mathematics and Mathematical Physics" dedicated to the 90th anniversary of Alexander Samarsky, Russian Academy of Sciences (2009) 113-114.

[18] N. Zyatkov, A. Ayzenberg, A.M. Aizenberg, A. Romanenko, Highly-optimized TWSM algorithm for modeling cascade diffraction in terms of propagation-absorption

matrices, Extended Abstracts, 75th EAGE Conference, London, UK, 10-13 June 2013, Th-P02-11.

[19] A.M. Aizenberg, N.Y. Zyatkov, A.A. Ayzenberg, E.Z. Rakshaeva, New concepts of the transmission-propagation oerator theory in seismic diffraction modeling and interpretation, Extended Abstracts, 76th EAGE Conference, Amsterdam, Netherlands, 16-19 June 2014, We-P06-07.

[20] A. Ayzenberg, N. Zyatkov, A. Stovas, A.M. Aizenberg, The feasible near-front wavefield below salt overhang in terms of cascade diffraction, Extended Abstracts, 76th EAGE Conference, Amsterdam, Netherlands, 16-19 June 2014, We-P06-06.

[21] M. Schanz, Poroelastodynamics: Linear Models, Analytical Solutions, and Numerical Methods, Applied Mechanics Reviews, 2009, 62(3), 030803-1–030803-15.

[22] M. Costabel, M. Dauge, On representation formulas and radiation conditions, Math. Methods Appl. Sci., 1997, 20, 2, 133-150.

[23] A.I. Madyarov, B.B. Guzina, A radiation condition for layered elastic media, J. Elast., 2006, 82, 73-98.

[24] P. Grisvard, Boundary Value Problems in Non-Smooth Domains, Pitman, London, 1985.

[25] M. Costabel, Boundary integral operators on lipschitz domains: Elementary results, SIAM J. Math. Anal., 1988, 613-626.

[26] M. Costabel, M. Dauge, R. Duduchava, Asymptotics without logarithmic terms for crack problems, Communications in PDE, 2003, 869-926.

[27] N. Omer, Z. Yosibash, M. Costabel, M. Dauge, Edge flux intensity functions in polyhedral domains and their extraction by a quasidual function method, International Journal of Fracture, 2004, 129, 97–130.

[28] S. Osher, Initial-boundary value problems for hyperbolic systems in regions with corners, I. Trans. Amer. Math. Soc., 1973, 176, 141–165.

[29] S. Osher, Initial-boundary value problems for hyperbolic systems in regions with corners, II. Trans. Amer. Math. Soc., 1974, 198, 155–175.

[30] Z. Yosibash, Computing singular solutions of elliptic boundary value problems in polyhedral domains using the *p*-FEM, Applied Numerical Mathematics, 2000, 33, 71–93.

[31] K. Wapenaar, General representations for wavefield modeling and inversion in geophysics, Geophysics, 2007, 72, 5, SM5-SM17.

[32] K. Wapenaar, J. Fokkema, Reciprocity theorems for diffusion, flow and waves, J. Appl. Mech, 2004, 71, 145-150.

[33] K. Wapenaar, H. Douma, A unified optical theorem for scalar and vectorial wave fields, J. Acoust. Soc. Am., 2012, 131, 5, 3611–3626.

[34] A. Huang, R. Temam, The linear hyperbolic initial and boundary value problems in a domain with corners, Math. AP., 2013.

[35] S.S. Kutateladze, Fundamentals of Functional Analysis, Kluwer Academic Publishers, Kluwer Texts in the Mathematical Sciences, 1996, Vol. XII, XIV+277 p.

[36] A.N. Kolmogorov, S.V. Fomin, Elements of the Theory of Functions and Functional Analysis, Addison Wesley, 2001.

[37] M.A. Krasnosel'skii, G.M. Vainikko, P.P. Zabreiko, Ya.B. Rutitskii, V.Ya. Stetsenko, Approximate Solution of Operator Equations, Volters/Noordhoff Publishing, Groningen, 1972, xii+484 p.p.

[38] S. Benzoni-Gavage, D. Serre, Multi-dimensional hyperbolic partial differential equations. First order systems and applications, Oxford Mathematical Monographs, Oxford University Press, New York, 2007.

[39] J. Rauch, Hyperbolic partial differential equations and geometric optics, Department of Mathematics, University of Michigan, 2012, p.p. 301.

[40] H. Hörmander, Linear Partial Differential Operators, Springer–Verlag, 1963.

[41] C. Miranda, Partial Differential Equations of Elliptic Type, N-Y, Berlin: Springer-Verlag, 1970.

[42] A.M. Blokhin, V. N. Dorovsky, Mathematical modelling in the theory of multivelocity continuum, Nova science publishers, Inc., USA, 1995.

[43] P. Li., Boundary Element Method for Wave Propagation in Partially Saturated Poroelastic Continua, volume 15 of Computation in Engineering and Science, Verlag der Technischen, Universität Graz, 2012.

[44] P. Maghoul, B. Gatmiri, D. Duhamel, Three–dimensional transient thermo–hydro–mechanical fundamental solutions of unsaturated soils, Int. J. Numer. Anal. Methods Geomech. , 2010, 34, 297–329.

[45] S.R. Pride, J.G. Berryman, Linear dynamics of double-porosity dual-permeability materials, I. Governing equations and acoustic attenuation, Physical Review E, 2003, 68, 036603, 1-10.

[46] S.K. Godunov, E.I. Romensky, Elements of Continuum Mechanics and Conservation Laws, Kluwer Acad. Publ., Dordrecht, 2003.

[47] L. Banjai, M. Schanz, Wave propagation problems treated with convolution quadrature and BEM, Max-Planck-Institute fur Mathematik, Leipzig, Preprint 60, 2010.

[48] M. de Hoop, A. de Hoop, Wavefield reciprocity and optimization in remote sensing, Proc. R. Soc. Lond. A, 2000, 456, 641-682.

[49] S. Penissi, A covariant approach to symmetrizable and constrained hyperbolic systems, Le Matematiche, 1999, 54, Fasc. I, 99-122.

[50] A. Morando, D. Serre, On the $L2$-well posedeness of an initial boundary value problem for the 3D linear elastisity, Commun. Math. Sci., 2005, 3, 4, 575-586.

[51] G.F. Roach, Scattering from unbounded surfaces, Proceedings of Dundee Conference, Pitman Research Notes, Longmans, London, 1993, 248-272.

Chapter 3

Feasible source wavefield for acoustic V-model with shadow in form of the double diffraction approximation

Alena A. Ayzenberg[a*], Nikolay Y. Zyatkov[b], Arkady M. Aizenberg[c], Alexey Stovas[a]

[a] Norwegian University of Science and Technology (NTNU), S.P. Andersens veg 15a, 7491 Trondheim, Norway,
tel.: +47 90 840 729, fax: +47 73 944 472, e-mail: alena.ayzenberg@ntnu.no
tel.: +47 73 597 139, fax: +47 73 944 472, e-mail: alexey.stovas@ntnu.no
[b] Novosibirsk State University, Pirogova str. 2, 630090 Novosibirsk, Russia,
tel.: +7 923 248 2157, fax: +7 383 333 2513, e-mail: nikolay.zyatkov@gmail.com
[c] Institute of Petroleum Geology and Geophysics, Russian Academy of Sciences,
Ac. Koptyug Pr. 3, 630090 Novosibirsk, Russia,
tel.: +7 383 335 6457, fax: +7 383 333 2513, e-mail: AizenbergAM@ipgg.sbras.ru

Presented at the ROSE Meeting, Trondheim, Norway, 2013; the 75th EAGE Conference & Exhibition, London, UK, 2013. Submitted to Geophysical Journal International on 26 January 2015, resubmitted on 11 August 2015.

3.1 Summary

Conventionally, seismic modeling uses different numerical methods in order to build a subsurface image. These methods give a total solution, which can be difficult to describe and separate into physical wave fragments. In our earlier papers, we proposed the rigorous Transmission-Propagation Operator Theory (TPOT) which is purely analytical and provides the solution in inhomogeneous 3D media both in total and separated form. The separate waves are computed on a Graphics Processing Unit (GPU) cluster and visualized on a seismogram by the Tip-Wave Superposition Method (TWSM) in the mid-frequency range. In this paper, we use the TPOT&TWSM technology and test it on a 2,5D acoustic overhang V-model, which simulates a salt overhang. The concept of 'feasibility', proposed in TPOT&TWSM, is applied to the model so that the obtained wavefields are 'feasible' with respect to shadow zones. The focus is on the receiver line below the V-overhang in order to demonstrate the ability of the method to handle the source wavefield description in geometrical shadow. The source wavefield is a combination of two separate wave fragments corresponding to the physical events: the source spherical wavefield and the wavefield diffracted by the overhang. We prove that this study corrects for the conventional overhang model solution with help of the double-diffraction correction. After this correction, the source wavefield becomes 'feasible'. Numerical examples illustrate the time arrivals and amplitudes of the source wavefield. The amplitudes computed by TPOT&TWSM are compared to the amplitudes analytically computed by the edge wave theory.

3.2 Introduction

Seismics exploits various imaging approaches based on the use of the free space Green's function for unbounded media as a point source wavefield to reconstruct the internal structure of the real subsurface from observed surface data. If the properties of the medium change significantly (for instance, if the medium has a salt body) then there is a problem to determine the source wavefield.

All the well-known analytical representations of the total wavefield for rigorous diffraction problems at a wedge account for the geometrical shadow zone of the source wavefield. Friedlander (1958) analyzes a classical problem of diffraction at a wedge (Figure 5.2), at a half-plane (Figure 5.3) and at a circular cylinder (Figure 6.1). Hewett *et al*. (2011) studies 2D time-dependent diffraction on a half-line. Babich *et al*. (2007) discusses the total wavefield for a wide range of canonical diffraction problems. In all canonical problems, the total wavefield is actually represented as the free space Green's function in the geometrical illuminated zone and the diffracted wavefield in both illuminated and shadow zones. The diffracted wavefield smoothes the amplitude discontinuity of the point source wavefield at the shadow boundary. The arrival time of the point source wavefield front satisfies the generalized Fermat's principle, as the front of the diffracted wavefield in shadow zone is delayed with respect to the classical Fermat's principle. This point source wavefield is considered as the physically 'feasible point source wave field'. Figures 1.1, 7.3, 7.6, 7.14 and 7.15 in Chandler-Wilde *et al*. (2012) prove that geometrical shadow zones of the point source wavefield are included in modern numerical solutions of diffraction problems at boundaries of complex shape and scattering at obstacles of complex shape. Borovikov & Kinber (1994) and Ferrand *et al*. (2014) demonstrate that a similar structure of the wavefield is obtained by the modeling of diffraction at irregular surface using the ray theory by Cerveny (2005) and the geometrical theory of diffraction by Keller (1962). Zaman (2000) and Chandler-Wilde *et al*. (2012) illustrate that the rigorous theory of acoustic scattering represents the total solution as the sum of the source and scattered wavefields. The latter theory assumes that the point source wavefield in any zone of the domain is the free space Green's function. In concave domains with shadow zones, the point source wavefield has an amplitude discontinuity at the shadow boundaries. In these cases, Klem-Musatov (1994) suggested that an edge diffracted wavefield is added to the point source wavefield in order to compensate this discontinuity. The mathematical description of the source wavefield for domains of arbitrary geometrical shape remains an important and challenging problem in the wave theory.

In this paper, we propose the new analytical Transmission-Propagation Operator Theory and the Tip-Wave Superposition Method (TPOT&TWSM) in the mid-frequency range to build the feasible source wavefield in the shadow zone caused by a salt overhang of V-shape. This feasible source wavefield, for a point source, below the salt overhang differs from the conventional free space Green's function by a cascade diffraction term. This cascade diffraction term performs the wave propagation and diffraction in shadow, illuminated and transition zones. The cascade diffraction term contains single and double edge waves at the sharp edge of the model.

TPOT by A.M. Aizenberg *et al*. (2011) and A.M. Aizenberg *et al*. (2014) provides an analytical description of the wave structure for the feasible source wavefield in layered and block media. The feasible source wavefield is represented by a surface Kirchhoff-type integral with the feasible fundamental solution of the actual domain in the kernel. This description is based on the splitting of the source wavefield into the sum of the wave events corresponding to the observed wavefield. The first term is the conventional point source wavefield (the free space Green's function), which propagates from the source to the receiver only in the geometrical illuminated zones, and the second term is a cascade diffraction term.

A.M. Aizenberg & A.A. Ayzenberg (2008a), A.M. Aizenberg & A.A. Ayzenberg (2008b), A.M. Aizenberg *et al*. (2010), A.A. Ayzenberg & A.M. Aizenberg (2009) and A.M. Aizenberg & A.A. Ayzenberg (2015)/Chapter 2 of this thesis introduce the feasible fundamental solution in the complex geometrical domains as the superposition of the conventional fundamental solution and a cascade diffraction term represented by an infinite series of diffraction terms of increasing order. The diffraction term of the n-th order is the result of the propagation-absorption operator acting on that of the $(n-1)$-th order. The cascade diffraction term compensates the unfeasible parts of the conventional fundamental solution and takes into account the shadowed parts of the boundary.

In papers Zyatkov *et al*. (2012) and Zyatkov *et al*. (2013), we represent an improved highly-optimized algorithm of TWSM in the mid-frequency range for computation of the first cascade diffraction term based on the propagation and absorption matrices. In this paper, we use TWSM for computation of the feasible source wavefield. The main interest of this paper is to utilize the simplest approximation for the feasible source wavefield of acoustic domains using the first cascade diffraction term solely. A.A. Ayzenberg *et al*. (2010), A.A. Ayzenberg *et al*. (2012), A.A. Ayzenberg *et al*. (2013) and A.A. Ayzenberg *et al*. (2014) demonstrate that this approximation explains the main kinematic and dynamic features of the feasible source wavefield in shadow zones. All the higher-order terms are dropped because we focus only on the double diffraction approximation, which totally is described by the first term. The accuracy, stability and efficiency of the algorithm are illustrated by a numerical test for an acoustic half-space with a canonical V-shaped boundary. The numerical examples illustrate the accuracy of the time arrivals, amplitude and pulse shape of the wave events computed by TWSM from A.M. Aizenberg & Klem-Musatov (2010) and M.A. Ayzenberg *et al*. (2009) in comparison with the formulae of the edge and tip wave theory by A.M. Aizenberg (1982) and A.M. Aizenberg (1993).

This paper describes the feasible source wavefield in an acoustic homogeneous domain with shadow zones and provides its comparison with the theoretical results by A.M. Aizenberg (1982) and A.M. Aizenberg (1993). The paper consists of: an Introduction, eight Sections and Conclusions. The Introduction formulates the feasibility problem. Section 3.3 gives the statement of the 2-block forward V-problem. Section 3.4 performs a derivation of the solution. Sections 3.5 and 3.6 explain how to choose the feasible source wavefield in the solution, in terms of mechanics and the TPOT wave theory. Section 3.7 presents approximations of the theoretical formulae and the TWSM algorithm. Section 3.8 gives the reduction of the source wavefield representation, obtained by TPOT, to the formulae of the edge wave theory. Section 3.9 describes the normalized diffraction amplitudes in terms of the Diffraction Attenuation Coefficients (DAC) of the edge wave theory. Section 3.10 contains the design for V-model and demonstrates the TWSM test seismograms and their comparison with the edge wave theory. Conclusions summarize the result of the paper: the source feasible wavefield has to be used for V-model solution in the shadow caused by the V-shaped boundary.

3.3 Forward V-problem for 2-block medium

We consider a 2-block model with V-interface (cylindrical wedge), concave inside the half-space (Figure 1a). The material parameters of the domains and the geometrical parameters of the interface are chosen to imitate a salt overhang surrounded by sediments. A strong velocity contrast imitates shadow below the overhang.

V-model consists of two homogeneous acoustic domains, $\mathbb{D}_1$ and $\mathbb{D}_2$, separated by V-interface composed from two plane faces, connected by an edge. A point source 1 is located at point ($x = 4.0\,\text{km}, y = 0\,\text{km}, z = 1.0\,\text{km}$) and a point source 2 is located at point ($x = 4.0\,\text{km}, y = 0\,\text{km}, z = 2.0\,\text{km}$). Radius-vectors $\mathbf{x}_m$ (Figure 1b,c) designate an arbitrary point in $\mathbb{D}_m$, $m = 1,2$. Parameters of domain $\mathbb{D}_1$ are: P-wave velocity $v_{P,1} = 2.0\,\text{km/sec}$ and density $\rho_1 = 2.0\,\text{g/cm}^3$. Parameters of domain $\mathbb{D}_2$ are: P-wave velocity $v_{P,2} = 4.0\,\text{km/sec}$ and density $\rho_2 = 3.0\,\text{g/cm}^3$.

V-interface is considered as a two-sided surface with sides $\mathbb{S}_m(\mathbf{s}_m)$ (Figure 1b,c), where $m = 1,2$ is the domain number. Radius-vector $\mathbf{s}_m$ denotes either a boundary point on $\mathbb{S}_m$ or a point in $\mathbb{D}_m$ which is infinitesimally close to $\mathbf{s}_m$. We denote the infinite parts of the interface as $\mathbb{S}_m^\infty$. The faces of the interface are denoted as $\mathbb{S}^j$, $j = 1,2$. The normal vectors are directed inwards domains $\mathbb{D}_m$ and denoted as $\mathbf{n}(\mathbf{s}_m^j)$, $\mathbf{s}_m^j \in \mathbb{S}_m^j$, where the lower index is the medium number, the upper index is the face number. The upper side $\mathbb{S}_1^1$ and lower side $\mathbb{S}_2^1$ of the upper face of V-interface are defined by formula $z = 0.41(4 - x)$. The upper side $\mathbb{S}_2^2$ and lower side $\mathbb{S}_1^2$ of the lower face of V-interface are defined by formula $z = -0.41(4 - x)$.

We introduce two receiver lines (arrays). Line 1: from $x = 3{,}25\,\text{km}$ to $x = 4{,}75\,\text{km}$ with step $\Delta x = 0{,}015\,\text{km}$ at $y = 0.0\,\text{km}, z = -1.0\,\text{km}$. Line 2: from $x = 2{,}0\,\text{km}$ to $x = 3{,}5\,\text{km}$ with step $\Delta x = 0{,}015\,\text{km}$ at $y = 0.0\,\text{km}, z = -2.0\,\text{km}$. Each of the lines contain 101 receivers. Line 1 intersects the shadow boundary of the spherical wave at $x = 4.0\,\text{km}$.

The receivers for $x < 4.0\,\mathrm{km}$ are located in the shadow zone, and the receivers for $x > 4.0\,\mathrm{km}$ are in the illuminated zone.

We represent temporal spectra of the wavefield as particle velocity-pressure vectors (4×1-columns)

$$\mathbf{u}(\mathbf{x}_m,\omega)=\begin{pmatrix} v_{1,m} \\ v_{2,m} \\ v_{3,m} \\ p_m \end{pmatrix} , \tag{1}$$

where $v_{1,m}$, $v_{2,m}$, $v_{3,m}$ are components of particle velocities, p_m is pressure in each domain. Function $\mathbf{u}(\mathbf{x}_m,\omega)$ is defined as follows

$$\begin{cases} \mathbf{u}=\mathbf{u}(\mathbf{x}_1,\omega), & \text{for} \quad \mathbf{x}_1 \in \mathbb{D}_1 , \\ \mathbf{u}=\mathbf{u}(\mathbf{x}_2,\omega), & \text{for} \quad \mathbf{x}_2 \in \mathbb{D}_2 . \end{cases} \tag{2}$$

Vectors (2) are connected with the wavefields by the Fourier transform

$$\mathbf{u}(\mathbf{x}_m,t)=\frac{1}{\sqrt{2\pi}}\int_{-\infty}^{+\infty}\mathbf{u}(\mathbf{x}_m,\omega)\,e^{-i\omega t}\,d\omega \ , \tag{3}$$

where ω is angular frequency. The temporal spectrum vectors $\mathbf{u}(\mathbf{x}_m,\omega)$ in (2) satisfy the wave motion equations from A.M. Aizenberg & A.A. Ayzenberg (2015)/Chapter 2 of this thesis

$$\mathbf{D}_{\mathbf{x}_m}\,\mathbf{u}(\mathbf{x}_m,\omega)+\mathbf{M}_m(\omega)\,\mathbf{u}(\mathbf{x}_m,\omega)=\mathbf{f}(\mathbf{x}_m,\omega) \ , \tag{4}$$

where the differential matrix operator and the matrix of material parameters are

$$\mathbf{D}_{\mathbf{x}_m} = \begin{pmatrix} 0 & 0 & 0 & \dfrac{\partial}{\partial x_1} \\ 0 & 0 & 0 & \dfrac{\partial}{\partial x_2} \\ 0 & 0 & 0 & \dfrac{\partial}{\partial x_3} \\ \dfrac{\partial}{\partial x_1} & \dfrac{\partial}{\partial x_2} & \dfrac{\partial}{\partial x_3} & 0 \end{pmatrix}, \quad \mathbf{M}_m(\omega) = (-i\,\omega) \begin{pmatrix} \rho_m & 0 & 0 & 0 \\ 0 & \rho_m & 0 & 0 \\ 0 & 0 & \rho_m & 0 \\ 0 & 0 & 0 & \dfrac{1}{\rho_m (v_{P,m})^2} \end{pmatrix}. \tag{5}$$

The point source is $\mathbf{f}(\mathbf{x}_1, \omega) = \dfrac{\psi(\omega)}{(-i\,\omega)\,\rho_1}\begin{pmatrix} 0 & 0 & 0 & \delta(\mathbf{x}_1 - \mathbf{y}_1) \end{pmatrix}^T$, the source radiates a spherical P-wave. Function $\psi(\omega)$ is the spectrum of the wavelet $\psi(t) = e^{-(2\tau)^2}\cos(2\pi\,\tau)$, where $\tau = t/T - 2$. The wave period $T = 0.032\,\mathrm{sec}$ corresponds to the dominant wavelength of 0.064 km and the dominant frequency of 38.25 Hz. In domain $\mathbb{D}_2$, there is no source: $\mathbf{f}(\mathbf{x}_2, \omega) = \begin{pmatrix} 0 & 0 & 0 & 0 \end{pmatrix}^T$.

In each domain (Figure 1c), vector (2) satisfies the radiation conditions $\langle RC \rangle_m$ at the infinite boundary $\mathbb{S}_m^\infty$ of domain $\mathbb{D}_m$, $m = 1,2$

$$\langle RC \rangle_m : \quad \iint_{\mathbb{S}_m^\infty} \mathbf{F}(\mathbf{x}_m, \mathbf{s}_m, \omega)\, \mathbf{N}(\mathbf{s}_m)\, \mathbf{u}(\mathbf{s}_m, \omega)\, dS(\mathbf{s}_m) = 0, \quad m = 1,2 \tag{6}$$

in terms of the feasible surface integral operators similar to (43) from A.M. Aizenberg & A.A. Ayzenberg (2015)/Chapter 2 of this thesis. A detailed description of the feasible kernel $\mathbf{F}(\mathbf{x}_m, \mathbf{s}_m, \omega)$ will be given by formulae (17)-(21) in Section 3.5. The normal matrix is

$$\mathbf{N}(\mathbf{s}_m) = \begin{pmatrix} 0 & 0 & 0 & n_1(\mathbf{s}_m) \\ 0 & 0 & 0 & n_2(\mathbf{s}_m) \\ 0 & 0 & 0 & n_3(\mathbf{s}_m) \\ n_1(\mathbf{s}_m) & n_2(\mathbf{s}_m) & n_3(\mathbf{s}_m) & 0 \end{pmatrix}. \tag{7}$$

We notice that everywhere in this paper we use the next integration rule

$$\iint_{\mathbb{S}} \mathbf{F}_1(\mathbf{x},\mathbf{s})\,\mathbf{f}_2(\mathbf{s})\,dS(\mathbf{s}) = \mathbf{f}_3(\mathbf{x}) \ , \tag{8}$$

which expresses that the integration variable $\mathbf{s}$ ‘dissapears’ after the integration operation.

At the cylindrical vicinity (Figure 1c) $\mathbb{S}_1^{\mathbb{E}} \cup \mathbb{S}_2^{\mathbb{E}}$ of edge $\mathbb{E}$ of V-boundary, vector (2) satisfies the edge conditions $\langle EC \rangle_m$, $m = 1,2$

$$\langle EC \rangle_m : \quad \iint_{\mathbb{S}_m^{\mathbb{E}}} \mathbf{F}(\mathbf{x}_m, \mathbf{s}_m, \omega)\,\mathbf{N}(\mathbf{s}_m)\,\mathbf{u}(\mathbf{s}_m, \omega)\,dS(\mathbf{s}_m) = 0\,, \quad m = 1,2 \tag{9}$$

in terms of the feasible surface integral operators similar to (43) from A.M. Aizenberg & A.A. Ayzenberg (2015)/Chapter 2 of this thesis.

At faces $\mathbb{S}^j$ of V-interface (Figure 1c), we consider two boundary conditions $\langle BC \rangle^j$, $j = 1,2$

$$\langle BC \rangle^j : \quad \mathbf{C}\,\mathbf{R}\left(\mathbf{s}_1^j\right)\mathbf{u}\left(\mathbf{s}_1^j, \omega\right) = \mathbf{J}\,\mathbf{C}\,\mathbf{R}\left(\mathbf{s}_2^j\right)\mathbf{u}\left(\mathbf{s}_2^j, \omega\right) \ , \quad j = 1,2\,, \tag{10}$$

where

$$\mathbf{C} = \begin{bmatrix} 0 & 0 & 1 & 0 \\ 0 & 0 & 0 & 1 \end{bmatrix} , \tag{11}$$

$$\mathbf{R}\left(\mathbf{s}_m^j\right) = \begin{bmatrix} \mathbf{i}_1\left(\mathbf{s}_m^j\right)\cdot\bar{\mathbf{i}}_1 & \mathbf{i}_1\left(\mathbf{s}_m^j\right)\cdot\bar{\mathbf{i}}_2 & \mathbf{i}_1\left(\mathbf{s}_m^j\right)\cdot\bar{\mathbf{i}}_3 & 0 \\ \mathbf{i}_2\left(\mathbf{s}_m^j\right)\cdot\bar{\mathbf{i}}_1 & \mathbf{i}_2\left(\mathbf{s}_m^j\right)\cdot\bar{\mathbf{i}}_2 & \mathbf{i}_2\left(\mathbf{s}_m^j\right)\cdot\bar{\mathbf{i}}_3 & 0 \\ \mathbf{i}_3\left(\mathbf{s}_m^j\right)\cdot\bar{\mathbf{i}}_1 & \mathbf{i}_3\left(\mathbf{s}_m^j\right)\cdot\bar{\mathbf{i}}_2 & \mathbf{i}_3\left(\mathbf{s}_m^j\right)\cdot\bar{\mathbf{i}}_3 & 0 \\ 0 & 0 & 0 & 1 \end{bmatrix} , \tag{12}$$

$\mathbf{u}\left(\mathbf{s}_m^j,\omega\right)$ is the limit value of vector $\mathbf{u}\left(\mathbf{x}_m,\omega\right)$ at face $\mathbb{S}_m^j$, $\mathbf{J}=\begin{bmatrix}-1 & 0\\ 0 & 1\end{bmatrix}$, $\left(\bar{\mathbf{i}}_1,\bar{\mathbf{i}}_2,\bar{\mathbf{i}}_3\right)$ is the global Cartesian basis independent of point $\mathbf{s}_m^j$ and $\left(\mathbf{i}_1\left(\mathbf{s}_m^j\right),\mathbf{i}_2\left(\mathbf{s}_m^j\right),\mathbf{n}\left(\mathbf{s}_m^j\right)\right)$ is the local basis dependent of point $\mathbf{s}_m^j$.

Equation (4), the radiation conditions $\left\langle RC\right\rangle_m$ (6), the edge conditions $\left\langle EC\right\rangle_m$ (9) and the boundary conditions $\left\langle BC\right\rangle^j$ (10) form the correct statement of the forward problem for V-model

$$\begin{cases}\mathbf{D}_{\mathbf{x}_m}\,\mathbf{u}\left(\mathbf{x}_m,\omega\right)+\mathbf{M}_m\left(\omega\right)\mathbf{u}\left(\mathbf{x}_m,\omega\right)=\mathbf{f}\left(\mathbf{x}_m,\omega\right),\\ \left\langle RC\right\rangle_m:\quad \iint\limits_{\mathbb{S}_m^\infty}\mathbf{F}\left(\mathbf{x}_m,\mathbf{s}_m,\omega\right)\mathbf{N}(\mathbf{s}_m)\,\mathbf{u}\left(\mathbf{s}_m,\omega\right)dS(\mathbf{s}_m)=0\,,\\ \left\langle EC\right\rangle_m:\quad \iint\limits_{\mathbb{S}_m^{\mathbb{E}}}\mathbf{F}\left(\mathbf{x}_m,\mathbf{s}_m,\omega\right)\mathbf{N}(\mathbf{s}_m)\,\mathbf{u}\left(\mathbf{s}_m,\omega\right)dS(\mathbf{s}_m)=0\,,\\ \left\langle BC\right\rangle^j:\quad \mathbf{C}\,\mathbf{R}\left(\mathbf{s}_1^j\right)\mathbf{u}\left(\mathbf{s}_1^j,\omega\right)=\mathbf{J}\,\mathbf{C}\,\mathbf{R}\left(\mathbf{s}_2^j\right)\mathbf{u}\left(\mathbf{s}_2^j,\omega\right),\end{cases}\qquad m=1,2\,,\quad j=1,2\,. \tag{13}$$

3.4 Analytical solution separation: source wavefield term as a separate wavefield

Problem (13) has an explicit solution according to Zaman (2000) and Chandler-Wilde *et al.* (2012)

$$\mathbf{u}(\mathbf{x}_1,\omega)=\mathbf{u}^{(0)}(\mathbf{x}_1,\omega)+\mathbf{u}^{sc}(\mathbf{x}_1,\omega) \ , \tag{14}$$

where $\mathbf{u}^{(0)}(\mathbf{x}_1,\omega)$ is the source wavefield and $\mathbf{u}^{sc}(\mathbf{x}_1,\omega)$ is the scattered wavefield. If we aim to compute the total wavefield $\mathbf{u}(\mathbf{x}_1,\omega)$ we could apply any modeling method, including numerical methods. But if the objective is to describe separate terms of the wavefield, we have to apply the proposed TPOT&TWSM method. In this paper, we focus on the source wavefield $\mathbf{u}^{(0)}(\mathbf{x}_1,\omega)$ description by TPOT&TWSM. The other term $\mathbf{u}^{sc}(\mathbf{x}_1,\omega)$ will be considered in Chapter 5.

In the theory from Costabel & Dauge (1997), this term is written as follows. The source wavefield radiated by a point source can be represented as a particular solution of equation (4) in the form of the volume integral

$$\mathbf{u}^{(0)}(\mathbf{x}_1,\omega)=\iiint\limits_{\mathbb{D}_1}\mathbf{F}\left(\mathbf{x}_1,\mathbf{y}_1,\omega\right)\mathbf{f}(\mathbf{y}_1,\omega)\,dV(\mathbf{y}_1) \tag{15}$$

with any fundamental solution $\mathbf{F}\left(\mathbf{x}_1,\mathbf{y}_1,\omega\right)$ of equation (4) as the integral kernel. (However, we cannot use the free space Green's function $\mathbf{G}\left(\mathbf{x}_1,\mathbf{y}_1,\omega\right)$ as the conventional kernel of integral (15) because this function can contain non-feasible parts in the shadow zones.) We consider the source wavefield (15) as the feasible source wavefield in a half-space of complex shape. In the next Section, we give a detailed description of the feasible source wavefield choice for the computation of this formula.

3.5 Feasible source wavefield in terms of mechanics

The feasible fundamental solution $\mathbf{F}(\mathbf{x}_1, \mathbf{y}_1, \omega)$ in formula (15) satisfies to the following problem from A.M. Aizenberg & A.A. Ayzenberg (2015)/Chapter 2 of this thesis

$$\begin{cases} \mathbf{D}_{\mathbf{x}_1} \mathbf{F}(\mathbf{x}_1, \mathbf{y}_1, \omega) + \mathbf{M}_1(\omega) \mathbf{F}(\mathbf{x}_1, \mathbf{y}_1, \omega) = \delta(\mathbf{x}_1 - \mathbf{y}_1) \mathbf{I}, \\ \langle RC \rangle_1 : \iint\limits_{\mathbb{S}_1^\infty} \mathbf{G}(\mathbf{x}_1, \mathbf{s}_1, \omega) \mathbf{N}(\mathbf{s}_1) \mathbf{F}(\mathbf{s}_1, \mathbf{y}_1, \omega) \, dS(\mathbf{s}_1) = 0, \\ \langle EC \rangle_1 : \iint\limits_{\mathbb{S}_1^{\mathrm{E}}} \mathbf{G}(\mathbf{x}_1, \mathbf{s}_1, \omega) \mathbf{N}(\mathbf{s}_1) \mathbf{F}(\mathbf{s}_1, \mathbf{y}_1, \omega) \, dS(\mathbf{s}_1) = 0, \\ \langle AC \rangle_1 : \left[\mathbf{K}_{\mathbf{G}}(\mathbf{s}_1, \mathbf{s}_1', \omega) - \mathbf{K}_{\mathbf{G}}(\mathbf{s}_1, \mathbf{s}_1'', \omega) \mathbf{K}_{h\mathbf{G}}(\mathbf{s}_1'', \mathbf{s}_1', \omega) \right] \mathbf{F}(\mathbf{s}_1', \mathbf{y}_1, \omega) \equiv 0, \end{cases} \tag{16}$$

where $\mathbf{I}$ is the identity matrix. In terms of rays, the feasible fundamental solution $\mathbf{F}(\mathbf{x}_1, \mathbf{y}_1, \omega)$ can be explained as follows (Figure 1b): if points $\mathbf{x}_1$ and $\mathbf{y}_1$ can be connected by a straight ray which entirely belongs to domain $\mathbb{D}_1$ the fundamental soluition $\mathbf{F}(\mathbf{x}_1, \mathbf{y}_1, \omega)$ satisfies the conventional Fermat's principle; but if points $\mathbf{x}_1$ and $\mathbf{y}_1$ cannot be connected by a straight ray which entirely belongs to domain $\mathbb{D}_1$, moreover, they can only be connected by a curved ray which entirely belongs to $\mathbb{D}_1$ the fundamental soluition $\mathbf{F}(\mathbf{x}_1, \mathbf{y}_1, \omega)$ satisfies the generalized Fermat's principle. This principle was introduced by Hadamard in 1910 (see Friedlander (1958)) and known as the 'stretched-thread' principle (M.A. Ayzenberg *et al.* (2009)). It states that two points are connected by a non-straight feasible ray such that the travel time is minimal. This feasible ray travels straight from the source point to the tangency point at the boundary, then creeps along the boundary and finally travels straight from the other tangency point to the receiver point.

As the considered domain $\mathbb{D}_1$ (Figure 1b) is concave there are points which cannot be connected by a straight ray entirely belonging to the domain. Those points will be connected by a curved ray, this ray will be called 'feasible' and the fundamental solution for these points will be called 'feasible'.

Therefore, we represent the kernel in (15) as the feasible fundamental solution (A.M. Aizenberg & A.A. Ayzenberg (2015)/Chapter 2 of this thesis) by

$$\mathbf{F}\left(\mathbf{x}_1,\mathbf{y}_1,\omega\right)=\mathbf{G}\left(\mathbf{x}_1,\mathbf{y}_1,\omega\right)+\sum_{n=1}^{\infty}\mathbf{F}^{[n]}\left(\mathbf{x}_1,\mathbf{y}_1,\omega\right)\ , \tag{17}$$

where

$$\mathbf{F}^{[n]}\left(\mathbf{x}_1,\mathbf{y}_1,\omega\right)=\mathbf{K}_{\mathbf{G}}\left(\mathbf{x}_1,\mathbf{s}_1,\omega\right)\mathbf{F}^{[n]}\left(\mathbf{s}_1,\mathbf{y}_1,\omega\right) \tag{18}$$

and

$$\begin{cases} \mathbf{F}^{[0]}\left(\mathbf{s}_1,\mathbf{y}_1,\omega\right)=\mathbf{G}\left(\mathbf{s}_1,\mathbf{y}_1,\omega\right), \\ \mathbf{F}^{[n]}\left(\mathbf{s}_1,\mathbf{y}_1,\omega\right)=\mathbf{K}_{\mathbf{G}}\left(\mathbf{s}_1,\mathbf{s}_1'',\omega\right)\mathbf{K}_{h\,\mathbf{G}}\left(\mathbf{s}_1'',\mathbf{s}_1',\omega\right)\mathbf{F}^{[n-1]}\left(\mathbf{s}_1',\mathbf{y}_1,\omega\right), \quad n=1,2,\dots\ . \end{cases} \tag{19}$$

The propagation operator in (18) and (19)

$$\mathbf{K}_{\mathbf{G}}(\mathbf{x}_1,\mathbf{s}_1',\omega)<\ldots>=\iint_{\mathbb{S}_1}\mathbf{G}(\mathbf{x}_1,\mathbf{s}_1',\omega)\,\mathbf{N}_{\mathbf{s}_1'}<\ldots>dS_1(\mathbf{s}_1') \tag{20}$$

describes Huygens secondary waves between point $\mathbf{s}_1'$ on boundary $\mathbb{S}_1$ and receiver $\mathbf{x}_1$. Point $\mathbf{x}_1$ also can be located on the boundary ($\mathbf{x}_1=\mathbf{s}_1$). The absorption operator in (19)

$$\mathbf{K}_{h\,\mathbf{G}}(\mathbf{s}_1,\mathbf{s}_1',\omega)<\ldots>=\iint_{\mathbb{S}_1}h(\mathbf{s}_1,\mathbf{s}_1')\,\mathbf{G}(\mathbf{s}_1,\mathbf{s}_1',\omega)\,\mathbf{N}_{\mathbf{s}_1'}<\ldots>dS_1(\mathbf{s}_1') \tag{21}$$

describes only non-feasible Huygens secondary waves between points $\mathbf{s}_1$ and $\mathbf{s}_1'$ on boundary $\mathbb{S}_1$. Function $h(\mathbf{s}_1,\mathbf{s}_1')$ determines the virtual illuminated zones of the boundary (Figure 1b), where points $\mathbf{s}_1$ and $\mathbf{s}_1'$ optically 'see' each other (i.e., can be connected by a straight ray within this zone), and shadow zones where points $\mathbf{s}_1$ and $\mathbf{s}_1'$ do not 'see' each other (i.e., cannot be connected by a straight ray within this zone). This shadow function equals to 0 in the illuminated zones and 1 in the shadow zones. If the boundary does not have shadow parts, the absorption operator (21) is zero due to $h(\mathbf{s}_1,\mathbf{s}_1')=0$ for all points $\mathbf{s}_1$ and $\mathbf{s}_1'$.

Substituting the feasible fundamental solution (17) into the volume integral (15) we obtain

$$\mathbf{u}^{(0)}(\mathbf{x}_1,\omega)=\iiint\limits_{\mathbb{D}_1}\mathbf{G}\left(\mathbf{x}_1,\mathbf{y}_1,\omega\right)\mathbf{f}(\mathbf{y}_1,\omega)\,dV(\mathbf{y}_1)+\sum_{n=1}^{\infty}\iiint\limits_{\mathbb{D}_1}\mathbf{F}^{(n)}\left(\mathbf{x}_1,\mathbf{y}_1,\omega\right)\mathbf{f}(\mathbf{y}_1,\omega)\,dV(\mathbf{y}_1)\ . \tag{22}$$

A.M. Aizenberg *et al*. (2010) and A.M. Aizenberg & A.A. Ayzenberg (2015)/Chapter 2 of this thesis demonstrate that wavefield $\mathbf{u}^{(0)}(\mathbf{x}_1,\omega)$ in (22) can be rewritten as

$$\mathbf{u}^{(0)}(\mathbf{x}_1,\omega)=\mathbf{u}^{\mathbf{G}}(\mathbf{x}_1,\omega)+\mathbf{u}^{cd}(\mathbf{x}_1,\omega)\ . \tag{23}$$

The first term in (23) is

$$\mathbf{u}^{\mathbf{G}}(\mathbf{x}_1,\omega)=\iiint\limits_{\mathbb{D}_1}\mathbf{G}\left(\mathbf{x}_1,\mathbf{y}_1,\omega\right)\mathbf{f}(\mathbf{y}_1,\omega)\,dV(\mathbf{y}_1)\ , \tag{24}$$

where $\mathbf{G}(\mathbf{x}_1,\mathbf{y}_1,\omega)$ is the Green's function for the unbounded homogeneous medium formed by the half-space $\mathbb{D}_1\subset\mathbb{R}^3$ and its 'mathematical' complement $\mathbb{R}^3\setminus\mathbb{D}_1$. This 'mathematical' complement has the geometrical shape of domain $\mathbb{D}_2$ but the properties of $\mathbb{D}_1$. It therefore is called 'mathematical' or 'nonphysical'. Function $\mathbf{G}(\mathbf{x}_1,\mathbf{y}_1,\omega)$ can contain non-feasible parts in the shadow zones. Term $\mathbf{u}^{\mathbf{G}}(\mathbf{x}_1,\omega)$, which has the Green's function for the unbounded homogeneous medium in the kernel, therefore also can contain non-feasible parts.

The second term in (23) is the so-called 'cascade diffraction' term

$$\mathbf{u}^{cd}(\mathbf{x}_1,\omega)=\sum_{n=1}^{\infty}\mathbf{u}^{[n]}(\mathbf{x}_1,\omega)\ , \tag{25}$$

where

$$\mathbf{u}^{[n]}(\mathbf{x}_1,\omega)=\mathbf{K}_{\mathbf{G}}(\mathbf{x}_1,\mathbf{s}_1,\omega)\,[\mathbf{K}_{\mathbf{G}}(\mathbf{s}_1,\mathbf{s}_1'',\omega)\,\mathbf{K}_{h\,\mathbf{G}}(\mathbf{s}_1'',\mathbf{s}_1',\omega)]^n\,\mathbf{u}^{\mathbf{G}}(\mathbf{s}_1',\omega) \tag{26}$$

describes the n-th act of the 'cascade diffraction'. The convergence of series (25) is proved in the paper by A.M. Aizenberg & A.A. Ayzenberg (2015)/Chapter 2 of this thesis.

In this paper, we consider only the two first terms in (23), which can be considered as a double-diffraction approximation

$$\mathbf{u}^{(0)}(\mathbf{x}_1,\omega)\cong\mathbf{u}^{\mathbf{G}}(\mathbf{x}_1,\omega)+\mathbf{u}^{[1]}(\mathbf{x}_1,\omega)\ , \tag{27}$$

where the double-diffraction term is represented by the formula

$$\mathbf{u}^{[1]}(\mathbf{x}_1,\omega)=\mathbf{K}_{\mathbf{G}}(\mathbf{x}_1,\mathbf{s}_1,\omega)\,\mathbf{K}_{\mathbf{G}}(\mathbf{s}_1,\mathbf{s}_1'',\omega)\,\mathbf{K}_{h\,\mathbf{G}}(\mathbf{s}_1'',\mathbf{s}_1',\omega)\,\mathbf{u}^{\mathbf{G}}(\mathbf{s}_1',\omega)\ . \tag{28}$$

Using the orthogonal projector property $\mathbf{K}_{\mathbf{G}}=\mathbf{K}_{\mathbf{G}}\,\mathbf{K}_{\mathbf{G}}$ of operator (20) we reduce formula (28) to the formula

$$\mathbf{u}^{[1]}(\mathbf{x}_1,\omega)=\mathbf{K}_{\mathbf{G}}(\mathbf{x}_1,\mathbf{s}_1,\omega)\,\mathbf{K}_{h\,\mathbf{G}}(\mathbf{s}_1,\mathbf{s}_1',\omega)\,\mathbf{u}^{\mathbf{G}}(\mathbf{s}_1',\omega)\ . \tag{29}$$

We rewrite formula (29), which is the intergals over the boundary surface, in the form of the integrals over the boundary faces

$$\mathbf{u}^{[1]}(\mathbf{x}_1,\omega)=\begin{bmatrix}\mathbf{K}_{\mathbf{G}}(\mathbf{x}_1,\mathbf{s}_1^1,\omega) & \mathbf{K}_{\mathbf{G}}(\mathbf{x}_1,\mathbf{s}_1^2,\omega)\end{bmatrix}\begin{bmatrix}\mathbf{K}_{h\,\mathbf{G}}(\mathbf{s}_1^1,\mathbf{s}_1^{1\prime},\omega) & \mathbf{K}_{h\,\mathbf{G}}(\mathbf{s}_1^1,\mathbf{s}_1^{2\prime},\omega)\\ \mathbf{K}_{h\,\mathbf{G}}(\mathbf{s}_1^2,\mathbf{s}_1^{1\prime},\omega) & \mathbf{K}_{h\,\mathbf{G}}(\mathbf{s}_1^2,\mathbf{s}_1^{2\prime},\omega)\end{bmatrix}\begin{pmatrix}\mathbf{u}^{\mathbf{G}}(\mathbf{s}_1^{1\prime},\omega)\\ \mathbf{u}^{\mathbf{G}}(\mathbf{s}_1^{2\prime},\omega)\end{pmatrix}\ . \tag{30}$$

3.6 Feasible source wavefield in terms of the TPOT wave theory

In this Section, we give the feasible source wavefield in terms of the TPOT wave theory. The particle velocity-pressure vector $\mathbf{u}^{(0)}$ in Cartesian coordinate system is transformed to vector $\mathbf{a}^{(0)}$ in the local coordinate system, one of the axes of which is oriented along the receiver line 1. This new local system of coordinates is defined in domain $\mathbb{D}_1 \cup \left(\mathbb{R}^3 \setminus \mathbb{D}_1\right)$, where domain $\mathbb{R}^3 \setminus \mathbb{D}_1$ is the 'mathematical' complement to domain $\mathbb{D}_1$. In addition, we define the Cartesian coordinates as follows

$$\mathbf{x}_1 = \left(\overline{\mathbf{x}}_1, (x_1)_3\right), \quad \overline{\mathbf{x}}_1 = \left((x_1)_1, (x_1)_2\right). \tag{31}$$

Vectors in (27) are decomposed in terms of the wave vectors $\mathbf{a}^{(0)} = \begin{pmatrix} a^{(0)+} \\ a^{(0)-} \end{pmatrix}$, where a^+ describes propagation outward the boundary and a^- describes propagation toward the boundary, by the formulae

$$\begin{aligned}
&\mathbf{u}^{(0)}(\mathbf{x}_1, \omega) = \mathbf{H}(\overline{\mathbf{x}}_1, \overline{\mathbf{x}}_1', \omega)\, \mathbf{a}^{(0)}(\overline{\mathbf{x}}_1', \omega), \\
&\mathbf{u}^{\mathbf{G}}(\mathbf{x}_1, \omega) = \mathbf{H}(\overline{\mathbf{x}}_1, \overline{\mathbf{x}}_1', \omega)\, \mathbf{a}^{\mathbf{G}}(\overline{\mathbf{x}}_1', \omega), \\
&\mathbf{u}^{[1]}(\mathbf{x}_1, \omega) = \mathbf{H}(\overline{\mathbf{x}}_1, \overline{\mathbf{x}}_1', \omega)\, \mathbf{a}^{[1]}(\overline{\mathbf{x}}_1', \omega), \\
&\mathbf{x}_1 = (\overline{\mathbf{x}}_1, (x_1)_3) = (\overline{\mathbf{x}}_1, const),
\end{aligned} \tag{32}$$

where the convolution operator

$$\mathbf{H}(\overline{\mathbf{x}}_1, \overline{\mathbf{x}}_1', \omega) = F^{-1}\left(\overline{\mathbf{x}}_1, \overline{\mathbf{k}}\right) \hat{\mathbf{H}}\left(\overline{\mathbf{k}}\right) F\left(\overline{\mathbf{k}}, \overline{\mathbf{x}}_1'\right) \tag{33}$$

with the spectral kernel

$$\hat{\mathbf{H}}\left(\mathbf{k}\right) = \left[\hat{\mathbf{h}}^+ \quad \hat{\mathbf{h}}^-\right], \quad \hat{\mathbf{h}}^{\pm} = \frac{1}{k_P} \begin{pmatrix} k_1 \\ k_2 \\ \pm k_3 \\ k_P \end{pmatrix}, \tag{34}$$

where k_1, k_2 and k_3 are the wave vector components, $k_p = \|\mathbf{k}\|$, $k_3 = \sqrt{k_p^2 - k_1^2 - k_2^2}$ and the double space Fourier transform operator is defined as

$$F\left(\overline{\mathbf{k}}, \overline{\mathbf{x}}_1'\right)\langle \ldots \rangle = \frac{1}{2\pi} \int_{-\infty}^{+\infty} \int_{-\infty}^{+\infty} e^{+i\left(k_1 x_1 + k_2 x_2\right)} \langle \ldots \rangle \, dx_1 \, dx_2, \quad \overline{\mathbf{k}} = \left(k_1, k_2\right). \tag{35}$$

Inserting relations (32) in expression (27) we obtain

$$\mathbf{a}^{(0)}\left(\overline{\mathbf{x}}_1, \omega\right) \cong \mathbf{a}^{\mathbf{G}}\left(\overline{\mathbf{x}}_1, \omega\right) + \mathbf{a}^{[1]}\left(\overline{\mathbf{x}}_1, \omega\right) . \tag{36}$$

We now apply the contraction matrix

$$\mathbf{C}_{\overline{\mathbf{x}}_1} = \begin{bmatrix} 0 & 0 & 1 & 0 \\ 0 & 0 & 0 & 1 \end{bmatrix} . \tag{37}$$

Multiplying (24) to matrix (37) from the left and applying (32) we obtain

$$\mathbf{a}^{\mathbf{G}}(\overline{\mathbf{x}}_1, \omega) = \iiint_{\mathbb{D}_1} \left[\mathbf{C}_{\overline{\mathbf{x}}_1} \; \mathbf{H}(\overline{\mathbf{x}}_1, \overline{\mathbf{x}}_1', \omega)\right]^{-1} \mathbf{C}_{\overline{\mathbf{x}}_1'} \; \mathbf{G}\left(\overline{\mathbf{x}}_1', \mathbf{y}_1, \omega\right) \mathbf{f}(\mathbf{y}_1, \omega) \, dV(\mathbf{y}_1) \tag{38}$$

and

$$\mathbf{a}^{\mathbf{G}}(\mathbf{s}_1^{j\prime\prime}, \omega) = \iiint_{\mathbb{D}_1} \left[\mathbf{C}_{\mathbf{s}_1^{j\prime\prime}} \; \mathbf{H}(\mathbf{s}_1^{j\prime\prime}, \mathbf{s}_1^{j\prime}, \omega)\right]^{-1} \mathbf{C}_{\mathbf{s}_1^{j\prime}} \; \mathbf{G}\left(\mathbf{s}_1^{j\prime}, \mathbf{y}_1, \omega\right) \mathbf{f}(\mathbf{y}_1, \omega) \, dV(\mathbf{y}_1) \; . \tag{39}$$

Applying (32) to (29) we obtain

$$\mathbf{a}^{[1]}(\overline{\mathbf{x}}_1, \omega) = \begin{bmatrix} \mathbf{P}_{\mathbf{G}}(\overline{\mathbf{x}}_1, \mathbf{s}_1^1, \omega) & \mathbf{P}_{\mathbf{G}}(\overline{\mathbf{x}}_1, \mathbf{s}_1^2, \omega) \end{bmatrix} \begin{bmatrix} \mathbf{P}_{h\mathbf{G}}(\mathbf{s}_1^1, \mathbf{s}_1^{1\prime}, \omega) & \mathbf{P}_{h\mathbf{G}}(\mathbf{s}_1^1, \mathbf{s}_1^{2\prime}, \omega) \\ \mathbf{P}_{h\mathbf{G}}(\mathbf{s}_1^2, \mathbf{s}_1^{1\prime}, \omega) & \mathbf{P}_{h\mathbf{G}}(\mathbf{s}_1^2, \mathbf{s}_1^{2\prime}, \omega) \end{bmatrix} \begin{pmatrix} \mathbf{a}^{\mathbf{G}}(\mathbf{s}_1^{1\prime}, \omega) \\ \mathbf{a}^{\mathbf{G}}(\mathbf{s}_1^{2\prime}, \omega) \end{pmatrix} , \tag{40}$$

where the propagation operator is

$$\mathbf{P}_{\mathbf{G}}(\bar{\mathbf{x}}_1,\mathbf{s}_1^{j\prime},\omega)=\left[\mathbf{C}_{\bar{\mathbf{x}}_1}\ \mathbf{H}(\bar{\mathbf{x}}_1,\bar{\mathbf{x}}_1',\omega)\right]^{-1}\mathbf{C}_{\bar{\mathbf{x}}_1'}\ \mathbf{K}_{\mathbf{G}}(\bar{\mathbf{x}}_1',\mathbf{s}_1^{j},\omega)\left[\mathbf{R}\left(\mathbf{s}_1^{j}\right)\right]^{-1}\mathbf{H}(\mathbf{s}_1^{j},\mathbf{s}_1^{j\prime},\omega) \tag{41}$$

and the absorption operator (the propagation operator accounting for shadow) is

$$\mathbf{P}_{h\,\mathbf{G}}(\mathbf{s}_1^{j\prime},\mathbf{s}_1^{l\prime\prime\prime},\omega)=\left[\mathbf{C}_{\mathbf{s}_1^{j\prime}}\ \mathbf{H}(\mathbf{s}_1^{j\prime},\mathbf{s}_1^{j\prime\prime},\omega)\right]^{-1}\mathbf{C}_{\mathbf{s}_1^{j\prime\prime}}\ \mathbf{K}_{h\,\mathbf{G}}(\mathbf{s}_1^{j\prime\prime},\mathbf{s}_1^{l},\omega)\left[\mathbf{R}\left(\mathbf{s}_1^{l}\right)\right]^{-1}\mathbf{H}(\mathbf{s}_1^{l},\mathbf{s}_1^{l\prime\prime\prime},\omega)\ . \tag{42}$$

In formulae (39), (41) and (42), we introduced a matrix convolution operator

$$\mathbf{H}(\mathbf{s}_1^{j},\mathbf{s}_1^{j\prime},\omega)=F^{-1}\left(\mathbf{s}_1^{j},\bar{\mathbf{k}}\right)\hat{\mathbf{H}}\left(\bar{\mathbf{k}}\right)F\left(\bar{\mathbf{k}},\mathbf{s}_1^{j\prime}\right). \tag{43}$$

Since $\mathbf{s}_1^{j\prime}\in\mathbb{S}_1^{j}$ the coordinate $x_1\in\left(0,+\infty\right)$ and the Fourier transform change the integration limits as follows

$$F\left(\bar{\mathbf{k}},\mathbf{s}_1^{j\prime}\right)\langle\ldots\rangle=\frac{1}{2\pi}\int_{0}^{+\infty}\int_{-\infty}^{+\infty}e^{+i\left(k_1x_1+k_2x_2\right)}\langle\ldots\rangle\,dx_1\,dx_2,\quad \bar{\mathbf{k}}=\left(k_1,k_2\right). \tag{44}$$

The transformation matrix at a face (by transformation we mean rotation (12) and contraction (11)) is

$$\mathbf{C}\,\mathbf{R}\left(\mathbf{s}_1^{j}\right)=\mathbf{C}_{\mathbf{s}_1^{j}}=\begin{bmatrix} n_1\left(\mathbf{s}_1^{j}\right) & n_2\left(\mathbf{s}_1^{j}\right) & n_3\left(\mathbf{s}_1^{j}\right) & 0\\ 0 & 0 & 0 & 1\end{bmatrix}. \tag{45}$$

3.7 TWSM algorithm for TPOT solution

In this Section, we explain the mid-frequency TWSM algorithm application to the TPOT source wavefield description. The main idea of TWSM, for V-model, is to transform the integral operators (41) and (42) into matrices and wavefields (38)-(40) into vectors.

An approach to computation of 3D seismic wavefields, based on the physically feasible analytical description of wave propagation in layered and macro-block media, is proposed by the Tip-Wave Superposition Method (TWSM) (Klem-Musatov *et al*. (2008) and A.M. Aizenberg *et al*. (2011)). The basic features of TWSM include computation (visualization) of different wave events separately and explicit treatment of interfaces.

We divide the faces of the interface into triangular elements. Typically, we choose the element size of the quarter-wavelength order. Each element becomes a set of secondary sources according to Huygens principle. Due to interference of the secondary sources, it generates a multi-wave beam propagating from the element towards each element of the same face, neighbouring face or a receiver. Since the element has three edges and three vertices (or six tips, each vertex is two coupled tips) the beam is formed by the geometrical wave, three edge-diffracted and six tip-diffracted waves. The tip-diffracted waves contribute most to the beams, which explains the name 'the Tip-Wave Superposition' of the method.

The algorithmic realization of wavefield propagation in layered medium is based on mapping of operators (41) and (42) to respective matrices and wavefields (38)-(40) to respective vectors (Zyatkov *et al*. (2012) and Zyatkov *et al*. (2013)). Each face is triangulated into N small elements with the size less than a quarter of the dominant wavelength. The wavefield vectors of the faces have dimension N. All the propagation-absorption matrices have dimension $N \times N$. The propagation interface-receivers matrix has dimension $M \times N$, where M is the number of receivers. The main chalenge of the algorithm realization is large arrays of data that must be stored and processed. We are considering the following example: suppose that all matrices are filled by complex single precision floating-point numbers (4×2); in the case of $N = 150\,000$ the required memory for storing a $N \times N$ matrix is equal to $N \times N \times 4 \times 2 = 150\,000 \times 150\,000 \times 4 \times 2 = 168\,GB$. It also should be noted that all matrices and vectors are non-sparse. When solving direct and inverse seismic problems using this algorithm, it is therefore necessary to optimize both the execution time of the algorithm and required memory.

The evaluation of the matrices is independent of the source position and the survey geometry. The layer matrices are thus computed prior to the evaluation of the multiply reflected and transmitted wavefields. For a particular ray path, the multiply reflected and transmitted wavefield is generated by the sequential multiplication of the layer matrices. Whenever the velocities and densities within a domain need to be updated, only the matrices describing this particular domain have to be re-evaluated. Hence, for minor changes of the model, this saves most of the computational time.

The algorithm realization for the wavefield propagation in medium with arbitrary interfaces is reduced to the realization of a highly-optimized procedure of the large matrix multiplication (about 100 GB of RAM) by the column vector of the wavefield for each discrete frequency ω_k from a set $\omega_1 \ldots \omega_k$. The required memory for storing the $N \times N$ matrix is so large that it is almost impossible to store the entire matrix. This problem is solved by dividing all matrices of $N \times N$ size into horizontal strips. Each of them has $M_1 \times N$ size. The memory is allocated only for one strip of the matrix (Figure 2). At each iteration loop for strips of the matrix, a new set of result vectors is calculated for each frequency ω_k. Then, all the result vectors are combined in one vector.

To avoid storing the entire matrix, we refill corresponding strips at each loop of iteration by the partition. Using this approach, the algorithm can adapt to any computer with limited RAM by changing M_1-parameter, the width of the strips.

Also, it is important to note that the virtual shadow matrix must be evaluated before the evaluation of the absorption matrix. Figure 3 illustrates a 3D view of a Gaussian-shape boundary (Figure 3a) and four projections of 0/1 values of $h(\mathbf{s}, \mathbf{s}')$ at four boundary points $\mathbf{s}'$ (the points on Figure 3b). Values 0 designate not interacting parts of the boundary (the illuminated zones), and values 1 designate interacting parts of the boundary (the shadow zones).

We use the NVIDIA CUDA technology for implementation of the TWSM software package. Figure 4 demonstrates a scheme of the realization of the matrix-vector transformation by TWSM for several GPUs. Each device is assigned for the corresponding matrix strip (or the set of strips). Each GPU does the matrix-vector multiplication in the corresponding strips of the matrix for each discrete frequency ω_k and writes the result into the corresponding parts of the vectors $\mathbf{F}_\mathbf{s}^{\omega_1} \ldots \mathbf{F}_\mathbf{s}^{\omega_K}$. Finally, the results of all GPUs are combined in a set of the transformed vectors $\mathbf{F}_\mathbf{s}^{\omega_1} \ldots \mathbf{F}_\mathbf{s}^{\omega_K}$.

Table 1 represents the results of the algorithm optimization and its adaptation for the parallel architectures. We obtained acceleration ~150 times using one GPU as compared with a sequential version on CPU for one TWSM matrix.

3.8 Reduction of the source wavefield representation to formulae of the edge wave theory

The computation of the point-source wavefield propagating around the V-shaped boundary is done by formulae (27), (32), (36), (38) and (40) using the TWSM code described in the preceding section. Because the approximation of the wavefield demonstrated on the seismograms has no analogues in the contemporary wave theory we need a comparison with results of an independent method. Such a comparison cannot be done by numerical methods because these methods only can model the total wavefield, and we need to test the separate fragments of the total wavefield. The only available option is the evaluation of these fragments by an analytical method. For this, we apply the well-known method of rigorous integrating in formula (40); in this Section, we reduce this formula to formulae of the edge wave theory (A.M. Aizenberg (1982) and A.M. Aizenberg (1993)) in case of V-boundary.

Everywhere further in this paper, we omit the domain index since we consider only domain $\mathbb{D}_1$ ($m=1$). Also for simplicity, we further write the upper indeces in the lower positions. In addition, we omit reduction to the lower dimension, and we omit frequency. So everywhere further, we have the notations

$$\begin{aligned} &(\cdot)_1^j \equiv (\cdot)_j \,, \\ &\bar{\cdot} \equiv \cdot \,, \\ &(\cdot,\omega) \equiv (\cdot) \,. \end{aligned} \tag{46}$$

We therefore rewrite the wave vector (36) in the block form

$$\mathbf{a}^{(0)}(\mathbf{x}) = \begin{pmatrix} 0 \\ a^{(0)-}(\mathbf{x}) \end{pmatrix} \,. \tag{47}$$

In case of the point source, the volume integral representation of vector $\mathbf{a}^{\mathbf{G}}(\mathbf{x})$ in (38) reduces to the spherical wavefield at the points of the receiver lines 1 and 2. Hence, vector (38) is represented as

$$\mathbf{a}^{\mathrm{G}}(\mathbf{x}) = \begin{pmatrix} 0 \\ p_{\mathrm{G}}(\mathbf{x}) \exp\left[i\, k_P\, l(\mathbf{x})\right] \end{pmatrix} , \tag{48}$$

where $l(\mathbf{x})$ (Figure 5) is the distance along the ray trajectory ‘source - receiver’, $p_{\mathrm{G}}(\mathbf{x}) = \dfrac{C\rho}{l(\mathbf{x})}\psi(\omega)$ is the spherical wave amplitude, ρ is the medium density, C is the source intensity.

The propagation operator from (40), acting from the faces to the receiver lines, is written as follows

$$\left[\mathbf{P}_{\mathbf{G}}(\overline{\mathbf{x}}_1, \mathbf{s}_1^1, \omega) \quad \mathbf{P}_{\mathbf{G}}(\overline{\mathbf{x}}_1, \mathbf{s}_1^2, \omega)\right] = \left[\mathbf{P}_{\mathbf{G}}(\mathbf{x}, \mathbf{s}_1) \quad \mathbf{P}_{\mathbf{G}}(\mathbf{x}, \mathbf{s}_2)\right] . \tag{49}$$

The shadow function $h(\mathrm{s}, \mathrm{s}')$ for V-boundary has the properties (Figure 1b)

$$h(\mathbf{s}_1, \mathbf{s}_1') = h(\mathbf{s}_2, \mathbf{s}_2') = 0 , \quad h(\mathbf{s}_1, \mathbf{s}_2') = h(\mathbf{s}_2, \mathbf{s}_1') = 1 . \tag{50}$$

Since faces $\mathbb{S}_1$ and $\mathbb{S}_2$ are plane we obtain the absorption matrix (40) reduced to the form

$$\begin{bmatrix} \mathbf{P}_{h\mathbf{G}}(\mathbf{s}_1^1, \mathbf{s}_1^{1\prime}, \omega) & \mathbf{P}_{h\mathbf{G}}(\mathbf{s}_1^1, \mathbf{s}_1^{2\prime}, \omega) \\ \mathbf{P}_{h\mathbf{G}}(\mathbf{s}_1^2, \mathbf{s}_1^{1\prime}, \omega) & \mathbf{P}_{h\mathbf{G}}(\mathbf{s}_1^2, \mathbf{s}_1^{2\prime}, \omega) \end{bmatrix} = \begin{bmatrix} & \mathbf{P}_{\mathbf{G}}(\mathbf{s}_1, \mathbf{s}_2') \\ \mathbf{P}_{\mathbf{G}}(\mathbf{s}_2, \mathbf{s}_1') & \end{bmatrix} , \tag{51}$$

where $\mathbf{O}$ is the zero matrix. As the action of submatrix $\mathbf{P}_{\mathbf{G}}(\mathbf{s}_1, \mathbf{s}_2')$ describes back scattering, which gives negligibly weak contribution at the receivers, we can say that the condition $\mathbf{P}_{\mathbf{G}}(\mathbf{s}_1, \mathbf{s}_2') \cong \mathbf{O}$ is valid. Consequently, the absorption matrix has got the final form

$$\begin{bmatrix} \mathbf{P}_{h\mathbf{G}}(\mathbf{s}_1^1, \mathbf{s}_1^{1\prime}, \omega) & \mathbf{P}_{h\mathbf{G}}(\mathbf{s}_1^1, \mathbf{s}_1^{2\prime}, \omega) \\ \mathbf{P}_{h\mathbf{G}}(\mathbf{s}_1^2, \mathbf{s}_1^{1\prime}, \omega) & \mathbf{P}_{h\mathbf{G}}(\mathbf{s}_1^2, \mathbf{s}_1^{2\prime}, \omega) \end{bmatrix} \cong \begin{bmatrix} \mathbf{O} & \mathbf{O} \\ \mathbf{P}_{\mathbf{G}}(\mathbf{s}_2, \mathbf{s}_1') & \mathbf{O} \end{bmatrix} . \tag{52}$$

After completing all the multiplications in formula (40) and accounting for formulae (47), (48), (49) and (52) we obtain vector (40) expressed by the matrices and columns at the faces in the form

$$\mathbf{a}^{[1]}(\mathbf{x}) = \mathbf{P}_{\mathbf{G}}\left(\mathbf{x},\mathbf{s}_2\right)\mathbf{P}_{\mathbf{G}}\left(\mathbf{s}_2,\mathbf{s}_1\right)\mathbf{a}^{\mathbf{G}}\left(\mathbf{s}_1\right) \ . \tag{53}$$

Vector (53) has the form of double integration over two semi-infinite faces with edges. The internal integration is over face $\mathbb{S}_1$ and the external integration is over face $\mathbb{S}_2$ having the common edge with face $\mathbb{S}_1$. Vector $\mathbf{a}^{\mathbf{G}}\left(\mathbf{s}_1\right)$ in (53) is the spherical wavefield at the points of face $\mathbb{S}_1$

$$\mathbf{a}^{\mathbf{G}}\left(\mathbf{s}_1\right) = \begin{pmatrix} 0 \\ p_{\mathbf{G}}\left(\mathbf{s}_1\right)\exp\left[i\,k_P\,l\left(\mathbf{s}_1\right)\right] \end{pmatrix} , \tag{54}$$

where $l\left(\mathbf{s}_1\right)$ is the distance along the ray trajectory 'source - point $\mathbf{s}_1$', $p_{\mathbf{G}}\left(\mathbf{s}_1\right)$ is the spherical wave amplitude.

Using the boundary values (54) we perform the exact integration $\mathbf{P}_{\mathbf{G}}\left(\mathbf{s}_2,\mathbf{s}_1\right)\mathbf{a}^{\mathbf{G}}\left(\mathbf{s}_1\right)$ in (53) using the approach described in Rubinowicz (1965) and Borovikov (1994), Section 5.9. In our case, this approach leads to the reduction of the Kirchhoff integral over the half-plane by the Stokes' theorem to three Maggi-Rubinowicz integrals. The first integral is over the inner circular contour around the intersection point of the direct ray 'source-receiver' with the half-plane. It describes the spherical wavefield at the points of face $\mathbb{S}_2$. The second integral is over the outer semi-circle with the infinite radius. It is equal to zero according to the radiation condition. The third integral is over the infinite straight edge. It describes the edge wave known also as the boundary diffracted wave. Applying the reciprocal modification of the far-field approximation from A.M. Aizenberg (1993) we can represent the edge wave amplitude for the infinite straight edge as the product of the actual spherical wave amplitude (48) and the corresponding diffraction attenuation function.

The integration over $\mathbb{S}_1$ leads to a vector at points of face $\mathbb{S}_2$

$$\mathbf{P_G}(\mathbf{s}_2,\mathbf{s}_1)\,\mathbf{a}^{\mathbf{G}}(\mathbf{s}_1)=\mathbf{a}_{\mathbf{G}}^{[1]}(\mathbf{s}_2)+\mathbf{a}_{\mathbb{E}_1}^{[1]}(\mathbf{s}_2)\ . \tag{55}$$

Vector $\mathbf{a}_{\mathbf{G}}^{[1]}(\mathbf{s}_2)$ in (55) is the spherical wavefield at points of face $\mathbb{S}_2$

$$\mathbf{a}_{\mathbf{G}}^{[1]}(\mathbf{s}_2)=\begin{pmatrix}-\,p_{\mathbf{G}}(\mathbf{s}_2)\exp\left[i\,k_P\,l(\mathbf{s}_2)\right]\\0\end{pmatrix}\ , \tag{56}$$

where $l(\mathbf{s}_2)$ is the distance along the ray trajectory 'source-point $\mathbf{s}_2$' and $p_{\mathbf{G}}(\mathbf{s}_2)$ is the spherical wave amplitude.

Vector $\mathbf{a}_{\mathbb{E}_1}^{[1]}(\mathbf{s}_2)$ in (55) is the edge wavefield propagating from edge $\mathbb{E}_1$ to the points of face $\mathbb{S}_2$

$$\mathbf{a}_{\mathbb{E}_1}^{[1]}(\mathbf{s}_2)=\begin{pmatrix}p_{\mathbb{E}_1}(\mathbf{s}_2)\exp\left[i\,k_P\,l_1(\mathbf{s}_2)\right]\\0\end{pmatrix}\ , \tag{57}$$

where $l_1(\mathbf{s}_2)$ is the distance along the ray trajectory 'source-$\mathbb{E}_1$-point $\mathbf{s}_2$'. The edge wave amplitude formula $p_{\mathbb{E}_1}(\mathbf{s}_2)=W(w_1)\,p_{\mathbf{G}}(\mathbf{s}_2)$ is valid inside the Fresnel volume and out of a small vicinity of edge $\mathbb{E}_1$ (for more details, see A.M. Aizenberg (1993)). The special function $W(w_1)$ is associated with the Fresnel integral according to Klem-Musatov *et al*. (2008) and depends of the dimensionless argument $w_1=\sqrt{\dfrac{2\,k_P}{\pi}}\,(l_1-l)$. This function is associated with the generalized Fresnel integral and is written as the integral formula (see details in A.M. Aizenberg (1982))

$$W(w)=\frac{1}{\pi}\int_0^{\infty}\frac{w}{w^2+\xi^2}\,e^{i\frac{\pi}{2}\xi^2}\,d\xi\ . \tag{58}$$

Substituting vector (55) in (53) and accounting for (56) and (57) we obtain

$$\mathbf{a}^{[1]}(\mathbf{x}) = \mathbf{P}_{\mathbf{G}}\left(\mathbf{x},\mathbf{s}_2\right)\mathbf{a}_{\mathbf{G}}^{[1]}\left(\mathbf{s}_2\right) + \mathbf{P}_{\mathbf{G}}\left(\mathbf{x},\mathbf{s}_2\right)\mathbf{a}_{\mathbb{E}_1}^{[1]}\left(\mathbf{s}_2\right) \ . \tag{59}$$

It is necessary to notice that each term in the right-hand side of (59) can be non-smooth function which has a discontinuity in the vicinity of the shadow boundary at $x = 4.0$. All the terms are therefore represented for $x < 4.0$ (the shadow zone) and $x > 4.0$ (the illiminated zone) separately.

To analytically evaluate the first term in formula (59) we use the similarity of this term and vector (55). Indeed, the first term represents the integration over the half-plane $\mathbb{S}_2$ with the spherical wave as the boundary value. As the result, we represent the first term in formula (59) in the form

$$\mathbf{P}_{\mathbf{G}}\left(\mathbf{x},\mathbf{s}_2\right)\mathbf{a}_{\mathbf{G}}^{[1]}\left(\mathbf{s}_2\right) = \mathbf{a}_{\mathbf{G}}^{[1]}\left(\mathbf{x}\right) + \mathbf{a}_{\mathbb{E}_2}^{[1]}\left(\mathbf{x}\right) \ , \tag{60}$$

which is similar to (55). Vector $\mathbf{a}_{\mathbf{G}}^{[1]}\left(\mathbf{x}\right)$ in (60) is the spherical wavefield at the points on the receiver line 1 or 2

$$\mathbf{a}_{\mathbf{G}}^{[1]}(\mathbf{x}) = \begin{cases} \begin{pmatrix} 0 \\ -\,p_{\mathbf{G}}\left(\mathbf{x}\right)\exp\left[i\,k_P\,l\left(\mathbf{x}\right)\right] \end{pmatrix}, & x < 4.0\,, \\ \begin{pmatrix} 0 \\ 0 \end{pmatrix} \quad, & x > 4.0\,, \end{cases} \tag{61}$$

where $l\left(\mathbf{x}\right)$ (Figure 5) is the distance along the ray trajectory ‘source-receiver’. Vector $\mathbf{a}_{\mathbb{E}_2}^{[1]}\left(\mathbf{x}\right)$ is the edge wavefield from edge $\mathbb{E}_2$ at the receiver line 1 or 2

$$\mathbf{a}_{\mathbb{E}_2}^{[1]}\left(\mathbf{x}\right) = \begin{cases} \begin{pmatrix} 0 \\ +\,p_{\mathbb{E}_2}\left(\mathbf{x}\right)\exp\left[i\,k_P\,l_2\left(\mathbf{x}\right)\right] \end{pmatrix}, & x < 4.0\,, \\ \begin{pmatrix} 0 \\ -\,p_{\mathbb{E}_2}\left(\mathbf{x}\right)\exp\left[i\,k_P\,l_2\left(\mathbf{x}\right)\right] \end{pmatrix}, & x > 4.0\,, \end{cases} \tag{62}$$

where $l_2(\mathbf{x})$ (Figure 5) is the distance along the ray trajectory 'source-$\mathbb{E}_2$-receiver'. The edge wave amplitude formula $p_{\mathbb{E}_2}(\mathbf{x}) = W(w_2)\, p_{\mathbb{G}}(\mathbf{x})$ is valid inside the Fresnel volume and out of a small vicinity of edge $\mathbb{E}_2$ (for more details, see A.M. Aizenberg (1993)). The special function $W(w_2)$ depends of the dimensionless argument $w_2 = \sqrt{\frac{2k_P}{\pi}(l_2 - l)}$.

To analytically evaluate the second term in formula (59) we reduce this term to two nonzero contour integrals using the approach described in Rubinowicz (1965) and Borovikov (1994), Section 5.9

$$\mathbf{P}_{\mathbf{G}}(\mathbf{x}, \mathbf{s}_2)\, \mathbf{a}_{\mathbb{E}_1}^{[1]}(\mathbf{s}_2) = \mathbf{a}_{\mathbb{E}_1}^{[1]}(\mathbf{x}) + \mathbf{a}_{\mathbb{E}_2\,\mathbb{E}_1}^{[1]}(\mathbf{x}) \quad . \tag{63}$$

The first integral in formula (63) is over the inner circular contour around the intersection point of the diffracted ray 'edge $\mathbb{E}_1$-receiver' with the half-plane. It is evident that this integral describes the edge wavefield propagating from edge $\mathbb{E}_1$ to the receivers located in the shadow zone at $x < 4.0$. In the illuminated zone at $x > 4.0$, this integral is equal to zero because the corresponding inner circular contour on the half-plane is absent.

The second integral in formula (63) is over the infinite straight edge $\mathbb{E}_2$ with the boundary value expressed by the edge wavefield propagating from edge $\mathbb{E}_1$. In terms of the diffraction wave theory, the repeated surface integral in (53) describes the solution of the well-known problem of the spherical wave diffraction at two half-planes. It is known from Jones (1973) and Borovikov (1994), Subsection 5.9 that the solution of this problem contains the double edge wave sequentially diffracted by the first edge $\mathbb{E}_1$ and then by the second edge $\mathbb{E}_2$. Edge $\mathbb{E}_1$ creates a primary shadow boundary and edge $\mathbb{E}_2$ creates a secondary shadow boundary. The rigorous mathematical description of the double edge wave can be represented by the double contour integrals. In a small vicinity of the shadow boundaries, these integrals can be approximated by the generalized Fresnel integrals if the edges are distant. Because our case is right opposite, and the edges coincide, we use the modification of this approximation from Jones (1973), Borovikov (1994), Subsection 5.9 and A.M. Aizenberg (1993), which is valid for coinciding edges also.

Using the above considerations we insert (63) in (59) and obtain the final formula

$$\mathbf{a}^{[1]}(\mathbf{x}) = \mathbf{a}_{\mathbf{G}}^{[1]}(\mathbf{x}) + \mathbf{a}_{\mathbb{E}_2}^{[1]}(\mathbf{x}) + \mathbf{a}_{\mathbb{E}_1}^{[1]}(\mathbf{x}) + \mathbf{a}_{\mathbb{E}_2\,\mathbb{E}_1}^{[1]}(\mathbf{x}) \ . \tag{64}$$

Vector $\mathbf{a}_{\mathbb{E}_1}^{[1]}(\mathbf{x})$ is the edge wavefield propagating from edge $\mathbb{E}_1$ to the points of the receiver line 1 or 2

$$\mathbf{a}_{\mathbb{E}_1}^{[1]}(\mathbf{x}) = \begin{cases} \begin{pmatrix} 0 \\ +p_{\mathbb{E}_1}(\mathbf{x}) \exp\left[i\, k_P\, l_1(\mathbf{x}) \right] \end{pmatrix}, & x < 4.0\,, \\ \begin{pmatrix} 0 \\ 0 \end{pmatrix}, & x > 4.0\,, \end{cases} \tag{65}$$

where $l_1(\mathbf{x})$ (Figure 5) is the distance along the ray trajectory 'source-$\mathbb{E}_1$-receiver'. The edge wave amplitude formula $p_{\mathbb{E}_1}(\mathbf{x}) = W(w_1)\, p_{\mathbf{G}}(\mathbf{x})$ is valid inside the Fresnel volume and out of a small vicinity of the edge $\mathbb{E}_1$ (for more details, see A.M. Aizenberg (1993)). The special function $W(w_1)$ depends of the dimensionless argument $w_1 = \sqrt{\dfrac{2\,k_P}{\pi}(l_1 - l)}$.

Vector $\mathrm{a}_{\mathbb{E}_2\,\mathbb{E}_1}^{[1]}(\mathbf{x})$ is the double edge wavefield

$$\mathbf{a}_{\mathbb{E}_2\,\mathbb{E}_1}^{[1]}(\mathbf{x}) = \begin{cases} \begin{pmatrix} 0 \\ -p_{\mathbb{E}_2\mathbb{E}_1}(\mathbf{x}) \exp\left[i\, k_P\, l_{12}(\mathbf{x}) \right] \end{pmatrix}, & x < 4.0\,, \\ \begin{pmatrix} 0 \\ -p_{\mathbb{E}_2\mathbb{E}_1}(\mathbf{x}) \exp\left[i\, k_P\, l_{12}(\mathbf{x}) \right] \end{pmatrix}, & x > 4.0\,, \end{cases} \tag{66}$$

where $l_{12}(\mathbf{x})$ (Figure 5) is the distance along the ray trajectory 'source-edge $\mathbb{E}_1$-edge $\mathbb{E}_2$-receiver'. The double edge wave amplitude in (66) is represented by the formula (Borovikov (1994) and Borovikov & Kinber (1994))

$$p_{\mathbb{E}_2\mathbb{E}_1}(\mathbf{x}) = \begin{cases} p_{\mathbf{G}}(\mathbf{x})\left[+H(w_1,u_1)+H(w_2,u_2)\right], & x<4.0\,, \\ p_{\mathbf{G}}(\mathbf{x})\left[-H(w_1,u_1)+H(w_2,u_2)\right], & x>4.0\,, \end{cases} \tag{67}$$

where the special function $H(w_j,u_j)$ ($j=1,2$) is dependent on the two arguments $w_j = \sqrt{\frac{2k_P}{\pi}\left(l_j - l\right)}$ and $u_j = \sqrt{\frac{2k_P}{\pi}\left(l_{12} - l_j\right)}$. The special function $H(w_1,u_1)$ compensates the discontinuity in amplitude of the edge wave propagating from edge $\mathbb{E}_1$, at the shadow boundary caused by edge $\mathbb{E}_2$. The special function $H(w_2,u_2)$ compensates the discontinuity in the gradient of the edge wave amplitude at the shadow boundary caused by edge $\mathbb{E}_2$.

The special function $H(w,u)$ is associated with the generalized Fresnel integral and is written by the formula (see details in A.M. Aizenberg (1982))

$$H(w,u) = \frac{1}{2\pi} e^{-i\frac{\pi}{2}u^2} \int_u^{\infty} \frac{w}{w^2+\xi^2} e^{i\frac{\pi}{2}\xi^2}\, d\xi \ . \tag{68}$$

It is essential that at point $w=u=0$ function (68) tends to an indefinite constant (see Borovikov (1994) and Borovikov & Kinber (1994))

$$\lim_{\substack{w\to 0\\ u\to 0}} H(w,u) = \frac{1}{4} - \frac{1}{2\pi}\arctan\left(\frac{u}{w}\right) , \tag{69}$$

depending on the direction of approaching point $w=u=0$. Because the limit value of $\arctan\left(\frac{u}{w}\right)$, when $w\to 0$ and $u\to 0$, depends on the direction of approaching point $w=u=0$, this point is irregular.

Formulae (47), (48) and (64) demonstrate that all the first components are zero, and that the nonzero components at the receiver line 1 or 2 give the relation

$$a^{(0)-}(\mathbf{x}) = a^{\mathrm{G}-}(\mathbf{x}) + a^{[1]-}(\mathbf{x}) \ , \tag{70}$$

where $a^{\mathbf{G}-}(\mathbf{x})$ is the conventional source wavefield which propagates not accounting for the shadow zones. This nonzero component of the first-term approximation of the cascade diffraction wavefield in (70) can be represented in the form

$$a^{[1]-}(\mathbf{x}) = a_{\mathbf{G}}^{[1]-}(\mathbf{x}) + a_{\mathbb{E}_2}^{[1]-}(\mathbf{x}) + a_{\mathbb{E}_1}^{[1]-}(\mathbf{x}) + a_{\mathbb{E}_2\mathbb{E}_1}^{[1]-}(\mathbf{x}) \ , \tag{71}$$

where the terms are described by formulae (61), (62), (65) and (66). In the shadow zone, the double-diffraction term (71) consists of the source spherical wave with negative amplitude $a_{\mathbf{G}}^{[1]-}(\mathbf{x})$, the single edge waves $a_{\mathbb{E}_1}^{[1]-}(\mathbf{x})$ and $a_{\mathbb{E}_2}^{[1]-}(\mathbf{x})$ and the double edge wave $a_{\mathbb{E}_2\mathbb{E}_1}^{[1]-}(\mathbf{x})$. In the illuminated zone, the double-diffraction term (71) consists of the single edge wave $a_{\mathbb{E}_2}^{[1]-}(\mathbf{x})$ and the double edge wave $a_{\mathbb{E}_2\mathbb{E}_1}^{[1]-}(\mathbf{x})$.

3.9 Diffraction Attenuation Coefficients (DAC) of the edge wave theory

Since all the amplitudes in formulae (70) and (71) contain the amplitude of the spherical wave as the common amplitude factor it is useful to normalize these amplitudes by this factor for further analysis. Hence, we introduce a Diffraction Attenuation Coefficient (DAC) as the norm

$$DAC(\mathbf{x}) = \left\| \frac{a^{(0)-}(\mathbf{x},t)}{p_{\mathbf{G}}(\mathbf{x},t)} \right\| . \tag{72}$$

We chose norm (72) as an energy norm and write it in the temporal form as

$$DAC(\mathbf{x}) = \sqrt{\frac{\int_{-\infty}^{+\infty} \left[a^{(0)-}(\mathbf{x},t) \right]^2 dt}{\int_{-\infty}^{+\infty} \left[p_{\mathbf{G}}(\mathbf{x},t) \right]^2 dt}} . \tag{73}$$

Using the Parseval's Theorem from Korn & Korn (2000), we obtain the spectral form of formula (73)

$$DAC(\mathbf{x}) = \sqrt{\frac{\int_{-\infty}^{+\infty} \left| a^{(0)-}(\mathbf{x},\omega) \right|^2 d\omega}{\int_{-\infty}^{+\infty} \left| p_{\mathbf{G}}(\mathbf{x},\omega) \right|^2 d\omega}} . \tag{74}$$

Assuming that the impulse shapes $a^{(0)-}(\mathbf{x},t)$ and $p_{\mathbf{G}}(\mathbf{x},t)$ are almost equal we rewrite formulae (73) and (74) in the form

$$DAC(\mathbf{x}) \cong \frac{\max_t \left| a^{(0)-}(\mathbf{x},t) \right|}{\max_t \left| p_{\mathbf{G}}(\mathbf{x},t) \right|} = \frac{\left| a^{(0)-}(\mathbf{x},\omega_{dom}) \right|}{\left| p_{\mathbf{G}}(\mathbf{x},\omega_{dom}) \right|} . \tag{75}$$

We note that $DAC(\mathbf{x})$ in formula (75) is the ratio of the maximal values of the feasible source wavefield amplitude in the double diffraction approximation and the amplitude of the conventional Green's function. We notice that the impulse shapes $a^{(0)-}(\mathbf{x}, t)$ and $p_{\mathbf{G}}(\mathbf{x}, t)$ are equal in case when the shadow boundaries coincide.

Substituting formulae (70) and (71) in (75) we obtain

$$DAC(\mathbf{x}) \cong \frac{\left|a^{\mathbf{G}-}(\mathbf{x}, \omega_{dom}) + a_{\mathbf{G}}^{[1]-}(\mathbf{x}, \omega_{dom}) + a_{\mathbb{E}_2}^{[1]-}(\mathbf{x}, \omega_{dom}) + a_{\mathbb{E}_1}^{[1]-}(\mathbf{x}, \omega_{dom}) + a_{\mathbb{E}_2\mathbb{E}_1}^{[1]-}(\mathbf{x}, \omega_{dom})\right|}{\left|p_{\mathbf{G}}(\mathbf{x}, \omega_{dom})\right|} . \quad (76)$$

In the illuminated zone, when the double-diffraction term (71) consists of the single edge wave $a_{\mathbb{E}_2}^{(1)-}(\mathbf{x})$ and the double edge wave $a_{\mathbb{E}_2\mathbb{E}_1}^{(1)-}(\mathbf{x})$, formula (76) simplifies to

$$DAC(\mathbf{x}) \cong \frac{\left|a^{\mathbf{G}-}(\mathbf{x}, \omega_{dom}) + a_{\mathbb{E}_2}^{[1]-}(\mathbf{x}, \omega_{dom}) + a_{\mathbb{E}_2\mathbb{E}_1}^{[1]-}(\mathbf{x}, \omega_{dom})\right|}{\left|p_{\mathbf{G}}(\mathbf{x}, \omega_{dom})\right|} . \quad (77)$$

The limit value of (77) at the shadow boundary $(\mathbf{x} \to \mathbf{x}_{shb} + 0)$ is

$$DAC(\mathbf{x}_{shb}) \cong \frac{\left|a^{\mathbf{G}-}(\mathbf{x}_{shb}, \omega_{dom}) + a_{\mathbb{E}_2}^{[1]-}(\mathbf{x}_{shb}, \omega_{dom}) + a_{\mathbb{E}_2\mathbb{E}_1}^{[1]-}(\mathbf{x}_{shb}, \omega_{dom})\right|}{\left|p_{\mathbf{G}}(\mathbf{x}_{shb}, \omega_{dom})\right|} . \quad (78)$$

Substituting formulae (48), (62) and (66) into formula (78) we obtain

$$DAC(\mathbf{x}_{shb}) \cong \left|1 - W(w_2) - \left[-H(w_1, u_1) + H(w_2, u_2)\right]\right|. \quad (79)$$

To calculate formula (79) we need to consider formulae (58) and (69) under these two specific conditions valid in the numerical tests:

1) coincidence of the two shadow boundaries from edges $\mathbb{E}_1$ and $\mathbb{E}_2$;

2) closely located edges $\mathbb{E}_1$ and $\mathbb{E}_2$.

Formula (58) does not have irregular points. At the shadow boundary, argument $w_2 = \sqrt{\frac{2k_P}{\pi}(l_2 - l)}$ tends to zero and

$$\lim_{w_2 \to 0} W(w_2) = \frac{1}{2}. \tag{80}$$

Formula (69) is weakly stable at the coinciding shadow boundaries due to both arguments $w_j = \sqrt{\frac{2k_P}{\pi}(l_j - l)}$ and $u_j = \sqrt{\frac{2k_P}{\pi}(l_{12} - l_j)}$ tend to zero. In this case, it is necessary to apply the Taylor's expansion of these arguments in a small vicinity of point $w = u = 0$ and use the L'Hopital rule for the evaluation of ratio $\frac{u_j}{w_j}$. The ray distances used in the Taylor's expansion are expressed as follows: $l(\mathbf{x}) = \sqrt{(r_S + r_{12} + r_R)^2 + (\delta x_R - \delta x_S)^2}$, $l_1(\mathbf{x}) = \sqrt{r_S^2 + (\delta x_S)^2} + \sqrt{(r_{12} + r_R)^2 + (\delta x_R)^2}$, $l_2(\mathbf{x}) = \sqrt{(r_S + r_{12})^2 + (\delta x_S)^2} + \sqrt{r_R^2 + (\delta x_R)^2}$ and $l_{12}(\mathbf{x}) = \sqrt{r_S^2 + (\delta x_S)^2} + r_{12} + \sqrt{r_R^2 + (\delta x_R)^2}$, in which r_S is the 'source-edge $\mathbb{E}_1$' distance, r_{12} is the distance between edges $\mathbb{E}_1$ and $\mathbb{E}_2$, r_R is the 'receiver-edge $\mathbb{E}_2$' distance, δx_S and δx_R are virtual deviations of the source and receiver from the coinciding shadow boundaries, respectively (Figure 5).

Let us consider the first special function $H(w_1, u_1)$. The coincidence of the edges leads to the application of the Taylor's expansion of the second order for both arguments in a small vicinity of point $w_1 = u_1 = 0$. The arguments can be represented by the formulae

$$w_1 \cong \sqrt{\frac{2k_P}{\pi}\frac{r_S}{2}}\,\frac{1}{2}\left(\frac{\delta x_S}{r_S} + \frac{\delta x_R}{r_R}\right), \quad u_1 \cong \sqrt{\frac{2k_P}{\pi} r_{12}}\,\frac{1}{2}\frac{\delta x_R}{r_R}. \tag{81}$$

Formulae (81) allow us considering ratio $\frac{u_1}{w_1} \cong \sqrt{2\frac{r_{12}}{r_S}}\left(1+\frac{r_R}{r_S}\frac{\delta x_S}{\delta x_R}\right)^{-1}$. In this case, we have to consider the double limit $\lim_{\substack{\delta x_S \to 0 \\ r_{12} \to 0}}\left(\frac{u_1}{w_1}\right)$ of this ratio for an infinitesimal deviation $\delta x_S \to 0$ of the source and an infinitesimal distance $r_{12} \to 0$ between the edges (Figure 5) with arbitrary deviation of the receiver δx_R along the receiver line including the zero deviation. We obtain the uniform double limit value of the ratio $\lim_{\substack{\delta x_S \to 0 \\ r_{12} \to 0}}\left(\frac{u_1}{w_1}\right)=0$ independently of the limits order. Thus, we can define the zero value of function $\arctan\left(\frac{u_1}{w_1}\right)=0$ for all the receivers at Line 1 or 2. Accounting for (69) and (81) we obtain

$$\lim_{\substack{w_1 \to 0 \\ u_1 \to 0}} H\left(w_1, u_1\right)=\frac{1}{4}. \tag{82}$$

Next, we consider the second special function $H\left(w_2, u_2\right)$. The coincidence of the edges leads to the application of the Taylor's expansion of both arguments in a small vicinity of point $w_2 = u_2 = 0$. The arguments can be represented by the formulae

$$w_2 \cong \sqrt{\frac{2k_P}{\pi}\frac{r_R}{2}}\frac{1}{2}\left(\frac{\delta x_S}{r_S}+\frac{\delta x_R}{r_R}\right), \quad u_2 \cong \sqrt{\frac{2k_P}{\pi}r_{12}}\frac{1}{2}\frac{\delta x_S}{r_S}. \tag{83}$$

Formulae (83) allow us to consider ratio $\frac{u_2}{w_2} \cong \sqrt{2\frac{r_{12}}{r_R}}\left(1+\frac{r_S}{r_R}\frac{\delta x_R}{\delta x_S}\right)^{-1}$. For this ratio, we have to consider the triple limit $\lim_{\substack{\delta x_S \to 0 \\ r_{12} \to 0 \\ \delta x_R \to 0}}\left(\frac{u_2}{w_2}\right)=\lim_{\substack{\delta x_S \to 0 \\ r_{12} \to 0 \\ \delta x_R \to 0}}\left[\sqrt{2\frac{r_{12}}{r_R}}\left(1+\frac{r_S}{r_R}\frac{\delta x_R}{\delta x_S}\right)^{-1}\right]$ under an infinitesimal deviation $\delta x_S \to 0$ of the source, an infinitesimal distance $r_{12} \to 0$ between the edges, and an infinitesimal deviation $\delta x_R \to 0$ of the receiver along the receiver line. If we assume

$\sqrt{2\frac{r_{12}}{r_R}}\left(1+\frac{r_S}{r_R}\frac{\delta x_R}{\delta x_S}\right)^{-1}=c=\text{const}$ we obtain a nonzero constant value of ratio $\frac{u_2}{w_2}=\tan\zeta_2=c$.

This assumption is correct if equality $\frac{\delta x_R}{r_R}=-\frac{\delta x_S}{r_S}\left(1-\frac{1}{c}\sqrt{2\frac{r_{12}}{r_R}}\right)$ is valid. In the event of $r_{12}\to 0$, $\delta x_S\to 0$, $\delta x_R\to 0$ with any nonzero constant c, we obtain identity $\frac{\delta x_R}{r_R}=-\frac{\delta x_S}{r_S}$ for the two infinitesimal quantities $\frac{\delta x_R}{r_R}$ and $\frac{\delta x_S}{r_S}$. The last identity can be interpreted, in the kinematical terms, as follows: the deviated receiver and the deviated source must be at the opposite end points of the straight ray crossing the edge. Using the limit value of function $\zeta_2=\arctan(c)$ for the receiver at the shadow boundary we obtain from (69) the limit value

$$\lim_{\substack{w_2\to 0\\ u_2\to 0}} H(w_2,u_2)=\frac{1}{4}-\frac{\zeta_2}{2\pi}\,. \tag{84}$$

In the particular case of $\frac{u_2}{w_2}=\tan\zeta_2=c=1$, we can define the value of function $\zeta_2=\arctan(1)=\frac{\pi}{4}$ for the receiver at the shadow boundary. Hence, from (69) follows $\lim\limits_{\substack{w_2\to 0\\ u_2\to 0}} H(w_2,u_2)=\frac{1}{8}$.

Limits (80), (82) and (84) result in

$$DAC(\mathbf{x}_{shb})\cong\left|1-\frac{1}{2}-\left(-\frac{1}{4}+\frac{1}{4}-\frac{\zeta_2}{2\pi}\right)\right|=\frac{1}{2}+\frac{\zeta_2}{2\pi}\;, \tag{85}$$

where $c=\lim\limits_{\substack{w_2\to 0\\ u_2\to 0}}\left(\frac{u_2}{w_2}\right)=\tan\zeta_2$. If $\zeta_2=\frac{\pi}{4}$ then we obtain

$$DAC(\mathbf{x}_{shb})\cong\frac{1}{2}+\frac{1}{8}=\frac{5}{8}=0.625\;. \tag{86}$$

Instead of wavefield $a^{-}(\mathbf{x},t)$ we can also use any of its constituent and calculate $DAC(\mathbf{x})$ for it. For example: for the single edge wavefield, we can consider the particular case of (77)

$$DAC_{\mathbb{E}_2}^{[1]}(\mathbf{x}) \cong \frac{\left| a_{\mathbb{E}_2}^{[1]-}(\mathbf{x}, \omega_{dom}) \right|}{\left| p_{\mathbf{G}}(\mathbf{x}, \omega_{dom}) \right|} \ . \tag{87}$$

Substituting formulae (48) and (62) in (87) we obtain

$$DAC_{\mathbb{E}_2}^{[1]}(\mathbf{x}) \cong \left| W\left[w_2(\mathbf{x}, \omega_{dom}) \right] \right| \tag{88}$$

in the shadow zone.

3.10 Verification of TWSM-seismograms by the edge wave theory

Figure 6 represents a test for source 1 and the receiver line 1. Figure 6a illustrates the scalar component $a^{(0)-}(\mathbf{x},t)$ in formula (70) for the V-shaped boundary. Figure 6b demonstrates component $a^{\mathbf{G}-}(\mathbf{x},t)$ in formula (70), which is the source spherical wave. This wave does not depend on the shape of the boundary. Figure 6c illustrates component $a^{[1]-}(\mathbf{x},t)$, which is the difference between the feasible source wavefield and the conventional source wavefield $a^{\mathbf{G}-}(\mathbf{x},t)$. The double-diffraction term $a^{[1]-}(\mathbf{x},t)$ in the shadow zone consists of the source spherical wave with negative amplitude $a^{[1]-}_{\mathbf{G}}(\mathbf{x},t)$, the single edge waves $a^{[1]-}_{\mathbb{E}_1}(\mathbf{x},t)$ and $a^{[1]-}_{\mathbb{E}_2}(\mathbf{x},t)$ and the double edge wave $a^{[1]-}_{\mathbb{E}_2\mathbb{E}_1}(\mathbf{x},t)$. The single and double edge waves are visible behind the source spherical wave. Their traveltime is very close to the edge-wave eikonal. The double-diffraction term $a^{[1]-}(\mathbf{x},t)$ in the illuminated zone consists of the single edge wave $a^{[1]-}_{\mathbb{E}_2}(\mathbf{x},t)$ and the double edge wave $a^{[1]-}_{\mathbb{E}_2\mathbb{E}_1}(\mathbf{x},t)$. The diffraction amplitudes are positive in the shadow zone ($x<4.0\ \mathrm{km}$) and negative in the illuminated zone ($x>4.0\ \mathrm{km}$). A weak asymmetry of the diffraction amplitudes is noticeable at receivers $x=3.25\ \mathrm{km}$ and $x=4.75\ \mathrm{km}$. This asymmetry is an amplitude asymmetry of the double-edge wave in formulae (66) and (67). Moreover, the diffraction amplitude at the shadow boundary ($x=4.0\ \mathrm{km}$) is not equal to a half of the spherical-wave amplitude. Figure 6d demonstrates the distribution of $DAC(\mathbf{x})$ for the scalar component $a^{(0)-}(\mathbf{x},t)$ (solid line) evaluated by the TWSM algorithm. It is visible that the computed $DAC(\mathbf{x})$ at the shadow boundary is approximately equal to +0.615. Substituting this value in formula (85), we obtain $\zeta_2=\frac{\pi}{4}-3.6^{\circ}$ at the shadow boundary. We see that the computed $DAC(\mathbf{x})=0.615$ and the edge wave theory $DAC(\mathbf{x})=0.625$ from (86) are different with the relative error 2 percent approximately.

In addition, we demonstrate $DAC^{[1]}_{\mathbb{E}_2}(\mathbf{x})$ for the single edge wavefield (dashed line) evaluated by the analytical formula (88). A stable difference at 25% of value between the computed $DAC(\mathbf{x})$ and the analytical edge-wave $DAC^{[1]}_{\mathbb{E}_2}(\mathbf{x})$ demonstrates that the first diffraction term of the cascade diffraction cannot be represented by the edge wave only, and that formula (71) must be used.

Figure 7 represents a test for source 1 and the receiver line 2. Figure 7a demonstrates the scalar component $a^{(0)-}(\mathbf{x},t)$ of formula (70) for the V-shaped boundary. Figure 7b illustrates component $a^{\mathbf{G}-}(\mathbf{x},t)$ of formula (70), which is the source spherical wave. This wave does not depend on the shape of the boundary. Figure 7c represents component $a^{[1]-}(\mathbf{x},t)$, which is the difference between the feasible source wavefield and the conventional source wavefield $a^{\mathbf{G}-}(\mathbf{x},t)$. A weak asymmetry of the diffraction amplitudes is noticeable at receivers $x = 3.25\,\mathrm{km}$ and $x = 4.75\,\mathrm{km}$. The double-diffraction term $a^{[1]-}(\mathbf{x},t)$ in the shadow zone consists of the source spherical wave with negative amplitude $a^{[1]-}_{\mathbf{G}}(\mathbf{x},t)$, the single edge waves $a^{[1]-}_{\mathbb{E}_1}(\mathbf{x},t)$ and $a^{[1]-}_{\mathbb{E}_2}(\mathbf{x},t)$ and the double edge wave $a^{[1]-}_{\mathbb{E}_2\mathbb{E}_1}(\mathbf{x},t)$. The single and double edge waves are visible behind the source spherical wave. Their traveltime is very close to the edge-wave eikonal. The double-diffraction term $a^{[1]-}(\mathbf{x},t)$ in the illuminated zone consists of the single edge wave $a^{[1]-}_{\mathbb{E}_2}(\mathbf{x},t)$ and the double edge wave $a^{[1]-}_{\mathbb{E}_2\mathbb{E}_1}(\mathbf{x},t)$. The diffraction amplitudes are positive in the shadow zone ($x < 4.0\,\mathrm{km}$) and negative in the illuminated zone ($x > 4.0\,\mathrm{km}$). A weak asymmetry of the diffraction amplitudes is noticeable at receivers $x = 3.25\,\mathrm{km}$ and $x = 4.75\,\mathrm{km}$. This asymmetry is an amplitude asymmetry of the doublen edge wave in formulae (66) and (67). Moreover, the diffraction amplitude at the shadow boundary ($x = 4.0\,\mathrm{km}$) is not equal to a half of the spherical-wave amplitude. Figure 7d demonstrates the distribution of $DAC(\mathbf{x})$ for the scalar component $a^{(0)-}(\mathbf{x},t)$ (solid line) evaluated by the TWSM algorithm. It is visible that the modeled $DAC(\mathbf{x})$ at the shadow boundary is approximately equal to +0.608. Substituting this value in formula (85), we obtain $\zeta_2 = \dfrac{\pi}{4} - 6.12^{\circ}$ at the shadow boundary. We see that the computed $DAC(\mathbf{x}) = 0.608$ and the edge wave theory $DAC(\mathbf{x}) = 0.625$ from (86) are different with the relative error 3 percent approximately.

Figures 8 represents a test for source 2 and the receiver line 1. Figure 8a gives the realization of the scalar component $a^{(0)-}(\mathbf{x},t)$ for the V-shaped boundary. Figure 8b illustrates component $a^{\mathbf{G}-}(\mathbf{x},t)$ of vector (70), which is the source spherical wave. This wave does not depend on the shape of the boundary. Figure 8c demonstrates component $a^{[1]-}(\mathbf{x},t)$, which is the difference between the feasible source wavefield and the conventional source wavefield $a^{\mathbf{G}-}(\mathbf{x},t)$. The double-diffraction term $a^{[1]-}(\mathbf{x},t)$ in the shadow zone consists of the source spherical wave with the negative amplitude $a^{[1]-}_{\mathbf{G}}(\mathbf{x},t)$, the single edge waves $a^{[1]-}_{\mathbb{E}_1}(\mathbf{x},t)$ and $a^{[1]-}_{\mathbb{E}_2}(\mathbf{x},t)$ and the double edge wave $a^{[1]-}_{\mathbb{E}_2\mathbb{E}_1}(\mathbf{x},t)$. The single and double edge waves are visible behind the source spherical wave. Their travel time is very close to the edge-wave eikonal. The double-diffraction term $a^{[1]-}(\mathbf{x},t)$ in the illuminated zone consists of the single edge wave $a^{[1]-}_{\mathbb{E}_2}(\mathbf{x},t)$ and the double edge wave $a^{[1]-}_{\mathbb{E}_2\mathbb{E}_1}(\mathbf{x},t)$. The diffraction amplitudes are positive in the shadow zone ($x < 4.0\text{ km}$) and negative in the illuminated zone ($x > 4.0\text{ km}$). A weak asymmetry of the diffraction amplitudes is noticeable at receivers $x = 3.25\text{ km}$ and $x = 4.75\text{ km}$. This asymmetry is an amplitude asymmetry of the double edge wave in formulae (66) and (67). Moreover, the diffraction amplitude at the shadow boundary ($x = 4.0\text{ km}$) is not equal to a half of the spherical-wave amplitude. Figure 8d represents the distribution of $DAC(\mathbf{x})$ for the scalar component $a^{(0)-}(\mathbf{x},t)$ (solid line) evaluated by the TWSM algorithm. It is visible that the modeled $DAC(\mathbf{x})$ at the shadow boundary is approximately equal to +0.603. Substituting this value in formula (85), we obtain $\zeta_2 = \frac{\pi}{4} - 7.92^{\circ}$ at the shadow boundary. We see that the computed $DAC(\mathbf{x}) = 0.603$ and the edge wave theory $DAC(\mathbf{x}) = 0.625$ from (86) are different with the relative error 3 percent approximately.

The absolute error of the time arrivals, amplitudes and pulse shapes of the computed by TWSM wave events can be estimated by the maximal absolute values of the residual amplitudes along the move-out for the conventional spherical wave in the shadow zone at receivers $x < 4.0\text{ km}$. We estimate the relative error in the amplitudes less than 4 percent and the absolute error in the time arrivals is approximately 0.002 s.

3.11 Conclusions

We derived a double-diffraction approximation of the feasible source wavefield below a salt overhang of V-shape, using the TPOT theory. We applied the TWSM algorithm for computation of the double-diffraction approximation in terms of the nonsparse propagation and absorption matrices. We developed and implemented this algorithm for evaluation of the virtual shadow function and tested the code for V-boundary. The examples of the computation illustrate the accuracy and efficiency of the computational technology. The correctness of the algorithm is justified by comparison of the travel times and amplitudes of the feasible source wavefield with the edge wave theory results. The comparison demonstrated that TPOT&TWSM is successfully applied to the evaluation of the feasible source wavefield in the geometrical shadow zone caused by V-shaped boundary of the acoustic half-space.

3.12 Acknowledgements

The work was partly supported by NTNU (Trondheim, Norway), the Research Centres Bergen and Trondheim of Statoil ASA (Norway) and the Swedish Foundation for International Cooperation in Research and Higher Education (University of Lund, Sweden). We express deep sorrow for Kamill D. Klem-Musatov who recently passed away and was allways one of our best colleagues and collaborators. We are thankful to our colleagues Hans B. Helle, Jan Pajchel, Ola-Petter Munkvold, Milana Ayzenberg, Gennady Demidenko, Gleb Dyatlov, Fredrik Andersson, Anton Duchkov and Alexey Romanenko for constructive discussions. We also acknowledge Marco D'oleire, Toan Dao and Anna Mackie for improving the language style in the paper.

3.13 References

Aizenberg, A.M., 1982. Scattering of seismic waves by the broken edge of a flat boundary, Russian Geology and Geophysics, 23, 5, 83-92.

Aizenberg, A.M., 1993. A system of irregular fundamental solutions to wave equation in a three-dimensional inhomogeneous medium, Russian Geology and Geophysics, 34, 4, 105-113.

Aizenberg, A.M. & Ayzenberg, A.A., 2008a. Fundamental solution of the acoustic wave equation which satisfies the integral absorption condition at a regular boundary of a half-space, Proceedings of the International Conference "Differential Equations. Function Spaces. Approximation Theory" dedicated to the 100th anniversary of Sergey Sobolev, Russian Academy of Sciences, 89 (in Russian).

Aizenberg, A.M. & Ayzenberg, A.A., 2008b. Feasible fundamental solution to the acoustic wave equation in a heterogeneous halfspace with a regular boundary, Proceedings of the International Conference on Mathematical Methods in Geophysics "MMG-2008" dedicated to the 80th anniversary of A.S. Alekseev, 1–6.

Aizenberg, A.M. & Ayzenberg, A.A., 2015. Feasible fundamental solution of the multiphysics wave equation in inhomogeneous domain of complex shape, Wave Motion, 53, 66-79.

Aizenberg, A.M., Ayzenberg, A.A. & Pajchel, J., 2010. Feasible fundamental matrix of the seismic-electromagnetic wave equation in a curved fractured and porous fluid-saturated layer, Dynamics of solid media, Proceedings of Lavrentiev's Institute of Hydrodynamics, Russian Academy of Sciences, 126, 20-25 (in Russian).

Aizenberg, A.M., Ayzenberg, M.A. & Klem-Musatov, K.D., 2011. Seismic diffraction modeling with the tip-wave superposition method, Extended Abstracts, 73-th EAGE Conference, Vienna, Austria, B018.

Aizenberg, A.M. & Klem-Musatov, K.D., 2010. Progress in seismic diffraction theory – From edge and tip waves to multiple reflections-transmissions with diffractions, Extended Abstracts, 72-th EAGE Conference, Barcelona, Spain, G034.

Aizenberg, A.M., Zyatkov, N.Y., Ayzenberg, A.A. & Rakshaeva, E.Z., 2014. New concepts of the transmission-propagation operator theory in seismic diffraction modeling and interpretation, Extended Abstracts, 76th EAGE Conference, Amsterdam, Netherlands, We-P06-07.

Ayzenberg, A.A. & Aizenberg, A.M., 2009. Feasible fundamental matrix of the seismic-electromagnetic wave equation in a curved elastic porous fluid-saturated layer, Proceedings of the International Conference “Contemporary Problems of Computational Mathematics and Mathematical Physics” dedicated to the 90th anniversary of Alexander Samarsky, Russian Academy of Sciences, 113-114.

Ayzenberg, A.A., Aizenberg, A.M., Zyatkov, N. & Andersson, F., 2012. Single-diffraction approximation of the feasible Green’s function in geometrical shadow zones, Extended Abstracts, 74th EAGE Conference, Denmark, Copenhagen, P287.

Ayzenberg, A.A., Ayzenberg, M.A. & Aizenberg, A.M., 2010. Feasible Green’s function for a domain with shadow zones, Extended Abstracts, 72th EAGE Conference, Barcelona, Spain, P094.

Ayzenberg, A., Zyatkov, N., Stovas, A. & Aizenberg, A.M., 2013. Double-diffraction approximation of the feasible Green’s function in geometrical shadow zones, Extended Abstracts, 75th EAGE Conference, London, UK, Th-P02-10.

Ayzenberg, A., Zyatkov, N., Stovas, A., & Aizenberg, A.M., 2014. The feasible near-front wavefield below salt overhang in terms of cascade diffraction, Extended Abstracts, 76th EAGE Conference, Amsterdam, Netherlands, We-P06-06.

Ayzenberg, M., Aizenberg, A.M. & Ursin, B., 2009. Tip-wave superposition method with effective reflection and transmission coefficients: A new 3D Kirchhoff-based approach to synthetic seismic modeling, Leading Edge, 28, 582-588.

Babich, V.M., Lyalinov, M.A., & Grikurov, V.E., 2007. Diffraction theory. The Sommerfeld-Malyuzhinets technique, Alpha Science, Oxford, UK.

Borovikov, V.A., 1994. Uniform stationary phase method. The Institution of Electrical Engineers, London, UK.

Borovikov, V.A. & Kinber, B.Ye., 1994. Geometrical theory of diffraction. Peter Pelegrinus.

Cerveny, V., 2005. Seismic Ray Theory, Cambridge University Press.

Chandler-Wilde, S.N., Graham, I.G., Langdon S. & Spence E.A., 2012. Numerical-asymptotic boundary integral methods in high-frequency acoustic scattering, Acta Numerica, Cambridge University Press, 89–305.

Costabel, M., Dauge, M., 1997. On representation formulas and radiation conditions, Math. Methods Appl. Sci., 20, 2, 133-150.

Ferrand, A., Darmon, M., Chatillon, S., & Deschamps, M., 2014. Modelling of wave propagation on irregular surfaces using ray tracing and GTD approaches: Application to head wave simulation in TOFD inspections for NDT, Journal of Physics: Conference Series, 498, 012011.

Friedlander, F.G., 1958. Sound Pulses, Cambridge, Cambridge University Press.

Hewett, D.P., Ockendon, J.R., & Allwright, D.J., 2011. Switching on a two-dimensional time-harmonic scalar wave in the presence of a diffracting edge. Wave Motion, 48, 197–213.

Jones, D.S., 1973. Double knife-edge diffraction and ray theory, Quart. J. Mech. and Appl. Math., 26, 1, 1-18.

Keller J.B., 1962. Geometrical theory of diffraction, Journal of the Optical Society of America, 52, 116-130.

Klem-Musatov, K., 1994. Theory of Seismic Diffractions, Investigations in Geophysics, No. 9, SEG, Tulsa, USA.

Klem-Musatov, K.D., Aizenberg, A.M., Pajchel, J., & Helle, H.B., 2008. Edge and Tip Diffractions: Theory and Applications in Seismic Prospecting, Geophysical Monograph Series, No. 14, SEG, Tulsa, USA.

Korn, G.A. & Korn, T.M., 2000. Mathematical handbook for scientists and engineers. Dover publications, New York.

Rubinowicz, A., 1965. The Miyamoto-Wolf diffraction wave, in Progress in Optics, Vol. IV, 199-240, ed. Wolf E., NorthHolland Publishing Co., Amsterdam.

Wapenaar, K., 2007. General representations for wavefield modeling and inversion in geophysics, Geophysics, 72, 5, SM5-SM17.

Wapenaar, K. & Douma, H., 2012. A unified optical theorem for scalar and vectorial wave fields, J. Acoust. Soc. Am., 131, 5, 3611–3626.

Wapenaar, K., & Fokkema, J., 2004. Reciprocity theorems for diffusion, flow and waves, J. Appl. Mech, 71, 145-150.

Zaman, S.I., 2000. A comprehensive review of boundary integral formulations of acoustic scattering problems, Science and Technology, Special Review, 281-310.

Zyatkov, N., Ayzenberg, A.A., Aizenberg, A.M., Romanenko, A. & Andersson, F., 2012. Modeling of cascade diffraction in terms of propagation-absorption matrices: realization and optimization for GPU, Extended Abstracts, 74th EAGE Conference, Denmark, Copenhagen, P288.

Zyatkov, N., Ayzenberg, A., Aizenberg, A.M. & Romanenko, A., 2013. Highly-optimized TWSM algorithm for modeling cascade diffraction in terms of propagation-absorption matrices, Extended Abstracts, 75th EAGE Conference, London, UK, Th-P02-11.

3.14 List of Tables

Table 1. Comparison of computing times for different versions of the TWSM algorithm using different parallel architectures.

Sequential program (1 kernel Intel(R) Xeon(R) CPU E5630 @2.53GHz), 1 TWSM matrix	27 hours
OpenMP+Intel MKL, optimization (8 kernels Intel(R) Xeon(R) CPU E5630 @2.53GHz), 1 TWSM matrix	2 hours
CUDA+CuBLAS (NVIDIA Tesla M2090) 1 GPU, 1 TWSM matrix	10 min
CUDA+CuBLAS (NVIDIA Tesla M2090) 18 GPU, 1 TWSM matrix	40 sec
Transmission through the W-shaped interface taking into account sextuple diffraction – 21 GPU, 32 TWSM matrices	19,5 min

3.15 List of Figures

Figure 1. V-shaped model.

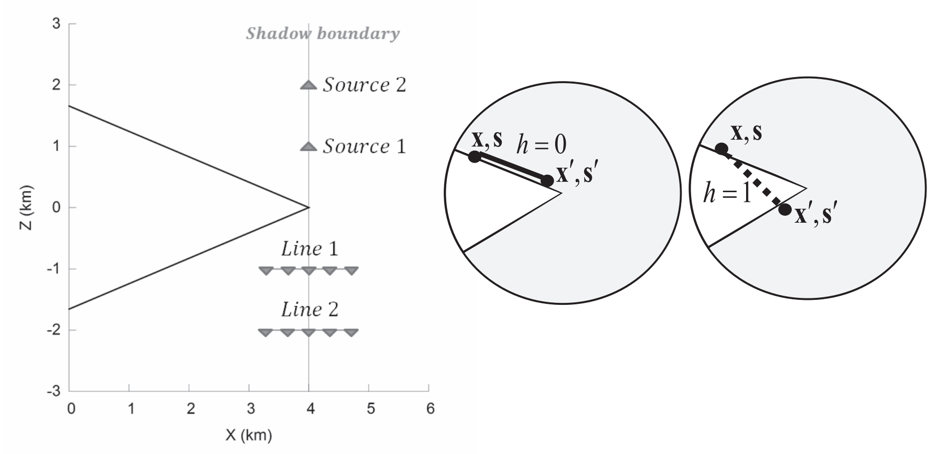

Figure 1a. Sketch and acquisition design. **Figure 1b.** Visibility of the points

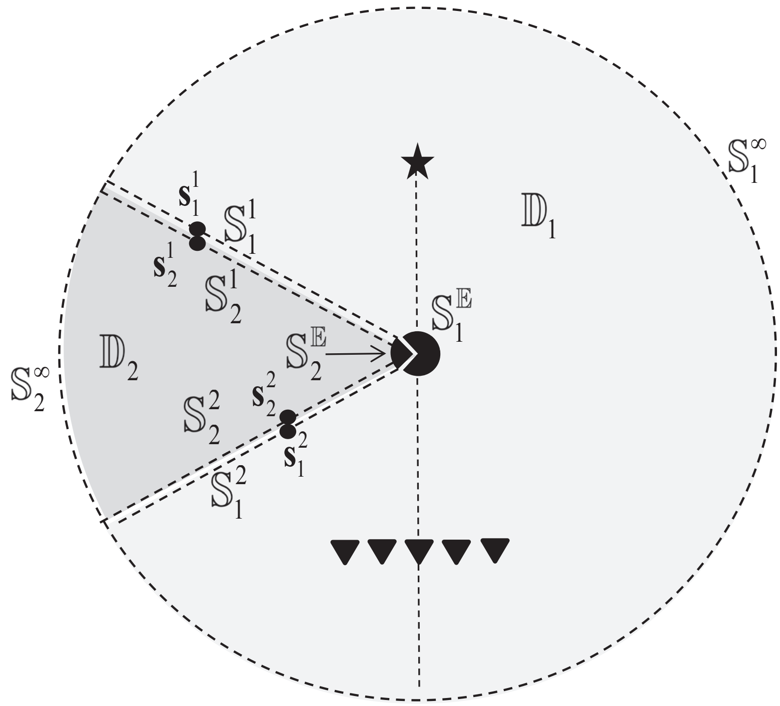

Figure 1c. Medium and faces notations

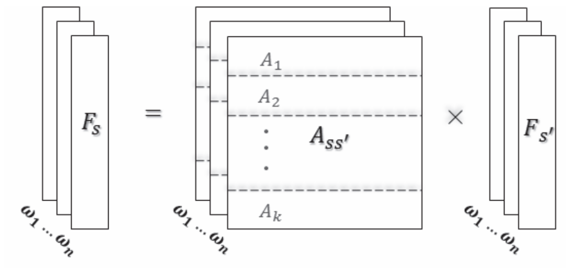

Figure 2. Scheme of realization of matrix-vector multiplication for each discrete frequency.

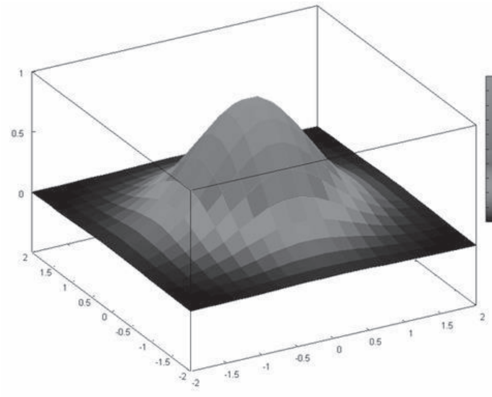

Figure 3a. 3D view of boundary in km.

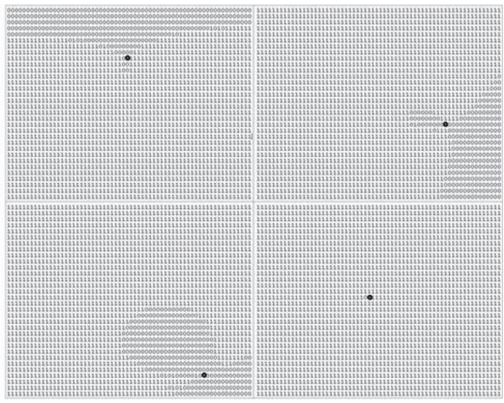

Figure 3b. Four matrix rows at boundary.

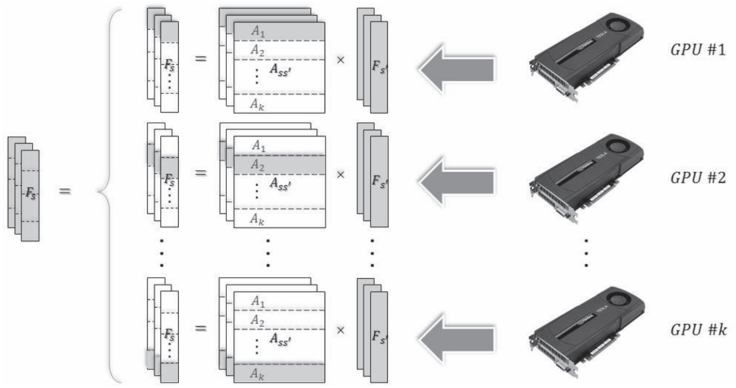

Figure 4. Scheme of the realization of matrix-vector transformation of TWSM for several GPUs.

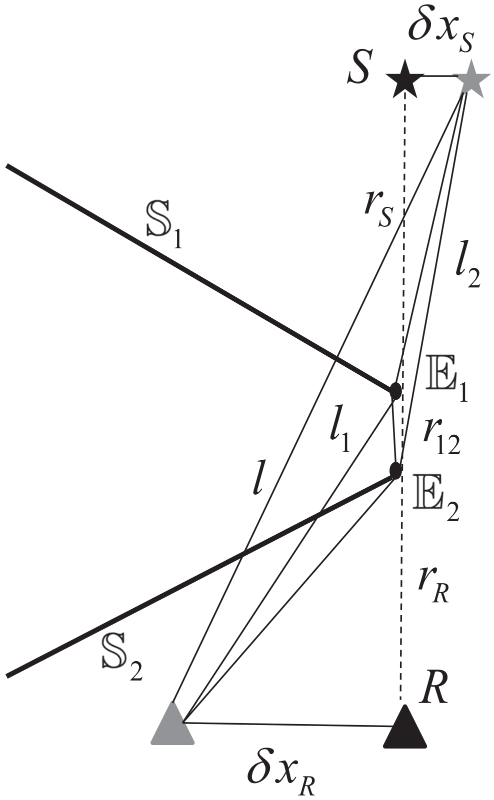

Figure 5. Edge waves rays. Deviations δx_S and δx_R can be positive and negative.

Figure 6. Source 1 and receiver line 1.

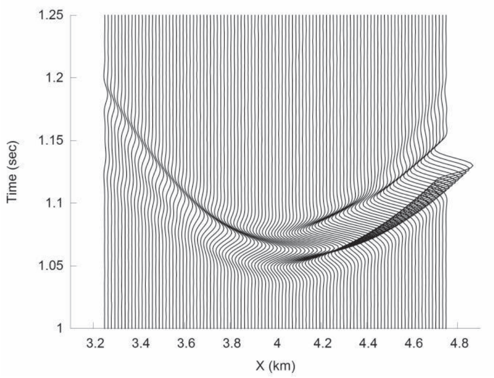

Figure 6a. Wavefield $a^{(0)-}(\mathbf{x},t)$.

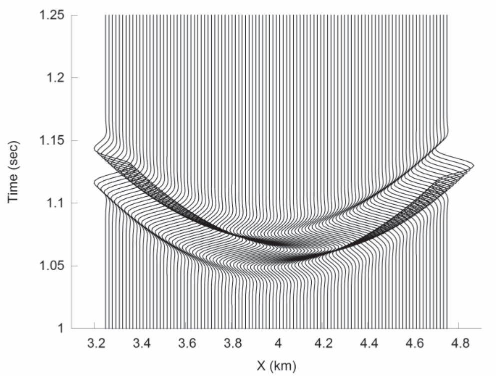

Figure 6b Wavefield $a^{\mathbf{G}-}(\mathbf{x},t)$.

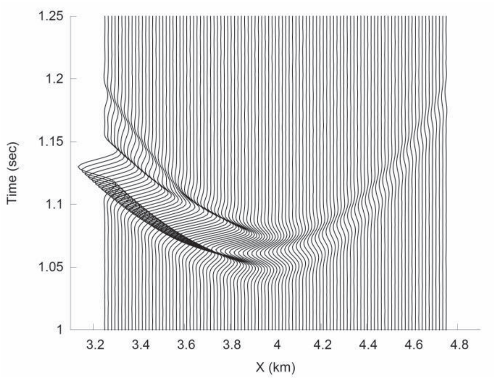

Figure 6c. Wavefield $a^{[1]-}(\mathbf{x},t)$.

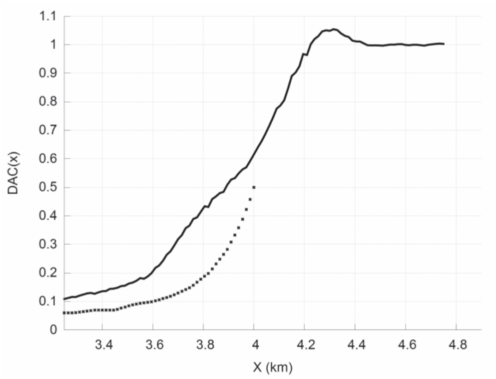

Figure 6d Curve of $DAC(\mathbf{x})$.

Figure 7. Source 1 and receiver line 2.

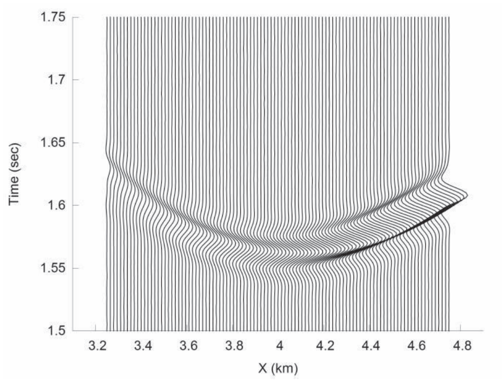

Figure 7a. Wavefield $a^{(0)-}(\mathbf{x},t)$.

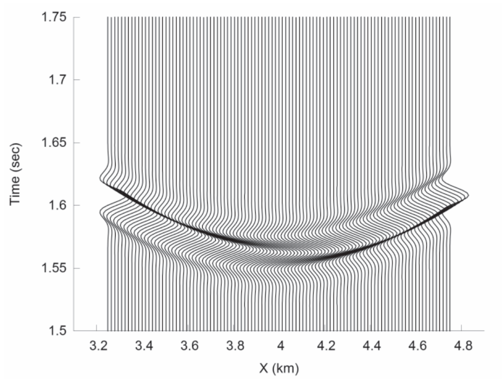

Figure 7b. Wavefield $a^{\mathbf{G}-}(\mathbf{x},t)$.

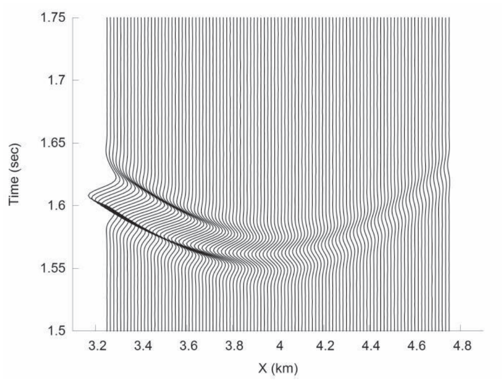

Figure 7c. Wavefield $a^{[1]-}(\mathbf{x},t)$.

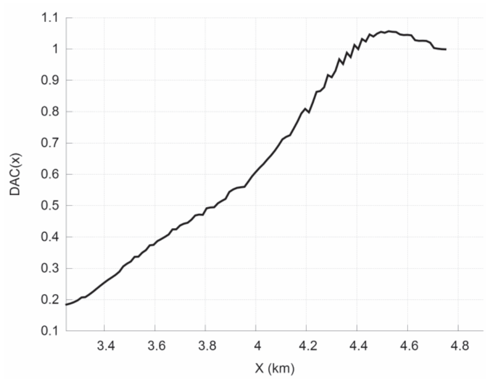

Figure 7d. Curve of $DAC(\mathbf{x})$.

Figure 8. Source 2 and receiver line 1.

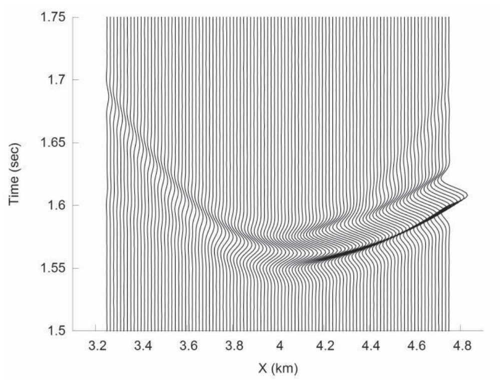

Figure 8a. Wavefield $a^{(0)-}(\mathbf{x},t)$.

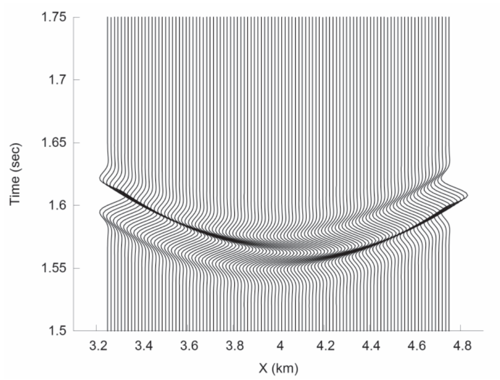

Figure 8b. Wavefield $a^{\mathrm{G}-}(\mathbf{x},t)$.

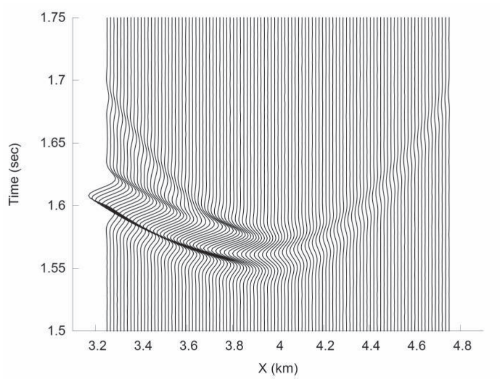

Figure 8c. Wavefield $a^{[1]-}(\mathbf{x},t)$.

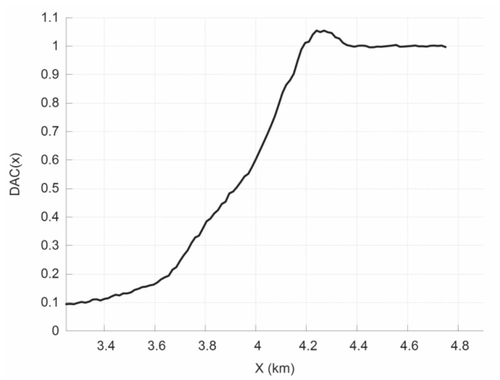

Figure 8d. Curve of $DAC(\mathbf{x})$.

Chapter 4

Feasible source wavefield for acoustic U- and W-model with shadow in the form of double diffraction approximation

Alena A. Ayzenberg[a*], Nikolay Y. Zyatkov[b], Arkady M. Aizenberg[c], Alexey Stovas[a]

[a] Norwegian University of Science and Technology (NTNU), S.P. Andersens veg 15a, 7491 Trondheim, Norway,

tel.: +47 90 840 729, fax: +47 73 944 472, e-mail: alena.ayzenberg@ntnu.no

tel.: +47 73 597 139, fax: +47 73 944 472, e-mail: alexey.stovas@ntnu.no

[b] Novosibirsk State University, Pirogova str. 2, 630090 Novosibirsk, Russia,

tel.: +7 923 248 2157, fax: +7 383 333 2513, e-mail: nikolay.zyatkov@gmail.com

[c] Institute of Petroleum Geology and Geophysics, Russian Academy of Sciences,

Ac. Koptyug Pr. 3, 630090 Novosibirsk, Russia,

tel.: +7 383 335 6457, fax: +7 383 333 2513, e-mail: AizenbergAM@ipgg.sbras.ru

Presented at the ROSE Meeting, Trondheim, Norway, 2014; the 76th EAGE Conference & Exhibition, Amsterdam, the Netherlands, 2014; Subsalt imaging workshop, Larnaca Cyprus, 2014. Submitted to Geophysical Journal International on 27 January 2015, resubmitted on 11 August 2015.

4.1 Summary

Earlier, we proposed a theoretical study of a source wavefield by the Transmission-Propagation Operator Theory (TPOT), which provides an analytical description of the wave structure for the physically feasible source wavefield below a salt V-overhang. The problem of the mathematical description of the wavefield below the salt overhang was solved by splitting the source wavefield in the wave fragments corresponding to the observed wavefield: the source spherical wavefield and the wavefield diffracted by the overhang. That study aimed to correct the overhang V-model solution with help of the double-diffraction approximation of the feasible source wavefield. The numerical examples, provoded by the Tip-Wave Superposition Method (TWSM), illustrated the time arrivals and amplitudes of the wavefield. In this paper, we consider other models, a parabolic and hyperbolic U-models and a double wedge W-model, and use the same theoretical basis of TPOT, the computation method of TWSM and the error estimation approach.

4.2 Introduction

In paper A.A. Ayzenberg *et al*. (2015)/Chapter 3 of this thesis, we derived the feasible source wavefield in the shadow zone of an acoustic canonical V-model. The theoretical results were taken from paper A.M. Aizenberg & A.A. Ayzenberg (2015)/Chapter 2 of this thesis. The numerical examples computed by the Tip-Wave Superposition Method (TWSM) (Klem-Musatov *et al*. (2008), A.M. Aizenberg & Klem-Musatov (2010), M.A. Ayzenberg *et al*. (2007), A.M. Aizenberg *et al*. (2011) and A.M. Aizenberg *et al*. (2014)) were compared with the formulae of the edge and tip wave theory by A.M. Aizenberg (1982) and A.M. Aizenberg (1993). We also represented an improved highly-optimized algorithm of TWSM for computation of the first cascade diffraction term based on the propagation and absorption matrices (A.A. Ayzenberg *et al.* (2012), A.A. Ayzenberg *et al.* (2013), A.A. Ayzenberg *et al.* (2014), Zyatkov *et al*. (2012) and Zyatkov *et al*. (2013)). The accuracy, stability and efficiency of the algorithm were illustrated by numerical tests for V-model.

In this paper, we consider similar tests but for another three types of boundary, a parabolic and hyperbolic U-model and a double wedge W-model. The paper performs computation (visualization) of the feasible source wavefield by TPOT&TWSM. Because the approximation of the wavefield represented on the seismograms has no analogs in the present wave theory, we need a comparison with results of an independent method. Such a comparison cannot be done by numerical methods because we need to test separate fragments of the total wavefield. For the comparison, we apply the well-known approach of rigorous integration using the formulae of the mathematical edge wave theory by A.M. Aizenberg (1982) and A.M. Aizenberg (1993) in case of U- and W-boundary.

This paper consists of an Introduction, six Sections and Conclusions. The Introduction contains a short theoretical description from A.A. Ayzenberg *et al.* (2015)/Chapter 3 of this thesis. Section 4.3 contains the statements of U- and W-problem. Section 4.4 gives the explicit analyticval solution of the problems. Section 4.5 describes the feasible source wavefield in terms of the single and double edge wavefields of the wave theory, for U-model. Section 4.6 demonstrates verification of the TWSM source wavefield seismograms by the edge wave theory, for U-model. Section 4.7 describes the feasible source wavefield in terms of the single and double edge wavefields of the wave theory, for W-model. Section 4.8

demonstrates verification of the TWSM source wavefield seismograms by the edge wave theory, for W-model. Conclusions summarize the results of the paper.

4.3 Forward U- and W-problem for 2-block medium

In this Section, we consider two models: U- and W-model.

U-model

The first of the considered models is a 2-block model with a cylindrical U-boundary of parabolic (Figure 1) and hyperbolic (Figure 2) shape, concave inside the half-space. The material parameters of the domains and the geometrical parameters of the interface are chosen to imitate a salt overhang surrounded by sediments. A strong velocity contrast simulates shadow below the overhang.

U-model consists of two homogeneous acoustic domains (Figure 3a), $\mathbb{D}_1$ and $\mathbb{D}_2$, separated by a smooth U-interface composed from two curved faces connected by a formal 'edge' ($x = 4.0\,\text{km}, y\,\text{km}, z = 0\,\text{km}$). We generally do not have an edge and introduce it only formally in order to later describe an edge effect which will present in this problem. A point source is located at point ($x = 4.0\,\text{km}, y = 0\,\text{km}, z = 1.0\,\text{km}$). Radius-vectors $\mathbf{x}_m$ designate an arbitrary point in $\mathbb{D}_m$, $m = 1,2$. Parameters of domain $\mathbb{D}_1$ are: P-wave velocity $v_{P,1} = 2.0\,\text{km}/\sec$ and density $\rho_1 = 2.0\,\text{g}/\text{cm}^3$. Parameters of domain $\mathbb{D}_2$ are: P-wave velocity $v_{P,2} = 4.0\,\text{km}/\sec$ and density $\rho_2 = 3.0\,\text{g}/\text{cm}^3$.

U-interface is considered as a two-sided surface with sides $\mathbb{S}_m(\mathbf{s}_m)$ (Figure 3a), where $m = 1,2$ is the domain number. Radius-vector $\mathbf{s}_m$ denotes either a boundary point on $\mathbb{S}_m$ or a point in $\mathbb{D}_m$ which is infinitesimally close to $\mathbf{s}_m$. We denote the infinite parts of the interface as $\mathbb{S}_m^\infty$. The faces of the interface are denoted as $\mathbb{S}^j$, $j = 1,2$. The normal vectors are directed inwards domains $\mathbb{D}_m$ and denoted as $\mathbf{n}(\mathbf{s}_m^j)$, $\mathbf{s}_m^j \in \mathbb{S}_m^j$, where the lower index denotes the medium number and the upper index denotes the face number. The upper side $\mathbb{S}_1^1$ and lower side $\mathbb{S}_2^1$ of the upper face of the parabolic U-interface are defined by formula $z = +\sqrt{4 - x}$, the upper side $\mathbb{S}_2^2$ and lower side $\mathbb{S}_1^2$ of the lower face of the parabolic U-interface are defined by formula $z = -\sqrt{4-x}$ (Figure 1). Faces $\mathbb{S}_1$ and $\mathbb{S}_2$ have a common line $(4.0, y, 0)$. The radius of curvature of the boundary is 0.5 km at the tangential ray and is comparable with eight dominant wavelengths. The upper side $\mathbb{S}_1^1$ and lower side $\mathbb{S}_2^1$ of the upper face of the hyperbolic U-interface are defined by formula $z = +0.4\sqrt{(5.25-x)^2 - (1.25)^2}$, the upper side $\mathbb{S}_2^2$ and lower side $\mathbb{S}_1^2$ of the lower face of the hyperbolic U-interface are defined by formula $z = -0.4\sqrt{(5.25-x)^2 - (1.25)^2}$ (Figure 2). Faces $\mathbb{S}_1$ and $\mathbb{S}_2$ also have a common line $(4.0, y, 0)$. The radius of curvature of the boundary is 0.2 km at the tangential ray. This value is comparable with three dominant wavelengths.

We define a receiver line: from $x = 3{,}25\,\text{km}$ to $x = 4{,}75\,\text{km}$ with step $\Delta x = 0{,}015\,\text{km}$ at $\text{y} = 0.0\,\text{km}, z = -1.0\,\text{km}$. This line contains 101 receivers and intersects the shadow boundary of the source spherical wavefield at $x = 4.0\,\text{km}$. The receivers for $x < 4.0\,\text{km}$ are located in the shadow zone and the receivers for $x > 4.0\,\text{km}$ are in the illuminated zone.

We represent temporal spectra of the wavefield as particle velocity-pressure vectors (4×1-columns)

$$\mathbf{u}(\mathbf{x}_m, \omega) = \begin{pmatrix} v_{1,m} \\ v_{2,m} \\ v_{3,m} \\ p_m \end{pmatrix}, \tag{1}$$

where $v_{1,m}$, $v_{2,m}$, $v_{3,m}$ are components of the particle velocities, p_m is pressure in each domain. Functions $\mathbf{u}(\mathbf{x}_m, \omega)$ are defined as follows

$$\begin{cases} \mathbf{u} = \mathbf{u}(\mathbf{x}_1, \omega), & \text{for} \quad \mathbf{x}_1 \in \mathbb{D}_1\,, \\ \mathbf{u} = \mathbf{u}(\mathbf{x}_2, \omega), & \text{for} \quad \mathbf{x}_2 \in \mathbb{D}_2\,. \end{cases} \tag{2}$$

Vectors (2) are connected with the wavefields by the Fourier transform

$$\mathbf{u}(\mathbf{x}_m,t)=\frac{1}{\sqrt{2\pi}}\int_{-\infty}^{+\infty}\mathbf{u}(\mathbf{x}_m,\omega)\,e^{-i\omega t}\,d\omega\ , \tag{3}$$

where ω is angular frequency. The temporal spectrum vectors $\mathbf{u}(\mathbf{x}_m,\omega)$ in (2) satisfy the wave motion equations from A.M. Aizenberg & A.A. Ayzenberg (2015)/Chapter 2 of this thesis and A.A. Ayzenberg *et al.* (2015)/Chapter 3 of this thesis

$$\mathbf{D}_{\mathbf{x}_m}\,\mathbf{u}(\mathbf{x}_m,\omega)+\mathbf{M}_m(\omega)\,\mathbf{u}(\mathbf{x}_m,\omega)=\mathbf{f}(\mathbf{x}_m,\omega),\quad m=1{,}2\,, \tag{4}$$

where the differential matrix operator and the matrix of material parameters are

$$\mathbf{D}_{\mathbf{x}_m}=\begin{pmatrix} 0 & 0 & 0 & \dfrac{\partial}{\partial x_1} \\ 0 & 0 & 0 & \dfrac{\partial}{\partial x_2} \\ 0 & 0 & 0 & \dfrac{\partial}{\partial x_3} \\ \dfrac{\partial}{\partial x_1} & \dfrac{\partial}{\partial x_2} & \dfrac{\partial}{\partial x_3} & 0 \end{pmatrix},\quad \mathbf{M}_m(\omega)=(-i\,\omega)\begin{pmatrix} \rho_m & 0 & 0 & 0 \\ 0 & \rho_m & 0 & 0 \\ 0 & 0 & \rho_m & 0 \\ 0 & 0 & 0 & \dfrac{1}{\rho_m\left(v_{P,m}\right)^2} \end{pmatrix}. \tag{5}$$

The point source is $\mathbf{f}(\mathbf{x}_1,\omega)=\dfrac{\psi(\omega)}{(-i\,\omega)\,\rho_1}\begin{pmatrix}0 & 0 & 0 & \delta(\mathbf{x}_1-\mathbf{y}_1)\end{pmatrix}^T$, the source radiates a spherical P-wave. Function $\psi(\omega)$ is the spectrum of the wavelet $\psi(t)=e^{-(2\tau)^2}\cos(2\pi\,\tau)$, where $\tau=t/T-2$. The wave period $T=0.032\,\mathrm{sec}$ corresponds to the dominant wavelength of 0.064 km and the dominant frequency of 38.25 Hz. In domain $\mathbb{D}_2$, there is no source: $\mathbf{f}(\mathbf{x}_2,\omega)=\begin{pmatrix}0 & 0 & 0 & 0\end{pmatrix}^T$.

In each domain (Figure 3a), vector (2) satisfies the radiation conditions $\langle RC\rangle_m$ at the infinite boundary $\mathbb{S}_m^\infty$ of domain $\mathbb{D}_m$

$$\langle RC\rangle_m:\ \iint_{\mathbb{S}_m^\infty}\mathbf{F}(\mathbf{x}_m,\mathbf{s}_m,\omega)\,\mathbf{N}(\mathbf{s}_m)\,\mathbf{u}(\mathbf{s}_m,\omega)\,dS(\mathbf{s}_m)=0\,,\quad m=1{,}2 \tag{6}$$

in terms of the feasible surface integral operators with the fesible fundamental solution $\mathbf{F}(\mathbf{x}_m, \mathbf{s}_m, \omega)$ in the kernel, similar to (6) from A.A. Ayzenberg *et al.* (2015)/Chapter 3 of this thesis. The normal matrix is

$$\mathbf{N}(\mathbf{s}_m) = \begin{pmatrix} 0 & 0 & 0 & n_1(\mathbf{s}_m) \\ 0 & 0 & 0 & n_2(\mathbf{s}_m) \\ 0 & 0 & 0 & n_3(\mathbf{s}_m) \\ n_1(\mathbf{s}_m) & n_2(\mathbf{s}_m) & n_3(\mathbf{s}_m) & 0 \end{pmatrix} . \tag{7}$$

At U-interface (Figure 3a), we consider a boundary condition $\langle BC \rangle$

$$\langle BC \rangle : \ \mathbf{C}\,\mathbf{R}(\mathbf{s}_1)\,\mathbf{u}(\mathbf{s}_1, \omega) = \mathbf{J}\,\mathbf{C}\,\mathbf{R}(\mathbf{s}_2)\,\mathbf{u}(\mathbf{s}_2, \omega) \ , \tag{8}$$

where

$$\mathbf{C} = \begin{bmatrix} 0 & 0 & 1 & 0 \\ 0 & 0 & 0 & 1 \end{bmatrix} , \tag{9}$$

$$\mathbf{R}(\mathbf{s}_m) = \begin{bmatrix} \mathbf{i}_1(\mathbf{s}_m)\cdot\bar{\mathbf{i}}_1 & \mathbf{i}_1(\mathbf{s}_m)\cdot\bar{\mathbf{i}}_2 & \mathbf{i}_1(\mathbf{s}_m)\cdot\bar{\mathbf{i}}_3 & 0 \\ \mathbf{i}_2(\mathbf{s}_m)\cdot\bar{\mathbf{i}}_1 & \mathbf{i}_2(\mathbf{s}_m)\cdot\bar{\mathbf{i}}_2 & \mathbf{i}_2(\mathbf{s}_m)\cdot\bar{\mathbf{i}}_3 & 0 \\ \mathbf{i}_3(\mathbf{s}_m)\cdot\bar{\mathbf{i}}_1 & \mathbf{i}_3(\mathbf{s}_m)\cdot\bar{\mathbf{i}}_2 & \mathbf{i}_3(\mathbf{s}_m)\cdot\bar{\mathbf{i}}_3 & 0 \\ 0 & 0 & 0 & 1 \end{bmatrix} , \tag{10}$$

$\mathbf{u}(\mathbf{s}_m, \omega)$ is the limit value of vector $\mathbf{u}(\mathbf{x}_m, \omega)$, $\mathbf{J} = \begin{bmatrix} -1 & 0 \\ 0 & 1 \end{bmatrix}$, $(\bar{\mathbf{i}}_1, \bar{\mathbf{i}}_2, \bar{\mathbf{i}}_3)$ is the global Cartesian basis independent on point $\mathbf{s}_m$ and $(\mathbf{i}_1(\mathbf{s}_m), \mathbf{i}_2(\mathbf{s}_m), \mathbf{n}(\mathbf{s}_m))$ is the local basis dependent on point $\mathbf{s}_m$.

Equation (4), the radiation conditions $\langle RC \rangle_m$ in (6) and the boundary condition $\langle BC \rangle$ in (8) form the correct statement of the forward problem for U-model

$$\begin{cases} \mathbf{D}_{\mathbf{x}_m}\, \mathbf{u}(\mathbf{x}_m, \omega) + \mathbf{M}_m(\omega)\, \mathbf{u}(\mathbf{x}_m, \omega) = \mathbf{f}(\mathbf{x}_m, \omega), \\ \langle RC \rangle_m : \displaystyle\iint_{\mathbb{S}_m^\infty} \mathbf{F}(\mathbf{x}_m, \mathbf{s}_m, \omega)\, \mathbf{N}(\mathbf{s}_m)\, \mathbf{u}(\mathbf{s}_m, \omega)\, dS(\mathbf{s}_m) = 0, \qquad m = 1, 2, \\ \langle BC \rangle : \; \mathbf{C}\,\mathbf{R}(\mathbf{s}_1)\, \mathbf{u}(\mathbf{s}_1, \omega) = \mathbf{J}\,\mathbf{C}\,\mathbf{R}(\mathbf{s}_2)\, \mathbf{u}(\mathbf{s}_2, \omega). \end{cases} \tag{11}$$

W-model

The second of the considered models is a 2-block model with a cylindrical W-boundary (Figure 4), concave inside the half-space. The material parameters of the domains and the geometrical parameters of the interface are chosen to imitate a salt overhang surrounded by sediments. A strong velocity contrast imitates shadow below the overhang.

W-model consists of two homogeneous acoustic domains (Figure 5a), $\mathbb{D}_1$ and $\mathbb{D}_2$, separated by W-interface composed from four plane faces connected by three edges. A point source is placed at point ($x = 4.0\,\text{km}, y = 0\,\text{km}, z = 1.0\,\text{km}$). Radius-vectors $\mathbf{x}_m$ designate an arbitrary point in $\mathbb{D}_m$, $m = 1, 2$. Parameters of domain $\mathbb{D}_1$ are: P-wave velocity $v_{P,1} = 2.0\,\text{km}/\text{sec}$ and density $\rho_1 = 2.0\,\text{g}/\text{cm}^3$. Parameters of domain $\mathbb{D}_2$ are: P-wave velocity $v_{P,2} = 4.0\,\text{km}/\text{sec}$ and density $\rho_2 = 3.0\,\text{g}/\text{cm}^3$.

W-interface is considered as a two-sided surface with sides $\mathbb{S}_m(\mathbf{s}_m)$ (Figure 5a), where $m = 1, 2$ is the domain number. Radius-vector $\mathbf{s}_m$ denotes either a boundary point on $\mathbb{S}_m$ or a point in $\mathbb{D}_m$ which is infinitesimally close to $\mathbf{s}_m$. We denote the infinite parts of the interface as $\mathbb{S}_m^\infty$. The faces of the interface are denoted as $\mathbb{S}^j$, $j = 1, 2, 3, 4$. The normal vectors are directed inwards domains $\mathbb{D}_m$ and denoted as $\mathbf{n}(\mathbf{s}_m^j)$, $\mathbf{s}_m^j \in \mathbb{S}_m^j$, where the lower index denotes the medium number and the upper index denotes the face number. The upper $\mathbb{S}_m^1$ and second $\mathbb{S}_m^2$ faces are defined by formula $z = \pm 0.41(4 - x)$ and form the upper concave V_1-shaped wedge with the edge at $x = 4.0\,\text{km}$ and $z = 0\,\text{km}$. The third $\mathbb{S}_m^3$ and lowest $\mathbb{S}_m^4$ faces are defined by formula $z = \pm 0.41(4 - x) - 1$ and form the lower concave V_2-shaped wedge with the edge at $x = 4.0\,\text{km}$ and $z = -1\,\text{km}$.

101 receivers are spread along a horizontal straight line: from $x = 3.25\,\text{km}$ to $x = 4.75\,\text{km}$ with step $\vartriangle x = 0.015\,\text{km}$ at $y = 0\,\text{km}$ and $z < -2.0\,\text{km}$. The receiver line intersects the shadow boundary of the source spherical wavefield at $x = 4.0\,\text{km}$. The receivers for $x < 4\,\text{km}$ are located in the shadow zone and the receivers for $x > 4\,\text{km}$ are in the illuminated zone.

In domains $\mathbb{D}_m$, we consider the same equation (4) and the same radiation condition $\langle RC \rangle_m$ from (6).

At the cylindrical surfaces $\mathbb{S}_1^{\mathbb{E}_{12}} \cup \mathbb{S}_2^{\mathbb{E}_{12}}$, $\mathbb{S}_1^{\mathbb{E}_{23}} \cup \mathbb{S}_2^{\mathbb{E}_{23}}$ and $\mathbb{S}_1^{\mathbb{E}_{34}} \cup \mathbb{S}_2^{\mathbb{E}_{34}}$ surrounding the three edges $\mathbb{E}_{12}$, $\mathbb{E}_{23}$ and $\mathbb{E}_{34}$ of W-boundary (Figure 5a), vector (2) satisfies the six edge conditions $\langle EC \rangle_m^{12}$, $\langle EC \rangle_m^{23}$ and $\langle EC \rangle_m^{34}$, $m = 1,2$

$$\langle EC \rangle_m^{j\,j+1} : \quad \iint\limits_{\mathbb{S}_m^{\mathbb{E}_{j\,j+1}}} \mathbf{F}(\mathbf{x}_m, \mathbf{s}_m, \omega)\, \mathbf{N}(\mathbf{s}_m)\, \mathbf{u}(\mathbf{s}_m, \omega)\, dS(\mathbf{s}_m) = 0\,, \quad m = 1,2, \quad j = 1,2,3 \tag{12}$$

in terms of the feasible surface integral operators with the feasible fundamental solution in the kernel similar to (6) from A.A. Ayzenberg *et al.* (2015)/Chapter 3 of this thesis.

At the four faces $\mathbb{S}^j$, $j = 1,2,3,4$, of W-interface (Figure 5a), we consider four boundary conditions

$$\langle BC \rangle^j : \quad \mathbf{C}\,\mathbf{R}(\mathbf{s}_1^j)\,\mathbf{u}(\mathbf{s}_1^j, \omega) = \mathbf{J}\,\mathbf{C}\,\mathbf{R}(\mathbf{s}_2^j)\,\mathbf{u}(\mathbf{s}_2^j, \omega), \quad j = 1,2,3,4, \tag{13}$$

where matrices $\mathbf{C}$ and $\mathbf{R}(\mathbf{s}_m^j)$ are defined according with formulae (9) and (10).

Equation (4), the two radiation conditions $\langle RC \rangle_m$ from (6), the six edge conditions $\langle EC \rangle_m^{12}$, $\langle EC \rangle_m^{23}$ and $\langle EC \rangle_m^{34}, m = 1,2$, in formula (12), and the four boundary conditions $\langle BC \rangle^j$, $j = 1,2,3,4$, in formula (13), form the correct statement of the forward problem for W-model

$$\begin{cases} \mathbf{D}_{\mathbf{x}_m}\, \mathbf{u}\left(\mathbf{x}_m, \omega\right) + \mathbf{M}_m\left(\omega\right) \mathbf{u}\left(\mathbf{x}_m, \omega\right) = \mathbf{f}\left(\mathbf{x}_m, \omega\right), \quad m = 1,2\,, \\ \langle RC \rangle_m : \quad \iint\limits_{\mathbb{S}_m^{\infty}} \mathbf{F}\left(\mathbf{x}_m, \mathbf{s}_m, \omega\right) \mathbf{N}(\mathbf{s}_m)\, \mathbf{u}\left(\mathbf{s}_m, \omega\right) dS(\mathbf{s}_m) = 0\,, \quad m = 1,2\,, \\ \langle EC \rangle_m^{j\, j+1} : \quad \iint\limits_{\mathbb{S}_m^{j\, j+1}} \mathbf{F}\left(\mathbf{x}_m, \mathbf{s}_m, \omega\right) \mathbf{N}(\mathbf{s}_m)\, \mathbf{u}\left(\mathbf{s}_m, \omega\right) dS(\mathbf{s}_m) = 0\,, \quad m = 1,2\,,\ j = 1,2,3\,, \\ \langle BC \rangle^j : \quad \mathbf{C}\,\mathbf{R}\left(\mathbf{s}_1^j\right) \mathbf{u}\left(\mathbf{s}_1^j, \omega\right) = \mathbf{J}\,\mathbf{C}\,\mathbf{R}\left(\mathbf{s}_2^j\right) \mathbf{u}\left(\mathbf{s}_2^j, \omega\right), \quad m = 1,2\,,\ j = 1,2,3,4\,. \end{cases} \tag{14}$$

4.4 Analytical solution by TPOT: source wavefield

The forward problems (11) and (14) has an explicit solution (Zaman (2000) and Chandler-Wilde *et al*. (2012))

$$\mathbf{u}(\mathbf{x}_1,\omega)=\mathbf{u}^{(0)}(\mathbf{x}_1,\omega)+\mathbf{u}^{sc}(\mathbf{x}_1,\omega) \ , \tag{15}$$

where $\mathbf{u}^{(0)}(\mathbf{x}_1,\omega)$ is the source wavefield and $\mathbf{u}^{sc}(\mathbf{x}_1,\omega)$ is the scattered wavefield. If we aim to compute the total wavefield $\mathbf{u}(\mathbf{x}_1,\omega)$ we could apply any modeling method, including numerical methods. But if we aim to describe the wavefield separate trerms we have to apply the proposed TPOT&TWSM method. In this paper, we focus on the source wavefield $\mathbf{u}^{(0)}(\mathbf{x}_1,\omega)$ description by TPOT&TWSM.

In the theory by Costabel & Dauge (1997), this term is written as follows. The incident wavefield radiated by a point source can be represented as a particular solution of equation (4) in the form of the volume integral

$$\mathbf{u}^{(0)}(\mathbf{x}_1,\omega)=\iiint\limits_{\mathbb{D}_1}\mathbf{F}\left(\mathbf{x}_1,\mathbf{y}_1,\omega\right)\mathbf{f}(\mathbf{y}_1,\omega)\,dV(\mathbf{y}_1) \tag{16}$$

with any fundamental solution $\mathbf{F}\left(\mathbf{x}_1,\mathbf{y}_1,\omega\right)$ of equation (4) as the integral kernel. However, we cannot use the Green's function $\mathbf{G}\left(\mathbf{x}_1,\mathbf{y}_1,\omega\right)$ for the unbounded homogeneous acoustic medium as the conventional kernel of integral (16) because this function can contain non-feasible parts in the shadow zones. We consider the incident wavefield (16) as the feasible source wavefield in the half-space of complex shape. As mentioned at the beginning of this Section, we cannot use any numerical method for the computation of $\mathbf{u}^{(0)}(\mathbf{x}_1,\omega)$ in formula (15). However, we can use formula (16). We do not bring the detailed derivations from Sections 4 and 5 from A.A. Ayzenberg *et al.* (2015)/Chapter 3 of this thesis.

Instead, we directly use the necessary formulae from A.A. Ayzenberg *et al.* (2015)/Chapter 3 of this thesis, where vector $\mathbf{u}^{(0)}(\mathbf{x}_1,\omega)$ in terms of particle motion is transformed to vector $\mathbf{a}^{(0)}\left(\overline{\mathbf{x}}_1,\omega\right)$ in terms of wave motion, and the following formulae are valid

$$\mathbf{a}^{(0)}\left(\overline{\mathbf{x}}_1,\omega\right)\cong\mathbf{a}^{\mathbf{G}}\left(\overline{\mathbf{x}}_1,\omega\right)+\mathbf{a}^{[1]}\left(\overline{\mathbf{x}}_1,\omega\right)\ , \tag{17}$$

where

$$\mathbf{a}^{\mathbf{G}}(\overline{\mathbf{x}}_1,\omega)=\iiint\limits_{\mathbb{D}_1}\left[\mathbf{C}_{\overline{\mathbf{x}}_1}\ \mathbf{H}(\overline{\mathbf{x}}_1,\overline{\mathbf{x}}_1',\omega)\right]^{-1}\mathbf{C}_{\overline{\mathbf{x}}_1'}\ \mathbf{G}\left(\overline{\mathbf{x}}_1',\mathbf{y}_1,\omega\right)\mathbf{f}(\mathbf{y}_1,\omega)\,dV(\mathbf{y}_1) \tag{18}$$

and

$$\mathbf{a}^{[1]}(\overline{\mathbf{x}}_1,\omega)=\left[\mathbf{P}_{\mathbf{G}}(\overline{\mathbf{x}}_1,\mathbf{s}_1^1,\omega)\quad \mathbf{P}_{\mathbf{G}}(\overline{\mathbf{x}}_1,\mathbf{s}_1^2,\omega)\right]\begin{bmatrix}\mathbf{P}_{h\,\mathbf{G}}(\mathbf{s}_1^1,\mathbf{s}_1^{1'},\omega) & \mathbf{P}_{h\,\mathbf{G}}(\mathbf{s}_1^1,\mathbf{s}_1^{2'},\omega)\\ \mathbf{P}_{h\,\mathbf{G}}(\mathbf{s}_1^2,\mathbf{s}_1^{1'},\omega) & \mathbf{P}_{h\,\mathbf{G}}(\mathbf{s}_1^2,\mathbf{s}_1^{2'},\omega)\end{bmatrix}\begin{pmatrix}\mathbf{a}^{\mathbf{G}}(\mathbf{s}_1^{1'},\omega)\\ \mathbf{a}^{\mathbf{G}}(\mathbf{s}_1^{2'},\omega)\end{pmatrix}\ , \tag{19}$$

$$\begin{aligned}\mathbf{a}^{[1]}(\overline{\mathbf{x}}_1,\omega)=&\left[\mathbf{P}_{\mathbf{G}}(\overline{\mathbf{x}}_1,\mathbf{s}_1^1,\omega)\quad \mathbf{P}_{\mathbf{G}}(\overline{\mathbf{x}}_1,\mathbf{s}_1^2,\omega)\quad \mathbf{P}_{\mathbf{G}}(\overline{\mathbf{x}}_1,\mathbf{s}_1^3,\omega)\quad \mathbf{P}_{\mathbf{G}}(\overline{\mathbf{x}}_1,\mathbf{s}_1^4,\omega)\right]\times\\ &\times\begin{bmatrix}\mathbf{P}_{h\,\mathbf{G}}(\mathbf{s}_1^1,\mathbf{s}_1^{1'},\omega) & \mathbf{P}_{h\,\mathbf{G}}(\mathbf{s}_1^1,\mathbf{s}_1^{2'},\omega) & \mathbf{P}_{h\,\mathbf{G}}(\mathbf{s}_1^1,\mathbf{s}_1^{3'},\omega) & \mathbf{P}_{h\,\mathbf{G}}(\mathbf{s}_1^1,\mathbf{s}_1^{4'},\omega)\\ \mathbf{P}_{h\,\mathbf{G}}(\mathbf{s}_1^2,\mathbf{s}_1^{1'},\omega) & \mathbf{P}_{h\,\mathbf{G}}(\mathbf{s}_1^2,\mathbf{s}_1^{2'},\omega) & \mathbf{P}_{h\,\mathbf{G}}(\mathbf{s}_1^2,\mathbf{s}_1^{3'},\omega) & \mathbf{P}_{h\,\mathbf{G}}(\mathbf{s}_1^2,\mathbf{s}_1^{4'},\omega)\\ \mathbf{P}_{h\,\mathbf{G}}(\mathbf{s}_1^3,\mathbf{s}_1^{1'},\omega) & \mathbf{P}_{h\,\mathbf{G}}(\mathbf{s}_1^3,\mathbf{s}_1^{2'},\omega) & \mathbf{P}_{h\,\mathbf{G}}(\mathbf{s}_1^3,\mathbf{s}_1^{3'},\omega) & \mathbf{P}_{h\,\mathbf{G}}(\mathbf{s}_1^3,\mathbf{s}_1^{4'},\omega)\\ \mathbf{P}_{h\,\mathbf{G}}(\mathbf{s}_1^4,\mathbf{s}_1^{1'},\omega) & \mathbf{P}_{h\,\mathbf{G}}(\mathbf{s}_1^4,\mathbf{s}_1^{2'},\omega) & \mathbf{P}_{h\,\mathbf{G}}(\mathbf{s}_1^4,\mathbf{s}_1^{3'},\omega) & \mathbf{P}_{h\,\mathbf{G}}(\mathbf{s}_1^4,\mathbf{s}_1^{4'},\omega)\end{bmatrix}\times\\ &\times\begin{pmatrix}\mathbf{a}^{\mathbf{G}}(\mathbf{s}_1^{1'},\omega)\\ \mathbf{a}^{\mathbf{G}}(\mathbf{s}_1^{2'},\omega)\\ \mathbf{a}^{\mathbf{G}}(\mathbf{s}_1^{3'},\omega)\\ \mathbf{a}^{\mathbf{G}}(\mathbf{s}_1^{4'},\omega)\end{pmatrix}.\end{aligned} \tag{20}$$

For U-model, we apply formulae (17)-(19); and for W-model, we apply formulae (17), (18) and (20). These formulae will be used for TWSM computation of (16).

4.5 Reduction of the source wavefield representation to formulae of the edge wave theory. U-model

For the U-model seismogram control, we will compare the feasible source wavefield with the results of the edge wave theory by A.M. Aizenberg (1982) and A.M. Aizenberg (1993).

We consider the receiver line as a line on a plane surface with the normal vector directed along axis z. We define the Cartesian coordinates as follows

$$\mathbf{x}_1 = \left(\overline{\mathbf{x}}_1, (x_1)_3\right), \quad \overline{\mathbf{x}}_1 = \left((x_1)_1, (x_1)_2\right). \tag{21}$$

Everywhere further in this paper, we omit the domain index since we consider only domain $\mathbb{D}_1$ ($m=1$). Also for simplicity, we further write the upper indeces in the lower positions. In addition, we omit reduction to the lower dimension, and we omit frequency. So everywhere further, we have the notation

$$\begin{aligned} &(\cdot)_1^j \equiv (\cdot)_j , \\ &\overline{\cdot} \equiv \cdot , \\ &(\cdot,\omega) \equiv (\cdot) . \end{aligned} \tag{22}$$

Therefore, we rewrite the wave vector (17) in the form

$$\mathbf{a}^{(0)}(\mathbf{x}) = \begin{pmatrix} 0 \\ a^{(0)-}(\mathbf{x}) \end{pmatrix} = \mathbf{a}^{\mathbf{G}}(\mathbf{x}) + \mathbf{a}^{[1]}(\mathbf{x}) = \begin{pmatrix} 0 \\ a^{\mathbf{G}-}(\mathbf{x}) \end{pmatrix} + \begin{pmatrix} 0 \\ a^{[1]-}(\mathbf{x}) \end{pmatrix}. \tag{23}$$

Vector (18) has the block form

$$\mathbf{a}^{\mathbf{G}}(\mathbf{x}) = \begin{pmatrix} 0 \\ p_{\mathbf{G}}(\mathbf{x}) \exp\left[i\, k_P\, l(\mathbf{x})\right] \end{pmatrix} , \tag{24}$$

where $l(\mathbf{x})$ is the distance along the ray trajectory ‘source - receiver’, $p_{\mathbf{G}}(\mathbf{x}) = \dfrac{C\rho}{l(\mathbf{x})}\psi(\omega)$ is the spherical wave amplitude, ρ is medium density, C is source intensity.

The propagation operator from formula (19) acting from the faces to the receiver line is

$$\left[\mathbf{P_G}(\overline{\mathbf{x}}_1, \mathbf{s}_1^1, \omega) \quad \mathbf{P_G}(\overline{\mathbf{x}}_1, \mathbf{s}_1^2, \omega)\right] = \left[\mathbf{P_G}(\mathbf{x}, \mathbf{s}_1) \quad \mathbf{P_G}(\mathbf{x}, \mathbf{s}_2)\right] \tag{25}$$

Since faces $\mathbb{S}_1$ and $\mathbb{S}_2$ are curved surfaces, the shadow function $h(\mathbf{s}, \mathbf{s}')$ for U-shape boundary has the properties (Figure 3b)

$$\begin{aligned} &h(\mathbf{s}_1, \mathbf{s}_2) = h(\mathbf{s}_2, \mathbf{s}_1) = 1\,, \\ &h(\mathbf{s}_1, \mathbf{s}_1') = \begin{cases} 1, & \mathbf{s}_1 \neq \mathbf{s}_1'\,, \\ 0, & \mathbf{s}_1 = \mathbf{s}_1'\,, \end{cases} \\ &h(\mathbf{s}_2, \mathbf{s}_2') = \begin{cases} 1, & \mathbf{s}_2 \neq \mathbf{s}_2'\,, \\ 0, & \mathbf{s}_2 = \mathbf{s}_2'\,. \end{cases} \end{aligned} \tag{26}$$

Using the shadow functions (26), we obtain the absorption matrix from (19) in the form

$$\begin{bmatrix} \mathbf{P}_{h\,\mathbf{G}}(\mathbf{s}_1^1, \mathbf{s}_1^{1'}, \omega) & \mathbf{P}_{h\,\mathbf{G}}(\mathbf{s}_1^1, \mathbf{s}_1^{2'}, \omega) \\ \mathbf{P}_{h\,\mathbf{G}}(\mathbf{s}_1^2, \mathbf{s}_1^{1'}, \omega) & \mathbf{P}_{h\,\mathbf{G}}(\mathbf{s}_1^2, \mathbf{s}_1^{2'}, \omega) \end{bmatrix} = \begin{bmatrix} \mathbf{P}_{h\,\mathbf{G}}(\mathbf{s}_1, \mathbf{s}_1') & \mathbf{P_G}(\mathbf{s}_1, \mathbf{s}_2') \\ \mathbf{P_G}(\mathbf{s}_2, \mathbf{s}_1') & \mathbf{P}_{h\,\mathbf{G}}(\mathbf{s}_2, \mathbf{s}_2') \end{bmatrix}. \tag{27}$$

As the action of the submatrices $\mathbf{P}_{h\,\mathbf{G}}(\mathbf{s}_1, \mathbf{s}_1')$ and $\mathbf{P_G}(\mathbf{s}_1, \mathbf{s}_2')$ describe back scattering, that gives negligibly weak contribution at the receivers, we can say that the conditions $\mathbf{P}_{h\,\mathbf{G}}(\mathbf{s}_1, \mathbf{s}_1') \cong \mathbf{O}$ and $\mathbf{P_G}(\mathbf{s}_1, \mathbf{s}_2') \cong \mathbf{O}$ are valid. Hence, the absorption matrix (27) has got the final form

$$\begin{bmatrix} \mathbf{P}_{h\,\mathbf{G}}(\mathbf{s}_1, \mathbf{s}_1') & \mathbf{P_G}(\mathbf{s}_1, \mathbf{s}_2') \\ \mathbf{P_G}(\mathbf{s}_2, \mathbf{s}_1') & \mathbf{P}_{h\,\mathbf{G}}(\mathbf{s}_2, \mathbf{s}_2') \end{bmatrix} = \begin{bmatrix} \mathbf{O} & \mathbf{O} \\ \mathbf{P_G}(\mathbf{s}_2, \mathbf{s}_1') & \mathbf{P}_{h\,\mathbf{G}}(\mathbf{s}_2, \mathbf{s}_2') \end{bmatrix}. \tag{28}$$

The wave vector in (19) is rewritten in the form, which represents the source spherical wave at the four faces of the boundary

$$\begin{pmatrix} \mathbf{a}^{\mathbf{G}}(\mathbf{s}_1^{1\prime},\omega) \\ \mathbf{a}^{\mathbf{G}}(\mathbf{s}_1^{2\prime},\omega) \end{pmatrix} = \begin{pmatrix} \mathbf{a}^{\mathbf{G}}(\mathbf{s}_1) \\ \mathbf{a}^{\mathbf{G}}(\mathbf{s}_2) \end{pmatrix}, \quad \mathbf{s}_1 \in \mathbb{S}_1, \mathbf{s}_2 \in \mathbb{S}_2 \,. \tag{29}$$

We notice that vectors $\mathbf{a}^{\mathbf{G}}(\mathbf{s}_1)$ and $\mathbf{a}^{\mathbf{G}}(\mathbf{s}_2)$ do not account for the shadow as if we would consider the free space model without the wedge. These vectors are

$$\mathbf{a}^{\mathbf{G}}(\mathbf{s}_1) = \begin{pmatrix} 0 \\ p_{\mathrm{G}}(\mathbf{s}_1)\exp\left[i\,k_P\,l(\mathbf{s}_1)\right] \end{pmatrix}, \quad \mathbf{a}^{\mathbf{G}}(\mathbf{s}_2) = \begin{pmatrix} p_{\mathrm{G}}(\mathbf{s}_2)\exp\left[i\,k_P\,l(\mathbf{s}_2)\right] \\ 0 \end{pmatrix}, \tag{30}$$

After completing all the multiplications in formula (19) and accounting for formulae (25), (28) and (29), we obtain vector (19) expressed by the matrices and columns at the faces in the form

$$\mathbf{a}^{[1]}(\mathbf{x}) = \mathbf{a}^{[1]}_{\mathbb{S}_2\mathbb{S}_1}(\mathbf{x}) + \mathbf{a}^{[1]}_{\mathbb{S}_2\mathbb{S}_2}(\mathbf{x}), \tag{31}$$

where

$$\mathbf{a}^{[1]}_{\mathbb{S}_2\mathbb{S}_1}(\mathbf{x}) = \mathbf{P}_{\mathbf{G}}(\mathbf{x},\mathbf{s}_2)\,\mathbf{P}_{\mathbf{G}}(\mathbf{s}_2,\mathbf{s}_1)\,\mathbf{a}^{\mathbf{G}}(\mathbf{s}_1) \tag{32}$$

and

$$\mathbf{a}^{[1]}_{\mathbb{S}_2\mathbb{S}_2}(\mathbf{x}) = \mathbf{P}_{\mathbf{G}}(\mathbf{x},\mathbf{s}_2')\,\mathbf{P}_{h\,\mathbf{G}}(\mathbf{s}_2',\mathbf{s}_2)\,\mathbf{a}^{\mathbf{G}}(\mathbf{s}_2) \;. \tag{33}$$

Vectors (32) and (33) have the form of double integration over the two semi-infinite curved faces with ‘edges’. By ‘edge’ we mean line (4.0, 0, y). In formula (32), the internal integration is over face $\mathbb{S}_1$ and the external integration is over face $\mathbb{S}_2$. In formula (33), both the internal and external integration are over face $\mathbb{S}_2$. Edges $\mathbb{E}_1$ and $\mathbb{E}_2$ of faces $\mathbb{S}_1$ and $\mathbb{S}_2$ are infinitesimally close to each other. The common edge of faces $\mathbb{S}_1$ and $\mathbb{S}_2$ belongs to the plane of the secondary shadow for the single (primary) edge wave generated at edge $\mathbb{E}_1$. Then, the double (secondary) edge wave is generated at edge $\mathbb{E}_2$.

Formula (32) is similar to formula (53) in A.A. Ayzenberg *et al*. (2015)/Chapter 3 of this thesis, but it is applied here for U-boundary, not V-boundary. Therefore, we can use it here. Omitting calculations, we represent formula (32) in the form

$$\mathbf{a}^{[1]}_{\mathbb{S}_2\mathbb{S}_1}(\mathbf{x}) = \mathbf{a}^{[1]}_{\mathbf{G}}(\mathbf{x}) + \mathbf{a}^{[1]}_{\mathbb{E}_2}(\mathbf{x}) + \mathbf{a}^{[1]}_{\mathbb{E}_1}(\mathbf{x}) + \mathbf{a}^{[1]}_{\mathbb{E}_2\mathbb{E}_1}(\mathbf{x}) \;, \tag{34}$$

where the terms are described by formulae (61), (62), (65) and (66) from A.A. Ayzenberg *et al*. (2015)/Chapter 3 of this thesis. In the shadow zone, the double-diffraction term (34) consists of the direct spherical wave with negative amplitude $\mathbf{a}^{[1]}_{\mathbf{G}}(\mathbf{x})$, the single edge waves $\mathbf{a}^{[1]}_{\mathbb{E}_1}(\mathbf{x})$ and $\mathbf{a}^{[1]}_{\mathbb{E}_2}(\mathbf{x})$ and the double edge wave $\mathbf{a}^{[1]}_{\mathbb{E}_2\mathbb{E}_1}(\mathbf{x})$. In the illuminated zone, the double-diffraction term (34) consists of the single edge wave $\mathbf{a}^{[1]}_{\mathbb{E}_2}(\mathbf{x})$ and the double edge wave $\mathbf{a}^{[1]}_{\mathbb{E}_2\mathbb{E}_1}(\mathbf{x})$.

Formula (33) represents the effect of the creeping wave which is an additional wave in case of the curved U-shaped boundary. The creeping wave is the difference between the wavefield at the U-shaped boundary (formula (31)) and the V-shaped boundary (formula (32)). We note that we only take the first term in the creeping wave. We think that we probably have to account for higher terms in some of models. We leave this question for further investigations.

In formula (23), the nonzero component of the feasible source wavefield at the receivers is represented in the form

$$a^{(0)-}(\mathbf{x}) = a^{\mathbf{G}-}(\mathbf{x}) + a^{[1]-}(\mathbf{x}) \;, \tag{35}$$

where $a^{\mathbf{G}-}(\mathbf{x})$ is the conventional source wavefield which propagates not accounting for the shadow zones. It has the form of the nonzero component in (24)

$$a^{\mathbf{G}-}(\mathbf{x}) = p_{\mathbf{G}}(\mathbf{x}) \exp\left[i k_P\, l(\mathbf{x})\right]. \tag{36}$$

The nonzero component of the first-term approximation of the cascade diffraction wavefield in (23) can be represented in the form

$$a^{[1]-}(\mathbf{x}) = a^{[1]-}_{\mathbb{S}_2\mathbb{S}_1}(\mathbf{x}) + a^{[1]-}_{\mathbb{S}_2\mathbb{S}_2}(\mathbf{x}). \tag{37}$$

Equation (37) is the nonzero component of equation (31). The first term in (37) can be represented in the form

$$a^{[1]-}_{\mathbb{S}_2\mathbb{S}_1}(\mathbf{x}) = a^{[1]-}_{\mathbf{G}}(\mathbf{x}) + a^{[1]-}_{\mathbb{E}_2}(\mathbf{x}) + a^{[1]-}_{\mathbb{E}_1}(\mathbf{x}) + a^{[1]-}_{\mathbb{E}_2\mathbb{E}_1}(\mathbf{x}) \ , \tag{38}$$

where the terms are the same as in formula (71) by A.A. Ayzenberg *et al*. (2015)/Chapter 3 of this thesis. In the shadow zone, the double-diffraction term (38) consists of the source spherical wave with negative amplitude $a^{[1]-}_{\mathbf{G}}(\mathbf{x})$, the single edge waves $a^{[1]-}_{\mathbb{E}_1}(\mathbf{x})$ and $a^{[1]-}_{\mathbb{E}_2}(\mathbf{x})$ and the double edge wave $a^{[1]-}_{\mathbb{E}_2\mathbb{E}_1}(\mathbf{x})$. In the illuminated zone, the double-diffraction term (38) consists of the single edge wave $a^{[1]-}_{\mathbb{E}_2}(\mathbf{x})$ and the double edge wave $a^{[1]-}_{\mathbb{E}_2\mathbb{E}_1}(\mathbf{x})$. We notice that formula (38) is the nonzero component of formula (34).

The second term $a^{[1]-}_{\mathbb{S}_2\mathbb{S}_2}(\mathbf{x})$ in formula (37) represents the first term of the creeping wave and is the nonzero component of (33). Here, we do not consider the other terms of the creeping wave.

4.6 Verification of TWSM-seismograms by the edge wave theory. U-model

Parabolic boundary

Figure 6a illustrates the scalar component $a^{(0)-}(\mathbf{x},t)$ of formula (35) at the receiver line. Figure 6b represents component $a^{\mathbf{G}-}(\mathbf{x},t)$ of formula (36), which is the source spherical wave at the receiver line. This wave does not depend of the shape of the boundary. Figure 6c illustrates component $a^{[1]-}(\mathbf{x},t)$ in formula (37). The strong asymmetry of the diffraction amplitudes with respect to $x = 4\,\mathrm{km}$ can be explained by the effect of the creeping wave and the edge wave propagating from edge $\mathbb{E}_1$. We do not show term (38) because it is the same as for the V-shaped case in Figure 6c from A.A. Ayzenberg *et al*. (2015)/Chapter 3 of this thesis. Figure 6d illustrates the creeping term $a^{[1]-}_{\mathbb{S}_2\mathbb{S}_2}(\mathbf{x},t)$ from formula (37). In the shadow zone, we see a strong creeping wavefield with retarded traveltimes and the amplitudes increasing in the direction of the deep shadow. Figure 6e demonstrates the distribution of the computed $DAC^{(0)-}_{\mathrm{U}}(\mathbf{x})$ for $a^{(0)-}(\mathbf{x},t)$ using formula (75) from A.A. Ayzenberg *et al*. (2015)/Chapter 3 of this thesis and applying it for the U-shaped case at the receiver line. This $DAC^{(0)-}_{\mathrm{U}}(\mathbf{x})$ at the shadow boundary is equal to 0.56. The curve in Figure 6f represents the computed $DAC^{[1]-}_{\mathbb{S}_2\mathbb{S}_2}(\mathbf{x})$ for the creeping wave $a^{[1]-}_{\mathbb{S}_2\mathbb{S}_2}(\mathbf{x},t)$. This $DAC^{[1]-}_{\mathbb{S}_2\mathbb{S}_2}(\mathbf{x})$ at the shadow boundary is equal to 0.058. The computed $DAC^{(0)-}_{\mathrm{V}}(\mathbf{x}) = DAC^{(0)-}_{\mathrm{U}}(\mathbf{x}) + DAC^{[1]-}_{\mathbb{S}_2\mathbb{S}_2}(\mathbf{x}) = 0.618$ is different from the edge wave theory $DAC^{(0)-}_{\mathrm{V}}(\mathbf{x}) = 0.625$ (formula (86) in A.A. Ayzenberg *et al*. (2015)/Chapter 3 of this thesis) with the relative error of 1 percent approximately.

Hyperbolic boundary

Figure 7a illustrates the scalar component $a^{(0)-}(\mathbf{x},t)$ of formula (35) at the receiver line. Figure 7b demonstrates component $a^{\mathbf{G}-}(\mathbf{x},t)$ of formula (36), which is the source spherical wave at the receiver line. This wave does not depend of the shape of the boundary. Figure 7c illustrates component $a^{[1]-}(\mathbf{x},t)$ of formula (37). We do not show term (38) because it is the same as for the V-shaped case in Figure 7d from A.A. Ayzenberg *et al*. (2015)/Chapter 3 of this thesis. Figure 7d illustrates the creeping term $a^{[1]-}_{\mathbb{S}_2\mathbb{S}_2}(\mathbf{x},t)$ from formula (37). In the shadow zone, we see a strong creeping wavefield with retarded traveltimes and the amplitudes increasing in the direction of the deep shadow. We observe that the amplitudes of the creeping wavefield for the hyperbolic boundary are weaker than those for the parabolic boundary. This effect is explained by the amplitude dependence on the boundary curvature in the vicinity of the tangential ray. The closer radius of curvature is to 0, the weaker is the creeping wave and the closer to the wedge the model is. Figure 7e demonstrates the distribution of the computed $DAC^{(0)-}_{\mathrm{U}}(\mathbf{x})$ for $a^{(0)-}(\mathbf{x},t)$ using formula (75) from A.A. Ayzenberg *et al*. (2015)/Chapter 3 of this thesis and applying it for the U-shaped case at the receiver line. This $DAC^{(0)-}_{\mathrm{U}}(\mathbf{x})$ at the shadow boundary is equal to 0.551. The curve in Figure 7f represents the computed $DAC^{[1]-}_{\mathbb{S}_2\mathbb{S}_2}(\mathbf{x})$ for the creeping wave $a^{[1]-}_{\mathbb{S}_2\mathbb{S}_2}(\mathbf{x},t)$. This $DAC^{[1]-}_{\mathbb{S}_2\mathbb{S}_2}(\mathbf{x})$ at the shadow boundary is equal to 0.069. The computed $DAC^{(0)-}_{\mathrm{V}}(\mathbf{x})DAC^{(0)-}_{\mathrm{U}}(\mathbf{x})+DAC^{[1]-}_{\mathbb{S}_2\mathbb{S}_2}(\mathbf{x})=0.62$ is different from the edge wave theory $DAC^{(0)-}_{\mathrm{V}}(\mathbf{x})=0.625$ (formula (86) in A.A. Ayzenberg *et al*. (2015)/Chapter 3 of this thesis) with the relative error of 1 percent approximately.

4.7 Reduction of the source wavefield representation to formulae of the edge wave theory. W-model

For the W-seismogram control, we compare the feasible source wavefield with the results of the edge wave theory by A.M. Aizenberg (1982) and A.M. Aizenberg (1993).

We consider the receiver line as a line on a plane surface with the normal vector directed along axis z. We further in this paper apply the same simplifications as in (22).

We therefore rewrite the wave vector (17) in the block form

$$\mathbf{a}^{(0)}(\mathbf{x}) = \begin{pmatrix} 0 \\ a^{(0)-}(\mathbf{x}) \end{pmatrix} = \mathbf{a}^{\mathrm{G}}(\mathbf{x}) + \mathbf{a}^{[1]}(\mathbf{x}) = \begin{pmatrix} 0 \\ a^{\mathrm{G}-}(\mathbf{x}) \end{pmatrix} + \begin{pmatrix} 0 \\ a^{[1]-}(\mathbf{x}) \end{pmatrix}. \tag{39}$$

Vector (18) has the block form

$$\mathbf{a}^{\mathrm{G}}(\mathbf{x}) = \begin{pmatrix} 0 \\ p_{\mathrm{G}}(\mathbf{x}) \exp\left[i k_P \, l(\mathbf{x})\right] \end{pmatrix}, \tag{40}$$

where $l(\mathbf{x})$ is the distance along the ray trajectory 'source - receiver', $p_{\mathrm{G}}(\mathbf{x}) = \dfrac{C\rho}{l(\mathbf{x})} \psi(\omega)$ is the spherical wave amplitude, ρ is medium density, C is source intensity.

The propagation operator from formula (20), acting from the four faces to the receiver line, is

$$\begin{aligned} &\left[\mathbf{P}_{\mathrm{G}}(\overline{\mathbf{x}}_1, \mathbf{s}_1^1, \omega) \quad \mathbf{P}_{\mathrm{G}}(\overline{\mathbf{x}}_1, \mathbf{s}_1^2, \omega) \quad \mathbf{P}_{\mathrm{G}}(\overline{\mathbf{x}}_1, \mathbf{s}_1^3, \omega) \quad \mathbf{P}_{\mathrm{G}}(\overline{\mathbf{x}}_1, \mathbf{s}_1^4, \omega)\right] = \\ &= \left[\mathbf{P}_{\mathrm{G}}(\mathbf{x}, \mathbf{s}_1) \quad \mathbf{P}_{\mathrm{G}}(\mathbf{x}, \mathbf{s}_2) \quad \mathbf{P}_{\mathrm{G}}(\mathbf{x}, \mathbf{s}_3) \quad \mathbf{P}_{\mathrm{G}}(\mathbf{x}, \mathbf{s}_4)\right]. \end{aligned} \tag{41}$$

Since the shadow function $h(\mathbf{s}, \mathbf{s}')$ is equal to zero for points $\mathbf{s}$ and $\mathbf{s}'$ belonging to the same face or faces $\mathbb{S}_2$ and $\mathbb{S}_3$, the shadow function $h(\mathbf{s}, \mathbf{s}')$ for W-shape boundary has the properties (Figure 5b)

$$\begin{gathered}h(\mathbf{s}_1,\mathbf{s}_1')=h(\mathbf{s}_2,\mathbf{s}_2')=h(\mathbf{s}_3,\mathbf{s}_3')=h(\mathbf{s}_4,\mathbf{s}_4')=h(\mathbf{s}_2,\mathbf{s}_3')=h(\mathbf{s}_3,\mathbf{s}_2')=0\,,\\ h(\mathbf{s}_1,\mathbf{s}_2')=h(\mathbf{s}_1,\mathbf{s}_3')=h(\mathbf{s}_1,\mathbf{s}_4')=h(\mathbf{s}_2,\mathbf{s}_1')=h(\mathbf{s}_2,\mathbf{s}_4')=\\ =h(\mathbf{s}_3,\mathbf{s}_1')=h(\mathbf{s}_3,\mathbf{s}_4')=h(\mathbf{s}_4,\mathbf{s}_1')=h(\mathbf{s}_4,\mathbf{s}_2')=h(\mathbf{s}_4,\mathbf{s}_3')=1\,.\end{gathered}\tag{42}$$

Since faces $\mathbb{S}_1$, $\mathbb{S}_2$, $\mathbb{S}_3$ and $\mathbb{S}_4$ are plane, we obtain the absorption matrix from (20) reduced to the form

$$\begin{gathered}\begin{bmatrix}\mathbf{P}_{h\mathbf{G}}(\mathbf{s}_1^1,\mathbf{s}_1^{1'},\omega) & \mathbf{P}_{h\mathbf{G}}(\mathbf{s}_1^1,\mathbf{s}_1^{2'},\omega) & \mathbf{P}_{h\mathbf{G}}(\mathbf{s}_1^1,\mathbf{s}_1^{3'},\omega) & \mathbf{P}_{h\mathbf{G}}(\mathbf{s}_1^1,\mathbf{s}_1^{4'},\omega)\\ \mathbf{P}_{h\mathbf{G}}(\mathbf{s}_1^2,\mathbf{s}_1^{1'},\omega) & \mathbf{P}_{h\mathbf{G}}(\mathbf{s}_1^2,\mathbf{s}_1^{2'},\omega) & \mathbf{P}_{h\mathbf{G}}(\mathbf{s}_1^2,\mathbf{s}_1^{3'},\omega) & \mathbf{P}_{h\mathbf{G}}(\mathbf{s}_1^2,\mathbf{s}_1^{4'},\omega)\\ \mathbf{P}_{h\mathbf{G}}(\mathbf{s}_1^3,\mathbf{s}_1^{1'},\omega) & \mathbf{P}_{h\mathbf{G}}(\mathbf{s}_1^3,\mathbf{s}_1^{2'},\omega) & \mathbf{P}_{h\mathbf{G}}(\mathbf{s}_1^3,\mathbf{s}_1^{3'},\omega) & \mathbf{P}_{h\mathbf{G}}(\mathbf{s}_1^3,\mathbf{s}_1^{4'},\omega)\\ \mathbf{P}_{h\mathbf{G}}(\mathbf{s}_1^4,\mathbf{s}_1^{1'},\omega) & \mathbf{P}_{h\mathbf{G}}(\mathbf{s}_1^4,\mathbf{s}_1^{2'},\omega) & \mathbf{P}_{h\mathbf{G}}(\mathbf{s}_1^4,\mathbf{s}_1^{3'},\omega) & \mathbf{P}_{h\mathbf{G}}(\mathbf{s}_1^4,\mathbf{s}_1^{4'},\omega)\end{bmatrix}=\\ =\begin{bmatrix}\mathbf{O} & \mathbf{P}_{\mathbf{G}}(\mathbf{s}_1,\mathbf{s}_2') & \mathbf{P}_{\mathbf{G}}(\mathbf{s}_1,\mathbf{s}_3') & \mathbf{P}_{\mathbf{G}}(\mathbf{s}_1,\mathbf{s}_4')\\ \mathbf{P}_{\mathbf{G}}(\mathbf{s}_2,\mathbf{s}_1') & \mathbf{O} & \mathbf{O} & \mathbf{P}_{\mathbf{G}}(\mathbf{s}_2,\mathbf{s}_4')\\ \mathbf{P}_{\mathbf{G}}(\mathbf{s}_3,\mathbf{s}_1') & \mathbf{O} & \mathbf{O} & \mathbf{P}_{\mathbf{G}}(\mathbf{s}_3,\mathbf{s}_4')\\ \mathbf{P}_{\mathbf{G}}(\mathbf{s}_4,\mathbf{s}_1') & \mathbf{P}_{\mathbf{G}}(\mathbf{s}_4,\mathbf{s}_2') & \mathbf{P}_{\mathbf{G}}(\mathbf{s}_4,\mathbf{s}_3') & \mathbf{O}\end{bmatrix},\end{gathered}\tag{43}$$

where $\mathbf{O}$ is the zero matrix. As the action of the submatrices $\mathbf{P}_{\mathbf{G}}(\mathbf{s}_1,\mathbf{s}_2')$, $\mathbf{P}_{\mathbf{G}}(\mathbf{s}_1,\mathbf{s}_3')$, $\mathbf{P}_{\mathbf{G}}(\mathbf{s}_1,\mathbf{s}_4')$, $\mathbf{P}_{\mathbf{G}}(\mathbf{s}_2,\mathbf{s}_4')$ and $\mathbf{P}_{\mathbf{G}}(\mathbf{s}_3,\mathbf{s}_4')$ describes back scattering, that gives negligibly weak contribution at the receivers, we can say that they are zero-matrices. Hence, the absorption matrix (43) has got the final form

$$\begin{gathered}\begin{bmatrix}\mathbf{P}_{h\mathbf{G}}(\mathbf{s}_1^1,\mathbf{s}_1^{1'},\omega) & \mathbf{P}_{h\mathbf{G}}(\mathbf{s}_1^1,\mathbf{s}_1^{2'},\omega) & \mathbf{P}_{h\mathbf{G}}(\mathbf{s}_1^1,\mathbf{s}_1^{3'},\omega) & \mathbf{P}_{h\mathbf{G}}(\mathbf{s}_1^1,\mathbf{s}_1^{4'},\omega)\\ \mathbf{P}_{h\mathbf{G}}(\mathbf{s}_1^2,\mathbf{s}_1^{1'},\omega) & \mathbf{P}_{h\mathbf{G}}(\mathbf{s}_1^2,\mathbf{s}_1^{2'},\omega) & \mathbf{P}_{h\mathbf{G}}(\mathbf{s}_1^2,\mathbf{s}_1^{3'},\omega) & \mathbf{P}_{h\mathbf{G}}(\mathbf{s}_1^2,\mathbf{s}_1^{4'},\omega)\\ \mathbf{P}_{h\mathbf{G}}(\mathbf{s}_1^3,\mathbf{s}_1^{1'},\omega) & \mathbf{P}_{h\mathbf{G}}(\mathbf{s}_1^3,\mathbf{s}_1^{2'},\omega) & \mathbf{P}_{h\mathbf{G}}(\mathbf{s}_1^3,\mathbf{s}_1^{3'},\omega) & \mathbf{P}_{h\mathbf{G}}(\mathbf{s}_1^3,\mathbf{s}_1^{4'},\omega)\\ \mathbf{P}_{h\mathbf{G}}(\mathbf{s}_1^4,\mathbf{s}_1^{1'},\omega) & \mathbf{P}_{h\mathbf{G}}(\mathbf{s}_1^4,\mathbf{s}_1^{2'},\omega) & \mathbf{P}_{h\mathbf{G}}(\mathbf{s}_1^4,\mathbf{s}_1^{3'},\omega) & \mathbf{P}_{h\mathbf{G}}(\mathbf{s}_1^4,\mathbf{s}_1^{4'},\omega)\end{bmatrix}=\\ =\begin{bmatrix}\mathbf{O} & \mathbf{O} & \mathbf{O} & \mathbf{O}\\ \mathbf{P}_{\mathbf{G}}(\mathbf{s}_2,\mathbf{s}_1') & \mathbf{O} & \mathbf{O} & \mathbf{O}\\ \mathbf{P}_{\mathbf{G}}(\mathbf{s}_3,\mathbf{s}_1') & \mathbf{O} & \mathbf{O} & \mathbf{O}\\ \mathbf{P}_{\mathbf{G}}(\mathbf{s}_4,\mathbf{s}_1') & \mathbf{P}_{\mathbf{G}}(\mathbf{s}_4,\mathbf{s}_2') & \mathbf{P}_{\mathbf{G}}(\mathbf{s}_4,\mathbf{s}_3') & \mathbf{O}\end{bmatrix}.\end{gathered}\tag{44}$$

The wave vector in (20) is rewritten in the form which represents the source spherical wave at the four faces of the boundary

$$\mathbf{a}^{\mathrm{G}}(\mathbf{s})=\begin{pmatrix}\mathbf{a}^{\mathrm{G}}(\mathbf{s}_1)\\ \mathbf{a}^{\mathrm{G}}(\mathbf{s}_2)\\ \mathbf{a}^{\mathrm{G}}(\mathbf{s}_3)\\ \mathbf{a}^{\mathrm{G}}(\mathbf{s}_4)\end{pmatrix},\quad \mathbf{s}_1\in\mathbb{S}_1,\mathbf{s}_2\in\mathbb{S}_2,\mathbf{s}_3\in\mathbb{S}_3,\mathbf{s}_4\in\mathbb{S}_4\,. \tag{45}$$

We notice that vectors $\mathbf{a}^{\mathrm{G}}(\mathbf{s}_1)$, $\mathbf{a}^{\mathrm{G}}(\mathbf{s}_2)$, $\mathbf{a}^{\mathrm{G}}(\mathbf{s}_3)$ and $\mathbf{a}^{\mathrm{G}}(\mathbf{s}_4)$ do not account for the shadow as if we would consider the free space model without the wedges. These vectors are

$$\begin{gathered}\mathbf{a}^{\mathrm{G}}(\mathbf{s}_1)=\begin{pmatrix}0\\ p_{\mathrm{G}}(\mathbf{s}_1)\exp\left[i\,k_P\,l(\mathbf{s}_1)\right]\end{pmatrix},\quad \mathbf{a}^{\mathrm{G}}(\mathbf{s}_2)=\begin{pmatrix}p_{\mathrm{G}}(\mathbf{s}_2)\exp\left[i\,k_P\,l(\mathbf{s}_2)\right]\\ 0\end{pmatrix},\\ \mathbf{a}^{\mathrm{G}}(\mathbf{s}_3)=\begin{pmatrix}0\\ p_{\mathrm{G}}(\mathbf{s}_3)\exp\left[i\,k_P\,l(\mathbf{s}_3)\right]\end{pmatrix},\quad \mathbf{a}^{\mathrm{G}}(\mathbf{s}_4)=\begin{pmatrix}p_{\mathrm{G}}(\mathbf{s}_4)\exp\left[i\,k_P\,l(\mathbf{s}_4)\right]\\ 0\end{pmatrix}.\end{gathered} \tag{46}$$

After completing all the multiplications in formula (20) and accounting for formulae (41), (43) and (45), we obtain vector $\mathbf{a}^{[1]}(\mathbf{x})$, expressed by the matrices and the columns at the faces, as the sum of the five vectors

$$\mathbf{a}^{[1]}(\mathbf{x})=\mathbf{a}^{[1]}_{\mathbb{S}_2\mathbb{S}_1}(\mathbf{x})+\mathbf{a}^{[1]}_{\mathbb{S}_4\mathbb{S}_3}(\mathbf{x})+\mathbf{a}^{[1]}_{\mathbb{S}_4\mathbb{S}_2}(\mathbf{x})+\mathbf{a}^{[1]}_{\mathbb{S}_4\mathbb{S}_1}(\mathbf{x})+\mathbf{a}^{[1]}_{\mathbb{S}_3\mathbb{S}_1}(\mathbf{x})\,. \tag{47}$$

Accounting for identity $\mathbf{P}_{\mathbf{G}}(\mathbf{x},\mathbf{s}_3)\,\mathbf{P}_{\mathbf{G}}(\mathbf{s}_3,\mathbf{s}_1)+\mathbf{P}_{\mathbf{G}}(\mathbf{x},\mathbf{s}_4)\,\mathbf{P}_{\mathbf{G}}(\mathbf{s}_4,\mathbf{s}_1)=\mathbf{O}$, we obtain

$$\mathbf{a}^{[1]}_{\mathbb{S}_4\mathbb{S}_1}(\mathbf{x})+\mathbf{a}^{[1]}_{\mathbb{S}_3\mathbb{S}_1}(\mathbf{x})=\left[\mathbf{P}_{\mathbf{G}}(\mathbf{x},\mathbf{s}_3)\,\mathbf{P}_{\mathbf{G}}(\mathbf{s}_3,\mathbf{s}_1)+\mathbf{P}_{\mathbf{G}}(\mathbf{x},\mathbf{s}_4)\,\mathbf{P}_{\mathbf{G}}(\mathbf{s}_4,\mathbf{s}_1)\right]\mathbf{a}^{\mathrm{G}}(\mathbf{s}_1)=0\ . \tag{48}$$

Inserting (48) in (47), we obtain vector $\mathbf{a}^{[1]}(\mathbf{x})$, expressed by the matrices and the columns at the faces, as the sum of the three nonzero vectors

$$\mathbf{a}^{[1]}(\mathbf{x})=\mathbf{a}^{[1]}_{\mathbb{S}_2\mathbb{S}_1}(\mathbf{x})+\mathbf{a}^{[1]}_{\mathbb{S}_4\mathbb{S}_3}(\mathbf{x})+\mathbf{a}^{[1]}_{\mathbb{S}_4\mathbb{S}_2}(\mathbf{x})\ , \tag{49}$$

where

$$\mathbf{a}^{[1]}_{\mathbb{S}_2\mathbb{S}_1}(\mathbf{x}) = \mathbf{P_G}(\mathbf{x}, \mathbf{s}_2)\,\mathbf{P_G}(\mathbf{s}_2, \mathbf{s}_1)\,\mathbf{a}^{\mathbf{G}}(\mathbf{s}_1) \;, \tag{50}$$

$$\mathbf{a}^{[1]}_{\mathbb{S}_4\mathbb{S}_3}(\mathbf{x}) = \mathbf{P_G}(\mathbf{x}, \mathbf{s}_4)\,\mathbf{P_G}(\mathbf{s}_4, \mathbf{s}_3)\,\mathbf{a}^{\mathbf{G}}(\mathbf{s}_3) \;, \tag{51}$$

and

$$\mathbf{a}^{[1]}_{\mathbb{S}_4\mathbb{S}_2}(\mathbf{x}) = \mathbf{P_G}(\mathbf{x}, \mathbf{s}_4)\,\mathbf{P_G}(\mathbf{s}_4, \mathbf{s}_2)\,\mathbf{a}^{\mathbf{G}}(\mathbf{s}_2) \;. \tag{52}$$

Each vector (50), (51) and (52) has the form of double integration over the two half-infinite faces with the edges. In formula (50), the internal integration is over face $\mathbb{S}_1$ and the external integration is over face $\mathbb{S}_2$. Edges $\mathbb{E}_1$ and $\mathbb{E}_2$ of faces $\mathbb{S}_1$ and $\mathbb{S}_2$ are infinitesimally close to each other. In formula (51), the internal integration is over face $\mathbb{S}_3$ and the external integration is over face $\mathbb{S}_4$. Edges $\mathbb{E}_3$ and $\mathbb{E}_4$ of faces $\mathbb{S}_3$ and $\mathbb{S}_4$ are infinitesimally close to each other. In formula (52), the internal integration is over face $\mathbb{S}_2$ and the external integration is over face $\mathbb{S}_4$. Edges $\mathbb{E}_2$ and $\mathbb{E}_4$ of faces $\mathbb{S}_2$ and $\mathbb{S}_4$ are distant from each other and have a finite distance. Also, there are two infinitesimally close to each other edges of faces $\mathbb{S}_2$ and $\mathbb{S}_3$ that form a convex wedge. Since the influence of this wedge on the wavefield at the receiver line is not significant, we will not take it into account. Hence, from the point of view of the diffraction theory, we can say that each repeated surface integral in (50), (51) and (52) describes the solution of the canonical problem of the spherical wave diffraction at two absolutely absorbing half-planes, see details in Section 5.10 in Borovikov & Kinber (1994) and in the paper by Klem-Musatov & A.M. Aizenberg (1989).

Vector (50) performs the double diffraction at the two faces $\mathbb{S}_1$ and $\mathbb{S}_2$. Since these faces form a wedge, we can rewrite vector (50) in the form of equation (62) with source 1 and line 2 from A.A. Ayzenberg *et al*. (2015)/Chapter 3 of this thesis

$$\mathbf{a}^{[1]}_{\mathbb{S}_2\mathbb{S}_1}(\mathbf{x}) = \mathbf{a}^{[1]}_{\mathbf{G}}(\mathbf{x}) + \mathbf{a}^{[1]}_{\mathbb{E}_2}(\mathbf{x}) + \mathbf{a}^{[1]}_{\mathbb{E}_1}(\mathbf{x}) + \mathbf{a}^{[1]}_{\mathbb{E}_2\,\mathbb{E}_1}(\mathbf{x}) \;, \tag{53}$$

where the terms are described by formulae similar to (61), (62), (65) and (66) from A.A. Ayzenberg *et al*. (2015)/Chapter 3 of this thesis. Therefore, we can use formulae (67)-(69) and (80)-(84) from A.A. Ayzenberg *et al*. (2015)/Chapter 3 of this thesis in this case, accounting for the conditions at the shadow boundary: $w_1 \to 0$ and $u_1 \to 0$ with $u_1 / w_1 \to 0$, and $w_2 \to 0$ and $u_2 \to 0$ with $u_2 / w_2 \to const \neq 0$. In the shadow zone, the double-diffraction term (53) consists of the source spherical wave with negative amplitude $\mathbf{a}_{\mathbf{G}}^{(1)}(\mathbf{x})$, the single edge waves $\mathbf{a}_{\mathbb{E}_1}^{[1]}(\mathbf{x})$ and $\mathbf{a}_{\mathbb{E}_2}^{[1]}(\mathbf{x})$ and the double edge wave $\mathbf{a}_{\mathbb{E}_2\mathbb{E}_1}^{[1]}(\mathbf{x})$. In the illuminated zone, the double-diffraction term (53) consists of the single edge wave $\mathbf{a}_{\mathbb{E}_2}^{[1]}(\mathbf{x})$ and the double edge wave $\mathbf{a}_{\mathbb{E}_2\mathbb{E}_1}^{[1]}(\mathbf{x})$.

Vector (51) performs the double diffraction at the two faces $\mathbb{S}_3$ and $\mathbb{S}_4$. Since these faces form a wedge, we can rewrite vector (51) in the form of equation (64) with source 2 and line 1 from A.A. Ayzenberg *et al*. (2015)/Chapter 3 of this thesis

$$\mathbf{a}_{\mathbb{S}_4\mathbb{S}_3}^{[1]}(\mathbf{x}) = \mathbf{a}_{\mathbf{G}}^{[1]}(\mathbf{x}) + \mathbf{a}_{\mathbb{E}_4}^{[1]}(\mathbf{x}) + \mathbf{a}_{\mathbb{E}_3}^{[1]}(\mathbf{x}) + \mathbf{a}_{\mathbb{E}_4\mathbb{E}_3}^{[1]}(\mathbf{x}) , \tag{54}$$

where the terms in (54) are described by formulae similar to (61), (62), (65) and (66) from A.A. Ayzenberg *et al*. (2015)/Chapter 3 of this thesis. Therefore, we can use the analog to formulae (67)-(69) and (80)-(84) from A.A. Ayzenberg *et al*. (2015)/Chapter 3 of this thesis, accounting for the conditions at the shadow boundary: $w_1 \to 0$ and $u_1 \to 0$ with $u_1 / w_1 \to 0$, and $w_2 \to 0$ and $u_2 \to 0$ with $u_2 / w_2 \to const \neq 0$. In the shadow zone, the double-diffraction term (54) consists of the source spherical wave with negative amplitude $\mathbf{a}_{\mathbf{G}}^{[1]}(\mathbf{x})$, the single edge waves $\mathbf{a}_{\mathbb{E}_1}^{[1]}(\mathbf{x})$ and $\mathbf{a}_{\mathbb{E}_2}^{[1]}(\mathbf{x})$ and the double edge wave $\mathbf{a}_{\mathbb{E}_2\mathbb{E}_1}^{[1]}(\mathbf{x})$. In the illuminated zone, the double-diffraction term (54) consists of the single edge wave $\mathbf{a}_{\mathbb{E}_2}^{[1]}(\mathbf{x})$ and the double edge wave $\mathbf{a}_{\mathbb{E}_2\mathbb{E}_1}^{[1]}(\mathbf{x})$.

Vector (52) performs the double diffraction at the upper face $\mathbb{S}_2$ and the lower face $\mathbb{S}_4$. We notice that the distance between these faces is constant and nonzero. In spite of this, formula (64) from A.A. Ayzenberg *et al*. (2015)/Chapter 3 of this thesis in combination with formulae (61), (62), (65) and (66) from A.A. Ayzenberg *et al*. (2015)/Chapter 3 of this thesis is valid. We therefore rewrite formula (52) without detailed explanation in the form

$$\mathbf{a}^{[1]}_{\mathbb{S}_4\mathbb{S}_2}(\mathbf{x})=\mathbf{a}^{[1]}_{\mathbf{G}}(\mathbf{x})+\mathbf{a}^{[1]}_{\mathbb{E}_4}(\mathbf{x})+\mathbf{a}^{[1]}_{\mathbb{E}_2}(\mathbf{x})+\mathbf{a}^{[1]}_{\mathbb{E}_4\mathbb{E}_2}(\mathbf{x}) \; . \tag{55}$$

In the shadow zone, the double-diffraction term (55) consists of the source spherical wave with negative amplitude $\mathbf{a}^{[1]}_{\mathbf{G}}(\mathbf{x})$, the single edge waves $\mathbf{a}^{[1]}_{\mathbb{E}_1}(\mathbf{x})$ and $\mathbf{a}^{[1]}_{\mathbb{E}_2}(\mathbf{x})$ and the double edge wave $\mathbf{a}^{[1]}_{\mathbb{E}_2\mathbb{E}_1}(\mathbf{x})$. In the illuminated zone, the double-diffraction term (55) consists of the single edge wave $\mathbf{a}^{[1]}_{\mathbb{E}_2}(\mathbf{x})$ and the double edge wave $\mathbf{a}^{[1]}_{\mathbb{E}_2\mathbb{E}_1}(\mathbf{x})$.

Formulae (39) and (40) lead to that the nonzero component of the feasible source wavefield at the receivers can be represented in the form

$$a^{(0)-}(\mathbf{x})=a^{\mathbf{G}-}(\mathbf{x})+a^{[1]-}(\mathbf{x}) \; , \tag{56}$$

where $a^{\mathbf{G}-}(\mathbf{x})$ is the conventional source wavefield which doesn not account for the shadow zones. It has the form of the nonzero component in (40) which is similar to formula (36).

The nonzero component of the first-term approximation of the cascade diffraction wavefield in (56) can be represented in the form

$$a^{[1]-}(\mathbf{x})=a^{[1]-}_{\mathbb{S}_2\mathbb{S}_1}(\mathbf{x})+a^{[1]-}_{\mathbb{S}_4\mathbb{S}_3}(\mathbf{x})+a^{[1]-}_{\mathbb{S}_4\mathbb{S}_2}(\mathbf{x}). \tag{57}$$

Equation (57) is the nonzero component of equation (49).

The first term in (57) describes the diffraction at the V_1-shaped wedge and can be represented in the form

$$a^{[1]-}_{\mathbb{S}_2\mathbb{S}_1}(\mathbf{x})=a^{[1]-}_{\mathbf{G}}(\mathbf{x})+a^{[1]-}_{\mathbb{E}_2}(\mathbf{x})+a^{[1]-}_{\mathbb{E}_1}(\mathbf{x})+a^{[1]-}_{\mathbb{E}_2\mathbb{E}_1}(\mathbf{x}) \; , \tag{58}$$

where the terms are the same as in formula (71) from A.A. Ayzenberg *et al*. (2015)/Chapter 3 of this thesis. In the shadow zone, the double-diffraction term (58) consists of the source spherical wave with negative amplitude $a_{\mathbf{G}}^{[1]-}(\mathbf{x})$, the single edge waves $a_{\mathbb{E}_1}^{[1]-}(\mathbf{x})$ and $a_{\mathbb{E}_2}^{[1]-}(\mathbf{x})$ and the double edge wave $a_{\mathbb{E}_2\mathbb{E}_1}^{[1]-}(\mathbf{x})$. In the illuminated zone, the double-diffraction term (58) consists of the single edge wave $a_{\mathbb{E}_2}^{[1]-}(\mathbf{x})$ and the double edge wave $a_{\mathbb{E}_2\mathbb{E}_1}^{[1]-}(\mathbf{x})$. We notice that formula (58) is the nonzero component of formula (53).

The second term in (57) describes diffraction at the V_2-shaped wedge and can be represented in the form

$$a_{\mathbb{S}_4\mathbb{S}_3}^{[1]-}(\mathbf{x}) = a_{\mathbf{G}}^{[1]-}(\mathbf{x}) + a_{\mathbb{E}_4}^{[1]-}(\mathbf{x}) + a_{\mathbb{E}_3}^{[1]-}(\mathbf{x}) + a_{\mathbb{E}_4\mathbb{E}_3}^{[1]-}(\mathbf{x}) , \tag{59}$$

where the terms are the same as in formula (71) from A.A. Ayzenberg *et al*. (2015)/Chapter 3 of this thesis. In the shadow zone, the double-diffraction term (59) consists of the source spherical wave with negative amplitude $a_{\mathbf{G}}^{[1]-}(\mathbf{x})$, the single edge waves $a_{\mathbb{E}_3}^{[1]-}(\mathbf{x})$ and $a_{\mathbb{E}_4}^{[1]-}(\mathbf{x})$ and the double edge wave $a_{\mathbb{E}_4\mathbb{E}_3}^{[1]-}(\mathbf{x})$. In the illuminated zone, the double-diffraction term (59) consists of the single edge wave $a_{\mathbb{E}_4}^{[1]-}(\mathbf{x})$ and the double edge wave $a_{\mathbb{E}_4\mathbb{E}_3}^{[1]-}(\mathbf{x})$. We notice that formula (59) is the nonzero component of formula (54).

The third term $a_{\mathbb{S}_4\mathbb{S}_2}^{[1]-}(\mathbf{x})$ in formula (57) represents the double diffraction at the pair of faces $\mathbb{S}_2$ and $\mathbb{S}_4$. This term is represented as

$$a_{\mathbb{S}_4\mathbb{S}_2}^{[1]-}(\mathbf{x}) = a_{\mathbf{G}}^{[1]-}(\mathbf{x}) + a_{\mathbb{E}_4}^{[1]-}(\mathbf{x}) + a_{\mathbb{E}_2}^{[1]-}(\mathbf{x}) + a_{\mathbb{E}_4\mathbb{E}_2}^{[1]-}(\mathbf{x}) , \tag{60}$$

where the terms are the same as in formula (71) from A.A. Ayzenberg *et al*. (2015)/Chapter 3 of this thesis but for the faces distant from each other. In the shadow zone, the double-diffraction term (60) consists of the source spherical wave with negative amplitude $a_{\mathbf{G}}^{[1]-}(\mathbf{x})$, the single edge waves $a_{\mathbb{E}_2}^{[1]-}(\mathbf{x})$ and $a_{\mathbb{E}_4}^{[1]-}(\mathbf{x})$ and the double edge wave $a_{\mathbb{E}_4\mathbb{E}_2}^{[1]-}(\mathbf{x})$. In the illuminated zone, the double-diffraction term (60) consists of the single edge wave $a_{\mathbb{E}_4}^{[1]-}(\mathbf{x})$

and the double edge wave $a^{[1]-}_{\mathbb{E}_4\mathbb{E}_2}(\mathbf{x})$. We notice that formula (60) is the nonzero component of formula (55).

To evaluate the terms in (60) and the coefficients $DAC(\mathbf{x})$ introduced in A.A. Ayzenberg *et al*. (2015)/Chapter 3 of this thesis, we have to rewrite formulae (81)-(84) from A.A. Ayzenberg *et al*. (2015)/Chapter 3 of this thesis in case of the distant edges of faces $\mathbb{S}_2$ and $\mathbb{S}_4$. The ray distances, used in the Taylor's expansion, are expressed as follows: $l(\mathbf{x}) = \sqrt{(r_S + r_{12} + r_R)^2 + (\delta x_R)^2}$, $l_1(\mathbf{x}) = r_S + \sqrt{(r_{12} + r_R)^2 + (\delta x_R)^2}$, $l_2(\mathbf{x}) = r_S + r_{12} + \sqrt{r_R^{\,2} + (\delta x_R)^2}$ and $l_{12}(\mathbf{x}) = r_S + r_{12} + \sqrt{r_R^{\,2} + (\delta x_R)^2}$, in which r_S is the distance 'source-edge $\mathbb{E}_2$', r_{12} is the distance between edges $\mathbb{E}_2$ and $\mathbb{E}_4$, r_R is the distance 'receiver line-edge $\mathbb{E}_4$', and δx_R is a virtual deviation of the receiver from the coinciding shadow boundaries. (Figure 5 from A.A. Ayzenberg *et al*. (2015)/Chapter 3 of this thesis for $\delta x_S = 0$ and replacing edges $\mathbb{E}_1$ and $\mathbb{E}_2$ by $\mathbb{E}_2$ and $\mathbb{E}_4$, correspondingly).

Formulae (81) from A.A. Ayzenberg *et al*. (2015)/Chapter 3 of this thesis is rewritten as

$$w_1 \cong \sqrt{\frac{k_P}{2\,\pi}\left(\frac{1}{r_{12} + r_R} - \frac{1}{r_S + r_{12} + r_R}\right)}\,\delta x_R\,, \quad u_1 \cong \sqrt{\frac{k_P}{2\,\pi}\left(\frac{1}{r_R} - \frac{1}{r_{12} + r_R}\right)}\,\delta x_R\ . \tag{61}$$

Considering the vicinity of the shadow boundary with $\delta x_R \to 0$, we obtain: $w_1 \to 0$ and $u_1 \to 0$. In the event of $r_{12} \neq 0$ formulae (61) allow us to consider ratio $\frac{u_1}{w_1} \cong \sqrt{\frac{r_{12}\,(r_S + r_{12} + r_R)}{r_S\, r_R}}$ for small values of δx_R and a finite distance between the edges. For W-shaped model, we have the equal values: $r_S = r_{12} = r_R$. Hence, we obtain ratio $\frac{u_1}{w_1} = \sqrt{3}$ and

$\zeta_1 = \arctan \dfrac{u_1}{w_1} = \dfrac{\pi}{3}$. Formula (69) from A.A. Ayzenberg *et al*. (2015)/Chapter 3 of this thesis gives us limit $\lim\limits_{\substack{w_1 \to 0 \\ u_1 \to 0}} H(w_1, u_1) = \dfrac{1}{4} - \dfrac{\zeta_1}{2\pi} = \dfrac{1}{12}$.

Formulae (83) from A.A. Ayzenberg *et al*. (2015)/Chapter 3 of this thesis is rewritten as

$$w_2 \cong \sqrt{\frac{k_P}{2\pi}\left(\frac{1}{r_R} - \frac{1}{r_S + r_{12} + r_R}\right)}\,\delta x_R\,, \quad u_2 = 0\ . \tag{62}$$

We obtain ratio $\dfrac{u_2}{w_2} = 0$ and $\zeta_2 = \arctan \dfrac{u_2}{w_2} = 0$. Formula (69) from A.A. Ayzenberg *et al*. (2015)/Chapter 3 of this thesis gives the following: $\lim\limits_{\substack{w_2 \to 0 \\ u_2 \to 0}} H(w_2, u_2) = \dfrac{1}{4} - \dfrac{\zeta_2}{2\pi} = \dfrac{1}{4}$.

The special functions $H(w_1, u_1)$ and $H(w_2, u_2)$ have different values for the distant edges $\mathbb{E}_2$ and $\mathbb{E}_4$ in comparison with the close edges $\mathbb{E}_1$ and $\mathbb{E}_2$ for V-shaped boundary. It changes the amplitude of the double edge wave $\mathbf{a}^{[1]}_{\mathbb{E}_2\mathbb{E}_1}(\mathbf{x})$ and the corresponding coefficient $DAC^{[1]}_{\mathbb{S}_4\mathbb{S}_2}(\mathbf{x})$ for the distant pair of edges. Substituting the actual values of $H(w_1, u_1)$ and $H(w_2, u_2)$ in formula (79) from A.A. Ayzenberg *et al*. (2015)/Chapter 3 of this thesis, we obtain an analog of formulae (85) and (86) from A.A. Ayzenberg *et al*. (2015)/Chapter 3 of this thesis as

$$DAC^{[1]}_{\mathbb{S}_4\mathbb{S}_2}(\mathbf{x}_{shb}) \cong \left|1 - \frac{1}{2} - \left(-\frac{1}{12} + \frac{1}{4}\right)\right| = \frac{1}{3}\ . \tag{63}$$

4.8 Verification of TWSM-seismograms by the edge wave theory. W-model

Figure 8a illustrates the scalar component $a^{(0)-}(\mathbf{x},t)$ of formula (56) at the receiver line. The TWSM seismogram demonstrates two hyperbolic moveouts in the shadow zone at $x<4.0\,\mathrm{km}$ and one hyperbolic moveout in the illuminated zone at $x>4.0\,\mathrm{km}$. The traveltimes of the diffracted wavefields correspond to the eikonals of the edge waves from V_1-edge and V_2-edge. Figure 8b represents the nonzero component $a^{\mathrm{G}-}(\mathbf{x},t)$ of vector $\mathbf{a}^{\mathrm{G}}(\mathbf{x},t)$. Figure 8c illustrates the nonzero component $a^{[1]-}(\mathbf{x},t)$ of vector $\mathbf{a}^{[1]}(\mathbf{x},t)$. The wave structures on Figures 8a and 8c are complex, they represent interference of several waves in accordance to formula (57). We will give their detailed explanation in the three paragraphs right below. We demonstrate the distribution of the computed DAC for $a^{(0)-}(\mathbf{x},t)$ over the receiver line on Figure 8d. This DAC at the shadow boundary is equal to 0.533.

On Figure 9a, we represent the scalar component $a^{[1]-}_{\mathbb{S}_2\mathbb{S}_1}(\mathbf{x},t)$ of formula (58) at the receiver line. This component is the double diffraction at the closely located edges of faces $\mathbb{S}_1$ and $\mathbb{S}_2$. Figure 9b illustrates the distribution of the computed DAC for $a^{[1]-}_{\mathbb{S}_2\mathbb{S}_1}(\mathbf{x},t)$ over the receiver line. The computed DAC at the shadow boundary is 0.38. Since V_1 is a wedge, it will cause the wavefield described in our paper A.A. Ayzenberg *et al*. (2015)/Chapter 3 of this thesis, case of source 1, receiver line 2, concerning wedge models.

Figure 10a represents the scalar component $a^{[1]-}_{\mathbb{S}_4\mathbb{S}_3}(\mathbf{x},t)$ of formula (59) at the receiver line. It is the double diffraction at the closely located edges of faces $\mathbb{S}_3$ and $\mathbb{S}_4$. Figure 10b gives the distribution of the computed DAC over the receiver line. The computed DAC for $a^{[1]-}_{\mathbb{S}_4\mathbb{S}_3}(\mathbf{x},t)$ at the shadow boundary is 0.39. Since V_2 is a wedge, it will cause the wavefield described in our paper A.A. Ayzenberg *et al*. (2015)/Chapter 3 of this thesis, case of source 2, receiver line 1, concerning wedge models.

Figure 11a demonstrates the scalar component $a^{[1]-}_{\mathbb{S}_4\mathbb{S}_2}(\mathbf{x},t)$ of formula (60) at the receiver line. It represents the double diffraction at the distantly located edges of faces S_2 and S_4. On Figure 11b we give the distribution of the computed DAC over the receiver line. This

DAC at the shadow boundary is equal to 0.302. Using formula (63), we obtain the analytical DAC at the shadow boundary equal to 0.333.

The absolute deviation of the computed DAC value from the analytical DAC value at the shadow boundary is approximately equal to 0.03 which gives the relative deviation of 9 percent approximately. The computed DAC curve (Figure 11b) corresponds to the discrete values at the receivers in the shadow boundary vicinity: $DAC(3.955) = 0.378$, $DAC(3.970) = 0.352$, $DAC(3.985) = 0.326$, $DAC(4.000) = 0.302$, $DAC(4.015) = 0.278$. The closest value $DAC(3.985) = 0.326$ to the analytical value 0.333 corresponds to the receiver $x = 3.985$ km, which is distant from the shadow boundary $x = 4.0$ km in 15 m. From the edge wave theory by A.M. Aizenberg (1993), Jones (1973), Borovikov (1994) and Borovikov & Kinber (1994), it is known that the maximal amplitude gradients, tangent to the wavefront, are located in a narrow vicinity of the shadow boundary. The gradient of DAC can lead to significant phase errors. From the discrete values of the computed DAC, we can obtain that the gradient of the computed DAC along axis x equals to 1.66 km^{-1}. The gradient of the computed DAC determines the phase error of the method. If the gradient of the computed DAC is less than 0.4 km^{-}1 then we have only an amplitude error. If the computed DAC is more than 0.4 km^{-1} then we have also a phase error. This 9 percent error is composed from an amplitude error of 2 to 4 percent and a phase error of 5 to 7 percent.

The tests proved that the absolute time error is not more than 0.001 sec. The comparison of the computed and the analytical DAC values demonstrates the relative amplitude errors between 2 and 4 percent. The comparison of the computed and the analytical DAC gradients prove that the relative phase errors are not more than 5 to 7 percent.

4.9 Conclusions

In this paper, we derive a double-diffraction approximation of the feasible source wavefield in an acoustic parabolic and hyperbolic U-model and W-model. We describe the wave structure of the feasible source wavefield in the shadow zone caused by the boundaries by TPOT&TWSM in terms of the nonsparse propagation and absorption matrices. The results of the computation illustrate the accuracy and efficiency of TWSM. Correctness of the algorithm is justified by comparison of the traveltimes and amplitudes of the feasible source wavefield fragments with the edge wave theory. The results indicate that the matrix technology of TPOT&TWSM is successfully applied to the evaluation of the feasible source wavefield in the geometrical shadow zones of the considered models.

4.10 Acknowledgements

The work was partly supported by NTNU (Trondheim, Norway), the Research Centres Bergen and Trondheim of Statoil ASA (Norway) and the Swedish Foundation for International Cooperation in Research and Higher Education (University of Lund, Sweden). We express deep sorrow for Kamill D. Klem-Musatov who recently passed away and was allways one of our best colleagues and collaborators. We are thankful to our colleagues Hans B. Helle, Jan Pajchel, Ola-Petter Munkvold, Milana Ayzenberg, Gennady Demidenko, Gleb Dyatlov, Fredrik Andersson, Anton Duchkov and Alexey Romanenko for constructive discussions. We also acknowledge Toan Dao and Anna Mackie for improving the language style in the paper.

4.11 References

Aizenberg, A.M., 1982. Scattering of seismic waves by the broken edge of a flat boundary, Russian Geology and Geophysics, 23, 5, 83-92.

Aizenberg, A.M., 1993. A system of irregular fundamental solutions to wave equation in a three-dimensional inhomogeneous medium, Russian Geology and Geophysics, 34, 4, 105-113.

Aizenberg, A.M. & Ayzenberg, A.A., 2015. Feasible fundamental solution of the multiphysics wave equation in inhomogeneous domain of complex shape, Wave Motion, 53, 66-79.

Aizenberg, A.M., Ayzenberg, M.A. & Klem-Musatov, K.D., 2011. Seismic diffraction modeling with the tip-wave superposition method, Extended Abstracts, 73-th EAGE Conference, Vienna, Austria, B018.

Aizenberg, A.M. & Klem-Musatov, K.D., 2010. Progress in seismic diffraction theory – From edge and tip waves to multiple reflections-transmissions with diffractions, Extended Abstracts, 72-th EAGE Conference, Barcelona, Spain, G034.

Aizenberg, A.M., Zyatkov, N.Y., Ayzenberg, A.A. & Rakshaeva, E.Z., 2014. New concepts of the transmission-propagation operator theory in seismic diffraction modeling and interpretation, Extended Abstracts, 76th EAGE Conference, Amsterdam, Netherlands, We-P06-07.

Ayzenberg, A.A., Aizenberg, A.M., Zyatkov, N. & Andersson, F., 2012. Single-diffraction approximation of the feasible Green's function in geometrical shadow zones, Extended Abstracts, 74th EAGE Conference, Denmark, Copenhagen, P287.

Ayzenberg, A., Zyatkov, N., Aizenberg, A.M. & Stovas, A., 2015. Feasible source wavefield for acoustic V-model with shadow in form of double diffraction approximation , Geophys. J. Int., (in review).

Ayzenberg, A., Zyatkov, N., Stovas, A. & Aizenberg, A.M., 2013. Double-diffraction approximation of the feasible Green's function in geometrical shadow zones, Extended Abstracts, 75th EAGE Conference, London, UK, Th-P02-10.

Ayzenberg, A., Zyatkov, N., Stovas, A., & Aizenberg, A.M., 2014. The feasible near-front wavefield below salt overhang in terms of cascade diffraction, Extended Abstracts, 76th EAGE Conference, Amsterdam, Netherlands, We-P06-06.

Ayzenberg, M.A., Aizenberg, A.M., Helle, H.B., Klem-Musatov, K.D., Pajchel, J. & Ursin, B., 2007. 3D diffraction modeling of singly scattered acoustic wavefields based on the combination of surface integral propagators and transmission operators, Geophysics, 72, 5, SM19-SM34.

Borovikov, V.A., 1994. Uniform stationary phase method. The Institution of Electrical Engineers, London, UK.

Borovikov, V.A. & Kinber, B.Ye., 1994. Geometrical theory of diffraction. Peter Pelegrinus.

Jones, D.S., 1973. Double knife-edge diffraction and ray theory, Quart. J. Mech. and Appl. Math., 26, 1, 1-18.

Klem-Musatov, K. & Aizenberg, A.M., 1989. The edge wave superposition method (2D scalar problem), Geophys. J. Int., 99, 351-367.

Klem-Musatov, K.D., Aizenberg, A.M., Pajchel, J., & Helle, H.B., 2008. Edge and Tip Diffractions: Theory and Applications in Seismic Prospecting, Geophysical Monograph Series, No. 14, SEG, Tulsa, USA.

Zyatkov, N., Ayzenberg, A.A., Aizenberg, A.M., Romanenko, A. & Andersson, F., 2012. Modeling of cascade diffraction in terms of propagation-absorption matrices: realization and optimization for GPU, Extended Abstracts, 74th EAGE Conference, Denmark, Copenhagen, P288.

Zyatkov, N., Ayzenberg, A., Aizenberg, A.M. & Romanenko, A., 2013. Highly-optimized TWSM algorithm for modeling cascade diffraction in terms of propagation-absorption matrices, Extended Abstracts, 75th EAGE Conference, London, UK, Th-P02-11.

4.12 List of Figures

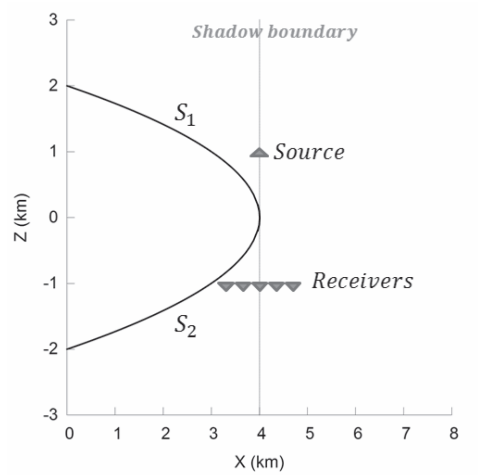

Figure 1. U-shaped parabolic model. Sketch and acquisition design.

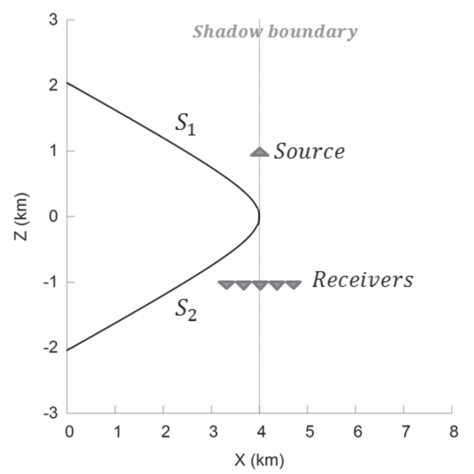

Figure 2. U-shaped hyperbolic model. Sketch and acquisition design.

Figure 3. U-shaped parabolic and hyperbolic model.

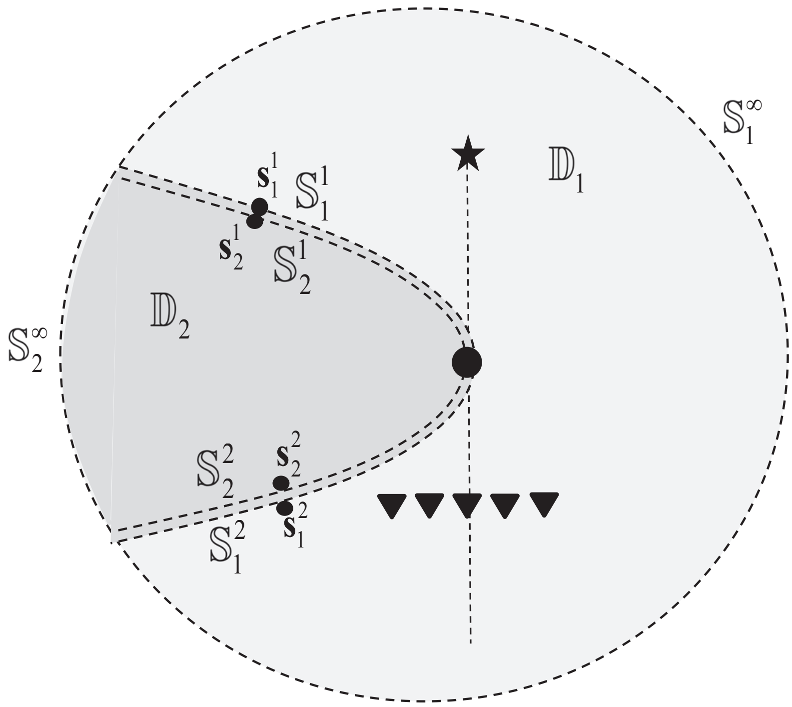

Figure 3a. Medium and interface notations

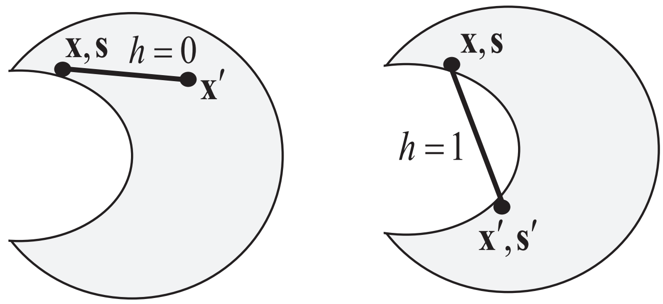

Figure 3b. Visibility of the points

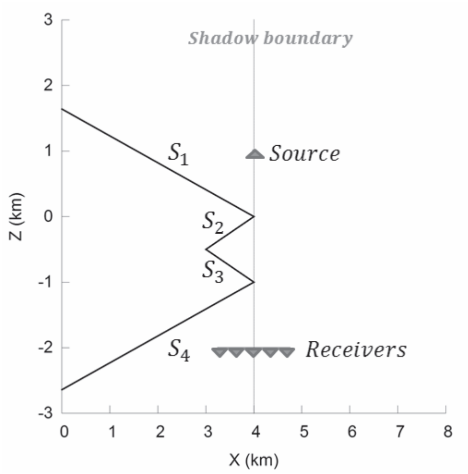

Figure 4. Sketch and acquisition design.

Figure 5. W-shaped model.

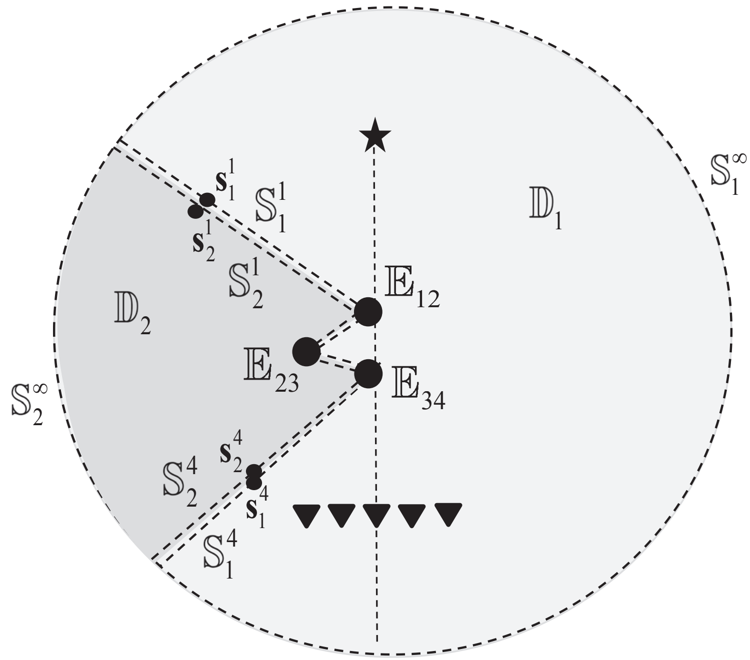

Figure 5a. Medium and interface notations

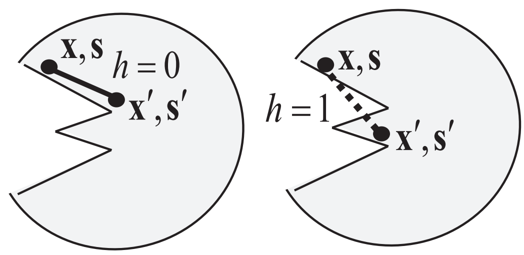

Figure 5b. Visibility of the points

Figure 6. U-shaped parabolic model.

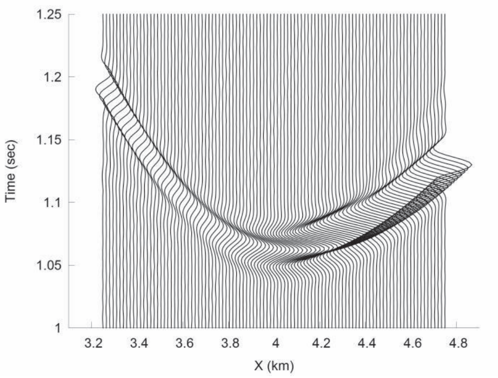

Figure 6a. Wavefield $a^{(0)-}(\mathbf{x},t)$.

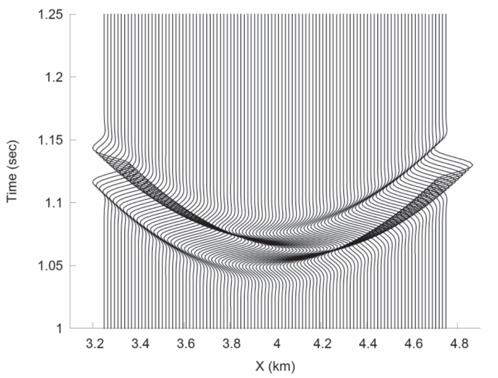

Figure 6b. Wavefield $a^{\mathbf{G}-}(\mathbf{x},t)$.

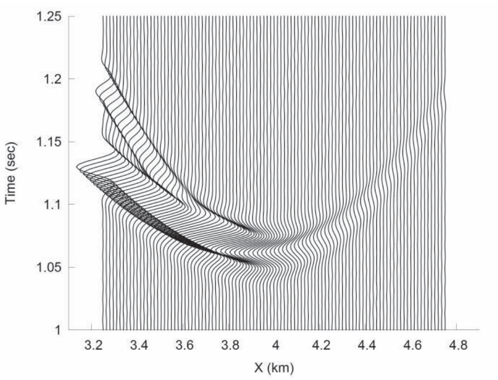

Figure 6c. Wavefield $a^{[1]-}(\mathbf{x},t)$.

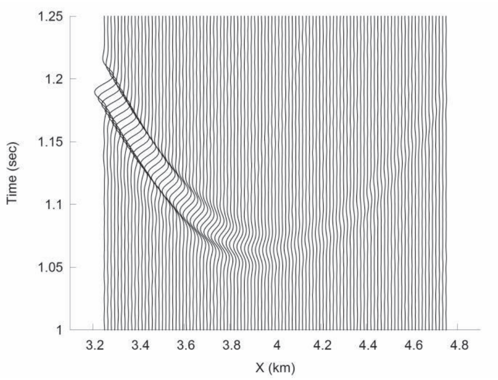

Figure 6d. Wavefield $a^{[1]-}_{\mathbb{S}_2\mathbb{S}_2}(\mathbf{x},t)$.

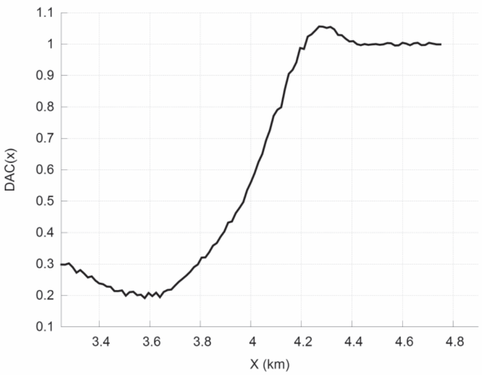

Figure 6e. Curve of $DAC(\mathbf{x})$ for $a^{(0)-}(\mathbf{x},t)$.

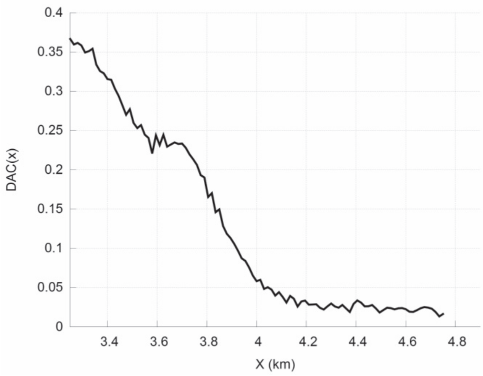

Figure 6f. Curve of $DAC(\mathbf{x})$ for $a^{[1]-}_{\mathbb{S}_2\mathbb{S}_2}(\mathbf{x},t)$.

Figure 7. U-shaped hyperbolic model.

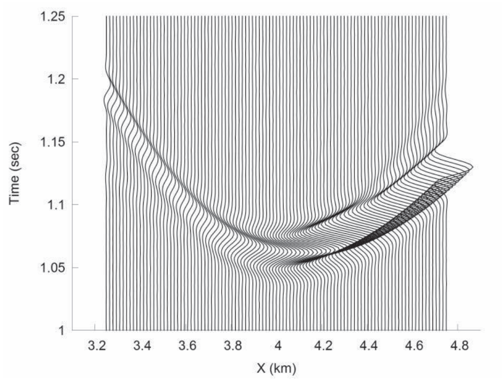

Figure 7a. Wavefield $a^{(0)-}(\mathbf{x}, t)$.

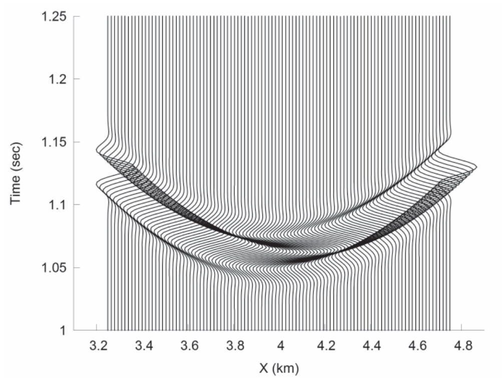

Figure 7b. Wavefield $a^{\mathbf{G}-}(\mathbf{x}, t)$.

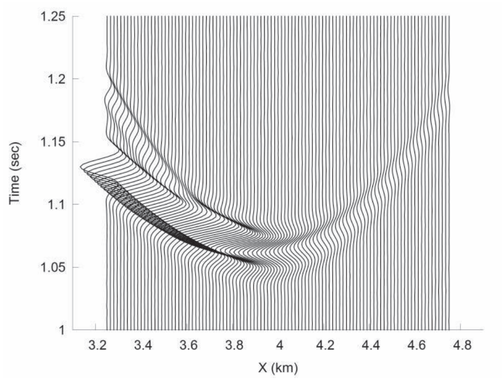

Figure 7c. Wavefield $a^{[1]-}(\mathbf{x}, t)$.

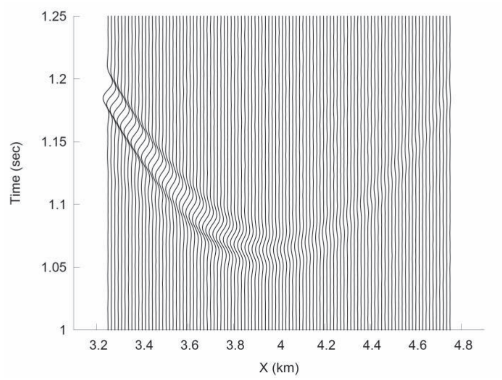

Figure 7d. Wavefield $a^{[1]-}_{\mathbb{S}_2\mathbb{S}_2}(\mathbf{x}, t)$.

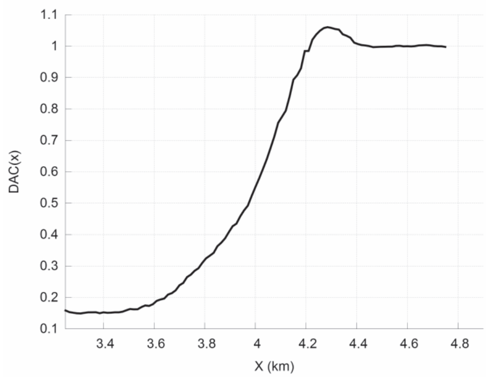

Figure 7e. Curve of $DAC(\mathbf{x})$ for $a^{(0)-}(\mathbf{x}, t)$.

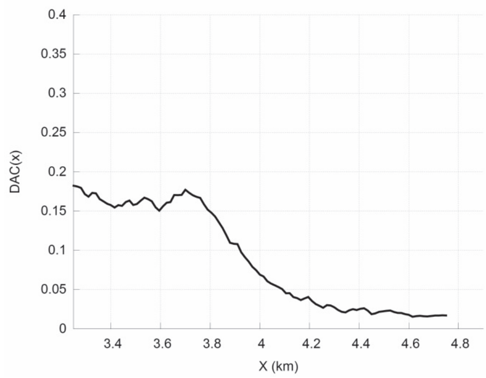

Figure 7f. Curve of $DAC(\mathbf{x})$ for $a^{[1]-}_{\mathbb{S}_2\mathbb{S}_2}(\mathbf{x}, t)$.

Figure 8. W-shaped model.

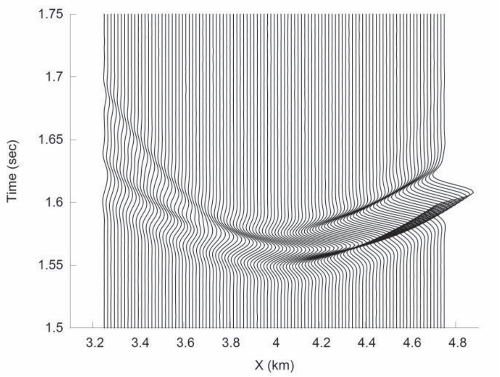

Figure 8a. Wavefield $a^{(0)-}(\mathbf{x},t)$.

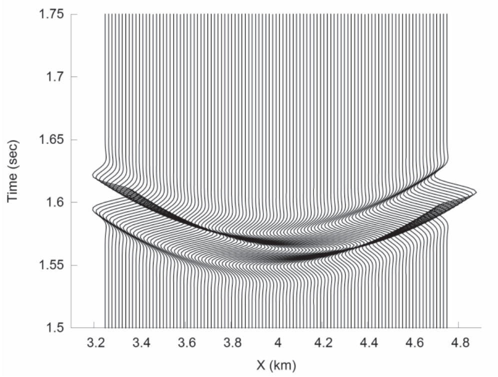

Figure 8b. Wavefield $a^{\mathbf{G}-}(\mathbf{x},t)$.

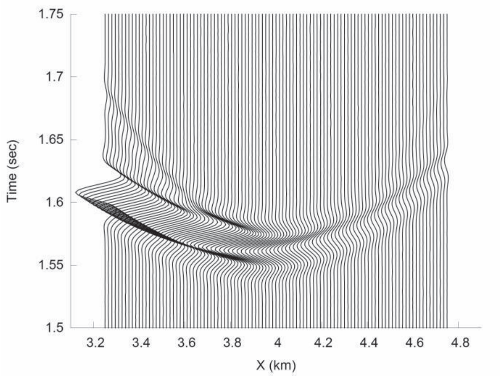

Figure 8c. Wavefield $a^{[1]-}(\mathbf{x},t)$.

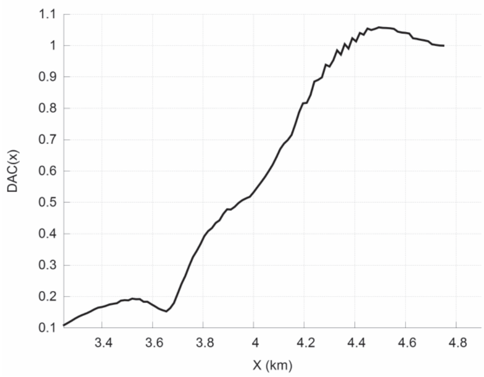

Figure 8d. Curve of $DAC(\mathbf{x})$ for $a^{(0)-}(\mathbf{x},t)$

.

Figure 9. W-shaped model.

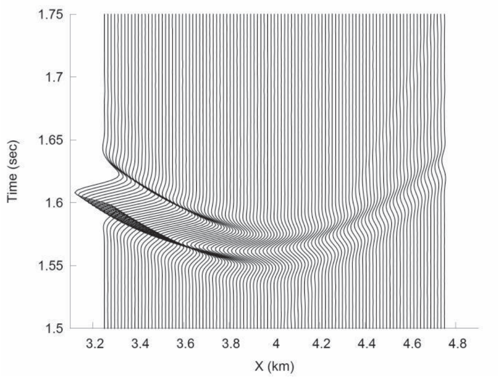

Figure 9a. Wavefield $a^{[1]-}_{\mathbb{S}_2\mathbb{S}_1}(\mathbf{x},t)$.

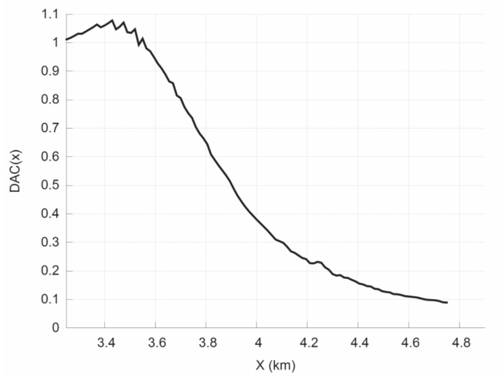

Figure 9b. Curve of $DAC(\mathbf{x})$.

Figure 10. W-shaped model.

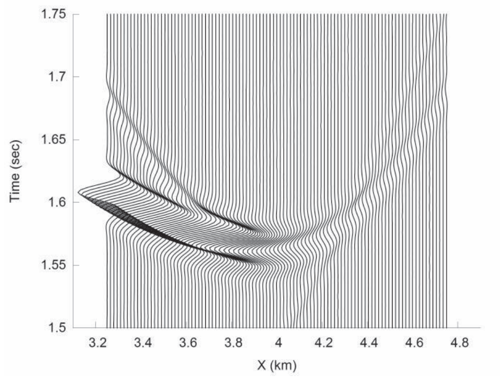

Figure 10a. Wavefield $a^{[1]-}_{\mathbb{S}_4\mathbb{S}_3}\left(\mathbf{x},t\right)$.

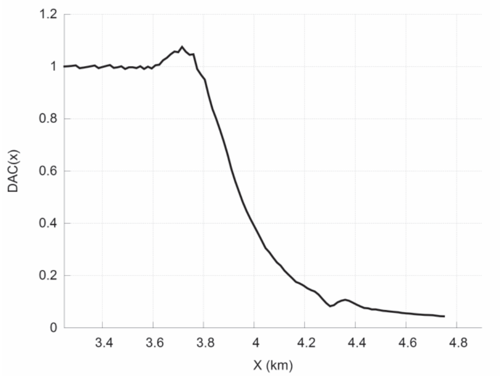

Figure 10b. Curve of $DAC\left(\mathbf{x}\right)$.

Figure 11. W-shaped model.

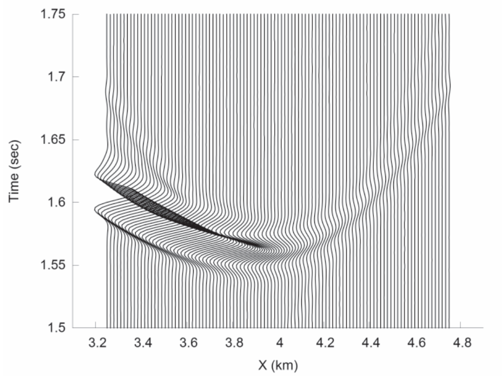

Figure 11a. Wavefield $a^{[1]-}_{\mathbb{S}_4\mathbb{S}_2}(\mathbf{x},t)$.

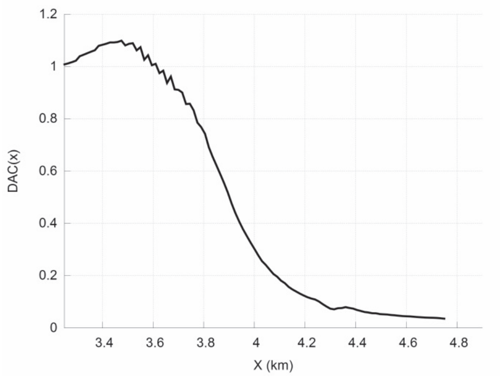

Figure 11b. Curve of $DAC(\mathbf{x})$.

Chapter 5

Primary source wavefield below overhang of 3D 2-block acoustic medium

Alena A. Ayzenberg[a*], Nikolay Y. Zyatkov[b], Arkady M. Aizenberg[c], Alexey Stovas[a]

[a] Norwegian University of Science and Technology (NTNU), S.P. Andersens veg 15a, 7491 Trondheim, Norway,
tel.: +47 90 840 729, fax: +47 73 944 472, e-mail: alena.ayzenberg@ntnu.no
tel.: +47 73 597 139, fax: +47 73 944 472, e-mail: alexey.stovas@ntnu.no
[b] Novosibirsk State University, Pirogova str. 2, 630090 Novosibirsk, Russia,
tel.: +7 923 248 2157, fax: +7 383 333 2513, e-mail: nikolay.zyatkov@gmail.com
[c] Institute of Petroleum Geology and Geophysics, Russian Academy of Sciences,
Ac. Koptyug Pr. 3, 630090 Novosibirsk, Russia,
tel.: +7 383 335 6457, fax: +7 383 333 2513, e-mail: AizenbergAM@ipgg.sbras.ru

Presented at the ROSE Meeting, Trondheim, Norway, 2015; Lofotenseminar, Svalbard, 2015; APSLIM workshop, Loucen Castle, Czech Republic 2015. Submitted to Geophysical Journal International on 30 June 2015.

5.1 Summary

We consider 3D 2-block models with V- and U-shaped interfaces similar to a geological salt overhang. We consider a contrast velocities case in order to simulate shadow below the V- and U-shaped overhang similar to shadow below a salt body. A source is placed above the overhang and a receiver line is located below the overhang so that a half-part is in the illuminated zone while the other half-part is in the shadow zone. We perform a detailed wavefield description at the receiver line of both models in terms of primary (analog of near-front) wavefield. The primary wavefield is obtained by the Transmission-Propagation Operator Theory (TPOT) and represents the superposition of the source wavefield and the double-transmitted wavefield. Both the source and double-transmitted wavefields contain so-called 'feasible fundamental solutions' and 'feasible propagation operators' which have a shadow correction. The primary solution is visualized on a GPU cluster by the Tip Wave Superposition Method (TWSM) in the mid-frequency range. We use 2-term approximations for the feasible fundamental solution and the feasible propagation operator. The seismograms represent the primary solution and its terms separately and in combinations in order to demonstrate that the method can analyze separate events. For both models, the final seismogram performs a complex wavefield with a combination of several waves.

5.2 Introduction

Shadow originally is an optic term. Shadow in optics is caused by an obstacle. The light rays are diffracted by the obstacle and penetrate into the shadow zone behind the obstacle. Diffraction can occur many times if the obstacle has complex shape. Such diffraction is called cascade diffraction. In acoustic, elastic, porous, fractured, fluid-saturated, microstructured and other media, the presence of shadow (sub-salt, sub-basalt zones etc.) can make a subsurface image and subsurface wavefield modeling and imaging very complicated. This study has been for many years devoted to improvement of wavefield description in complex 3D media with shadow zones.

The wavefield description in shadow and illuminated zones is done by the Transmission-Propagation Operator Theory (TPOT) (A.M. Aizenberg *et al.* (2011)) which analytically describes wavefield at any 3D point in 3D block medium consisting of several inhomogeneous domains with acoustic, elastic, porous etc. parameters. This theory proposes a solution for the block medium in the form of the superposition of the source wavefield and the double-transmitted wavefield. The source and double-transmitted wavefields contain so-called 'feasible fundamental solutions' and 'feasible propagation operators' of the given medium as described in A.M. Aizenberg & A.A. Ayzenberg (2015)/Chapter 2 of this thesis.

After the medium solution has been obtained, its visualization is performed using the Tip-Wave Superposition Method (TWSM) (Klem-Musatov *et al.* (2008) and Zyatkov *et al.* (2015)) which computes the medium solution in the mid-frequency range on a GPU cluster. Due to memory expenses, we use the 2 term–approximation of the feasible fundamental solution and the feasible propagation operator.

The TPOT theoretical approach and TWSM method were tested by a comparison with laboratory data (Tantsereva *et al.* (2014)), theoretical approaches as given in M.A. Ayzenberg *et al.* (2007), A.A. Ayzenberg *et al.* (2015a)/Chapter 3 of this thesis, A.A. Ayzenberg *et al.* (2015b)/Chapter 4 of this thesis and A.A. Ayzenberg *et al.* (2013) and the FD modeling method (Rakshaeva *et al.* (2015)).

The first test model (V-model) is a medium of 2 homogeneous domains. The wedge-like domain simulates a salt overhang of V-shape. Another one simulates sediments around the salt body. The second test model (U-model) is a medium of 2 homogeneous domains. The smooth wedge-like domain simulates a salt overhang of U-shape. Another one simulates sediments around the salt body. For both tests, the domains have contrast velocities which simulate a shadow effect below V- and U-overhangs.

This paper consists of an Introduction, 3 Sections and Conclusions. The Introduction gives a brief description of the proposed approach and tests. Section 5.3 formulates the statement of the forward problem for V- or U-models. Section 5.4 derives the solution of the problem in the form of primary wavefield, which is the superposition of the source wavefield (A.A. Ayzenberg *et al.* (2015a)/Chapter 3 of this thesis and A.A. Ayzenberg *et al.* (2015b)/Chapter 4 of this thesis) and the double-transmitted wavefield, both with the feasible fundamental solutions and the feasible propagations operators as basis. Section 5.5 provides the seismograms as a visualization of the proposed solution and its components. Conclusions summarize the obtained results.

5.3 Forward V- and U-problem for 2-block medium

We consider two 2-block models: with V- and U-interface. For both models, the material parameters of both medium domains and the geometrical parameters of the interface are chosen to imitate a salt overhang surrounded by sediments. A strong velocity contrast imitates shadow below the overhang. On Figure 1, we demonstrate V-model with two homogeneous acoustic domains, $\mathbb{D}_1$ and $\mathbb{D}_2$, separated by a V-shaped interface. On Figure 2, we consider U-model with two homogeneous acoustic domains, $\mathbb{D}_1$ and $\mathbb{D}_2$, separated by a U -shaped interface. Parameters of domain $\mathbb{D}_1$ are: P-wave velocity $v_{P,1} = 2.0\,\mathrm{km/sec}$ and density $\rho_1 = 2.0\,\mathrm{g/cm^3}$. Parameters of domain $\mathbb{D}_2$ are: P-wave velocity $v_{P,2} = 4.0\,\mathrm{km/sec}$ and density $\rho_2 = 3.0\,\mathrm{g/cm^3}$.

We represent temporal spectra of the wavefield as particle velocity-pressure vectors (4×1-columns)

$$\mathbf{u}(\mathbf{x}_m,\omega) = \begin{pmatrix} v_{1,m} \\ v_{2,m} \\ v_{3,m} \\ p_m \end{pmatrix}, \tag{1}$$

where $v_{1,m}$, $v_{2,m}$, $v_{3,m}$ are components of the particle velocities, p_m is pressure in each domain. Function $\mathbf{u}(\mathbf{x}_m,\omega)$ is defined as follows

$$\begin{cases} \mathbf{u} = \mathbf{u}(\mathbf{x}_1,\omega), & \text{for} \quad \mathbf{x}_1 \in \mathbb{D}_1, \\ \mathbf{u} = \mathbf{u}(\mathbf{x}_2,\omega), & \text{for} \quad \mathbf{x}_2 \in \mathbb{D}_2. \end{cases} \tag{2}$$

Vectors (2) are connected with the wavefields by the Fourier transform

$$\mathbf{u}(\mathbf{x}_m,t) = \frac{1}{\sqrt{2\pi}} \int_{-\infty}^{+\infty} \mathbf{u}(\mathbf{x}_m,\omega)\, e^{-i\omega t}\, d\omega , \tag{3}$$

where ω is angular frequency. The temporal spectrum vectors $\mathbf{u}(\mathbf{x}_m, \omega)$ in (2) satisfy the wave motion equations from A.M. Aizenberg & A.A. Ayzenberg (2015)/Chapter 2 of this thesis and A.A. Ayzenberg *et al.* (2015a)/Chapter 3 of this thesis

$$\mathbf{D}_{\mathbf{x}_m} \mathbf{u}(\mathbf{x}_m, \omega) + \mathbf{M}_m(\omega)\, \mathbf{u}(\mathbf{x}_m, \omega) = \mathbf{f}(\mathbf{x}_m, \omega) \ , \tag{4}$$

where the differential matrix operator and the matrix of material parameters are

$$\mathbf{D}_{\mathbf{x}_m} = \begin{pmatrix} 0 & 0 & 0 & \dfrac{\partial}{\partial x_1} \\ 0 & 0 & 0 & \dfrac{\partial}{\partial x_2} \\ 0 & 0 & 0 & \dfrac{\partial}{\partial x_3} \\ \dfrac{\partial}{\partial x_1} & \dfrac{\partial}{\partial x_2} & \dfrac{\partial}{\partial x_3} & 0 \end{pmatrix}, \quad \mathbf{M}_m(\omega) = (-i\,\omega) \begin{pmatrix} \rho_m & 0 & 0 & 0 \\ 0 & \rho_m & 0 & 0 \\ 0 & 0 & \rho_m & 0 \\ 0 & 0 & 0 & \dfrac{1}{\rho_m \left(v_{P,m}\right)^2} \end{pmatrix}. \tag{5}$$

In each domain, vector (2) satisfies the radiation conditions $\langle RC \rangle_m$ and the edge conditions $\langle EC \rangle_m$ (system (2) from A.M. Aizenberg & A.A. Ayzenberg (2015)/Chapter 2 of this thesis). The point source $\mathbf{f}(\mathbf{x}_1, \omega) = \dfrac{\psi(\omega)}{(-i\,\omega)\,\rho_1} \begin{pmatrix} 0 & 0 & 0 & \delta(\mathbf{x}_1 - \mathbf{y}_1) \end{pmatrix}^T$ is located in domain $\mathbb{D}_1$ at point $\mathbf{y}_1(4.0\,\mathrm{km}, 0.0\,\mathrm{km}, 1.0\,\mathrm{km})$ and radiates a spherical P-wave. Function $\psi(\omega)$ is the spectrum of the wavelet $\psi(t) = e^{-(2\tau)^2} \cos(2\pi\,\tau)$, where $\tau = t/T - 2$. The wave period $T = 0.032\,\mathrm{sec}$ corresponds to the dominant frequency of 38.25 Hz. In domain $\mathbb{D}_2$, there is no source: $\mathbf{f}(\mathbf{x}_2, \omega) = \begin{pmatrix} 0 & 0 & 0 & 0 \end{pmatrix}^T$.

In TPOT, all interfaces are considered as two-sided surfaces with two normals and consisting of two faces. We denote these faces as $\mathbb{S}_m^j$ and the corresponding normals as $\mathbf{n}(\mathbf{s}_m^j)$, $\mathbf{s}_m^j \in \mathbb{S}_m^j$, where the lower index denotes the domain number and the upper index denotes the face number. On Figure 1, the upper side $\mathbb{S}_1^1$ and lower side $\mathbb{S}_2^1$ of the upper face of V-shaped interface are defined by formula $z = 0.41(4 - x)$. The upper side $\mathbb{S}_2^2$ and lower side $\mathbb{S}_1^2$ of the lower face of the V-shaped interface are defined by formula $z = -0.41(4 - x)$. At the interfaces, we consider boundary conditions (Figure 1c from A.A. Ayzenberg *et al.* (2015a)/Chapter 3 of this thesis)

$$\langle BC \rangle : \begin{cases} \mathbf{C}\,\mathbf{R}\left(\mathbf{s}_1^1\right)\mathbf{u}\left(\mathbf{s}_1^1, \omega\right) = \mathbf{J}\,\mathbf{C}\,\mathbf{R}\left(\mathbf{s}_2^1\right)\mathbf{u}\left(\mathbf{s}_2^1, \omega\right), \\ \mathbf{C}\,\mathbf{R}\left(\mathbf{s}_1^2\right)\mathbf{u}\left(\mathbf{s}_1^2, \omega\right) = \mathbf{J}\,\mathbf{C}\,\mathbf{R}\left(\mathbf{s}_2^2\right)\mathbf{u}\left(\mathbf{s}_2^2, \omega\right), \end{cases} \tag{6}$$

where

$$\mathbf{C} = \begin{bmatrix} 0 & 0 & 1 & 0 \\ 0 & 0 & 0 & 1 \end{bmatrix}, \tag{7}$$

$$\mathbf{R}\left(\mathbf{s}_m^j\right) = \begin{bmatrix} \mathbf{i}_1\left(\mathbf{s}_m^j\right)\cdot\bar{\mathbf{i}}_1 & \mathbf{i}_1\left(\mathbf{s}_m^j\right)\cdot\bar{\mathbf{i}}_2 & \mathbf{i}_1\left(\mathbf{s}_m^j\right)\cdot\bar{\mathbf{i}}_3 & 0 \\ \mathbf{i}_2\left(\mathbf{s}_m^j\right)\cdot\bar{\mathbf{i}}_1 & \mathbf{i}_2\left(\mathbf{s}_m^j\right)\cdot\bar{\mathbf{i}}_2 & \mathbf{i}_2\left(\mathbf{s}_m^j\right)\cdot\bar{\mathbf{i}}_3 & 0 \\ \mathbf{i}_3\left(\mathbf{s}_m^j\right)\cdot\bar{\mathbf{i}}_1 & \mathbf{i}_3\left(\mathbf{s}_m^j\right)\cdot\bar{\mathbf{i}}_2 & \mathbf{i}_3\left(\mathbf{s}_m^j\right)\cdot\bar{\mathbf{i}}_3 & 0 \\ 0 & 0 & 0 & 1 \end{bmatrix}, \tag{8}$$

$\mathbf{u}\left(\mathbf{s}_m^j, \omega\right)$ is the limit value of vector $\mathbf{u}\left(\mathbf{x}_m, \omega\right)$ at face $\mathbb{S}_m^j$, $\mathbf{J} = \begin{bmatrix} -1 & 0 \\ 0 & 1 \end{bmatrix}$, $\left(\bar{\mathbf{i}}_1, \bar{\mathbf{i}}_2, \bar{\mathbf{i}}_3\right)$ is the global Cartesian basis independent of point $\mathbf{s}_m^j$ and $\left(\mathbf{i}_1\left(\mathbf{s}_m^j\right), \mathbf{i}_2\left(\mathbf{s}_m^j\right), \mathbf{n}\left(\mathbf{s}_m^j\right)\right)$ is the local basis dependent of point $\mathbf{s}_m^j$.

Equation (4), the radiation conditions $\langle RC \rangle_m$ and the edge conditions $\langle EC \rangle_m$ from A.A. Ayzenberg *et al.* (2015a)/Chapter 3 of this thesis and the boundary condition $\langle BC \rangle$ (6) form the correct statement of the forward problem for V-model

$$
\begin{cases}
\mathbf{D}_{\mathbf{x}_m}\,\mathbf{u}\left(\mathbf{x}_m,\omega\right)+\mathbf{M}_m\left(\omega\right)\mathbf{u}\left(\mathbf{x}_m,\omega\right)=\mathbf{f}\left(\mathbf{x}_m,\omega\right), \\
\left\langle RC\right\rangle_m: \quad \iint\limits_{\mathbb{S}_m^\infty}\mathbf{F}\left(\mathbf{x}_m,\mathbf{s}_m,\omega\right)\mathbf{N}(\mathbf{s}_m)\,\mathbf{u}\left(\mathbf{s}_m,\omega\right)dS(\mathbf{s}_m)=0, \\
\left\langle EC\right\rangle_m: \quad \iint\limits_{\mathbb{S}_m^E}\mathbf{F}\left(\mathbf{x}_m,\mathbf{s}_m,\omega\right)\mathbf{N}(\mathbf{s}_m)\,\mathbf{u}_m\left(\mathbf{s}_m,\omega\right)dS(\mathbf{s}_m)=0, \quad m=1,2. \\
\left\langle BC\right\rangle: \quad \begin{cases}\mathbf{C}\,\mathbf{R}\left(\mathbf{s}_1^1\right)\mathbf{u}\left(\mathbf{s}_1^1,\omega\right)=\mathbf{J}\,\mathbf{C}\,\mathbf{R}\left(\mathbf{s}_2^1\right)\mathbf{u}\left(\mathbf{s}_2^1,\omega\right), \\ \mathbf{C}\,\mathbf{R}\left(\mathbf{s}_1^2\right)\mathbf{u}\left(\mathbf{s}_1^2,\omega\right)=\mathbf{J}\,\mathbf{C}\,\mathbf{R}\left(\mathbf{s}_2^2\right)\mathbf{u}\left(\mathbf{s}_2^2,\omega\right),\end{cases}
\end{cases}
\tag{9}
$$

System (9) has the feasible fundamental solution $\mathbf{F}\left(\mathbf{x}_m,\mathbf{s}_m,\omega\right)$ as the kernel of the feasible surface integral operators (A.M. Aizenberg & A.A. Ayzenberg (2015)/Chapter 2 of this thesis and A.A. Ayzenberg *et al.* (2015a)/Chapter 3 of this thesis).

The statement of the forward problem for U-model is formulated similar to V-model. U-interface is smooth and does not have any edges. Hence, we consider the straight line $\left(4.0\,\text{km}, y\,\text{km}, 1.0\,\text{km}\right)$ of the interface as a formal 'edge' since this line leads to a shadow boundary similar to a usual edge case. We therefore formally divide U-interface into faces S_m^j, like V- interface, in order to obtain a similar statement of the forward problem. On Figure 2, the upper side $\mathbb{S}_1^1$ and lower side $\mathbb{S}_2^1$ of the upper face of U-shaped interface are defined by formula $z=+\sqrt{4-x}$. The upper side $\mathbb{S}_2^2$ and lower side $\mathbb{S}_1^2$ of the lower face of the U-shaped interface are defined by formula $z=-\sqrt{4-x}$. The radius of curvature of this boundary is $0,5\,\text{km}$ at the formal 'edge'. After introducing this formal 'edge', the statement of the forward problem for U-model is the same as for V-model.

For both models, the receivers are spread along a straight line 1: from $x=3,25\,\text{km}$ to $x=4,75\,\text{km}$ with the step $\Delta x=0,015\,\text{km}$ at $y=0.0\,\text{km}$ and $z=-1,0\,\text{km}$. The auxiliary receiver line 2 is placed from $x=2,0\,\text{km}$ to $x=3,5\,\text{km}$ with the step $\Delta x=0,015\,\text{km}$ at $y=0,0\,\text{km}$ and $z=0,0\,\text{km}$.

5.4 Analytical solution by TPOT and its visualization by TWSM

The analytical solution of the forward problem is provided by the Transmission-Propagation Operator Theory (TPOT) from A.M. Aizenberg *et al.* (2011). This theory uses the propagation integral operator $\mathbf{P}$ for domain with and without shadow (formulae (41)-(42) from A.A. Ayzenberg *et al.* (2015a)/Chapter 3 of this thesis) and the transmission (reflection / refraction) operator $\mathbf{T}$ (Appendix A from M.A. Ayzenberg *et al.* (2007)). The propagation operator $\mathbf{P}$ is based on the feasible Kirchhoff operator $\mathbf{K}$ (formula (43) from A.M. Aizenberg & A.A. Ayzenberg (2015)/Chapter 2 of this thesis) and the plane-wave spectral operators $\mathbf{H}$. In this Section in some of the formulae, we will omit indices and angular frequency ω if they are not important for the analysis.

Applying formula (72) from Wapenaar (2007) to equation (4) and noticing that the scattered field is $\mathbf{u}\left(\mathbf{s}_m^j\right)-\mathbf{u}^{(0)}\left(\mathbf{s}_m^j\right)$, where the upper index denotes the face number ($j=1,2$) and the lower index denotes the domain number ($m=1,2$), we obtain the surface integral equation for vector $\mathbf{u}\left(\mathrm{s}_m^j\right)$

$$\mathbf{u}\left(\mathbf{s}_m^j\right)=\mathbf{K}\left(\mathbf{s}_m^j,\mathbf{s}_m^1\right)\mathbf{u}\left(\mathbf{s}_m^1\right)+\mathbf{K}\left(\mathbf{s}_m^j,\mathbf{s}_m^2\right)\mathbf{u}\left(\mathbf{s}_m^2\right)+\mathbf{u}^{(0)}\left(\mathbf{s}_m^j\right). \tag{10}$$

In (10), the operator

$$\mathbf{K}\left(\mathbf{s}_m^{j'},\mathbf{s}_m^j\right)\langle\ldots\rangle=\iint\limits_{\mathbb{S}_m^j}\mathbf{F}\left(\mathbf{s}_m^{j'},\mathbf{s}_m^j\right)\mathbf{N}(\mathbf{s}_m^j)\langle\ldots\rangle\, dS\left(\mathbf{s}_m^j\right) \tag{11}$$

is Kirchhoff integral operator with the feasible fundamental kernel $\mathbf{F}\left(\mathbf{s}_m^{j'},\mathbf{s}_m^j\right)$ as described in A.M. Aizenberg & A.A. Ayzenberg (2015)/Chapter 2 of this thesis, $\mathbf{u}^{(0)}\left(\mathbf{s}_1^j\right)$ is the feasible source wavefield from A.A. Ayzenberg *et al.* (2015a)/Chapter 3 of this thesis and $\mathbf{u}^{(0)}\left(\mathbf{s}_2^j\right)=\mathbf{0}$ since we have a source only in domain $\mathbb{D}_1$. Using operator $\mathbf{R}^{-1}\,\mathbf{H}$ by formulae (41) and (42) from A.A. Ayzenberg *et al.* (2015a)/Chapter 3 of this thesis, we obtain vector $\mathbf{u}\left(\mathbf{s}_m^j\right)$ in the form

$$\mathbf{u}\left(\mathbf{s}_m^j\right)=\left[\mathbf{R}\left(\mathbf{s}_m^j\right)\right]^{-1}\mathbf{H}\left(\mathbf{s}_m^j,\tilde{\mathbf{s}}_m^j\right)\mathbf{a}\left(\tilde{\mathbf{s}}_m^j\right), \tag{12}$$

where $\mathbf{H}\left(\mathbf{s}_m^j,\tilde{\mathbf{s}}_m^j\right)$ is the convolution-type operator of the composition of the plane-wave analogs at only one fixed face $\mathbb{S}_m^j$ (formulae (33) and (43) from A.A. Ayzenberg *et al.* (2015a)/Chapter 3 of this thesis). Substituting formula (12) in (10) and multiplying by $\mathbf{R}\left(\mathbf{s}_m^j\right)$ from the left, we obtain

$$\begin{aligned}\mathbf{H}\left(\mathbf{s}_m^j,\tilde{\mathbf{s}}_m^j\right)\mathbf{a}\left(\tilde{\mathbf{s}}_m^j\right)=\mathbf{R}\left(\mathbf{s}_m^j\right)\mathbf{K}\left(\mathbf{s}_m^j,\mathbf{s}_m^1\right)\mathbf{R}^{-1}\left(\mathbf{s}_m^1\right)\mathbf{H}\left(\mathbf{s}_m^1,\tilde{\mathbf{s}}_m^1\right)\mathbf{a}\left(\tilde{\mathbf{s}}_m^1\right)+\\+\mathbf{R}\left(\mathbf{s}_m^j\right)\mathbf{K}\left(\mathbf{s}_m^j,\mathbf{s}_m^2\right)\mathbf{R}^{-1}\left(\mathbf{s}_m^2\right)\mathbf{H}\left(\mathbf{s}_m^2,\tilde{\mathbf{s}}_m^2\right)\mathbf{a}\left(\tilde{\mathbf{s}}_m^2\right)+\\+\mathbf{H}\left(\mathbf{s}_m^j,\tilde{\mathbf{s}}_m^j\right)\mathbf{a}^{(0)}\left(\tilde{\mathbf{s}}_m^j\right).\end{aligned} \tag{13}$$

Multiplying (13) by $\mathbf{C}$ from the left, we have

$$\begin{aligned}\mathbf{C}\,\mathbf{H}\left(\mathbf{s}_m^j,\tilde{\mathbf{s}}_m^j\right)\mathbf{a}\left(\tilde{\mathbf{s}}_m^j\right)=\mathbf{C}\,\mathbf{R}\left(\mathbf{s}_m^j\right)\mathbf{K}\left(\mathbf{s}_m^j,\mathbf{s}_m^1\right)\mathbf{R}^{-1}\left(\mathbf{s}_m^1\right)\mathbf{H}\left(\mathbf{s}_m^1,\tilde{\mathbf{s}}_m^1\right)\mathbf{a}\left(\tilde{\mathbf{s}}_m^1\right)+\\+\mathbf{C}\,\mathbf{R}\left(\mathbf{s}_m^j\right)\mathbf{K}\left(\mathbf{s}_m^j,\mathbf{s}_m^2\right)\mathbf{R}^{-1}\left(\mathbf{s}_m^2\right)\mathbf{H}\left(\mathbf{s}_m^2,\tilde{\mathbf{s}}_m^2\right)\mathbf{a}\left(\tilde{\mathbf{s}}_m^2\right)+\\+\mathbf{C}\,\mathbf{H}\left(\mathbf{s}_m^j,\tilde{\mathbf{s}}_m^j\right)\mathbf{a}^{(0)}\left(\tilde{\mathbf{s}}_m^j\right).\end{aligned} \tag{14}$$

Matrix $\mathbf{C}\,\mathbf{H}\left(\mathbf{s}_m^j,\tilde{\mathbf{s}}_m^j\right)$ is quadratic and has its inverse matrix, therefore we can multiply (14) by $\left[\mathbf{C}\,\mathbf{H}\left(\mathbf{s}_m^j,\tilde{\mathbf{s}}_m^j\right)\right]^{-1}$, after which we obtain the equation

$$\mathbf{a}\left(\mathbf{s}_m^j\right)=\mathbf{P}\left(\mathbf{s}_m^j,\tilde{\mathbf{s}}_m^1\right)\mathbf{a}\left(\tilde{\mathbf{s}}_m^1\right)+\mathbf{P}\left(\mathbf{s}_m^j,\tilde{\mathbf{s}}_m^2\right)\mathbf{a}\left(\tilde{\mathbf{s}}_m^2\right)+\mathbf{a}^{(0)}\left(\mathbf{s}_m^j\right), \tag{15}$$

where

$$\mathbf{P}\left(\mathbf{s}_m^j,\tilde{\mathbf{s}}_m^{j'}\right)=\left[\mathbf{CH}\left(\mathbf{s}_m^j,\tilde{\mathbf{s}}_m^j\right)\right]^{-1}\mathbf{CR}\left(\tilde{\mathbf{s}}_m^j\right)\mathbf{K}\left(\tilde{\mathbf{s}}_m^j,\mathbf{s}_m^{j'}\right)\mathbf{R}^{-1}\left(\mathbf{s}_m^{j'}\right)\mathbf{H}\left(\mathbf{s}_m^{j'},\tilde{\mathbf{s}}_m^{j'}\right),\quad j'=1,2\ . \tag{16}$$

The feasible source wavefield $\mathbf{a}^{(0)}\left(\mathbf{s}_1^1\right)$ in domain $\mathbb{D}_1$ on face $\mathbb{S}_1^1$ and the feasible source wavefield $\mathbf{a}^{(0)}\left(\mathbf{s}_1^2\right)$ in domain $\mathbb{D}_1$ on face $\mathbb{S}_1^2$ are

$$\mathbf{a}^{(0)}\left(\mathbf{s}_1^1\right)=\begin{pmatrix} a^{(0)+}\left(\mathbf{s}_1^1\right) \\ a^{(0)-}\left(\mathbf{s}_1^1\right) \end{pmatrix}, \quad \mathbf{a}^{(0)}\left(\mathbf{s}_1^2\right)=\begin{pmatrix} a^{(0)+}\left(\mathbf{s}_1^2\right) \\ a^{(0)-}\left(\mathbf{s}_1^2\right) \end{pmatrix}, \tag{17}$$

where $a^{(0)\pm}\left(\mathbf{s}_m^j\right)$ are the wave components of vector $\mathbf{a}\left(\mathbf{s}_m^j\right)$ propagating from face $\mathbb{S}_m^j$ in domain $\mathbb{D}_m$ and from domain $\mathbb{D}_m$ to face $\mathbb{S}_m^j$, respectively. Since the source is located in domain $\mathbb{D}_1$, the feasible source wavefield $\mathbf{a}^{(0)}\left(\mathbf{s}_2^1\right)$ in domain $\mathbb{D}_2$ at face $\mathbb{S}_2^1$ and the feasible source wavefield $\mathbf{a}^{(0)}\left(\mathbf{s}_2^2\right)$ in domain $\mathbb{D}_2$ at face $\mathbb{S}_1^2$ are zero

$$\mathbf{a}^{(0)}\left(\mathbf{s}_2^1\right)=\mathbf{a}^{(0)}\left(\mathbf{s}_2^2\right)=\mathbf{0} \ . \tag{18}$$

Combining all the components of 8×1-vector $\mathbf{a}$ in one vector, we have

$$\mathbf{a}=\begin{pmatrix} \mathbf{a}\left(\mathbf{s}_1\right) \\ \mathbf{a}\left(\mathbf{s}_2\right) \end{pmatrix}, \quad \mathbf{a}_m=\begin{pmatrix} \mathbf{a}\left(\mathbf{s}_m^1\right) \\ \mathbf{a}\left(\mathbf{s}_m^2\right) \end{pmatrix}, \quad \mathbf{a}\left(\mathbf{s}_m^j\right)=\begin{pmatrix} a^{+}\left(\mathbf{s}_m^j\right) \\ a^{-}\left(\mathbf{s}_m^j\right) \end{pmatrix}. \tag{19}$$

Therefore equation (15) will get the form

$$\mathbf{a}=\mathbf{P}\,\mathbf{a}+\mathbf{a}^{(0)}, \tag{20}$$

where $\mathbf{P}$ is the 8×8-matrix composite integral operator

$$\mathbf{P} = \begin{bmatrix} \mathbf{P}(\mathbf{s}_1, \tilde{\mathbf{s}}_1) & \mathbf{O} \\ \mathbf{O} & \mathbf{P}(\mathbf{s}_2, \tilde{\mathbf{s}}_2) \end{bmatrix},$$

$$\mathbf{P}(\mathbf{s}_m, \tilde{\mathbf{s}}_m) = \begin{bmatrix} \mathbf{P}(\mathbf{s}_m^1, \tilde{\mathbf{s}}_m^1) & \mathbf{P}(\mathbf{s}_m^1, \tilde{\mathbf{s}}_m^2) \\ \mathbf{P}(\mathbf{s}_m^2, \tilde{\mathbf{s}}_m^1) & \mathbf{P}(\mathbf{s}_m^2, \tilde{\mathbf{s}}_m^2) \end{bmatrix}, \tag{21}$$

$$\mathbf{P}(\mathbf{s}_m^j, \tilde{\mathbf{s}}_m^{j'}) = \begin{bmatrix} \mathrm{P}^{++}(\mathbf{s}_m^j, \tilde{\mathbf{s}}_m^{j'}) & \mathrm{P}^{+-}(\mathbf{s}_m^j, \tilde{\mathbf{s}}_m^{j'}) \\ \mathrm{P}^{-+}(\mathbf{s}_m^j, \tilde{\mathbf{s}}_m^{j'}) & \mathrm{P}^{--}(\mathbf{s}_m^j, \tilde{\mathbf{s}}_m^{j'}) \end{bmatrix}.$$

Substituting the space-spectral decomposition of the solution $\mathbf{u}(\mathbf{s}_m^j, \omega)$ (12) in the boundary conditions (6), we obtain the boundary conditions rewritten in the form

$$\begin{cases} \mathbf{C}\,\mathbf{H}(\mathbf{s}_1^1, \tilde{\mathbf{s}}_1^1)\,\mathbf{a}(\tilde{\mathbf{s}}_1^1) = \mathbf{J}\,\mathbf{C}\,\mathbf{H}(\mathbf{s}_2^1, \tilde{\mathbf{s}}_2^1)\,\mathbf{a}(\tilde{\mathbf{s}}_2^1), & \text{(a)} \\ \mathbf{C}\,\mathbf{H}(\mathbf{s}_1^2, \tilde{\mathbf{s}}_1^2)\,\mathbf{a}(\tilde{\mathbf{s}}_1^2) = \mathbf{J}\,\mathbf{C}\,\mathbf{H}(\mathbf{s}_2^2, \tilde{\mathbf{s}}_2^2)\,\mathbf{a}(\tilde{\mathbf{s}}_2^2). & \text{(b)} \end{cases} \tag{22}$$

Condition (a) in (22) is a system of 2 equations with respect to the four unknown functions: $a^+(\mathbf{s}_1^1)$, $a^-(\mathbf{s}_1^1)$, $a^+(\mathbf{s}_2^1)$ and $a^-(\mathbf{s}_2^1)$. We rewrite this condition with respect to the two unknown functions $a^+(\mathbf{s}_1^1)$ and $a^-(\mathbf{s}_1^1)$ as follows

$$\mathbf{a}(\mathbf{s}_1^1) = \mathbf{T}(\mathbf{s}_1^1, \tilde{\mathbf{s}}_1^1)\,\mathbf{a}(\tilde{\mathbf{s}}_1^1) + \mathbf{T}(\mathbf{s}_1^1, \tilde{\mathbf{s}}_2^1)\,\mathbf{a}(\tilde{\mathbf{s}}_2^1)\ . \tag{23}$$

Condition (b) in (22) is a system of 2 equation and four unknown functions: $a^+(\mathbf{s}_1^2)$, $a^-(\mathbf{s}_1^2)$, $a^+(\mathbf{s}_2^2)$ and $a^-(\mathbf{s}_2^2)$. We rewrite this condition with respect to the two unknown functions $a^+(\mathbf{s}_1^2)$ and $a^-(\mathbf{s}_1^2)$ in the form

$$\mathbf{a}(\mathbf{s}_1^2) = \mathbf{T}(\mathbf{s}_1^2, \tilde{\mathbf{s}}_1^2)\,\mathbf{a}(\tilde{\mathbf{s}}_1^2) + \mathbf{T}(\mathbf{s}_1^2, \tilde{\mathbf{s}}_2^2)\,\mathbf{a}(\tilde{\mathbf{s}}_2^2)\ . \tag{24}$$

By analogy, we can obtain two more equations

$$\mathbf{a}\left(\mathbf{s}_2^1\right)=\mathbf{T}\left(\mathbf{s}_2^1,\tilde{\mathbf{s}}_2^1\right)\mathbf{a}\left(\tilde{\mathbf{s}}_2^1\right)+\mathbf{T}\left(\mathbf{s}_2^1,\tilde{\mathbf{s}}_2^2\right)\mathbf{a}\left(\tilde{\mathbf{s}}_2^2\right) \tag{25}$$

and

$$\mathbf{a}\left(\mathbf{s}_2^2\right)=\mathbf{T}\left(\mathbf{s}_2^2,\tilde{\mathbf{s}}_1^2\right)\mathbf{a}\left(\tilde{\mathbf{s}}_1^2\right)+\mathbf{T}\left(\mathbf{s}_2^2,\tilde{\mathbf{s}}_2^2\right)\mathbf{a}\left(\tilde{\mathbf{s}}_2^2\right) \ . \tag{26}$$

Combining equations (23)-(26), we obtain the convolution-type transmission equation

$$\mathbf{a}=\mathbf{T}\,\mathbf{a} \ . \tag{27}$$

In (27), we use the transmission operator in 8×8 -form

$$\begin{aligned}
&\mathbf{T}=\begin{bmatrix}\mathbf{T}\left(\mathbf{s}_1,\tilde{\mathbf{s}}_1\right) & \mathbf{T}\left(\mathbf{s}_1,\tilde{\mathbf{s}}_2\right)\\ \mathbf{T}\left(\mathbf{s}_2,\tilde{\mathbf{s}}_1\right) & \mathbf{T}\left(\mathbf{s}_2,\tilde{\mathbf{s}}_2\right)\end{bmatrix},\\
&\mathbf{T}\left(\mathbf{s}_m,\tilde{\mathbf{s}}_{m'}\right)=\begin{bmatrix}\mathbf{T}\left(\mathbf{s}_m^1,\tilde{\mathbf{s}}_{m'}^1\right) & \mathbf{O}\\ \mathbf{O} & \mathbf{T}\left(\mathbf{s}_m^2,\tilde{\mathbf{s}}_{m'}^2\right)\end{bmatrix},\\
&\mathbf{T}\left(\mathbf{s}_m^j,\tilde{\mathbf{s}}_{m'}^j\right)=T\left(\mathbf{s}_m^j,\tilde{\mathbf{s}}_{m'}^j\right)\begin{bmatrix}0 & 1\\ 1 & 0\end{bmatrix},
\end{aligned} \tag{28}$$

where

$$T\left(\mathbf{s}_m^j,\tilde{\mathbf{s}}_{m'}^j\right)=F^{-1}\left(\mathbf{s}_m^j,\overline{\mathrm{k}}\right)\hat{T}_{mm'}\left(\overline{\mathrm{k}},\omega\right)F\left(\overline{\mathrm{k}},\tilde{\mathbf{s}}_{m'}^j\right) \ , \tag{29}$$

$T\left(\mathbf{s}_m^j,\tilde{\mathbf{s}}_{m'}^j\right)$ is the double convolution-type operator over a smooth face, $\hat{T}_{mm'}\left(\overline{\mathrm{k}},\omega\right)$ is the plane-wave transmission (reflection/refraction) coefficients, $F\left(\overline{\mathrm{k}},\tilde{\mathbf{s}}_{m'}^j\right)$ is the space-spectral double Fourier operator over a plane or curved face, and $F^{-1}\left(\mathbf{s}_m^j,\overline{\mathrm{k}}\right)$ is the inverse Fourier operator.

Substituting the transmission equation (27) in the propagation equation (15), we obtain

$$\mathbf{a} = \mathbf{P}\,\mathbf{T}\,\mathbf{a} + \mathbf{a}^{(0)}\,. \tag{30}$$

System (30) is a wave terminology equivalent of the problem statement (9). Iterating once equation (30), we obtain

$$\mathbf{a} = \left[\mathbf{P}\,\mathbf{T}\right]^2 \mathbf{a} + \left\{\mathbf{a}^{(0)} + \mathbf{a}^{(1)}\right\}, \quad \mathbf{a}^{(1)} = \mathbf{P}\,\mathbf{T}\,\mathbf{a}^{(0)}\,, \tag{31}$$

where $\mathbf{a}^{(1)}$ is the feasible single transmitted (reflected / refracted) wavefield. Iterating twice equation (30), we obtain

$$\mathbf{a} = \left[\mathbf{P}\,\mathbf{T}\right]^3 \mathbf{a} + \left\{\mathbf{a}^{(0)} + \mathbf{a}^{(1)} + \mathbf{a}^{(2)}\right\}, \quad \mathbf{a}^{(2)} = \mathbf{P}\,\mathbf{T}\,\mathbf{a}^{(1)}\,, \tag{32}$$

where $\mathbf{a}^{(2)}$ is the feasible double transmitted (reflected / refracted) wavefield. After N iterations, equation (30) will have the form

$$\mathbf{a} = \left[\mathbf{P}\,\mathbf{T}\right]^{N+1} \mathbf{a} + \left\{\sum_{n=0}^{n=N} \mathbf{a}^{(n)}\right\}, \quad \mathbf{a}^{(n)} = \mathbf{P}\,\mathbf{T}\,\mathbf{a}^{(n-1)} \quad n = \overline{1, N}\,, \tag{33}$$

where $\mathbf{a}^{(n)}$ is the feasible n-times transmitted (reflected / refracted) wavefield. The sum $\mathbf{a} = \lim_{N\to\infty}\left\{\sum_{n=0}^{n=N} \mathbf{a}^{(n)}\right\}$ is the solution of (30), see A.M. Aizenberg *et al.* (2011) and A.M. Aizenberg *et al.* (2014).

After substituting operators (21) and (28) into (31), we obtain

$$\begin{aligned}
\mathbf{a}^{(1)} = \begin{pmatrix} \mathbf{a}^{(1)}(\mathbf{s}_1) \\ \mathbf{a}^{(1)}(\mathbf{s}_2) \end{pmatrix} &= \begin{bmatrix} \mathbf{P}(\mathbf{s}_1, \breve{\mathbf{s}}_1) & \mathbf{O} \\ \mathbf{O} & \mathbf{P}(\mathbf{s}_2, \breve{\mathbf{s}}_2) \end{bmatrix} \begin{bmatrix} \mathbf{T}(\breve{\mathbf{s}}_1, \tilde{\mathbf{s}}_1) & \mathbf{T}(\breve{\mathbf{s}}_1, \tilde{\mathbf{s}}_2) \\ \mathbf{T}(\breve{\mathbf{s}}_2, \tilde{\mathbf{s}}_1) & \mathbf{T}(\breve{\mathbf{s}}_2, \tilde{\mathbf{s}}_2) \end{bmatrix} \begin{pmatrix} \mathbf{a}_1^{(0)}(\tilde{\mathbf{s}}_1) \\ 0 \end{pmatrix} = \\
&= \begin{pmatrix} \mathbf{P}(\mathbf{s}_1, \tilde{\mathbf{s}}_1)\,\mathbf{T}(\breve{\mathbf{s}}_1, \tilde{\mathbf{s}}_1)\,\mathbf{a}^{(0)}(\tilde{\mathbf{s}}_1) \\ \mathbf{P}(\mathbf{s}_2, \tilde{\mathbf{s}}_2)\,\mathbf{T}(\breve{\mathbf{s}}_2, \tilde{\mathbf{s}}_1)\,\mathbf{a}^{(0)}(\tilde{\mathbf{s}}_1) \end{pmatrix}.
\end{aligned} \tag{34}$$

After substituting operators (21) and (28) into (32), we obtain

$$
\begin{aligned}
\mathbf{a}^{(2)} &= \begin{pmatrix} \mathbf{a}^{(2)}(\mathbf{s}_1) \\ \mathbf{a}^{(2)}(\mathbf{s}_2) \end{pmatrix} = \begin{bmatrix} \mathbf{P}(\mathbf{s}_1, \breve{\mathbf{s}}_1) & \mathbf{O} \\ \mathbf{O} & \mathbf{P}(\mathbf{s}_2, \breve{\mathbf{s}}_2) \end{bmatrix} \begin{bmatrix} \mathbf{T}(\breve{\mathbf{s}}_1, \tilde{\mathbf{s}}_1) & \mathbf{T}(\breve{\mathbf{s}}_1, \tilde{\mathbf{s}}_2) \\ \mathbf{T}(\breve{\mathbf{s}}_2, \tilde{\mathbf{s}}_1) & \mathbf{T}(\breve{\mathbf{s}}_2, \tilde{\mathbf{s}}_2) \end{bmatrix} \begin{pmatrix} \mathbf{a}^{(1)}(\tilde{\mathbf{s}}_1) \\ \mathbf{a}^{(1)}(\tilde{\mathbf{s}}_2) \end{pmatrix} = \\
&= \begin{pmatrix} \mathbf{P}(\mathbf{s}_1, \breve{\mathbf{s}}_1)\,\mathbf{T}(\breve{\mathbf{s}}_1, \tilde{\mathbf{s}}_1)\,\mathbf{a}^{(1)}(\tilde{\mathbf{s}}_1) + \mathbf{P}(\mathbf{s}_1, \breve{\mathbf{s}}_1)\,\mathbf{T}(\breve{\mathbf{s}}_1, \tilde{\mathbf{s}}_2)\,\mathbf{a}^{(1)}(\tilde{\mathbf{s}}_2) \\ \mathbf{P}(\mathbf{s}_2, \breve{\mathbf{s}}_2)\,\mathbf{T}(\breve{\mathbf{s}}_2, \tilde{\mathbf{s}}_1)\,\mathbf{a}^{(1)}(\tilde{\mathbf{s}}_1) + \mathbf{P}(\mathbf{s}_2, \breve{\mathbf{s}}_2)\,\mathbf{T}(\breve{\mathbf{s}}_2, \tilde{\mathbf{s}}_2)\,\mathbf{a}^{(1)}(\tilde{\mathbf{s}}_2) \end{pmatrix}.
\end{aligned}
\tag{35}
$$

The first component $\mathbf{a}^{(2)}(\mathbf{s}_1)$ of (35) is the wavefield coming to the receivers, while the second component $\mathbf{a}^{(2)}(\mathbf{s}_2)$ is the wavefield propagating away from the receivers which is not of our interest. We can represent the first component as

$$
\mathbf{a}^{(2)}(\mathbf{s}_1) = \mathbf{P}(\mathbf{s}_1, \breve{\mathbf{s}}_1)\,\mathbf{T}(\breve{\mathbf{s}}_1, \tilde{\mathbf{s}}_1)\,\mathbf{a}^{(1)}(\tilde{\mathbf{s}}_1) + \mathbf{P}(\mathbf{s}_1, \breve{\mathbf{s}}_1)\,\mathbf{T}(\breve{\mathbf{s}}_1, \tilde{\mathbf{s}}_2)\,\mathbf{a}^{(1)}(\tilde{\mathbf{s}}_2) \ . \tag{36}
$$

The term $\mathbf{P}(\mathbf{s}_1, \breve{\mathbf{s}}_1)\,\mathbf{T}(\breve{\mathbf{s}}_1, \tilde{\mathbf{s}}_1)\,\mathbf{a}^{(1)}(\tilde{\mathbf{s}}_1)$ is zero since we do not consider the reflection $\mathbf{T}(\breve{\mathbf{s}}_1, \tilde{\mathbf{s}}_1) = \mathbf{O}$, therefore

$$
\mathbf{a}^{(2)}(\mathbf{s}_1) \approx \mathbf{P}(\mathbf{s}_1, \breve{\mathbf{s}}_1)\,\mathbf{T}(\breve{\mathbf{s}}_1, \tilde{\mathbf{s}}_2)\,\mathbf{a}^{(1)}(\tilde{\mathbf{s}}_2) \ . \tag{37}
$$

In the paper, we are evaluating the primary wavefield

$$
\mathbf{a}^{\text{primary}}(\mathbf{x}_1) = \mathbf{a}^{(0)}(\mathbf{x}_1) + \mathbf{a}^{(2)}(\mathbf{x}_1) \ , \tag{38}
$$

which is the superposition of the double-transmitted wavefield $\mathbf{a}^{(2)}(\mathbf{s}_1)$ (36) and the source wavefield at the receiver line 1 $\mathbf{a}^{(0)}(\mathbf{s}_1)$ (formulae (70)-(71) in A.A. Ayzenberg *et al.* (2015a)/Chapter 3 of this thesis). The wavefield $\mathbf{a}^{(2)}(\mathbf{s}_1)$ is performed in five stages: the propagation in domain $\mathbb{D}_1$ from the source to interface $\mathbb{S}_1$; the transmission from interface $\mathbb{S}_1$ of domain $\mathbb{D}_1$ to interface $\mathbb{S}_2$ of domain $\mathbb{D}_2$; the propagation in domain $\mathbb{D}_2$ within its interface $\mathbb{S}_2$ from each to each point; the transmission from interface $\mathbb{S}_2$ of domain $\mathbb{D}_2$ back to interface $\mathbb{S}_1$ of domain $\mathbb{D}_1$; and then the propagation in domain $\mathbb{D}_1$ from its interface $\mathbb{S}_1$ to the receiver line 1.

At stage 1, we compute the 2-terms-approximation of the source wavefield at interface $\mathbb{S}_1$ (A.M. Aizenberg & A.A. Ayzenberg *et al.* (2015)/Chapter 2 of this thesis)

$$\mathbf{a}^{(0)}(\mathbf{s}_1) = \mathbf{a}_{\mathbf{G}}^{(0)}(\mathbf{s}_1) + \mathbf{P}_{\mathbf{G}}(\mathbf{s}_1, \breve{\mathbf{s}}_1)\,\mathbf{P}_{h\,\mathbf{G}}(\breve{\mathbf{s}}_1, \tilde{\mathbf{s}}_1)\mathbf{a}_{\mathbf{G}}^{(0)}(\tilde{\mathbf{s}}_1) \ , \tag{39}$$

where $\mathbf{P}_{\mathbf{G}}(\mathbf{s}_1, \breve{\mathbf{s}}_1)$ is the propagation integral operator in domain $\mathbb{D}_1$ (formula (11) from A.M. Aizenberg & A.A. Ayzenberg (2015)/Chapter 2 of this thesis), $\mathbf{P}_{h\,\mathbf{G}}(\breve{\mathbf{s}}_1, \tilde{\mathbf{s}}_1)$ is the absorption operator in domain $\mathbb{D}_1$ by formula (30) from A.M. Aizenberg & A.A. Ayzenberg (2015)/Chapter 2 of this thesis and $\mathbf{a}_{\mathbf{G}}^{(0)}(\tilde{\mathbf{s}}_1)$ is the free-space source wavefield as in A.A. Ayzenberg *et al.* (2015a)/Chapter 3 of this thesis.

At stage 2, we obtain the transmitted wavefield from interface $\mathbb{S}_1$ to interface $\mathbb{S}_2$

$$\mathbf{a}^{(1)}(\mathbf{s}_2) = \mathbf{T}(\mathbf{s}_2, \tilde{\mathbf{s}}_1)\,\mathbf{a}^{(0)}(\tilde{\mathbf{s}}_1) \ , \tag{40}$$

where $\mathbf{T}(\mathbf{s}_2, \tilde{\mathbf{s}}_1)$ is the transmission operator through the upper interface (M.A. Ayzenberg *et al.* (2007)).

At stage 3, we perform the propagation of the wavefield at points $\mathbf{x}_2$ of medium $\mathbb{D}_2$ and within points $\mathbf{s}_2$ of interface $\mathbb{S}_2$

$$\begin{aligned} \mathbf{a}^{(1)}(\mathbf{x}_2) &= \mathbf{P}_{\mathbf{G}}(\mathbf{x}_2, \tilde{\mathbf{s}}_2)\,\mathbf{a}^{(1)}(\tilde{\mathbf{s}}_2), \\ \mathbf{a}^{(1)}(\mathbf{s}_2) &= \mathbf{P}_{\mathbf{G}}(\mathbf{s}_2, \tilde{\mathbf{s}}_2)\,\mathbf{a}^{(1)}(\tilde{\mathbf{s}}_2), \end{aligned} \tag{41}$$

where $\mathbf{P_G}\left(\mathbf{x}_2, \tilde{\mathbf{s}}_2\right)$ and $\mathbf{P_G}\left(\mathbf{s}_2, \tilde{\mathbf{s}}_2\right)$ are the propagation operator at points of domain $\mathbb{D}_2$ and within points of interface $\mathbb{S}_2$.

At stage 4, we perform the transmission wavefield from interface $\mathbb{S}_2$ to interface $\mathbb{S}_1$ in the form

$$\mathbf{a}^{(2)}\left(\mathbf{s}_1\right) = \mathbf{T}\left(\mathbf{s}_1, \tilde{\mathbf{s}}_2\right) \mathbf{a}^{(1)}\left(\tilde{\mathbf{s}}_2\right) \ , \tag{42}$$

where $\mathbf{T}\left(\mathbf{s}_1, \tilde{\mathbf{s}}_2\right)$ is the transmission operator from interface $\mathbb{S}_2$ to interface $\mathbb{S}_1$ as described in M.A. Ayzenberg *et al.* (2007).

At stage 5, we obtain the double-transmitted wavefield at the receiver line 1

$$\mathbf{a}^{(2)}\left(\mathbf{x}_1\right) = \left[\mathbf{P_G}\left(\mathbf{x}_1, \mathbf{s}_1\right) + \mathbf{P_G}\left(\mathbf{x}_1, \mathbf{s}_1\right) \mathbf{P}_{h\mathbf{G}}\left(\mathbf{s}_1, \breve{\mathbf{s}}_1\right) \mathbf{P_G}\left(\breve{\mathbf{s}}_1, \tilde{\mathbf{s}}_1\right)\right] \mathbf{a}^{(2)}\left(\tilde{\mathbf{s}}_1\right), \tag{43}$$

where $\mathbf{P_G}\left(\mathbf{x}_1, \mathbf{s}_1\right)$ is the propagation operator from interface $\mathbb{S}_1$ to the receiver line 1 in domain $\mathbb{D}_1$ (formula (41) from A.A. Ayzenberg *et al.* (2015a)/Chapter 3 of this thesis) and $\mathbf{P}_{h\mathbf{G}}\left(\mathbf{s}_1, \breve{\mathbf{s}}_1\right)$ is the absorption operator in domain $\mathbb{D}_1$ by formula (42) from A.A. Ayzenberg *et al.* (2015a)/Chapter 3 of this thesis. We rewrite formula (43) in a short form without arguments, for simplicity

$$\mathbf{a}^{(2)} = \left[\mathbf{P_G} + \mathbf{P_G}\ \mathbf{P}_{h\mathbf{G}}\ \mathbf{P_G}\right] \mathbf{T}\ \mathbf{P_G}\ \mathbf{T}\left[\mathbf{a}_{\mathbf{G}}^{(0)} + \mathbf{P_G}\ \mathbf{P}_{h\mathbf{G}}\ \mathbf{a}_{\mathbf{G}}^{(0)}\right] \ . \tag{44}$$

This formula has corrections accounting for shadow $\mathbf{P_G}\ \mathbf{P}_{h\mathbf{G}}\ \mathbf{a}_{\mathbf{G}}^{(0)}$ in the point-source wavefield and $\mathbf{P_G}\ \mathbf{P}_{h\mathbf{G}}\ \mathbf{P_G}$ in the propagation operator to the receiver line 1. We therefore can analyse how strong the impact of the correction in the formula dividing the formula into four parts: the noncorrected part (mark a); the correction in the source wavefield (mark b); the correction in the propagation to the receiver line 1 (mark c); and the correction to the source wavefield and the receiver line 1 (mark d) as follows

$$
\begin{aligned}
\mathbf{a}^{(2)} = & \left[\mathbf{P}_{\mathbf{G}}\right] \mathbf{T}\, \overset{a}{\mathbf{P}_{\mathbf{G}}}\, \mathbf{T} \left[\mathbf{a}_{\mathbf{G}}^{(0)}\right] + \\
& + \left[\mathbf{P}_{\mathbf{G}}\right] \mathbf{T}\, \mathbf{P}_{\mathbf{G}}\, \overset{b}{\mathbf{T}} \left[\mathbf{P}_{\mathbf{G}}\, \mathbf{P}_{h\mathbf{G}}\, \mathbf{a}_{\mathbf{G}}^{(0)}\right] + \\
& + \left[\mathbf{P}_{\mathbf{G}}\, \mathbf{P}_{h\mathbf{G}}\, \mathbf{P}_{\mathbf{G}}\right] \overset{c}{\mathbf{T}}\, \mathbf{P}_{\mathbf{G}}\, \mathbf{T} \left[\mathbf{a}_{\mathbf{G}}^{(0)}\right] + \\
& + \left[\mathbf{P}_{\mathbf{G}}\, \mathbf{P}_{h\mathbf{G}}\, \mathbf{P}_{\mathbf{G}}\right] \mathbf{T}\, \overset{d}{\mathbf{P}_{\mathbf{G}}}\, \mathbf{T} \left[\mathbf{P}_{\mathbf{G}}\, \mathbf{P}_{h\mathbf{G}}\, \mathbf{a}_{\mathbf{G}}^{(0)}\right].
\end{aligned}
\tag{45}
$$

The evaluation (visualization) of the primary wavefield (38) can be, therefore, done by taking the superposition of $\mathbf{a}^{(2)}$ by formula (45) and $\mathbf{a}^{(0)}$ (formulae (70)-(71) in A.A. Ayzenberg *et al.* (2015a)/Chapter 3 of this thesis). In this paper, we perform the modeling of $\mathbf{a}^{(2)}$ by formula (45) using (17)-(43) by the Tip-Wave Superposition Method (TWSM) from A.M. Aizenberg *et al.* (2011); after that we add $\mathbf{a}^{(0)}$ (formulae (29)-(30) in A.A. Ayzenberg *et al.* (2015a)/Chapter 3 of this thesis) to the result. The primary wavefield (38) has been computed on a GPU cluster in order to obtain a seismogram (Zyatkov *et al.* (2015)).

5.5 Wavefield below overhang

V-overhang

Figure 3 represents the single-transmitted wavefield at the receiver line 2 which is the superposition of the transmitted wave from domain $\mathbb{D}_1$ to domain $\mathbb{D}_2$ by formulae (40)-(41) and the edge wave diffracted by the edge by formula (41). The edge wave has a linear traveltime and a weak amplitude in comparison to the single-transmitted wave. Figures 4a performs a-term of the double-transmitted wavefield in domain $\mathbb{D}_1$ computed at the receiver line 1 by formula (45). Figure 4b illustrates the sum of b,c,d-terms of the double-transmitted wavefield in domain $\mathbb{D}_1$ computed at the receiver line 1 by formula (45). This seismogram is zero, therefore the shadow correction is zero for V-model. Figure 4c represents the double-transmitted wavefield (the sum of a,b,c,d-terms) in domain $\mathbb{D}_1$ computed at the receiver line 1 by formula (45). The shadow boundary of the double-transmitted wavefield crosses the receiver line 1 at $x = 4.466\,\mathrm{km}$ approximately. At $x > 4.466\,\mathrm{km}$, we can see the diffracted wave only. At $x < 4.466\,\mathrm{km}$, we can see the double-transmitted wave in superposition with the diffracted wavefield. The primary wavefield at the receiver line 1 (38) is demonstrated on Figure 5.

U-overhang

Figure 6 represents the single-transmitted wavefield at the receiver line 2 which is the superposition of the transmitted wave from domain $\mathbb{D}_1$ to domain $\mathbb{D}_2$ by formula (40)-(41) and the edge wave diffracted by the edge by formula (41). The diffraction occurs due to the amplitude discontinuity at the tangency line $(4.0\,\mathrm{km}, 0.0\,\mathrm{km}, \mathrm{y}\,\mathrm{km})$ of the parabola. It has a weak amplitude in comparison to the single-transmitted wavefield. Figures 7a performs a-term of the double-transmitted wavefield in domain $\mathbb{D}_1$ computed at the receiver line 1 by formula (45). Figure 7b illustrates the sum of b,c,d-terms of the double-transmitted wavefield in domain $\mathbb{D}_1$ computed at the receiver line 1 by formula (45). This seismogram is almost zero for U-model but a bit larger than for V-model. We suppose that for more complex interfaces, this effect will be more visible. In this paper, we do not consider more complex interfaces and we leave this for future investigations. Figure 7c represents the double-transmitted wavefield (the sum of a,b,c,d-terms) in domain $\mathbb{D}_1$ computed at the receiver line 1 by formula (45). The shadow zone for the receiver line 1 is defined by $x > 4.8\,\mathrm{km}$. Figure 8 demonstrates the source wavefield. The primary wavefield at the receive line 1 (38) is calculated by analogy to the V-model test and demonstrated on Figure 9. The primary wavefield is the superposition of the direct, double-transmitted and diffracted wavefields which compose two separate events. The retarded wavefield with later time arrivals is the source wavefield with its diffraction component. The advanced wave with earlier time arrivals represents the double-transmitted wavefield with its diffraction component.

5.6 Conclusions

We performed a detailed wavefield description in the shadow and lit zone of V- and U-overhang block models. Shadow is caused by velocity contrast: V- and U-overhangs have strong velocity similar to salt body, while surrounding domain has weak velocity close to sediments. The solution is obtained by TPOT theory and represents the primary wavefield which is the superposition of the source wavefield and the double-transmitted wavefield. The source and double-transmitted wavefield are based on ‘feasible fundamental solution’ and ‘feasible propagation operator’ of the domain of the given medium. The primary solution is visualized by TWSM visualization approach with 2-term approximation for both feasible fundamental solution and for the feasible propagation operator. The seismograms represent the primary solution and its terms separately and in combinations in order to demonstrate the impact of the shadow correction. For V- and U-overhang, the primary wavefield seismogram demonstrates that the wavefield has a complex shape with several waves. The separate wave description, demonstrated on the seismograms, is one of the advantages of the TPOT theory and the TWSM visualization.

5.7 Acknowledgements

Alena Ayzenberg and Alexey Stovas acknowledge NTNU and the Research Centre of Statoil ASA (Trondheim, Norway). We express our deep respect and sorrow for Kamill D. Klem-Musatov who recently passed away, and who encouraged our research very strongly. We are thankful to our colleagues and friends Hans B. Helle, Jan Pajchel, Ola-Petter Munkvold, Milana Ayzenberg, Kees Wapenaar, Wiktor Weibull, Kamal'deen Omosanya, Gennady Demidenko, Gleb Dyatlov, Fredrik Andersson, Anton Duchkov and Alexey Romanenko for constructive discussions.

5.8 References

Aizenberg, A.M. & Ayzenberg, A.A., 2015. Feasible fundamental solution of the multiphysics wave equation in inhomogeneous domain of complex shape, Wave Motion, 53, 66-79.

Aizenberg, A.M., Ayzenberg, M.A. & Klem-Musatov, K.D., 2011. Seismic diffraction modeling with the tip-wave superposition method, Extended Abstracts, 73-th EAGE Conference, Vienna, Austria, B018.

Aizenberg, A.M., Zyatkov, N.Y., Ayzenberg, A.A. & Rakshaeva, E.Z., 2014. New concepts of the transmission-propagation operator theory in seismic diffraction modeling and interpretation, Extended Abstracts, 76^{th} EAGE Conference, Amsterdam, Netherlands, We-P06-07.

Ayzenberg, A., Zyatkov, N., Stovas, A. & Aizenberg, A.M., 2013. Double-diffraction approximation of the feasible Green's function in geometrical shadow zones, Extended Abstracts, 75^{th} EAGE Conference, London, UK, Th-P02-10.

Ayzenberg, A., Zyatkov, N., Aizenberg, A.M. & Stovas, A., 2015a. Feasible source wavefield for acoustic V-model with shadow in form of double diffraction approximation , Geophys. J. Int., (in review).

Ayzenberg, A., Zyatkov, N., Aizenberg, A.M. & Stovas, A., 2015b. Feasible source wavefield for acoustic U- and W-model with shadow in form of double diffraction approximation, Geophys. J. Int., (in review).

Ayzenberg, M.A., Aizenberg, A.M., Helle, H.B., Klem-Musatov, K.D., Pajchel, J. & Ursin, B., 2007. 3D diffraction modeling of singly scattered acoustic wavefields based on the combination of surface integral propagators and transmission operators, Geophysics, 72, 5, SM19-SM34.

Ayzenberg, M., Tsvankin, I., Aizenberg, A.M. & Ursin, B., 2009. Effective refection coefficients for curved interfaces in TI media, Geophysics, 74, WB33-WB53.

Klem-Musatov, K.D., Aizenberg, A.M., Pajchel, J., & Helle, H.B., 2008. Edge and Tip Diffractions: Theory and Applications in Seismic Prospecting, Geophysical Monograph Series, No. 14, SEG, Tulsa, USA.

Rakshaeva, E.Z., Nefedkina, T.V., Aizenberg A.M., Vilegzhanin, & R.I. Lykhin P.A., 2015. AVO inversion of post-critical PP reflections from curved interfaces based on modified effective reflection coefficients, Extended Abstracts, 77th EAGE Conference, Madrid, Spain, We-N110-04.

Tantsereva, A., Ursin, B., Favretto-Cristini, N., Cristini, P., & Aizenberg, A.M., 2014. Numerical modeling of three-dimensional zero-offset laboratory data by a discretized Kirchhoff integral, Geophysics, V. 77 (2), pp. T77-T90.

Wapenaar, K., 2007. General representations for wavefield modeling and inversion in geophysics, Geophysics, 72, 5, SM5-SM17.

Zyatkov, N., Ayzenberg, A.A., & Aizenberg, A.M., 2015. Highly-optimized TWSM software package for seismic diffraction modeling adapted for GPU-cluster, Geophysical research abstracts, EGU General Assembly, Vienna, Austria. Vol. 17, EGU2015-706.

5.9 List of Figures

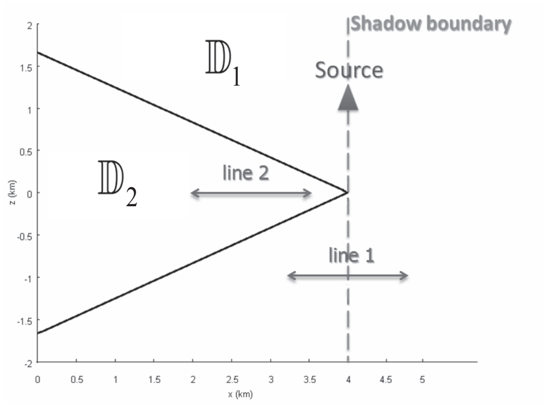

Figure 1. Sketch of V-model.

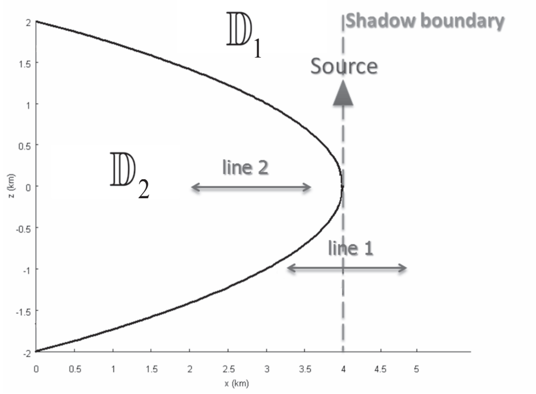

Figure 2. Sketch of U-model.

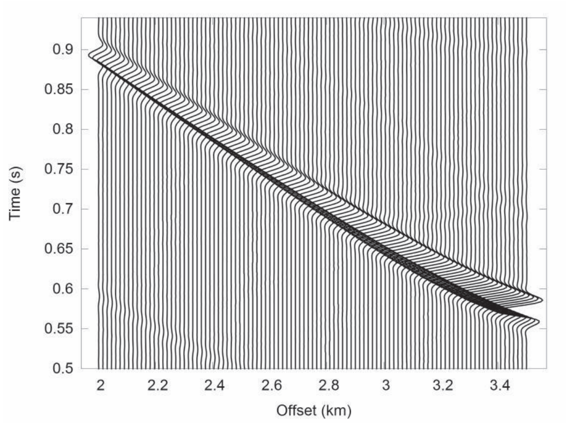

Figure 3. V-model, line 2: single-transmission $a^{(1)-}$.

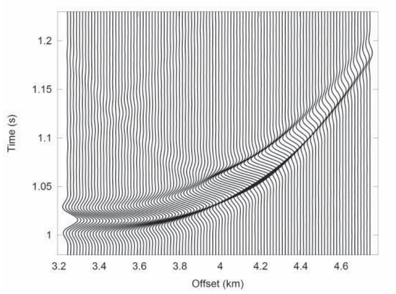

Figure 4a. V-model, line 1:
a-term of double-transmission $a^{(2)-}$.

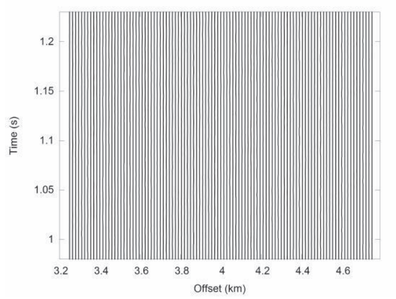

Figure 4b. V-model, line 1:
sum of b,c,d-terms of double-transmission $a^{(2)-}$.

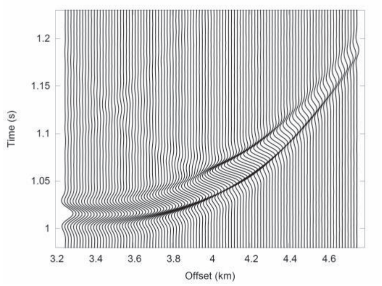

Figure 4c. V-model, line 1:
double-transmission $a^{(2)-}$.

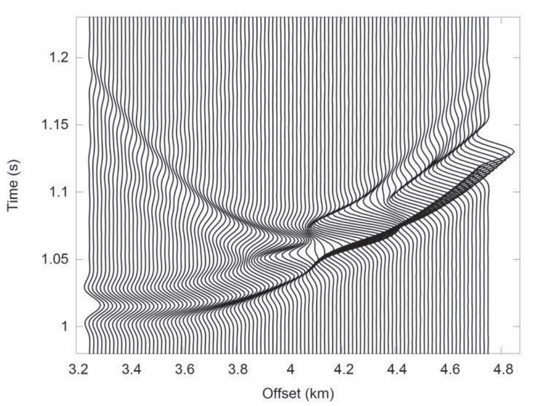

Figure 5. V-model, line 1: primary wavefield $a^{(0)-} + a^{(2)-}$.

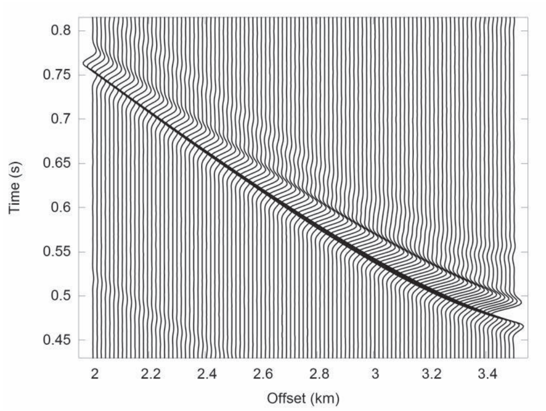

Figure 6. U-model, line 2: single-transmission $a^{(1)-}$.

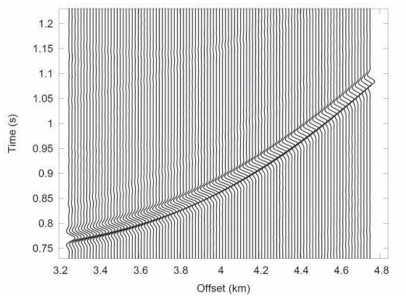

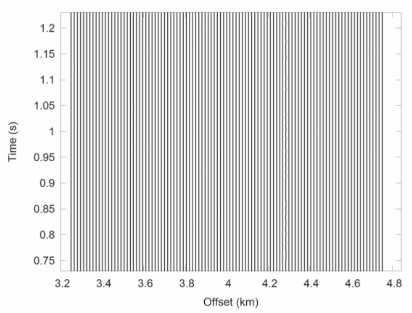

Figure 7a. U-model, line 1: a-term of double-transmission $a^{(2)-}$.

Figure 7b. U-model, line 1: sum of b,c,d-terms of double-transmission $a^{(2)-}$.

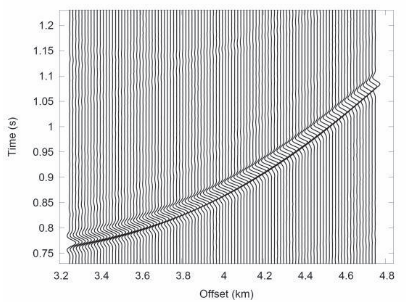

Figure 7c. U-model, line 1: double-transmission $a^{(2)-}$.

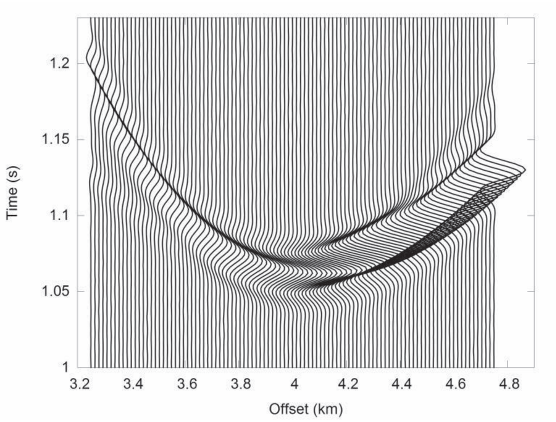

Figure 8. U-model, line 1: source wavefield $a^{(0)-}$.

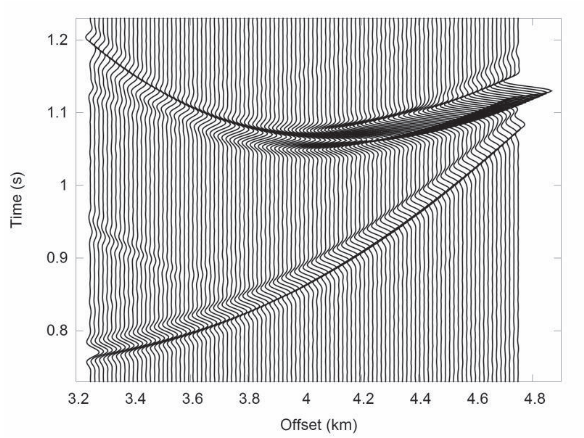

Figure 9. U-model, line 1: primary wavefield $a^{(0)-} + a^{(2)-}$.

Closing remarks

Models. We consider 3D 2-block models with V- U- and W-shaped interfaces simulating a geological salt overhang. We choose a contrast velocities case in order to simulate shadow below the overhang similar to shadow below a geological salt body. A source is placed above the overhang and a receiver line is located below the overhang so that the right half-part of the receivers is in the illuminated zone while the left half-part is in the shadow zone.

TPOT and FFS. We perform a detailed wavefield description at the receiver line in terms of primary (near-front) wavefield. The primary wavefield is obtained by TPOT and represents the superposition of the source wavefield and the double-transmitted wavefield. Both the source and double-transmitted wavefields contain so-called 'feasible fundamental solutions' (FFS) and 'feasible propagation operators' which account for shadow in the model. The feasible fundamental solutions and propagation operators have the form of infinite series with the composite operator of norm less than 1, which provides the necessary convergence of the series. The first term of the series represents the free space fundamental solution and the free space propagation operator (based on the Kirchhoff operator) correspondingly, all the higher order terms are cascade diffraction terms, which account for shadow.

TWSM. The primary wavefield is visualized by TWSM on a GPU cluster. This programming code uses two types of approximation: 1) an interface triangulation which leads to an approximation of the propagation integral operator by a tip-wave beam matrix, where each narrow beam corresponds to the wave propagation from a small triangle at the interface; 2) a truncation of the series for the 'feasible propagation operator' and the 'feasible fundamental solution' after the second term. The seismograms represent the primary wavefield and its terms separately and in combinations in order to demonstrate the impact of the shadow correction. For the models, the primary wavefield seismograms perform a complex wavefield with a combination of several waves.

Advantages of TPOT&TWSM. TPOT and its TWSM software package differ conceptually from the numerical methods being exploited for direct and inverse seismic problems. They solve the equation system in terms of the total wavefield while TPOT provides the solution with possibility of wave fragments separation. TPOT gives the rigorous explicit solution of the medium particles oscillation system in terms of the mathematical wave theory. This solution represents the total wavefield and its wave structure. Since the solution is analytical, there is no need to use a discretization of the equation system. The solution visualization by TWSM gives a seismogram of any separate wave fragment or group of them in the mid-frequency range. This means that the approach is applied to primaries computation (multiples removal).

Comparisons. The TWSM algorithm of TPOT was compared to laboratory methods, other theoretical approaches and the finite difference method. The relative error of the computation of any wave fragment does not depend on its amplitude. Since the relative error is universal for each wave fragment, the relative error does not change when the amplitude changes. The comparison with laboratory data demonstrates an error of 1-4 percent approximately. The comparison with the edge wave theory gives a 3-4 percent error. The comparison with the finite difference method demonstrates the error of 3 percent approximately.